# AZIMUTHAL DISTRIBUTIONS IN INTERMEDIATE ENERGY HEAVY-ION COLLISIONS

By

William Kenneth Wilson

A DISSERTATION

Submitted to
Michigan State University
in partial fulfillment of the requirements
for the Degree of

DOCTOR OF PHILOSOPHY

Department of Physics and Astronomy

1991

ABSTRACT

AZIMUTHAL DISTRIBUTIONS IN INTERMEDIATE ENERGY HEAVY-ION COLLISIONS

By

William Kenneth Wilson

The azimuthal distributions of light particles (Z=1,2) with respect to the entrance channel reaction plane are investigated with a view towards characterizing the modes of collective motion in intermediate energy heavy-ion collisions. A new technique for reaction plane determination from the distribution of light particles produced in a collision is developed and applied to Ar+V data. The data were acquired using the MSU $4\pi$ Array, a new 215 element large solid angle detector system. At a beam energy of 35 MeV/nucleon, light charged particles are found to exhibit an enhanced emission in the reaction plane which increases with the mass of the detected particle. As the beam energy is increased to 100 MeV/nucleon, the anisotropy nearly vanishes, providing clues to the dynamics of these reactions in a transitional energy regime.

The observed anisotropy contains signatures of two distinct modes of collective motion: attractive mean field deflection, and rotation of the fused system. A microscopic calculation based on mean-field mediated interactions plus nucleon-nucleon collisions reproduces both forms of collective motion and their associated azimuthal distributions. The calculation also suggests that the anisotropy due to mean-field deflection is established during the initial stages of the collision.

The nature of the nuclear mean-field is further explored using data taken by the

$4\pi$ Array for peripheral 50 MeV/nucleon C induced reactions on C and Au targets. Although projectile fragments in grazing collisions are positively deflected by the coulomb force, a specific set of protons are found to be simultaneously attractively deflected by the mean-field towards the opposite side of the reaction plane. This direct observation of attractive mean field deflection supports aspects of the interpretation of the Ar+V data.

Lastly, the experimental results are summarized and the potential for extracting more information about the dynamics of heavy-ion collisions using azimuthal distributions is assessed. The key areas of promising future experimental research in this subject are delineated along with the outstanding problems to be solved.

Dedicated with love to Mary.

# ACKNOWLEDGEMENTS

A heartfelt "thank you" goes to my research advisor, Gary Westfall. Without Gary's blend of patience, encouragement, and enthusiasm, it would not have been possible for me to reach the end of this project. More importantly, Gary's irrepressible sense of humor made the process fun. I benefited from his guidance and teaching during each step of the experiments and analysis. Whoop.

This work was also shaped by important contributions from Craig Ogilvie and Roy Lacey. It was a joy discussing my analysis with them and leaving a trail of "Hindenburgs" on the blackboards all over the lab. Special credit must be given to Craig, who originally developed the reaction plane determination technique presented in chap. 3.

Several people deserve thanks for their generosity in donating their time to various aspects of this project. Wolfgang Bauer performed the theoretical calculations presented in chap. 6, and guided me in their interpretation. Skip Vandermolen, Pawel Danielewicz, and Dennis Swan answered innumerable questions, and seemed to enjoy pondering each new problem I brought to them. Len Morris turned my rough sketches into functioning detector mounts for the Forward Array. Chadin Djalali, David Kroftcheck, and Thierry Reposeur provided moral support.

It has been a pleasure working with the other graduate students at the Cyclotron Lab, past and present. Jim Clayton, Dan Fox, Dan Cebra, Jeff Karn, Steve Howden, Mats Cronqvist, Brian Young, and Tong Li have helped, encouraged, and shared their knowledge with me, making this project easier than it would have been otherwise.

I owe a great debt to my parents and my wife for putting up with the agony and ecstasy of a physics graduate student. My parents displayed unshakable confidence in me, and supported all of my decisions that led me over a circuitous route to this

final result. My wife Mary Samuel generously gave of herself to help me through the darkest times, and so I dedicate this thesis to her. Since she read and commented on this thesis, she is literally on every page.

Advice from Epictetus (ca. 50-138 A.D.) "*When a man is proud because he can understand and explain the writings of Chrysippus, say to yourself, 'If Chrysippus had not written obscurely, this man would have nothing to be proud of.'* "

# Contents

**LIST OF TABLES** x

**LIST OF FIGURES** xi

**1 Introduction** 1

1.1 Organization . . . . . 2

1.2 The Bulk Properties of Nuclear Matter . . . . . 3

1.3 Review of Results from Relativistic Heavy-Ion Collisions . . . . . 6

1.4 Extension to Lower Beam Energies . . . . . 19

1.5 Earlier Observations of Collective Motion in Intermediate Energy Collisions . . . . . 24

**2 Description of the $4\pi$ Array Experiments** 27

2.1 Beam and Target . . . . . 27

2.2 Detector Geometry . . . . . 28

2.3 Detector Design . . . . . 29

2.4 Calibration . . . . . 39

2.5 Triggering . . . . . 40

2.6 Momentum Acceptance . . . . . 41

2.7 Simple Observables . . . . . 41

**3 Reaction Plane Determination** **48**

3.1 Introduction . . . . . 48

3.2 Previously Established Techniques . . . . . 50

3.3 Preliminary Analysis . . . . . 52

3.4 The Azimuthal Correlation Method . . . . . 53

3.5 Checks of the New Technique . . . . . 64

3.6 Comparison with Transverse Momentum Analysis . . . . . 68

3.7 Accuracy . . . . . 71

**4 Azimuthal Anisotropies and Collective Motion** **82**

4.1 Introduction . . . . . 82

4.2 Effects of Collective Motion on Azimuthal Distributions . . . . . 83

4.3 Parameterization of Azimuthal Distributions . . . . . 87

4.4 The Influence of Detector Acceptance . . . . . 93

4.5 35 MeV/nucleon Ar+V Data . . . . . 97

4.6 Beam Energy Dependence . . . . . 103

4.7 Summary . . . . . 111

**5 Comparison With Theory** **112**

5.1 Introduction . . . . . 112

5.2 Background on the Rotating Sphere Model . . . . . 113

5.3 Particle Emission From a Rotating Sphere . . . . . 114

5.4 Comparison of Rotating Sphere With Data . . . . . 116

5.5 Deformation . . . . . 119

5.6 Decay Channels of Rotating Systems . . . . . 123

5.7 Description of the BUU Approach to Solving Nuclear Dynamics . . . 125

5.8 The Direction of the Flow . . . . . 128

5.9 Goals of our BUU Calculation . . . . . 129

5.10 Initial Conditions Used in the BUU Calculation . . . . . 132

5.11 Results of the BUU Calculation 1: The Residue . . . . . 132

5.12 Results of the BUU Calculation 2: Emitted Nucleons . . . . . 139

5.13 Conclusions . . . . . 155

5.14 Improvements to the Model . . . . . 155

**6 Flow Analysis of Peripheral Collisions** **157**

6.1 Introduction . . . . . 157

6.2 Analysis Technique . . . . . 159

6.3 Results . . . . . 162

6.4 Discussion . . . . . 173

6.5 Conclusion . . . . . 178

**7 Conclusion** **179**

7.1 Summary . . . . . 179

7.2 Directions for Future Research . . . . . 180

**A Trigger Stream** 183

**B The $4\pi$ Filter Code** 187

B.1 Introduction . . . . . 187

B.2 The Original Filter . . . . . 188

B.3 The Fast Filter . . . . . 191

**C Impact Parameter Determination** 193

**D Parameterization of Azimuthal Anisotropy** 198

D.1 Peak/Valley Ratios . . . . . 198

D.2 Expansion in Cosines . . . . . 199

**LIST OF REFERENCES** 201

# List of Tables


2.1 Solid Angles of Main Ball Telescopes . . . . . 29

2.2 Properties of the Fast and Slow Plastic Scintillators . . . . . 33

2.3 Low Energy Thresholds of Main Ball . . . . . 38

2.4 Low Energy Thresholds of Forward Array . . . . . 38

3.1 Fit parameters for double Gaussian fits to the distribution of differences between reaction planes of sub-events . . . . . 75

# List of Figures


1.1 The equation of state for two different values of the compressibility of nuclear matter. . . . . 5
1.2 Summary of measurements of $K$ . . . . . 7
1.3 The participant-spectator geometry used in the Nuclear Fireball Model. 8
1.4 Fluid dynamical and cascade calculation of a 400 MeV/nucleon Nb+Nb collision. . . . . 10
1.5 Computer reconstruction of the tracks seen on a Streamer Chamber photographic plate. . . . . 12
1.6 Explanation of transverse momentum analysis used for measuring the collective flow of the participants. . . . . 14
1.7 Illustration of the squeeze-out effect. . . . . 16
1.8 Flow as a function of beam energy in heavy-ion collisions . . . . . 17
1.9 Squeeze-out as a function of beam energy in heavy-ion collisions . . . 18
1.10 The difference between the concepts of attractive and repulsive flow. . 20
1.11 BUU predictions of average transverse momentum in the reaction plane as a function of rapidity. . . . . 21
1.12 The Wilczyński plot. . . . . 22
1.13 Explanation of the Wilczyński plot. . . . . 23
1.14 Azimuthal distribution of alpha particles around the reaction plane defined by fission fragments. . . . . 26

2.1 A truncated icosahedron, the basic geometry of the $4\pi$ Array . . . . . 30
2.2 The positions of the front faces of the Forward Array telescopes. The beam axis goes into the page. . . . . 31
2.3 A phoswich (phosphor sandwich) detector. . . . . 32
2.4 Counts as a function of the integrated fast ($\Delta$E) and slow (E) signals for a Forward Array phoswich telescope. . . . . 34
2.5 Counts as a function of the integrated fast ($\Delta$E) and slow (E) signals for a Main Ball phoswich telescope. . . . . 35
2.6 Schematic diagram of the features of a phoswich $\Delta$E-E plot. . . . . 36

2.7 Acceptance of $4\pi$ Main Ball + Forward Array system in momentum space. . . . . 42
2.8 Multiplicity of charged particles detected by the $4\pi$ Array. . . . . 43
2.9 Kinetic energy spectra for He produced in Ar+V collisions. . . . . 45
2.10 Temperature of the mid-rapidity source as a function of beam energy. 46

3.1 A geometrical description of the reaction plane. . . . . 49
3.2 The definition of the forward flow side of the reaction plane for both attractive and repulsive scattering. . . . . 51
3.3 The cross section for charged particles from 35 MeV/nucleon Ar+V collisions. . . . . 54
3.4 The quantities used in finding the reaction plane for an event projected on the $p^x$–$p^y$ plane. . . . . 56
3.5 The spurious in-plane enhancement due to including the particle of interest in the reaction plane determination for simulated events. . . . 58
3.6 The azimuthal distribution of differences between reaction planes found for the entire events and reaction planes found leaving out a particle of interest. . . . . 59
3.7 Comparison of azimuthal distributions of particles of interest with respect to the reaction plane using different weightings in determining the plane. . . . . 61
3.8 The effects of momentum conservation are investigated using simulated events. . . . . 63
3.9 A search for azimuthal anisotropies due to detector bias in the analysis of randomized events. . . . . 66
3.10 The distribution of reaction plane azimuthal angles in the detector coordinate system for 35 MeV/nucleon Ar+V. . . . . 67
3.11 The distribution of azimuthal angle differences between reaction planes found using the transverse momentum analysis and the azimuthal correlation technique. . . . . 69
3.12 A comparison of the azimuthal angle of particles of interest with respect to the reaction planes found using two different techniques. . . . . 70
3.13 The distribution of differences between found and true reaction planes for multiplicity 4 to 50 simulated events. . . . . 72
3.14 The distribution of differences between azimuthal angles of reaction planes found for sub-events is shown for simulated data. . . . . 76
3.15 The same simulation as the previous figure, after filtering through a software representation of the detector acceptance. . . . . 77
3.16 Results from the analysis of 35 MeV/nucleon Ar+V collisions are shown in the same manner as previous two figures. . . . . 78
3.17 The extracted widths ($\sigma_o$) from the Gaussian fits the data in previous three figures are shown as a function of multiplicity. . . . . 79

3.18 An exploration of the accuracy of the reaction plane determination for simulated events. The panels are described in the text. . . . . 81

4.1 Schematic representation of the two forms of collective motion under investigation. . . . . 84
4.2 Azimuthal distributions with respect to the reaction plane for an oblate momentum distribution. . . . . 85
4.3 Azimuthal distributions with respect to the reaction plane for a simulated source with transverse momentum flow. . . . . 86
4.4 Geometrical definition of the anisotropy parameters $F_{ip}$ and $F_{fs}$ projected onto the $p_x - p_y$ plane. . . . . 89
4.5 Azimuthal angles of the in-plane and forward flow side gates are shown for a hypothetical azimuthal distribution . . . . . 90
4.6 Anisotropy fractions $F_{ip}$ and $F_{fs}$ for a simulated oblate momentum distribution. . . . . 91
4.7 Anisotropy fractions $F_{ip}$ and $F_{fs}$ for a simulated prolate momentum distribution with transverse momentum flow. . . . . 92
4.8 Anisotropy fractions for a simulated oblate momentum distribution after filtering through a software model of the detector acceptance. . 94
4.9 Anisotropy fractions for a simulated prolate momentum distribution with transverse momentum flow after filtering through a software model of the detector acceptance. . . . . 95
4.10 Anisotropy fractions as function of rapidity for 35 MeV/nucleon Ar+V data. . . . . 98
4.11 Azimuthal distributions of hydrogen produced in 35 MeV/nucleon Ar+V collisions divided into six rapidity bins. . . . . 100
4.12 Azimuthal distributions of helium produced in 35 MeV/nucleon Ar+V collisions divided into six rapidity bins. . . . . 101
4.13 Anisotropy fractions for 35 MeV/nucleon Ar+V data with $p^{\perp} \geq 210$ MeV/c per nucleon, and smeared in angular assignments as described in the text. . . . . 102
4.14 Anisotropy fractions for 35 MeV/nucleon Ar+V data as function of $p^{\perp}$/nucleon. . . . . 104
4.15 Anisotropy fractions as function of rapidity for 65 MeV/nucleon Ar+V data. . . . . 105
4.16 Anisotropy fractions as function of rapidity for 100 MeV/nucleon Ar+V data. . . . . 106
4.17 Anisotropy fractions for 100 MeV/nucleon Ar+V data as function of $p^{\perp}$/nucleon. . . . . 108
4.18 The slope of $F_{fs}$ at mid-rapidity is used to measure the transverse momentum flow Ar+V collisions as a function of beam energy. . . . . 109
4.19 The maximum of $F_{ip}$ is used to measure the in-plane enhancement in Ar+V collisions as a function of beam energy. . . . . 110

5.1 Maximum angular momentum that a nucleus with mass number $A$ can support. . . . . 115
5.2 A fit to He emitted from 35 MeV/nucleon Ar+V collisions using the rotating sphere parameterization. . . . . 118
5.3 Energy dependence of the in-plane enhancement for He emitted emitted from 35 MeV/nucleon Ar+V collisions. . . . . 120
5.4 Hill-Wheeler coordinates for a $^{158}$Yb nucleus are shown as a function of the angular momentum (I) using the liquid drop model. . . . . 122
5.5 BUU predictions for the evolution of an excited Ca nucleus with high angular momentum. . . . . 124
5.6 Fraction of collisions Pauli blocked in Nb+Nb collisions. . . . . 127
5.7 BUU calculations of the transverse momentum flow for different equations of state and in-medium n-n cross sections. . . . . 130
5.8 Coordinate space density distribution projected on to the x-z plane. . 133
5.9 Coordinate space density distribution projected on to the x-y plane. . 134
5.10 Number density in coordinate space at t=150 fm/c. . . . . 136
5.11 Evolution of BUU residue in Hill-Wheeler coordinate space. . . . . 137
5.12 Hill-Wheeler coordinates as a function of time. . . . . 138
5.13 Angular momentum in the BUU calculation as a function of time. . . 140
5.14 The number of nucleons in the residue and the number of nucleons emitted is shown as a function of time. . . . . 141
5.15 Emission rate of nucleons with various energies. . . . . 142
5.16 Anisotropy fractions 570 fm/c after the beginning of the collision . . . 143
5.17 Anisotropy fractions 570 fm/c after the beginning of the collision using a 25 MeV low energy threshold. . . . . 145
5.18 Snapshots of the anisotropy fractions as a function of time. . . . . 146
5.19 Snapshots of the anisotropy fractions as a function of time for nucleons with at least 25 MeV/nucleon. . . . . 147
5.20 Anisotropy fractions in 5 MeV wide windows as a function of the energy in the center of the window. . . . . 149
5.21 Anisotropy fractions for nucleons emitted in specific time windows. . 150
5.22 Anisotropy fractions for nucleons emitted in specific time windows. . 151
5.23 Final anisotropy fractions calculated with and without including PEPs. 152
5.24 Momentum distribution of particles emitted in the first 60 fm/c projected onto the reaction plane. . . . . 154

6.1 Velocity spectra for projectile fragments detected in the Forward Array. 160
6.2 Histogram of the transverse momentum distribution projected on to the reaction plane for mid-rapidity protons . . . . . 161

6.3 The center of the transverse momentum distribution of protons in the reaction plane as a function of rapidity. . . . . 163
6.4 The mean transverse momentum distribution of light particles in the reaction plane as a function of rapidity for collisions using 45 and 200 MeV/nucleon projectiles. . . . . 164
6.5 The negative offset for the center of the mid-rapidity proton transverse momentum distribution is shown as a function of the transverse momentum of the projectile fragment. . . . . 166
6.6 Two source fit of the $P^x$ distribution near the projectile fragment rapidity 169
6.7 Momentum correlation functions for proton/projectile fragment coincidences . . . . . 170
6.8 The center of the transverse momentum distribution in the reaction plane gated on the mid-rapidity source . . . . . 172
6.9 Flow analysis of uncorrelated events. . . . . 174
6.10 Schematic drawing of the proposed deflections in peripheral events. . 175
6.11 Results of a three body dynamical simulation of projectile fragmentation. 177

A.1 Electronics diagram for the $4\pi$ trigger system. . . . . 184

B.1 Steps followed in the original simulated event filter. . . . . 189
B.2 Fast filter event loop. . . . . 192

C.1 Impact parameter dependence of mid-rapidity change in Ca+Ca FREESCO simulations. . . . . 195
C.2 Impact parameter dependence of He kinetic energy spectra at 7° from the beam axis in the lab frame produced by 50 MeV/nucleon C+C collisions. . . . . 197

# Chapter 1

# Introduction

In this thesis we will investigate the properties of heavy-ion collisions at beam energies ranging from near the Fermi energy ($\approx$ 37 MeV/nucleon) to 100 MeV/nucleon. The motivation for studying these collisions is two fold. Ultimately, we hope to contribute to the characterization of the bulk properties of nuclear matter. No results which constrain the properties of nuclear matter will be presented in this initial analysis, but techniques which may do so in the future will be developed. The more immediate aim of this work is simply to characterize the dynamics of the events. These reactions are quite complex because they involve a finite number of particles which have access to a nearly innumerable number of final states. Therefore, detailed descriptions of these collisions should provide motivation and some of the tools for improving our ability to calculate the dynamics of complex finite systems in general.

This beam energy region is particularly interesting because it is expected to be transitional. At beam energies just above the Coulomb barrier, reactions are dominated by the attractive component of the nuclear mean field. **Central collisions** (head on) result in compound nucleus formation, while **peripheral collisions** give rise to an attractive deflection of the projectile or its capture to form an orbiting system. On the other hand, at relativistic beam energies, the overlap region of the projectile and target becomes highly compressed, and the hard core repulsive compo-

nent of the nuclear mean field comes into play. The beam energy range studied in this thesis spans the region in which the dominant interaction is expected to change from attractive to repulsive. We will refer to this as the **intermediate energy** range.

Since progress was made in the understanding of relativistic collisions by confronting theory with the observed modes of collective motion, we will maintain this approach in our examination of intermediate energy collisions. Collective motion occurs with respect to the plane initially containing the beam axis and target, called the **reaction plane**. We will focus particularly on azimuthal distributions with respect to the reaction plane, which we find to be useful indicators of the presence of collective motion.

In order to determine the reaction plane from the final distribution of particles, it is generally necessary to detect as many of the outgoing particles as possible. To this end, a large acceptance detection system called the **MSU $4\pi$ Array** was constructed. The data taken with the MSU $4\pi$ and presented in this thesis represent some of the first explorations of collective motion in intermediate energy collisions.

## 1.1 Organization

The organization of this thesis is as follows. In the introduction we will begin by introducing some of the concepts used in describing bulk nuclear matter. Since our work began as an extension of the approaches employed to characterize relativistic collisions, we will also review what was learned about collective motion in relativistic collisions. Finally we will outline some of the differences between the collision dynamics at relativistic beam energies and those expected at intermediate energies.

In the second chapter we will describe the experimental apparatus and early stages of the analysis. Chapter three presents the technique we have developed to determine

the reaction plane for central and medium impact parameters. The next chapter presents our data in the form of azimuthal distributions of particles with respect to the reaction plane. The observed anisotropies are interpreted in terms of simple modes of collective motion. The data will be compared to a microscopic calculation in the fifth chapter, and we will draw conclusions about the nature of observed collective motion. In the sixth chapter we will shift the focus to analysis of peripheral events, in which we will be able to observe the attractive nature of the nuclear mean-field directly. Finally, in the seventh chapter, we will summarize what has been learned and suggest possible directions for future development. Subjects on the periphery of the main thread of the thesis have been placed in appendices to streamline the presentation.

## 1.2 The Bulk Properties of Nuclear Matter

Outside of neutron stars and perhaps the early universe, infinite nuclear matter exists only as a theoretical construct used to test our understanding of the nuclear force. For example, if we can deduce the equation of state of bulk nuclear matter from nucleus-nucleus collisions, this would provide some guidance to theorists attempting to write down the strong force Hamiltonian in a baryon-rich environment.

Two properties of infinite nuclear matter are apparent from the examination of nuclei in there ground state.[Wong90] From letting the atomic mass number $A$ go towards infinity in the Weizacker semi-empirical mass formula, and ignoring the Coulomb force, we find the the binding energy ($E_b$) per nucleon is

$$E_b \approx 16 MeV. \tag{1.1}$$

We also know that nuclear matter saturates at a density

$$\rho_o \approx 0.17 \,\text{nucleons fm}^{-3} \tag{1.2}$$

from the study of the charge distribution in heavy nuclei. Thus we can demand that the nuclear **equation of state (EOS)**, which describes how nuclear matter responds to changes in density, reproduce these values. One commonly used form of this expression is[Bert88]

$$U(\rho) = A\frac{\rho}{\rho_o} + B\left(\frac{\rho}{\rho_o}\right)^{\sigma}, \tag{1.3}$$

where $U(\rho)$ is the density dependent potential field and $\sigma$ is greater than one. In eq. 1.3 the constant $A$ is attractive (negative) and the constant $B$ is repulsive (positive). The EOS is usually taken as the nuclear compressional potential energy ($E_{cp}$) as a function of density given by

$$U(\rho) = \frac{\partial}{\partial\rho}(\rho E_{cp}) \tag{1.4}$$

The unknown factors $A$, $B$, and $\sigma$ can be fixed in terms of binding energy, saturation density, and a new parameter $K$, the **nuclear compressibility**. The compressibility is defined as $\frac{9}{\rho}$ times the bulk modulus $k$, which is the logarithmic derivative of the pressure with respect to the density. A derivation of these equations can be found in [Bert88]. The compressibility $K$ is a measure of how difficult it is to push the system away from its equilibrium density, and is thus important in certain astrophysics applications. For example, it determines the density of neutron stars and the propagation of shock waves created in supernova explosions. In Figure 1.1 we show the nuclear compressional energy (the sum of the potential energy and the Fermi energy) as a function of density for two different values of the compressibility.[Moli85a]

Larger values for $K$ would mean that it takes more energy to compress nuclear matter, a situation referred to as a **stiff** equation of state, while smaller values indicate a **soft** EOS. The compressibility can only be inferred from observing the properties of nuclear matter away from the equilibrium density. Placing constraints on $K$ has

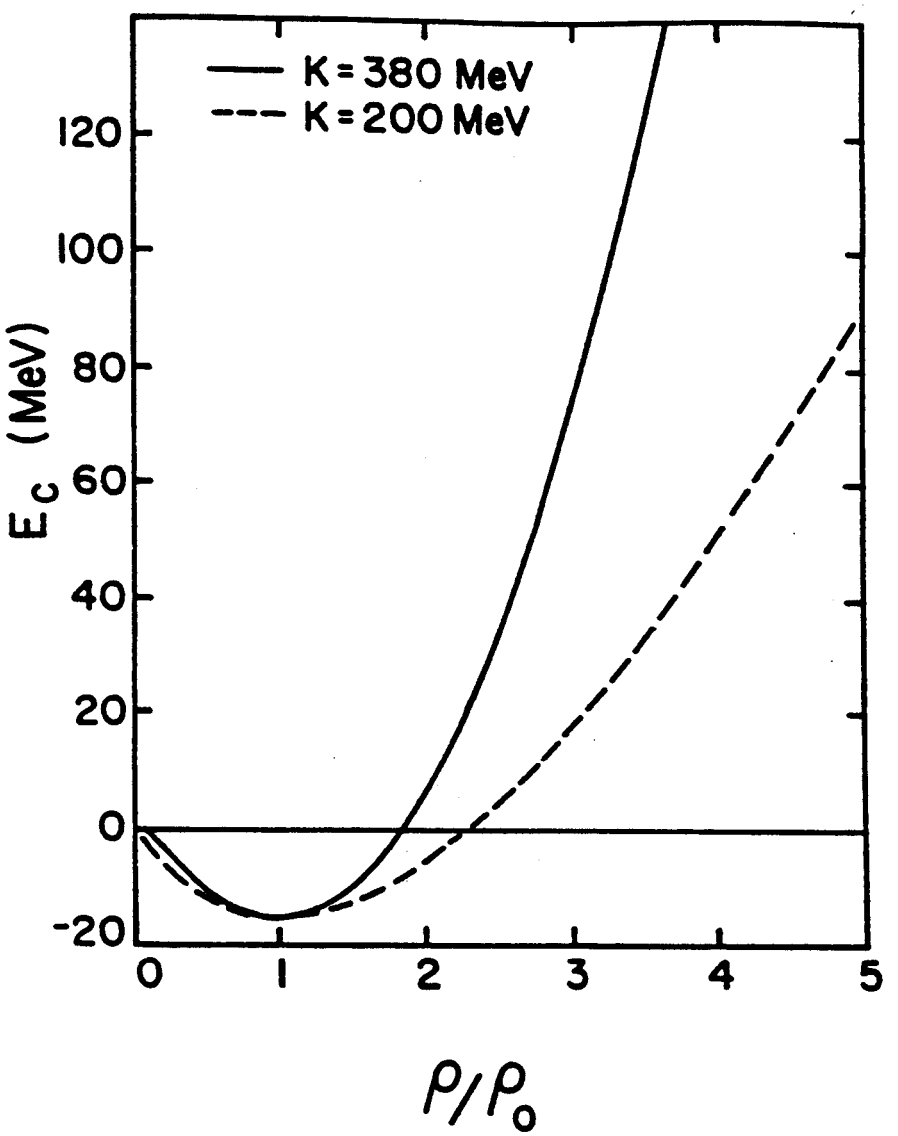


Figure 1.1: The equation of state for two different values of the compressibility of nuclear matter.[Moli85a]

been one of the major goals of heavy-ion physics. In Figure 1.2 we show the results of several different techniques used to measure $K$, including the flow angle measurements of relativistic heavy-ion collisions which will be described in detail in this introduction. The best constraints placed on the equation of state so far have come from the study of frequency of vibrating nuclei (giant monopole resonance).[Shar89] (The new data on vibrating nuclei result from the systematic study of a larger number of nuclei than the original data.) The extremely low $K$ values found to be necessary in simulations of supernovae are thought to represent a failing of current supernova theory. We can conclude from the graph that the compressibility is $\approx$ 300 MeV with large error bars. In the next section, we review how the study of relativistic heavy-ion collisions has been used to constrain the equation of state.

## 1.3 Review of Results from Relativistic Heavy-Ion Collisions

Beams of **relativistic heavy-ions** (Z> 4, $E_{beam}$ >100 MeV/nucleon) became available at Lawrence Berkeley Laboratory (LBL) in 1974. Early experiments, which detected only one particle per event, showed that particles were produced by three distinct sources. A **participant-spectator** geometry was successfully applied describe the observed energy spectra.[West76] In this picture, the parts of the projectile and target that do not overlap during the collision (spectators) are less strongly disturbed. The projectile remnant forms a **projectile-like source** which continues on with nearly the same velocity as the original projectile, and similarly the target remnant forms a **target-like source**. The overlapping participant region forms a hot **fireball** whose velocity and excitation energy can be deduced from the assumption of a completely inelastic collision and clean cut geometry, as shown in Figure 1.3. We will use this terminology to describe sources of light particles in chap. 6.

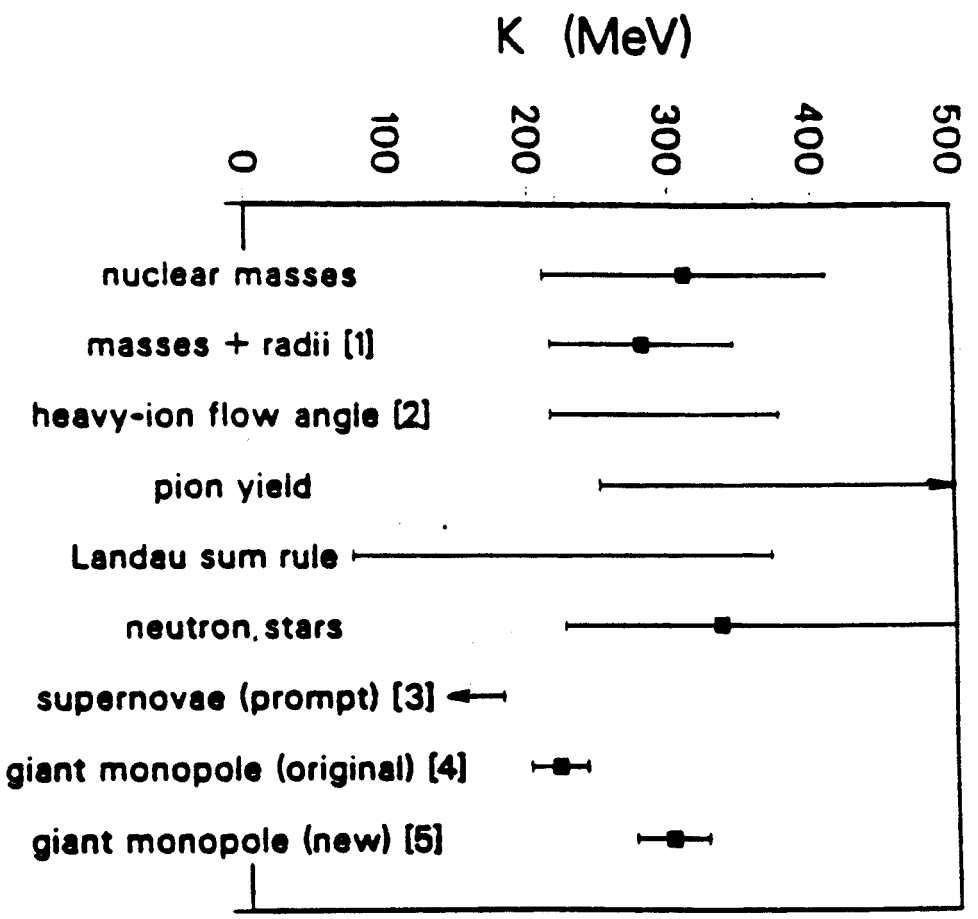


Figure 1.2: Summary of measurements of $K$.[Glen88]

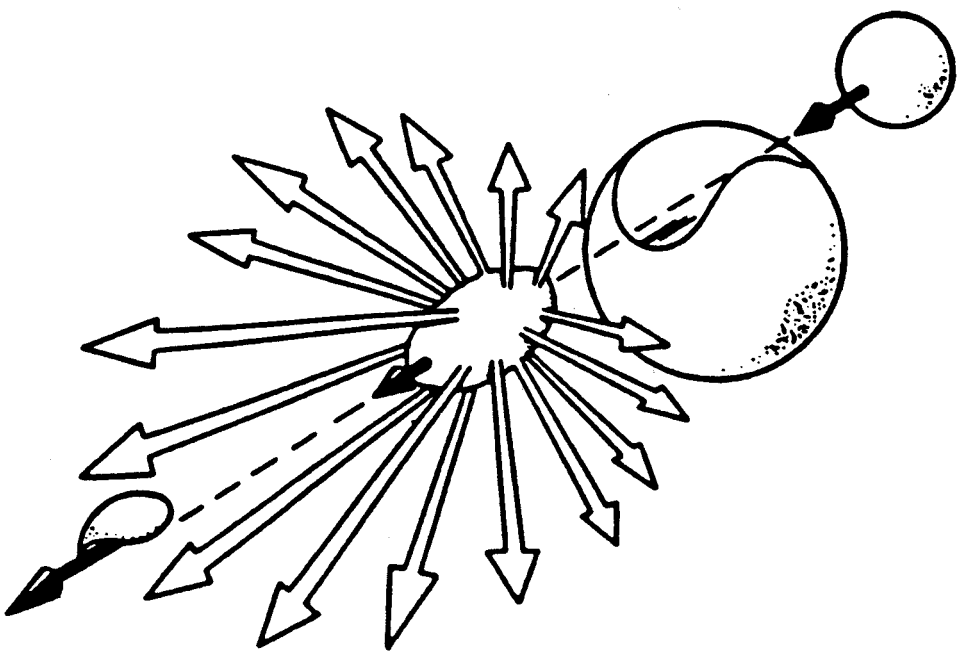

Figure 1.3: The participant-spectator geometry used in the Nuclear Fireball Model.[West76]

Early experiments did not provide enough information about the collisions to distinguish definitively between competing models of reaction mechanisms because they were mainly single particle experiments. It was the observation of collective motion using detectors capable of observing many particles in each event that played the central role in driving forward the theory of relativistic reactions.

Two of the early competing models were the **Hydrodynamic Model**[Stöc82, Buch84] and the **Intranuclear Cascade.**[Yari79, Cugn83] In figure 1.4 we show the results of fluid-dynamical and cascade calculations for the system 400 MeV/nucleon Nb+Nb. Note that there is a considerable **side-splash** of nucleons in the final frame of the hydrodynamical calculation, while the cascade produces a more nearly isotropic distribution.

The hydrodynamical model assumes that the mean free path of nucleons in nuclear matter is very short, leading quickly to **local equilibrium**, and allowing the nuclear matter to be treated **macroscopically** in terms of variables like pressure and temperature. The short mean free path causes compressional energy to be built up very efficiently, leading to the side-splash or **collective flow**[Stöc80] observed in the figure. One drawback of the theory is that real heavy-ion collisions involve a finite number of particles, not a smooth continuum, making it difficult to compare the calculations to actual observations of nuclei, especially in collisions of lighter ions.[Stöc86]

Intranuclear cascade calculations avoid this problem since they track the progression of each nucleon through time. For this reason they are referred to as **microscopic** calculations, and need not assume local equilibrium. The nucleons interact with each other only through collisions, whose cross sections are taken from free nucleon nucleon scattering. This causes the nuclei to be more transparent to each other than in the hydrodynamical model, and the lack of compressional energy shows up in the weaker collective flow in the figure. Since there is no **mean field** created by the

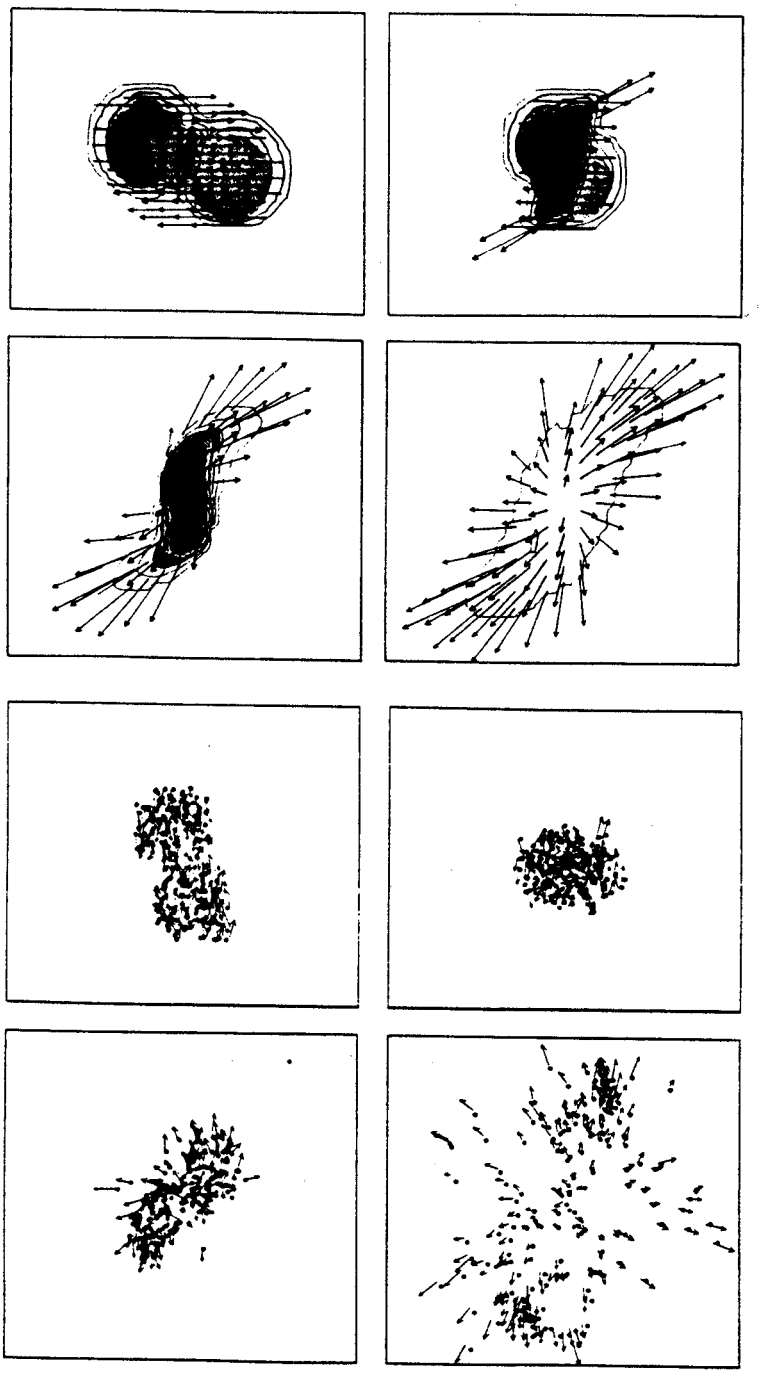

Figure 1.4: Fluid dynamical (top panels) and cascade (bottom panels) calculation of a 400 MeV/nucleon Nb+Nb collision. The impact parameter is 3 fm and $\approx$ 10 fm/c in time separates the snapshots. [Grei85] The view is looking down on the reaction plane. The beam axis is left to right in the upper panels and top to bottom in the lower panels.

nucleons, there is no potential well and thus the Fermi momentum causes nuclei to be unstable. Therefore an undisturbed nucleus will evaporate nucleons over time. This flaw can be overcome by several artificial initialization procedures, but it reflects the incompleteness of the cascade picture.[Stöc86] Due to the lack of a proper quantum mechanical initialization, quantum effects such as the Pauli exclusion principle cannot be included during the calculation of reactions.

Because the azimuthal angle (around the beam axis) of the reaction plane varies randomly from event to event, the effects of collective flow tend to average out for single particle observables. For example, both models could reproduce the energy spectra and angular distributions observed using one detected particle per event. To provide more sensitivity to collective effects, large acceptance detection systems were developed to measure as many charged particles as possible emerging from a single event, allowing determination of the event's shape in momentum space. From the shape of the event, experimentalists could determine the reaction plane and then rotate each event to a common orientation. Quantities could then be measured relative to the reaction plane, eliminating azimuthal averaging. We will take up the details of reaction plane determination in the third chapter.

The two primary experimental facilities which were used to study collective flow were the LBL Streamer Chamber and the Plastic Ball. A computer reconstruction of a Streamer Chamber image is shown in Figure 1.5. Because the violence of relativistic collisions can lead to the total disintegration of the projectile and target in central collisions, the charged particle multiplicity can exceed 100. The Plastic Ball[Gutb89a] consisted of more than 1000 charged particle detectors, arranged into an modified icosahedron plus a forward array.

In 1985 Danielewicz and Odyniec[Dani85] developed a method of displaying the experimental data that made it possible to quantify reliably the side-splash in the

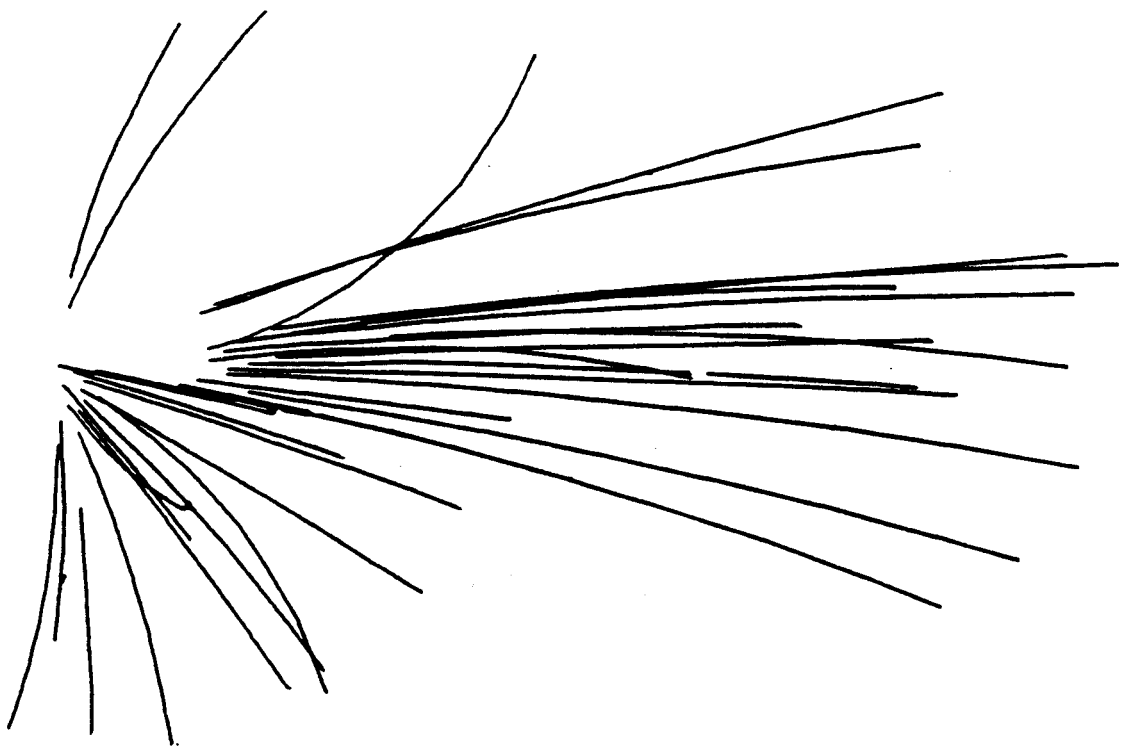

Figure 1.5: Computer reconstruction of the tracks seen on a Streamer Chamber photographic plate. The projectile (not visible) enters from the left travelling horizontally. This was a central collision of a relatively light system, Ar+KCl at 1.8 GeV/nucleon. A magnetic field perpendicular to the page produces the curvature observed in the tracks. (Positive ions curve clockwise, negative pions curve counterclockwise.)[Bibb85]

participant zone. This **transverse momentum analysis** is illustrated in Figure 1.6 for 400 MeV nucleon Nb+Nb central collisions. The side-splash is revealed by plotting the average transverse momentum projected into the reaction plane as a function of rapidity. The **rapidity** variable ($y$) is a Galilean invariant function of the velocity parallel to the beam axis $\beta_{||}$,

$$y = \frac{1}{2} \ln \left( \frac{1 + \beta_{||}}{1 - \beta_{||}} \right). \tag{1.5}$$

If the velocity is small compared to the speed of light, then the rapidity reduces to $\beta_{||}$. The slope of the transverse momentum as a function of rapidity is called the **flow**, and can be compared to theoretical models once the uncertainty in the reaction plane determination is taken into account.

Danielewicz et al. found that the hydrodynamical model over-predicted the flow, while the intranuclear cascade under-predicted it. Clearly, the assumption of local equilibrium and a very short mean free path in the hydrodynamical model was an approximation. A new model was developed that retained the microscopic approach of the intranuclear cascade, but added an additional interaction mediated by the nuclear mean field.[Bert88] The addition of the mean field interaction requires a specific value of the compressibility ($K$) in the equation of state, so the effects of a soft versus a stiff EOS on the collective flow could be evaluated. The treatment of collisions in the cascade model was also carried over to the new calculation. The new approach goes by different names, each group of theorists coining their own terminology, such as **Boltzmann-Uehling-Uhlenbeck (BUU)**,[Uehl33, Bert84] **Vlasov-Uehling-Uhlenbeck (VUU)**,[Krus85] **Boltzmann-Nordheim equation**,[Nord28] or **Landau-Vlasov equation**.[Greg87] We will compare our observations to BUU theory in the fifth chapter.

The comparisons between the initial BUU simulations and the flow observed in

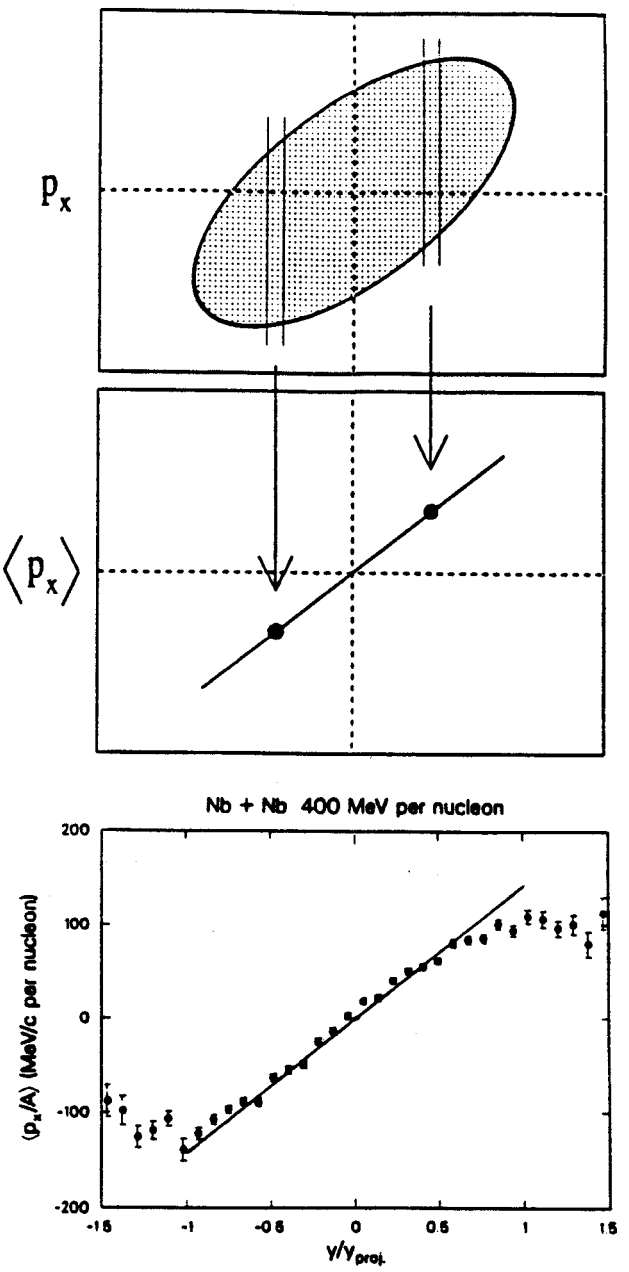


Figure 1.6: Explanation of transverse momentum analysis used for measuring the collective flow of the participants. The top panel is a schematic picture of the momentum distribution, the bottom panel is the average transverse momentum in the reaction plane as a function of rapidity for actual Plastic Ball data.[Gutb89a]

heavy-ion reactions led to a surprisingly stiff equation of state, $K \approx 380$ MeV.[Moli85a, Dani88] This was much higher than the value being used in supernova calculations, for example. Later, it was discovered that inclusion of the expected momentum dependence of the nuclear interaction into eq. 1.3 could reproduce the observed flow using a lower compressibility of $\approx 200$ MeV.[Gale87] This trade off between $K$ and momentum dependent interactions produces the large uncertainty bars in Figure 1.2. Thus, we can conclude that observations of relativistic heavy-ion collisions have the potential to constrain the equation of state, dependent on improvements of microscopic models and a better understanding of nucleon-nucleon collisions in nuclear matter.

In 1989,[Gutb89b] a new component of the collective motion was discovered, the so-called **squeeze-out** in which the compression of the participant zone forces particles out of the reaction plane at mid-rapidity.[Gutb90] Squeeze-out, illustrated in Figure 1.7, was also predicted by hydrodynamical models.[Stöc86]

The Plastic Ball data on collective motion are summarized by the plots in figs. 1.8 and 1.9. We see that both the flow and the squeeze-out peak at a beam energy around 300 to 400 MeV/nucleon. (The flow in Figure 1.8 has been rendered beam energy scale invariant in a manner suggested by hydrodynamical considerations.[Bona87]) The magnitude of both effects drops rapidly as the beam energy is decreased towards 100 MeV/nucleon. This trend can be understood in terms of the competition between the attractive and repulsive components of the nuclear mean field visible in Figure 1.1. At the lower beam energies, the compression is too small to access the density region dominated by hard core repulsion for very long, and longer range attractive part of the mean field becomes important. In fact, BUU calculations predict that the flow should actually change directions for lower beam energies.

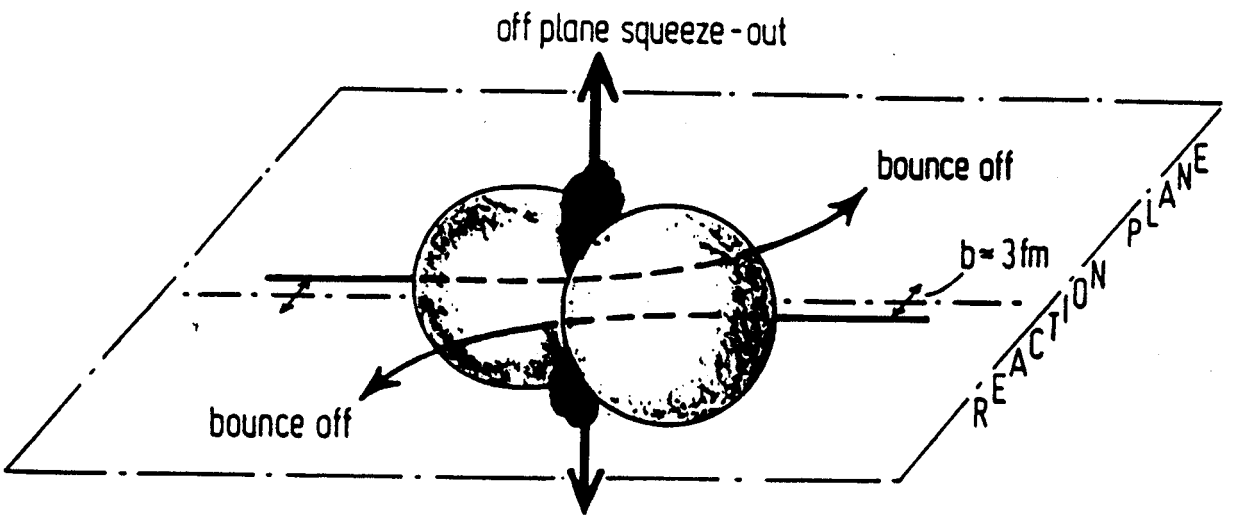


Figure 1.7: Illustration of the squeeze-out effect predicted by fluid dynamics.[Stöc86]

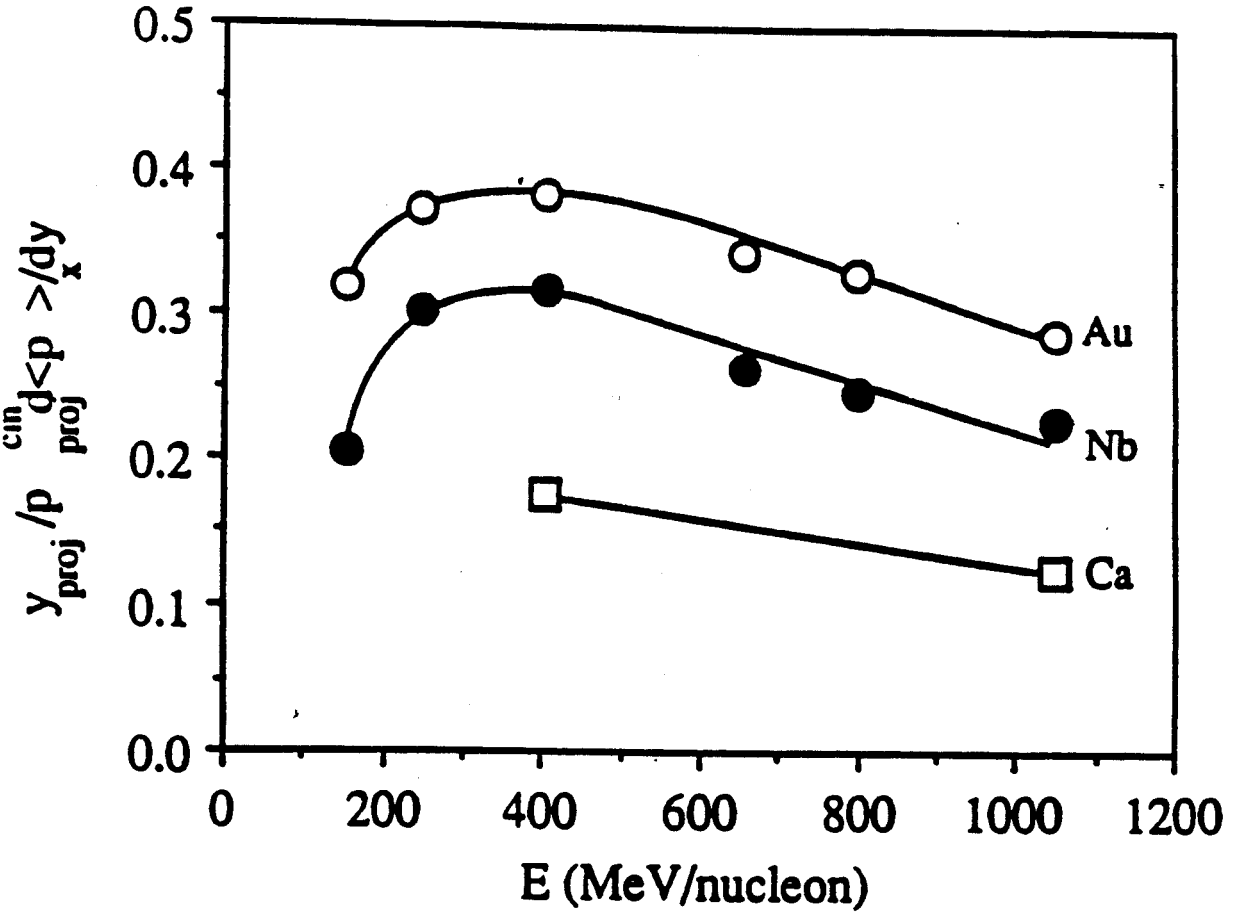


Figure 1.8: Flow as a function of beam energy in heavy-ion collisions in data taken with the Plastic Ball.[Schm91] The scaled flow (F) is proportional to the slope of the transverse momentum projected into the reaction plane as a function of rapidity, and calculated at mid-rapidity

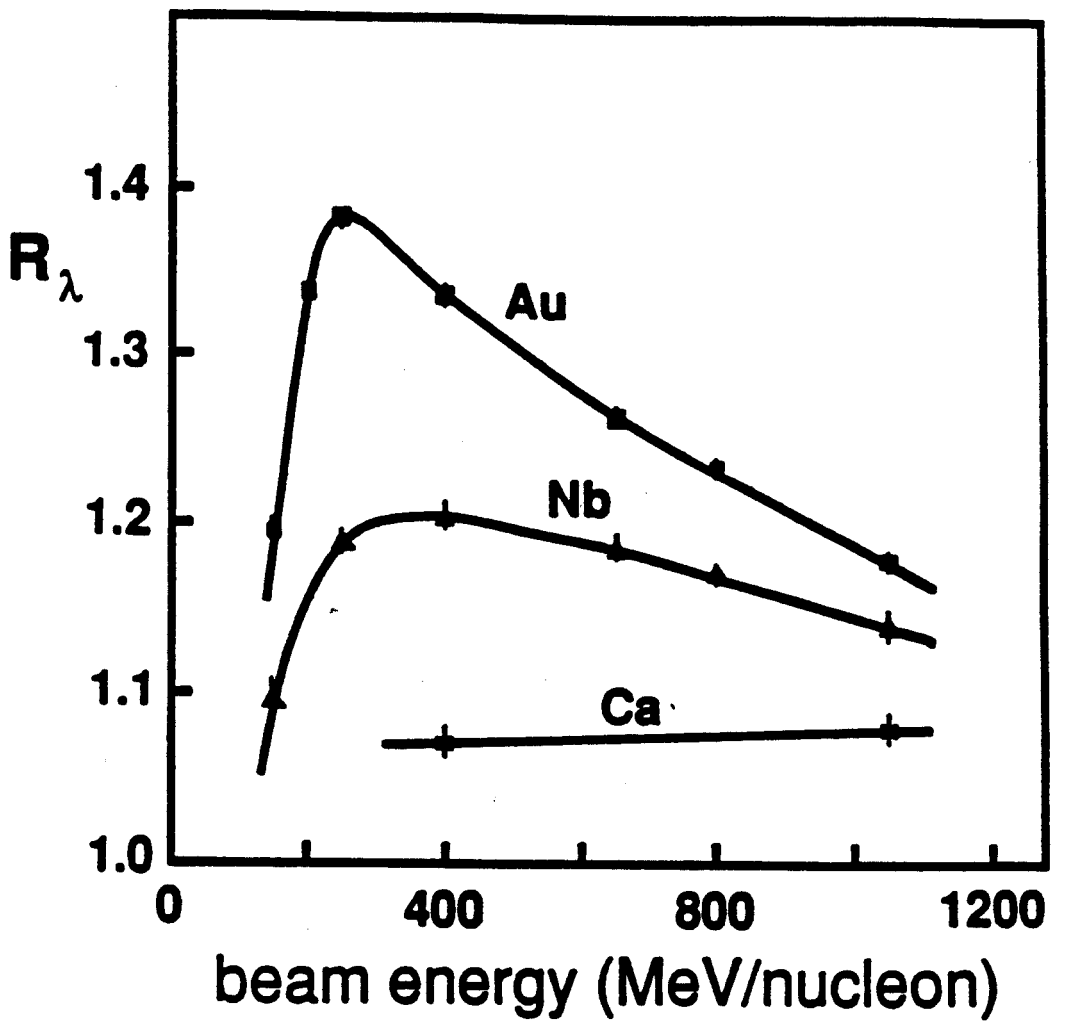


Figure 1.9: Squeeze-out as a function of beam energy in heavy-ion collisions in data taken with the Plastic Ball.[Schm91] The squeeze-out ratio (R) is the ratio of the out-of-plane to in-plane axis of an ellipsoid used to parameterize the observed momentum distribution.

## 1.4 Extension to Lower Beam Energies

In Figure 1.10 we show schematically the difference between repulsive flow, in which the particles are pushed away from the high compression region, and attractive flow where the particles are deflected negatively. These sketches should not be taken as a detailed description of the momentum distributions produced in these collisions, but as a simplification of the collective motion in the mid-rapidity region. BUU calculations, shown in Figure 1.11 performed by Molitoris et al.[Moli85b] predicted "inverted" flow at beam energies around 50 MeV/nucleon for the Nb+Nb system. Later BUU calculations[Bert87] have also produced attractive flow in systems of mass 40 projectile on mass 40 to 197 targets at beam energies $\leq$ 100 MeV/nucleon.

The attractive nature of the nuclear force in collisions with beam energies on the order of 10 MeV/nucleon has been established experimentally. We will review here two examples, Wilczyński orbiting and residue gamma ray polarization.

In 1973, Wilczyński plotted the cross section for production of K fragments in 9.7 MeV/nucleon Ar+Th collisions as a function of both center of mass (c.m.) energy and angle.[Wilc73] This novel mode of presenting the data, shown in Figure 1.12, revealed the relationship between two components in the observed energy spectra.[Artu73] Wilczyński's interpretation is shown schematically in Figure 1.13. He held that the ions observed near the beam energy had been repulsively scattered by the Coulomb force in peripheral collisions, while the ions in the lower energy peak resulted from collisions with smaller impact parameters in which the attractive mean field caused the projectile to orbit partially the heavier target. Note that although the sign of the scattering angle of a single particle is undetermined, the overall pattern shows the effects of both positive and negative scattering.

Collisions of the latter sort are said to be **deep inelastic**, with the velocity of the

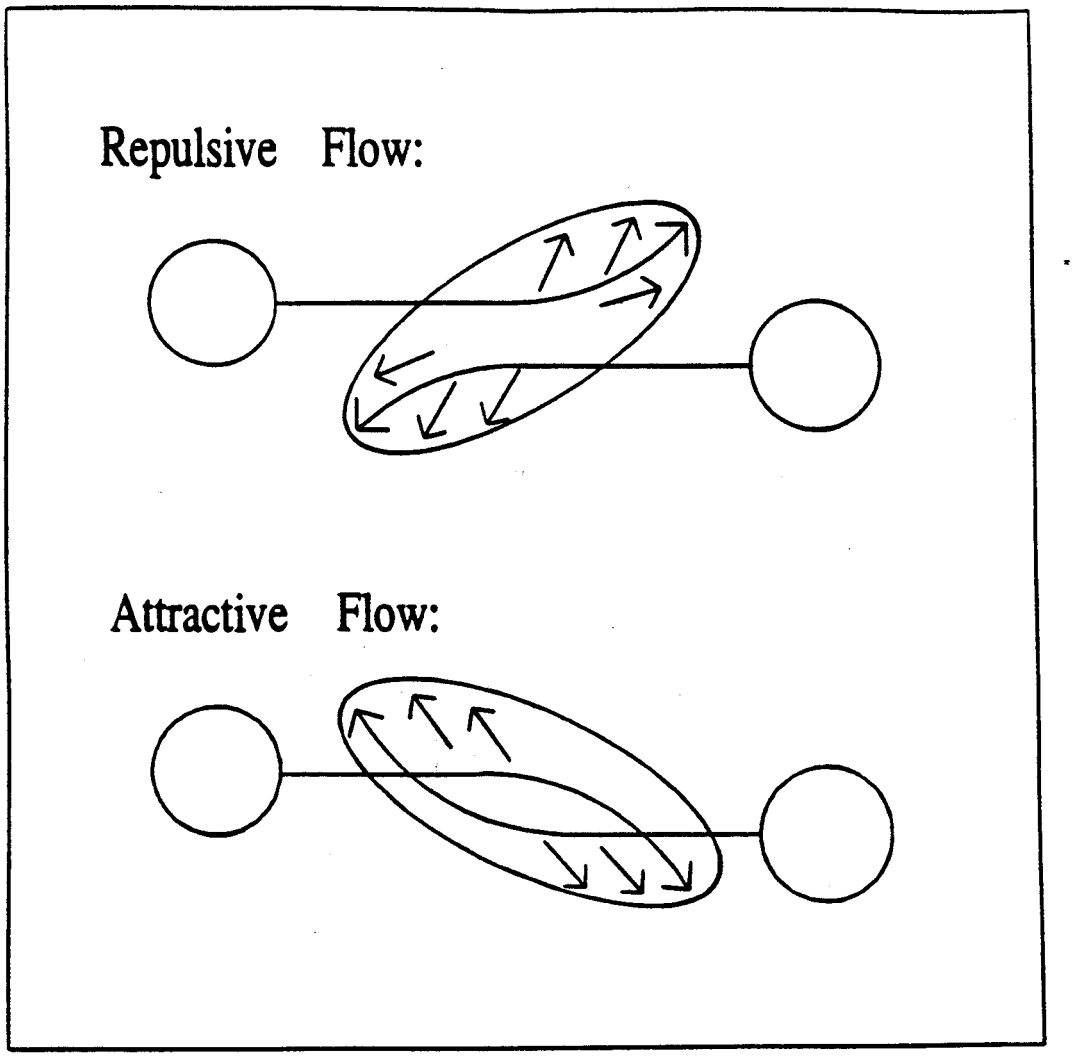


Figure 1.10: The difference between the concepts of attractive and repulsive flow.

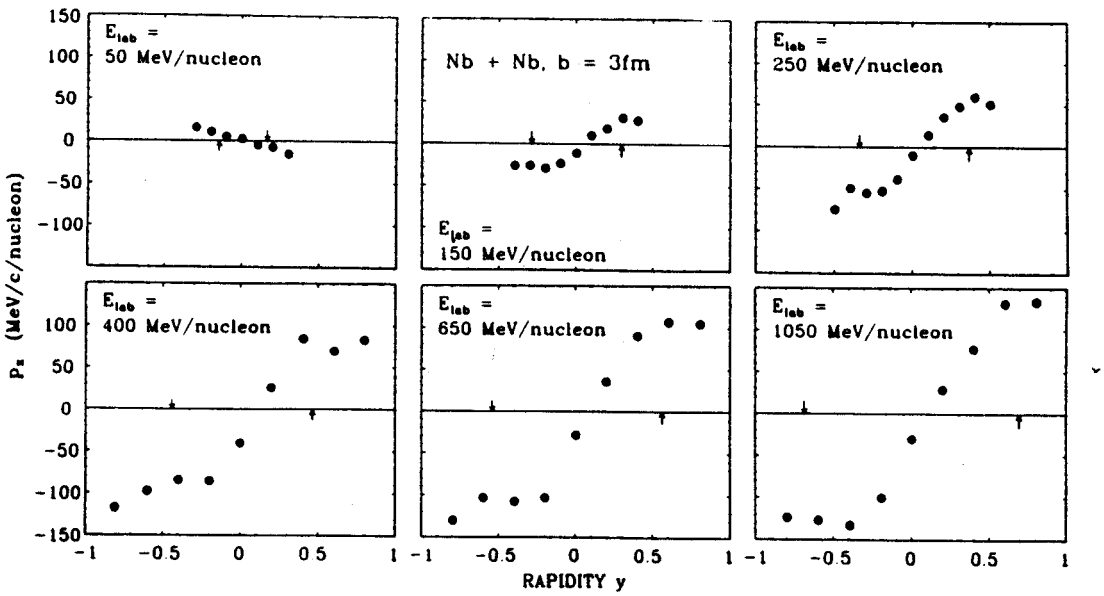


Figure 1.11: BUU predictions of average transverse momentum in the reaction plane as a function of rapidity is shown for the Nb+Nb for several beam energies. Note that the flow is inverted in the lowest beam energy calculation.[Moli85b]

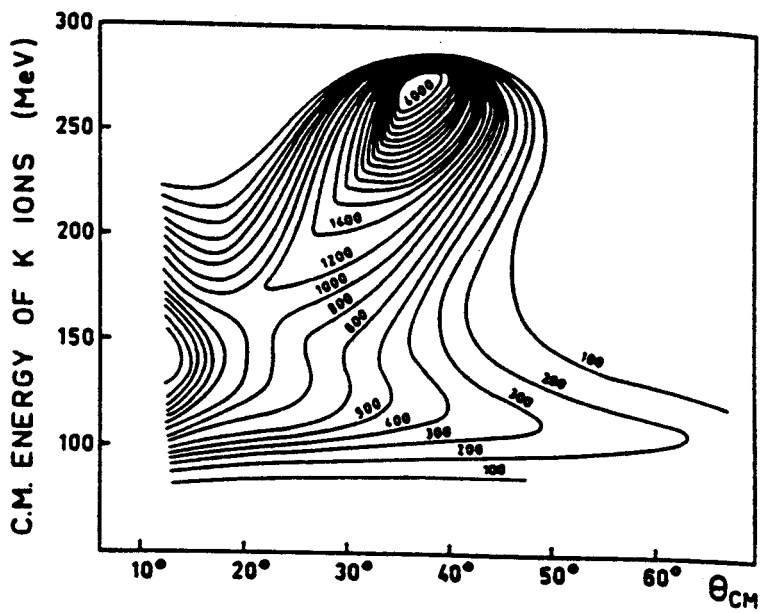


Figure 1.12: Contour map of the K cross section produced in 9.7 MeV/nucleon Ar+Th collisions. ,This method of presenting the data is called a **Wilczyński plot.**[Wilc73]

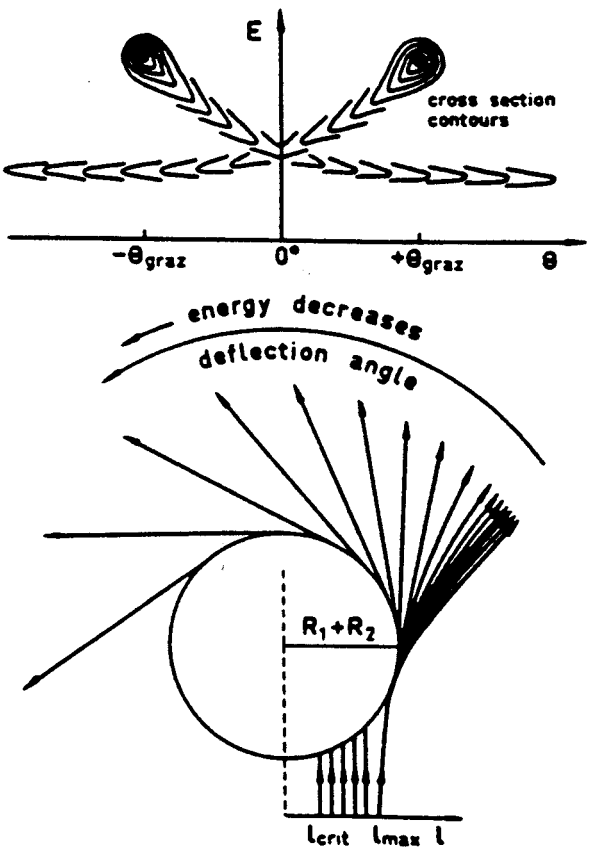


Figure 1.13: Scattering processes which create the ridges on a Wilczyński plot.[Wilc73]

projectile being strongly **damped**. The most peripheral collisions are referred to as **quasi-elastic** since the projectile fragment appears with almost all of the projectile's original momentum per nucleon. If the beam energy is above the Coulomb barrier, central collisions result in **fusion** forming a compound nucleus that can have a large amount of rotational collective motion which is dissipated by neutron and gamma ray emission.[Step65]

The circular polarization of the deexcitation gamma rays can be exploited to measure the direction of the mean field deflection directly when detected in coincidence with charged particles. Observation of collisions of O and N projectiles ranging from 8 to 35 MeV/nucleon with Nb and Sm targets indicate that high energy light particles are attractively deflected by the nuclear mean field.[Trau84, Tsan86] Further direct evidence for the attractive nature of mean field deflection in these energy ranges will be presented in chap. 6 using data taken using the MSU $4\pi$ Array.[Wils91]

The goal of this thesis is to investigate the transitional regime in which attractive mean field deflection gives way, as the beam energy is increased, to compressional phenomena such as side-splash and squeeze-out. We will do this by classifying the modes of collective motion that we observe at 35 MeV/nucleon, and investigating their evolution as the beam energy is increased to 100 MeV/nucleon.

## 1.5 Earlier Observations of Collective Motion in Intermediate Energy Collisions

Beyond the mean-field deflection described earlier, the only other evidence of possible collective motion in this transitional beam energy regime has come from the two particle correlation measurements of Tsang et al. and Fox et al. Both experimental groups found that one light particle tends to be found preferentially in the

same plane as that defined by the beam axis and an additional light particle detected from the same event.[Tsan84a, Chit86, Fox88] In addition, Tsang and coworkers found that light particles are preferentially emitted in the same plane with respect to the beam axis as fission fragments detected in heavy ion collisions with Au and U targets.[Tsan84b, Tsan90] In Figure 1.14 we show the azimuthal distribution of alpha particles with respect to the reaction plane obtained by Tsang et al. for collisions with a U target. Since fission fragments produced in heavy-ion collisions are thought to be focused in the reaction plane,[Vaz83] a simultaneous explanation of all the correlation results was made by invoking the existence of a rotating source spinning off particles preferentially in the reaction plane. The angular momentum of such a source would originate from at least partial fusion between the projectile and target, so the angular momentum vector would be perpendicular to the reaction plane.

In our presentation of the data in chap. 4, we will use the idealized concepts of attractive flow, as shown in Figure 1.10, and a rotating source, as invoked by Tsang et al.,[Tsan84a] to provide a starting point for interpreting the data. In chap. 5 a more rigorous comparison between the data and these models will be carried out.

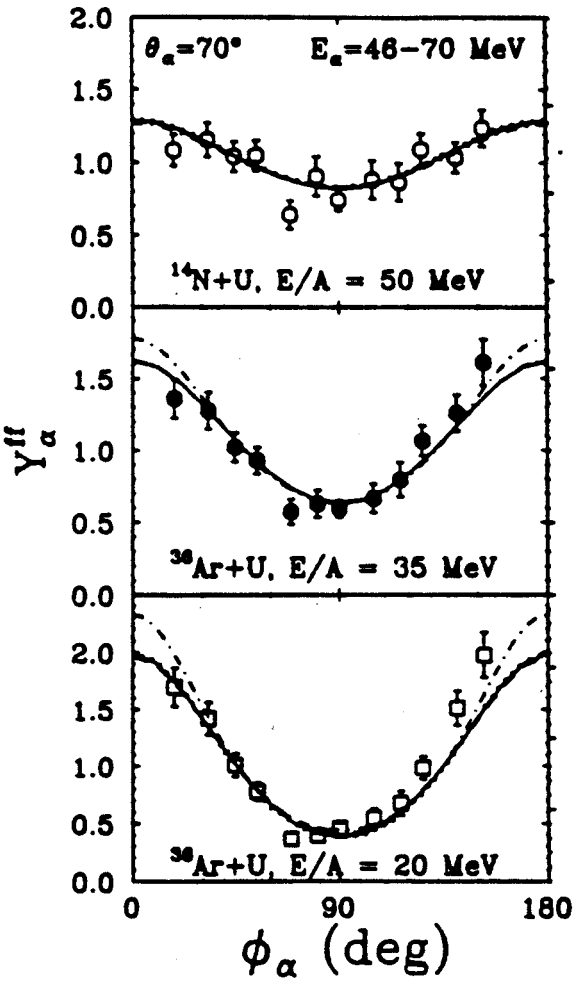


Figure 1.14: Azimuthal distribution of alpha particles around the reaction plane defined by fission fragments.[Tsan90]

# Chapter 2

# Description of the $4\pi$ Array Experiments

## 2.1 Beam and Target

The majority of the data presented in this thesis was taken using an $^{40}$Ar projectile on a $^{51}$V target. We chose this projectile because Ar was the heaviest ion that could be accelerated to beam energies up to 100 MeV/nucleon, increasing the probability that we could reach the regime where the dominant interaction becomes repulsive. V was the target closest to mass 40 available. It is desirable to have equal mass projectile and target because then it can be assumed that the projectile and target contribute equally to the participant (overlap) region, producing a source that moves with the center of mass velocity regardless of impact parameter.

A 35 MeV/nucleon Ar beam was produced by the MSU K500 superconducting cyclotron, and beams of 45, 55, 65, 75, 85, and 100 MeV/nucleon Ar were produced by the newer K1200 cyclotron. The target was a 3.34 mg/cm$^2$ V foil held in an aluminium frame. During the experiments, runs were also performed on an empty target frame to determine the amount of beam-frame interactions due to the possible presence around the beam spot of a low intensity halo. As a rule of thumb, the beam was focused until the target-in/target-out count rate ratio was greater than 10.

Ratios as high as 40 were not uncommon.

The beam current used varied from 50 to 100 electrical pA, depending on the amount available from the cyclotron and the count rate of the most forward large solid angle detectors. With beam bursts approximately every 50 ns, these currents corresponded to only 1 to 2 Ar ions in each burst, so the possibility of multiple events in a single beam burst was quite small and did not limit the allowed beam current. However, at detector count rates for single hits greater than $\approx$ 10000/second, the charge resolution was degraded due to pile up of signals, limiting the maximum beam current. Since this limit changes with the beam energy, the resolution of the detectors was monitored on line for any sign of reduced resolution and the beam current was adjusted accordingly.

For the chapter on peripheral events, a 50 MeV/nucleon $^{12}$C beam from the K500 cyclotron was incident on $^{12}$C and $^{197}$Au targets. The asymmetric system C+Au was used in order to evaluate the role of momentum conservation recoil by comparison with the lighter C+C system. The C projectile allowed allowed detection of projectile fragments (particles close to the beam in charge that appear in the forward direction due to peripheral collisions) down to lower energies in relation to the beam energy than an Ar projectile.

## 2.2 Detector Geometry

The choice of the geometry for the $4\pi$ Array was primarily governed by two requirements. The geometry had to allow closest packing of detector modules to allow nearly full $4\pi$ angular coverage, and ideally the modules would be interchangeable. This second requirement simplifies construction and allows "speciality modules" to be easily swapped in for coincidence experiments. The geometrical shape that was chosen was

a 32 faced truncated icosahedron, similar to a soccer ball, shown in Figure 2.1.

Twenty of the faces are hexagonal, and twelve are pentagonal. Two of the pentagonal faces are reserved for beam entrance and exit; all of the remaining sites are filled by detector modules. Each module is further subdivided into the triangular wedges which make up the **Main Ball** telescopes, 5 wedges for the pentagonal and 6 for the hexagonal modules, 170 in all. We exploited a previously built set of 30 cylindrical and 15 rectangular telescopes to partially fill the beam exit pentagonal site as a **Forward Array.** They were arranged about the beam axis as is shown in figure 2.2.

The solid angles covered by the telescopes are shown in Table 2.1 for Main Ball detectors. The true solid angles are slightly smaller than those predicted by ideal geometry due dead spaces between the modules. The Forward Array telescopes subtend a solid angle of $\approx$ 3 msr each, bringing the total coverage of the Main Ball/Forward Array system to 84% of $4\pi$.

Table 2.1: Solid Angles of Main Ball Telescopes

| Module Type | Geometric (msr) | True (msr) |
|---|---|---|
| Hex | 75.2 | 66.0 |
| Pent | 59.0 | 49.9 |

## 2.3 Detector Design

The detectors that make up the $4\pi$ Array are all of the same basic design, **phoswich** scintillator telescopes. As shown in Figure 2.3, the telescope is made of a thin layer of "fast" plastic scintillator in front of a larger piece of "slow" plastic scintillator which is optically coupled to a photomultiplier tube.[Wilk52] When any charged particle

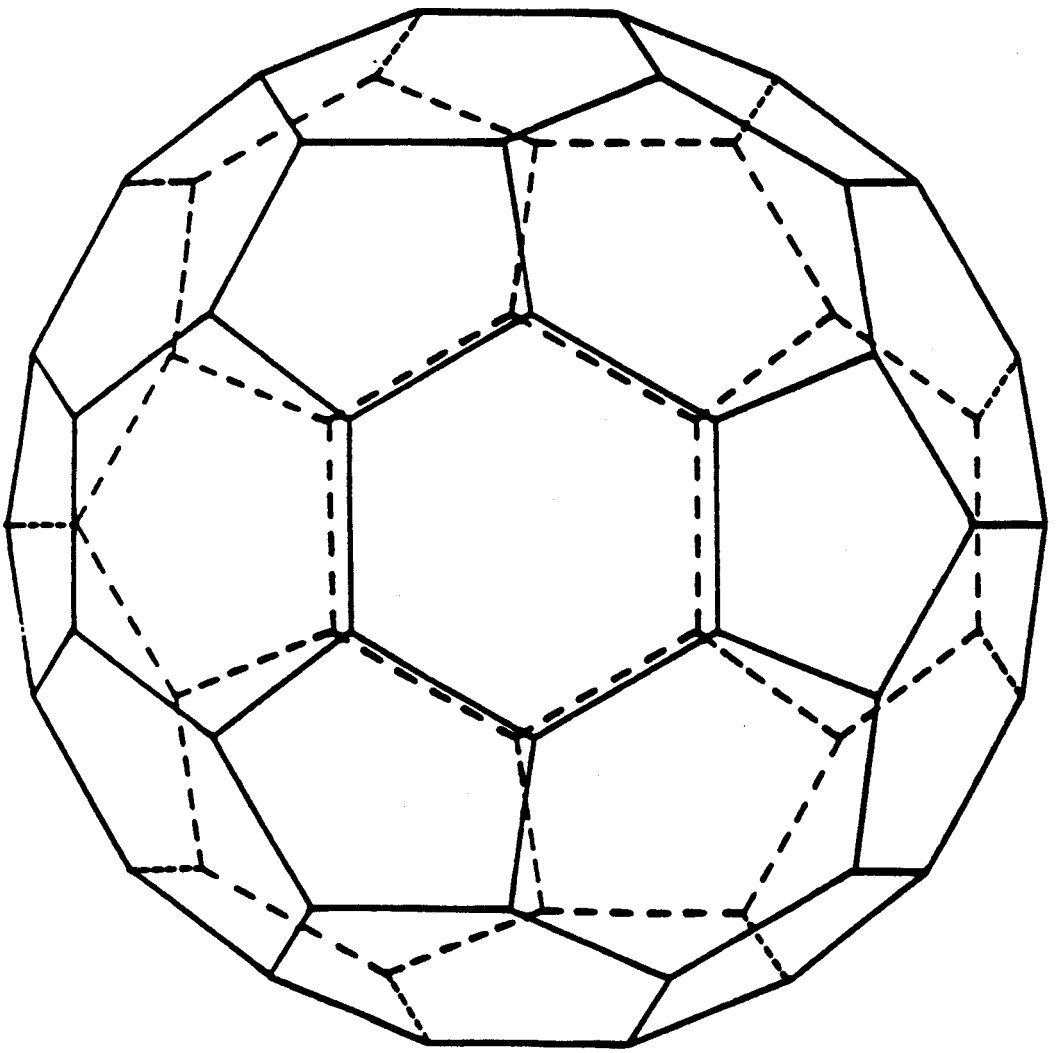

Figure 2.1: A truncated icosahedron, the basic geometry of the $4\pi$ Array

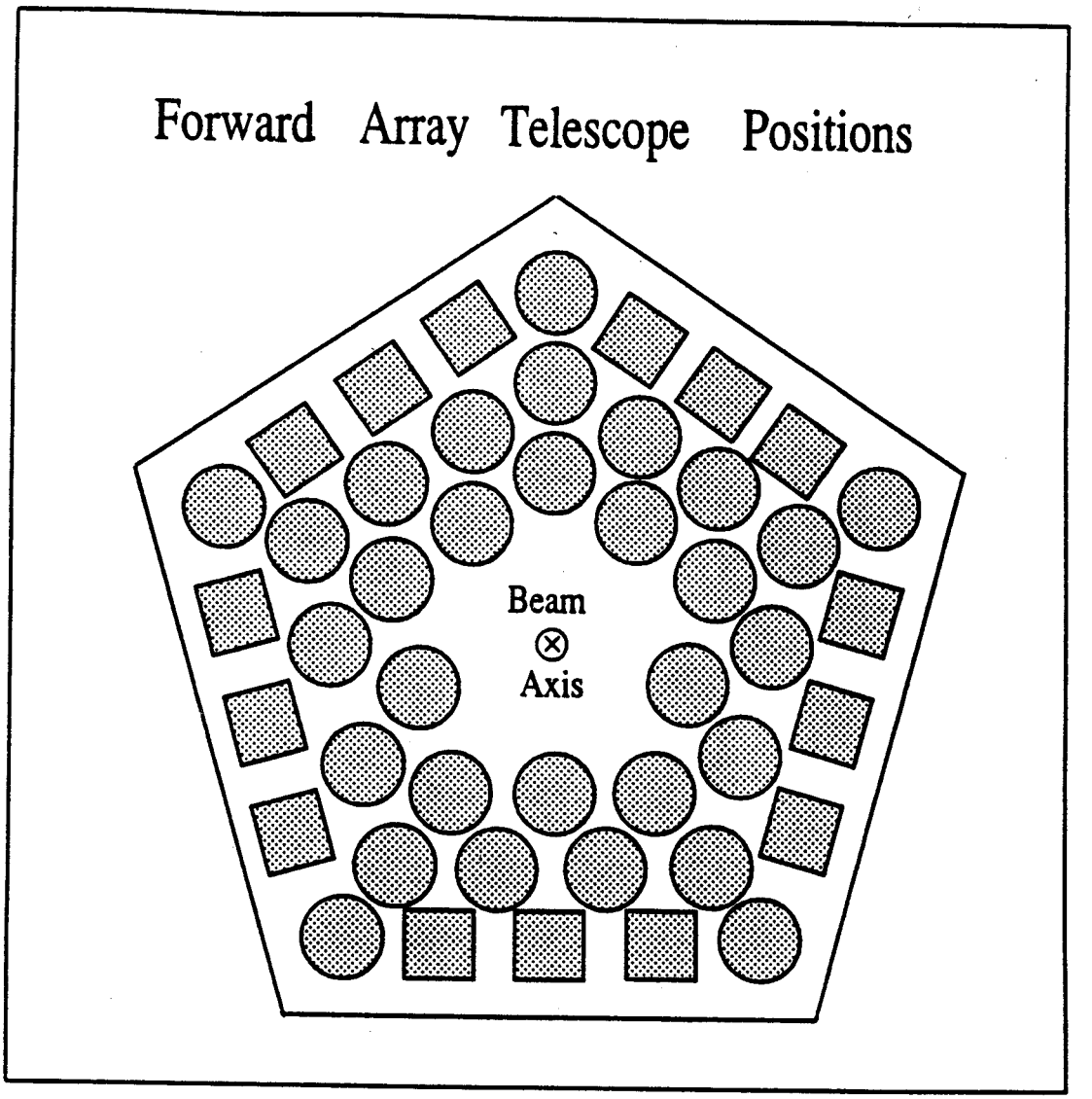


Figure 2.2: The positions of the front faces of the Forward Array telescopes. The beam axis goes into the page.

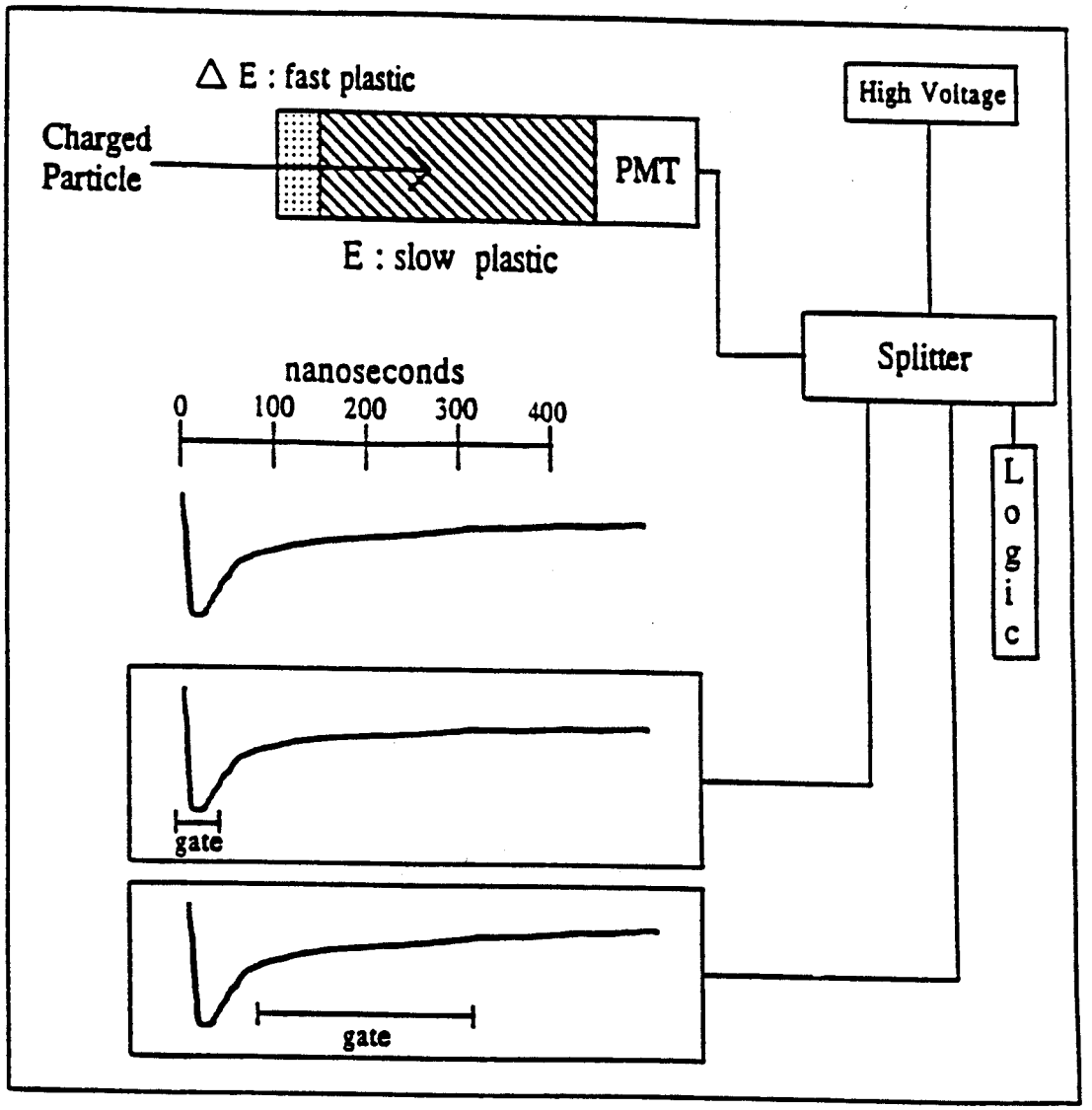


Figure 2.3: A phoswich (phosphor sandwich) detector. The positions of the gates used in the current integrating analog to digital converters (QDCs) are shown.

passes through the scintillator, its energy loss produces light, which is gathered by the photomultiplier tube and turned into a current pulse. The fast and slow plastic have shorter and longer decay times, shown in Table 2.2,[Bicr85] and thus their individual contributions to the current pulse can be separated. Figure 2.3 shows that the current from the photomultiplier is divided three ways: one stream is integrated over the time period during which the fast signal dominates, another is integrated to pick out the slow signal, while the third goes off to form the trigger stream, which will be discussed in Appendix A.

Table 2.2: Properties of the Fast and Slow Plastic Scintillators

| BICRON plastic | rise time (ns) | fall time (ns) |
|---|---|---|
| BC-412 (fast) | 1.0 | 3.3 |
| BC-444 (slow) | 19.5 | 179.7 |

The fast and slow components of the signal can be used together to identify charged particles which punch through the fast plastic using the **ΔE-E** technique. Since the energy loss is

$$-\frac{dE}{dx} \propto \frac{Z^2}{A} \tag{2.1}$$

at any given velocity, if the number of counts are plotted against the integrated fast (ΔE) and slow (E) signals, particles with different charges and masses will fall into different bands. A ΔE-E plot of 35 MeV/nucleon Ar+V data is shown in Figure 2.4 for a Forward Array telescope, and in Figure 2.5 for a Main Ball telescope. The characteristic features of a phoswich ΔE-E spectra are described schematically in Figure 2.6.

Particles with insufficient energy to punch through the fast plastic fall in the **punch-in line.** In this case, no energy is deposited in the slow plastic, but since the slow gate picks up a little of the decaying fast signal, the punch-in line has a finite

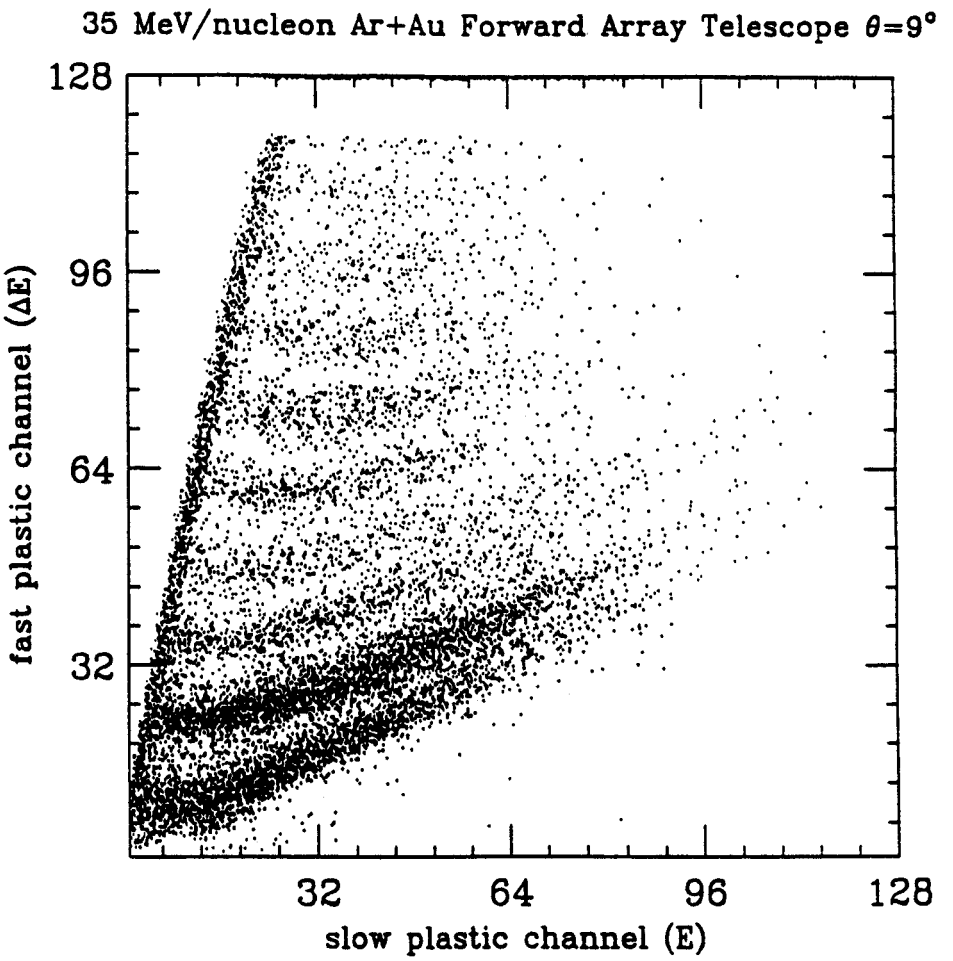


Figure 2.4: Counts as a function of the integrated fast ($\Delta$E) and slow (E) signals for a Forward Array phoswich telescope.

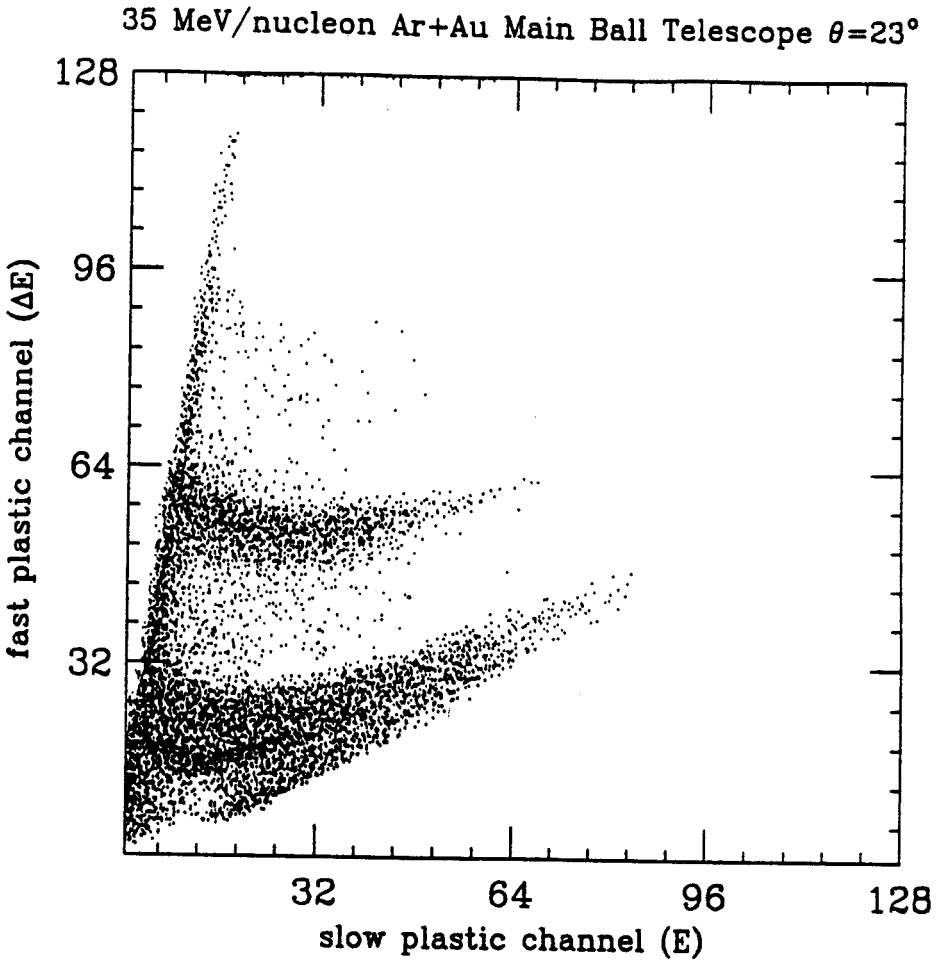


Figure 2.5: Counts as a function of the integrated fast ($\Delta$E) and slow (E) signals for a Main Ball phoswich telescope.

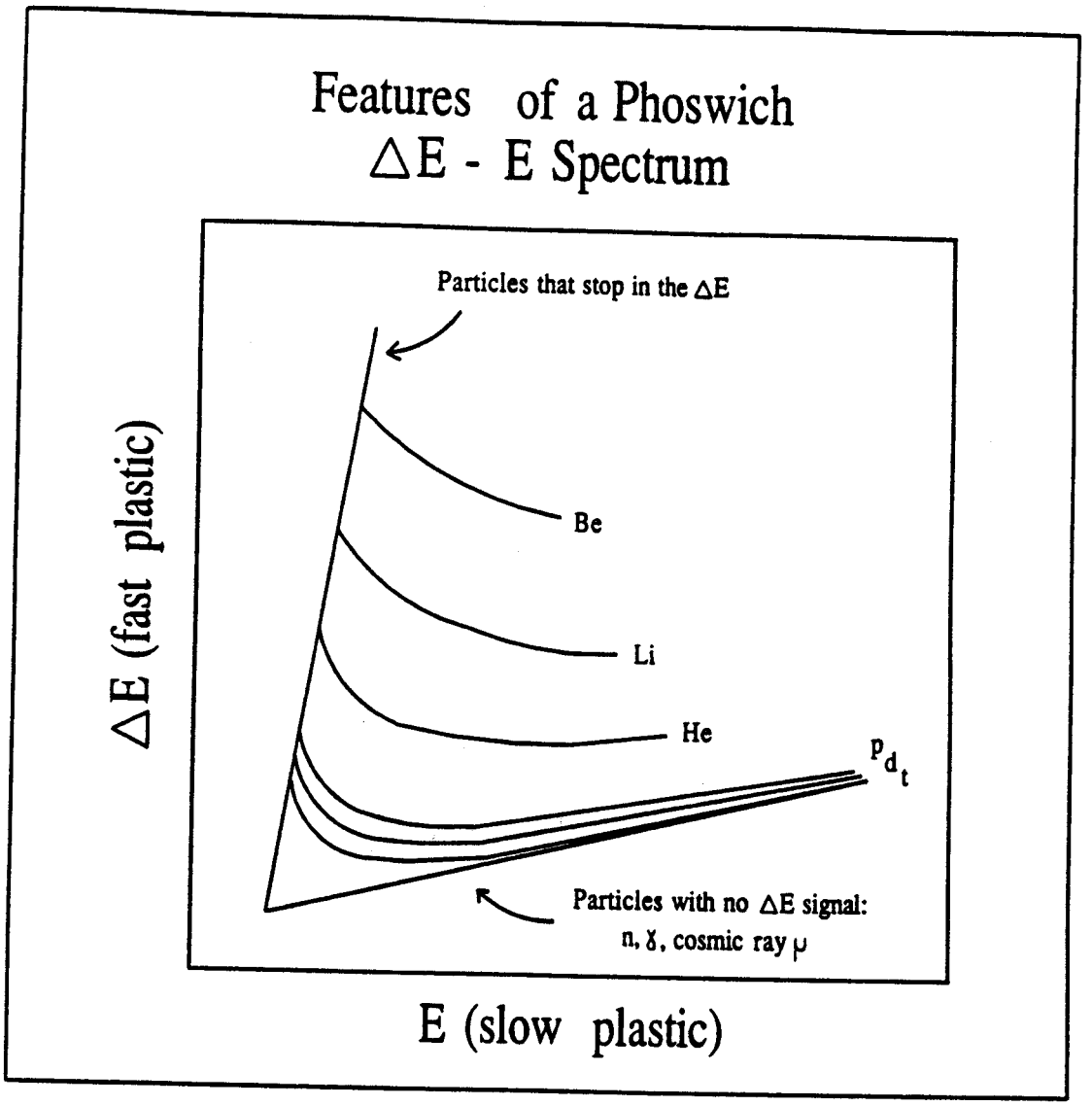


Figure 2.6: Schematic diagram of the features of a phoswich ΔE-E plot.

slope. Particles which do not pass through the fast plastic but strike the slow plastic, such as cosmic ray muons, and neutral particles which have a one time energy loss in the slow plastic, such as neutrons and gamma rays, fall in the **neutral line**. Again, although the particles have no fast signal, the fast gate picks up some of the rising slow signal and gives the neutral line a small slope. The point at which the two lines intersect corresponds to 0 energy, and thus represents an offset in the electronics. As the energy of particles striking the telescope is increased from 0, particles appear higher and higher in the punch-in line until they have enough energy to punch into the slow plastic, forming the different bands in the figure.

Particles which punch into the slow plastic can be positively identified, but particles which stop in the fast plastic can only be assigned a tentative charge and mass based on their position in the punch-in line. Since the cross section for particle production falls with increasing charge, we assign each region of the punch-in line the lowest allowed Z as an approximate identification. For example, particles in the punch-in line above the punch-through point of helium must have Z>2, those above the punch-through point of lithium must have Z>3, so we assign Z=3 for all the punch-in particles between these two points.

A particle must have a minimum of at least $\approx$ 4 MeV/Z in order to be detected in the fast scintillator. The thickness of the fast plastic determines the low energy threshold for well identified particles. The thickness of the fast plastic in the 170 Main Ball telescopes is 3.175 mm, and that of the 45 Forward Array telescopes is 1.566 mm, the value being smaller because these telescopes were originally designed for experiments at lower beam energies. These provide the low energy thresholds shown in Table 2.3 for the Main Ball and in Table 2.4 for the Forward Array. The upper energy threshold, the energy at which particles punch out back of the slow plastic, is > 200 MeV/nucleon, which is higher than the energies observed in these

experiments. There is, however, a practical limiting energy of $\approx$ 160 MeV for protons above which they are indistinguishable from the particles in the neutral line.

Table 2.3: Low Energy Thresholds of Main Ball

| Particle Type | Punch-in Energy (MeV) | Particle Type | Punch-in Energy (MeV) |
|---|---|---|---|
| p | 17 | Li | 140 |
| d | 24 | Be | 214 |
| t | 28 | B | 287 |
| He | 70 | C | 380 |

Table 2.4: Low Energy Thresholds of Forward Array

| Particle Type | Punch-in Energy (MeV) | Particle Type | Punch-in Energy (MeV) | Particle Type | Punch-in Energy (MeV) |
|---|---|---|---|---|---|
| p | 12 | C | 259 | Al | 816 |
| d | 16 | N | 328 | Si | 927 |
| t | 19 | O | 403 | P | 1009 |
| He | 47 | F | 472 | S | 1124 |
| Li | 95 | Ne | 570 | Cl | 1216 |
| Be | 146 | Na | 636 | Ar | 1403 |
| B | 195 | Mg | 737 | | |

The phototube gains of the Forward Array were set lower than those of the Main Ball in order to allow highly ionizing projectile fragments to be on scale in the Forward Array $\Delta$E-E plots. These high energy heavy fragments are only found at the most forward angles, so the Main Ball detectors could run with higher gain to improve their mass resolution without sacrificing detection of any particles. This difference in gains caused the Main Ball telescopes to be able to resolve the isotopes of H, and have charge resolution up to C. The Forward Array provided only charge resolution, but up to higher Zs. The maximum Z seen by the Forward Array telescopes was 8 for the

35 MeV/nucleon Ar beam, and was subsequently extended to 18 for the remaining beams.

## 2.4 Calibration

The detectors were energy calibrated by gain matching their ΔE-E spectra (figs. 2.4 and 2.5) to that of a previously calibrated detector.[Cebr90] The calibrated template spectra was obtained by fragmenting a heavy-ion beam on a target and using a dipole spectrometer to select particles of a known momentum to charge ratio. We found the response function of the fast plastic to be well described by the equation

$$L = C\sqrt{E} \tag{2.2}$$

in transmission mode and response of the slow plastic to be

$$L = C\frac{E^{1.4}}{Z^{0.8}A^{0.4}} \tag{2.3}$$

in stopping mode.[Cebr90] In the above equations, $L$ is the total light that the plastic generates in response to the charged particle, E is the kinetic energy of the particle, $A$ is its mass number, and $C$ is a detector specific normalization constant.

The procedure used for matching the spectra to the calibrated template proceeded through the following steps. Since the intersection of the neutral and punch-in lines corresponds to 0 energy loss in both the ΔE and E plastic, any deviation of this point from channel (0,0) represents an offset in the current integrating QDCs. The first step was to subtract this offset from the spectra. We have already noted that there is contamination in the E gate due to overlap with the decaying ΔE signal; this was eliminated in the next step by subtracting the E value of the neutral line from each point on the spectra according to the point's ΔE position. This operation left the neutral line with a 0 ΔE value. As a fourth step, the analogous operation

was performed on the ΔE channel to give a punch-in line with a 0 E value in order to eliminate contamination in the ΔE gate due to the rising E signal. Finally, the ΔE and E gains were adjusted by multiplicative factors to match the spectra to the calibrated template. We estimate the resulting energy calibration of the gain matched detectors to be better than 10%.

## 2.5 Triggering

The triggering system of the $4\pi$ Array allows one to select events by their multiplicity for storage on magnetic tape. The trigger condition can be on the multiplicity of ΔE hits in the Main Ball or the Forward Array. In addition, for the 45 to 85 MeV/nucleon Ar induced reactions, the capability to select on the total multiplicity was added. In general, a Forward Array multiplicity trigger will enrich the sample of peripheral events due to the forward focusing of particles, while a Main Ball trigger will emphasize more central events in which particles are emitted to larger polar angles with respect to the beam axis. Both types of data were acquired during the experimental runs.

Almost all of the data in this thesis were acquired in a nearly minimum bias mode, i.e. such that as few demands as were possible were placed on the events. For the 35 MeV/nucleon Ar+V data, events with one or more hit in the main ball were stored on tape. For the 45 to 100 MeV/nucleon Ar+V data, most of the runs used in the analysis were acquired under the condition that at least two particles were detected by the Main Ball + Forward Array system. A few runs had higher multiplicity requirements, and before the results from analysis of these runs were combined with the other runs, we checked that the overall trends in the data were similar. Because more stringent constraints were placed on the events in the process

of analysis, the different data acquisition constraints had no effects on the observables we will be examining. For the peripheral event analysis, in which the relationship between projectile fragments in the Forward Array and protons in the Main Ball was studied, the data were acquired under the condition that there be at least one hit in the main ball or one hit in the forward array.

## 2.6 Momentum Acceptance

The combination of kinetic energy thresholds and telescope angles produces the acceptance map in momentum space shown in Figure 2.7. In order to punch through the $\Delta$E plastic of the Main Ball, particles need about 195 MeV/c per nucleon, while for the Forward Array they need about 150 MeV/c per nucleon. This difference, along with the angular coverage of the telescopes, causes the minimum $P^{\perp}$ threshold to vary as a function of the parallel velocity. This effect will be important in our interpretation of experimental results in chaps. 4 and 6.

## 2.7 Simple Observables

Before concluding this chapter describing the $4\pi$ Array experiments, we will present some simple results which will provide an initial introduction to the data before we begin a more complex analysis.

In Figure 2.8 we display the number of charged particles detected in the Main Ball and Forward Array system using a minimum bias trigger for 45 and 100 MeV/nucleon Ar+V collisions. The higher multiplicity encountered at the larger beam energy reflects the increased kinetic energy available to push particles over the phoswich low energy thresholds. It may also imply that the composite system breaks up into smaller pieces as the beam energy increases.

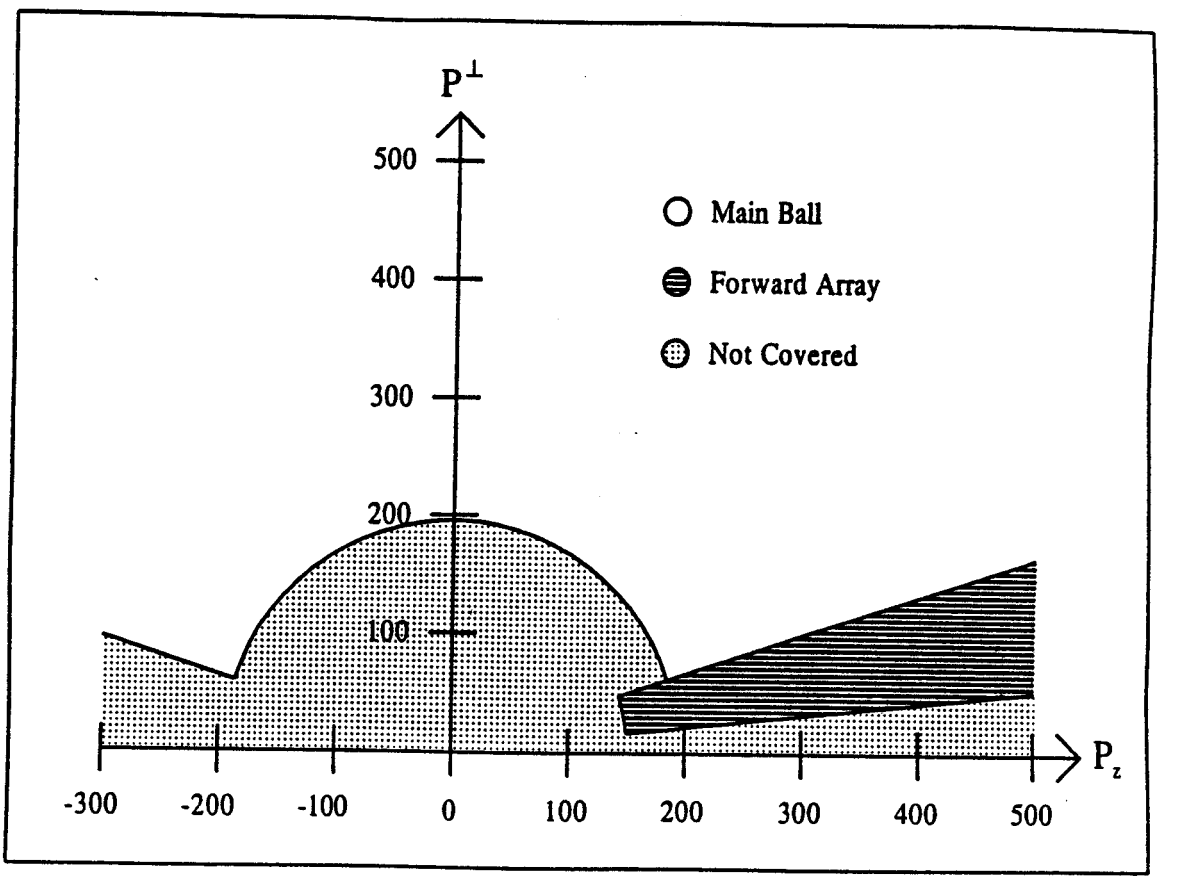


Figure 2.7: Acceptance of $4\pi$ Main Ball + Forward Array system in momentum space.

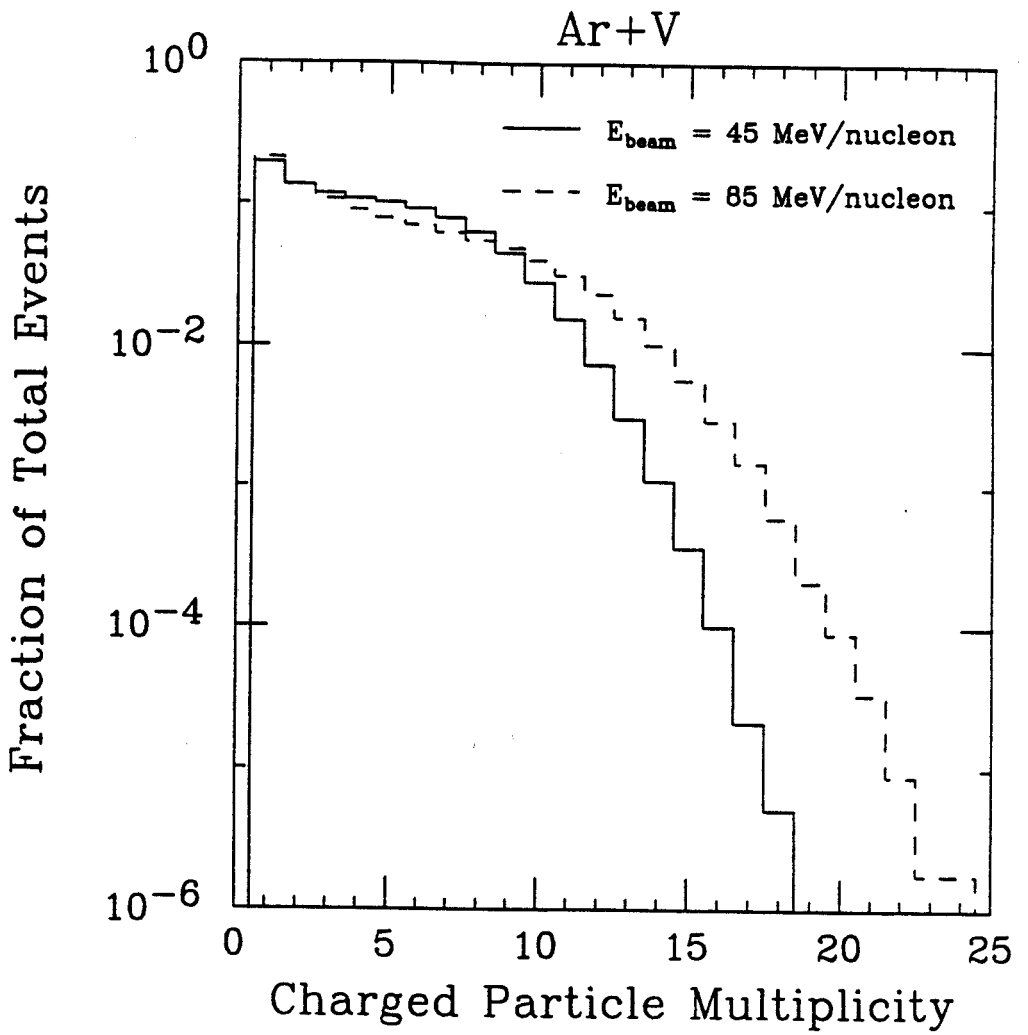


Figure 2.8: Multiplicity of charged particles detected by the $4\pi$ Array.

The kinetic energy spectra of light particles produced in intermediate energy heavy-ion collisions are well described by volume emission from thermal sources,

$$\frac{dN}{dE\,d\Omega} \propto \sqrt{E}e^{-\frac{E}{\tau}} \tag{2.4}$$

in the source frame of reference. In the equation above, $E$ is the kinetic energy of an emitted particle, and $N$ is the number of particles emitted into a solid angle $\Omega$. The relationship between the temperature parameter $\tau$ in eq. 2.4 and the actual temperature of excited systems produced in these collisions is the subject of debate. The temperatures yielded by fitting the participant source with this equation are much higher than those implied by the relative population of excited states in emitted fragments.[Morr84, Poch85, Fox88, Naya89] It is not clear that the assumption of thermodynamic equilibrium is justified given the complex dynamics of the reactions. The analysis presented in this thesis is a first step toward untangling the competing effects of collective motion and random thermal velocities.

In Figure 2.9 we display lab kinetic energy for He produced in central events at several beam energies. See Appendix C for the details of the impact parameter selection. The largest cross sections are at the smallest angles because the source is moving forward in the lab frame of reference.

A fit using the relativistic form of eq. 2.4 yields the curves shown in Figure 2.9. The low energy thresholds of the Main Ball detectors and the centrality cut limit contributions from the decay of the relatively "cool" spectator sources in this angular range. Only the "hot" mid-rapidity (participant) source is visible in these spectra, and this source dominates the Main Ball data presented throughout this thesis. The temperature parameter of this source increases smoothly with beam energy, as shown in Figure 2.10.

To summarize, the $4\pi$ Array detects several charged particles in an event. The

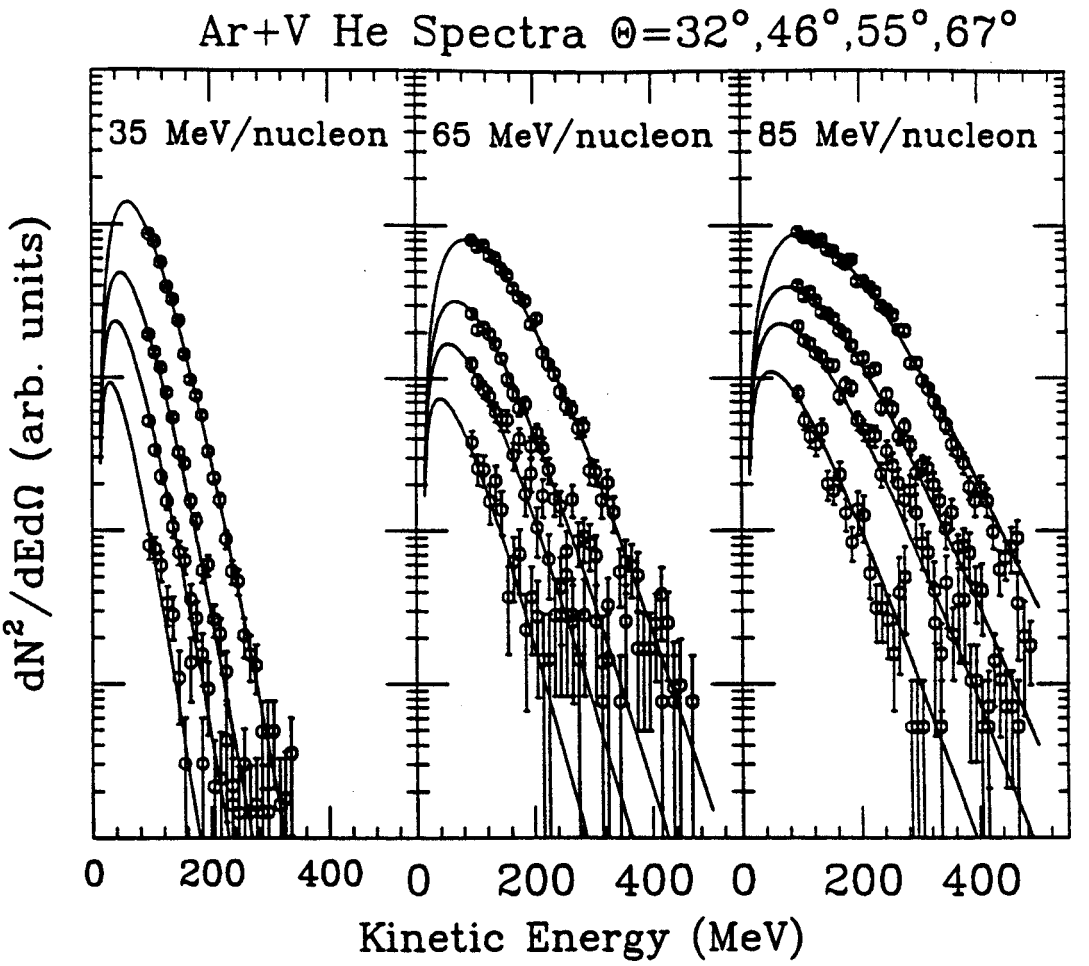


Figure 2.9: Kinetic energy spectra for He produced in central Ar+V collisions. The lines represent a fit using a single moving thermal source.

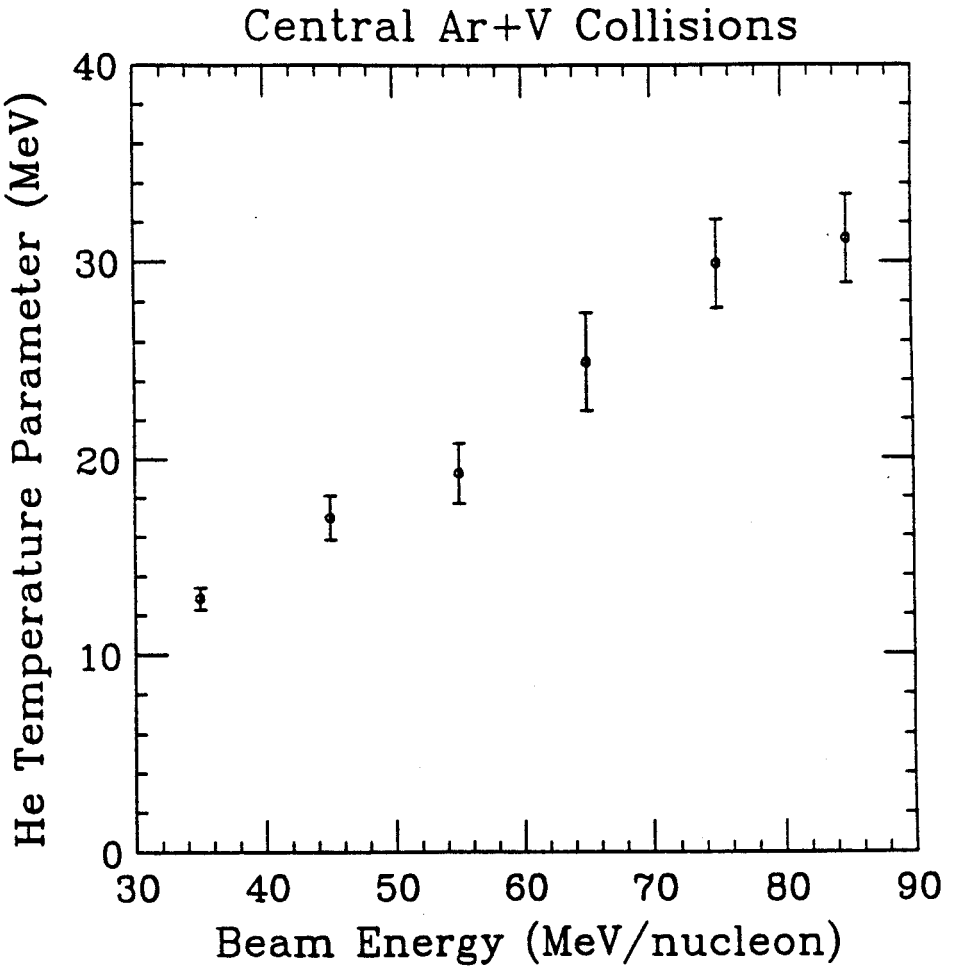


Figure 2.10: Temperature of the mid-rapidity source as a function of beam energy.[Li91]

particles observed in the Main Ball come predominantly from the highly excited participant region. The energy spectra are smooth exponential curves, suggesting a thermal character for the source of the particles. In the following chapters, we will focus on ordered collective motion in the mid-rapidity region.

# Chapter 3

# Reaction Plane Determination

## 3.1 Introduction

Collective motion is manifested in the velocity distribution with respect to the reaction plane. In order to study collective motion, a technique for determining the reaction plane based on the final distribution of reaction products is necessary. In this chapter, after reviewing two techniques which have been employed at larger beam energies, we present a new method of reaction plane determination particularly suited to the 10 to 100 MeV/nucleon beam energy regime. The consistency of the technique is checked, and we explore for any bias in the reaction plane determination due to detector acceptance. Finally, the accuracy of the technique is assessed.

The reaction plane can be geometrically defined as the plane containing the momentum vector of the projectile and the center of the target. The impact vector, $\vec{b}$, which joins the centers of the projectile and target at their closest approach, lies within this plane. These geometrical relationships are shown schematically in Figure 3.1. It is useful to distinguish between the two sides of the reaction plane as divided by the beam axis, which will be referred to as the forward flow side and the backward flow side. These two sides contain the forward going and backward going sections of the particle flow in the center of mass frame of reference as shown

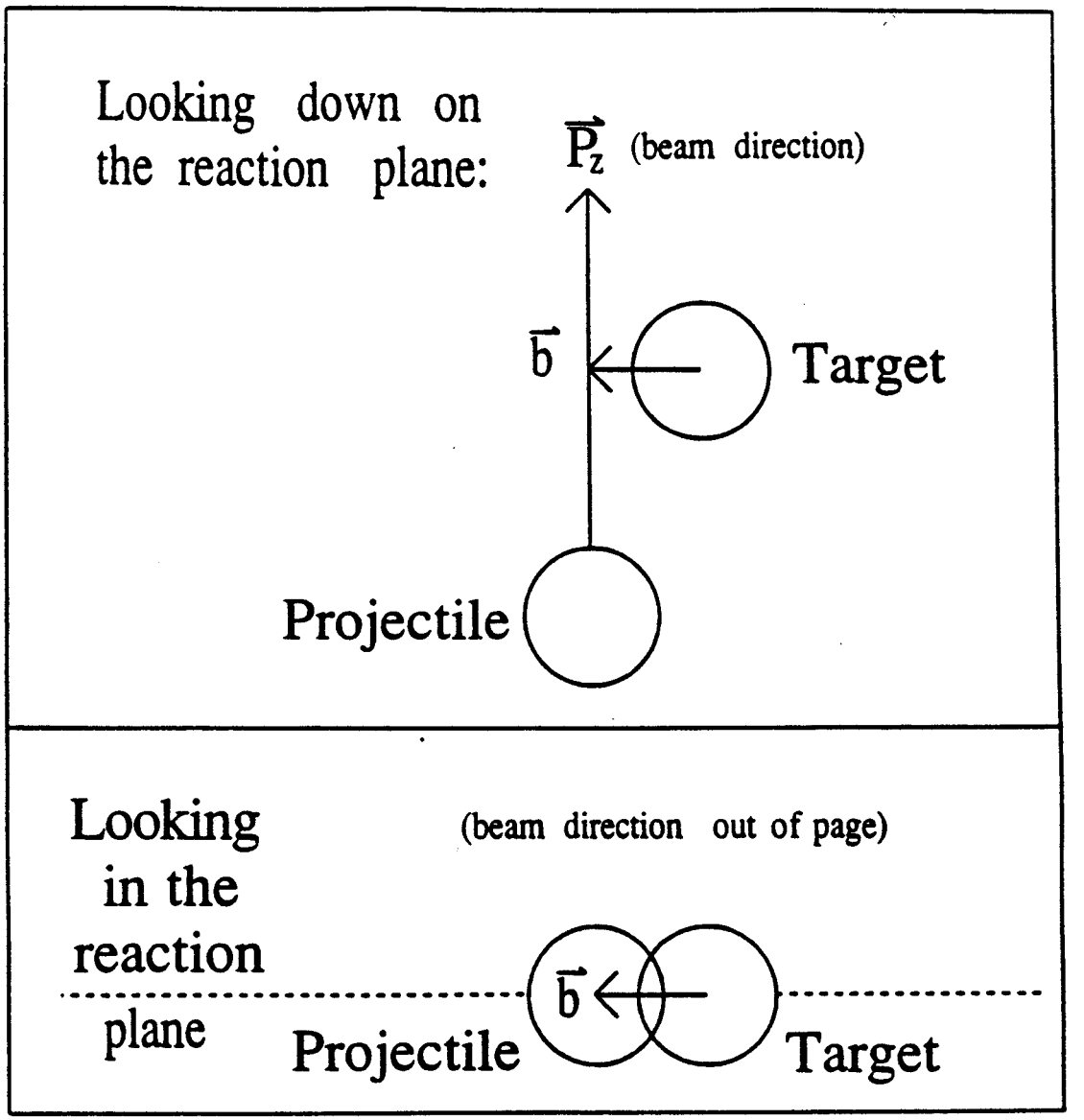


Figure 3.1: A geometrical description of the reaction plane.

in Figure 3.2. Attractive and repulsive flow cannot be distinguished from each other experimentally using the techniques described in this chapter. We will return to the question of the direction of the deflection in chap. 6.

## 3.2 Previously Established Techniques

Two techniques are commonly used to determine the reaction plane from the observed distribution of light fragments produced in heavy-ion collisions, the **sphericity tensor method** and **transverse momentum analysis.**[Gyul82, Dani85] Both techniques exploit the presence of transverse momentum flow in the reaction plane on an event by event basis. These methods have been applied successfully in collective motion analysis of collisions at beam energies ranging from around 100 MeV/nucleon to more than 1 GeV/nucleon[Gutb89a]. We will describe each method in turn, and then discuss the difficulties encountered in applying them to collisions in the 10 to 100 MeV/nucleon range.

In the sphericity tensor method, the shape of the event in momentum space is determined by diagonalizing the the flow tensor $F_{ij}$:

$$F_{ij} = \sum_{\nu=1}^{N} w_\nu p_i(\nu) p_j(\nu), \tag{3.1}$$

where $N$ is the number of particles in an event, $p_i(\nu)$ are the cartesian components of the momentum of particle $\nu$, and $w_\nu$ is a weighting factor associated with that particle, typically $\frac{1}{2m_\nu}$. The reaction plane is taken as the plane defined by the beam axis and the major axis of the resulting flow ellipsoid.

In transverse momentum analysis, the vector $\vec{Q}$ is constructed:

$$\vec{Q} = \sum_{\nu=1}^{N} w_\nu \vec{p}_\nu^{\perp}, \tag{3.2}$$

where $\vec{p}_\nu^{\perp}$ is the component of the momentum of particle $\nu$ perpendicular to the beam

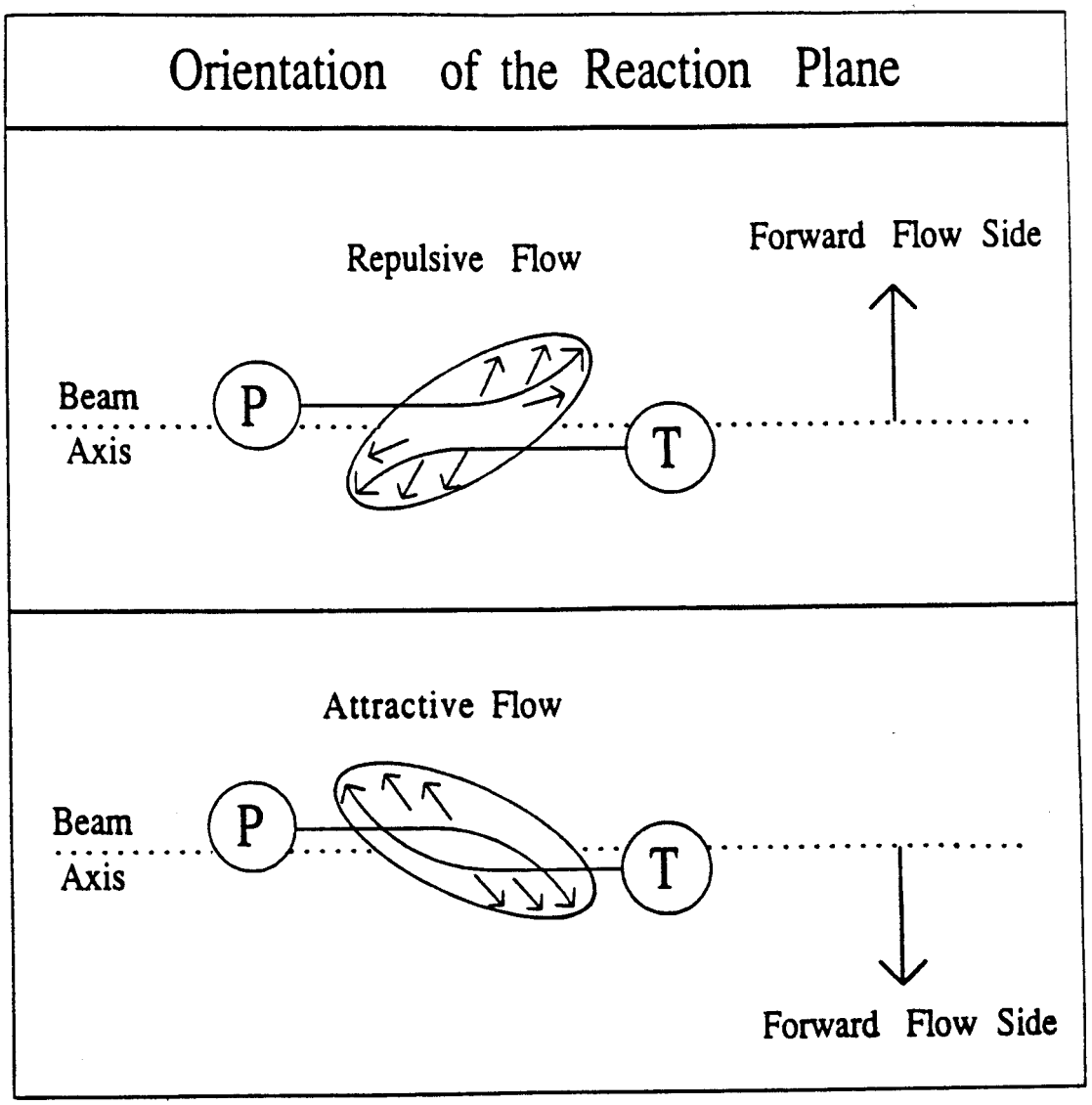


Figure 3.2: The definition of the forward flow side of the reaction plane for both attractive and repulsive scattering. The perspective of the figure is looking down on the reaction plane.

axis. The reaction plane is defined by the beam axis and $\vec{Q}$. The weight, $w_\nu$, is taken to be positive for particles emitted in the forward center of mass hemisphere and negative for particles emitted in the backward hemisphere. The absolute value of $w_\nu$ is chosen to provide the maximum sensitivity to the reaction plane. In practice this is achieved by randomly dividing events into two sub-events, calculating $\vec{Q}$ for each sub-event, and selecting $w_\nu$ to minimize the difference between the resulting reaction planes. Typical values for $\mid w_\nu \mid$ are 1.0[Dani85, Gutb89a] and $m_\nu$[Ogil89b], the mass of particle $\nu$.

Both of these techniques depend on the existence of collective flow in the reaction plane. The transverse momentum and sphericity tensor approaches have recently been shown to be equally sensitive to flow[Gutb90]. Transverse momentum analysis of 35 MeV/nucleon Ar+V data taken with the MSU $4\pi$ Array, however, has shown comparatively weak flow for this system[Ogil89b], making the application of these techniques problematic at this beam energies. Fortunately, during our preliminary analysis using the transverse momentum technique, we found a substantial enhancement of particle emission in the reaction plane[Wils90] that can be exploited to determine the plane.

## 3.3 Preliminary Analysis

The weighting used in eq. 3.2 for the preliminary analysis with the transverse momentum technique was $\mid w_\nu \mid = m_\nu$. Only events with at least three identified particles were analyzed to enhance the accuracy of the reaction plane determination. The data were smoothed along the $\phi$ axis to remove structure due to the azimuthal granularity of the $4\pi$ Array.

Enhanced emission in the reaction plane is evident in the data of Figure 3.3, a contour map of $\frac{dN}{d\phi}$ as a function of $\phi$ and rapidity. $N$ is the number of particles

detected, $\phi$ is the azimuthal angle around the beam axis measured with respect to the forward flow side of the reaction plane, and $y$ is the parallel rapidity of the detected particle in the lab frame of reference. There are simultaneous peaks on both the forward flow side ($\phi = 0°, 360°$) and the backward flow side ($\phi = 180°$) of the reaction plane near the center of mass rapidity. A similar in-plane enhancement was observed by Tsang et al.[Tsan90] in heavy-ion reactions with U targets in which the reaction plane was determined using the azimuthal angles of fission fragments.

This pattern of enhancement is different from that expected from strong flow, i.e. peaks on the forward flow side at $y > y_{c.m.}$ and peaks on the backward flow side for $y < y_{c.m.}$. Since flow is weak, the sphericity tensor method would lead to small angles between the major axis of the flow ellipsoid and the beam axis, providing an imprecise reaction plane determination. Transverse momentum analysis would also have difficulty with this emission pattern since $\sum_{\nu=1}^{N} \vec{p}_\nu^{\perp}$ would tend towards zero for the forward and backward rapidity regions in the center of mass. The observed weakness of flow and strength of in-plane emission for this system led us to develop a new technique for determining the reaction plane that could exploit any form of in-plane enhancement, not just flow.

## 3.4 The Azimuthal Correlation Method

In essence, the new technique consists of finding the reaction plane that aligns best with the enhancement plane. We proceed by first projecting the event on the $p^x$–$p^y$ plane with the $p^z$ axis defined by the beam axis. The projection of the reaction plane is taken as a line in the $p^x$–$p^y$ plane passing through the origin (beam axis) with slope $a$. The square of the deviation of the particles from the reaction plane, $D^2$, is parameterized by the sum of the squares of the perpendicular distances $d_\nu^2$

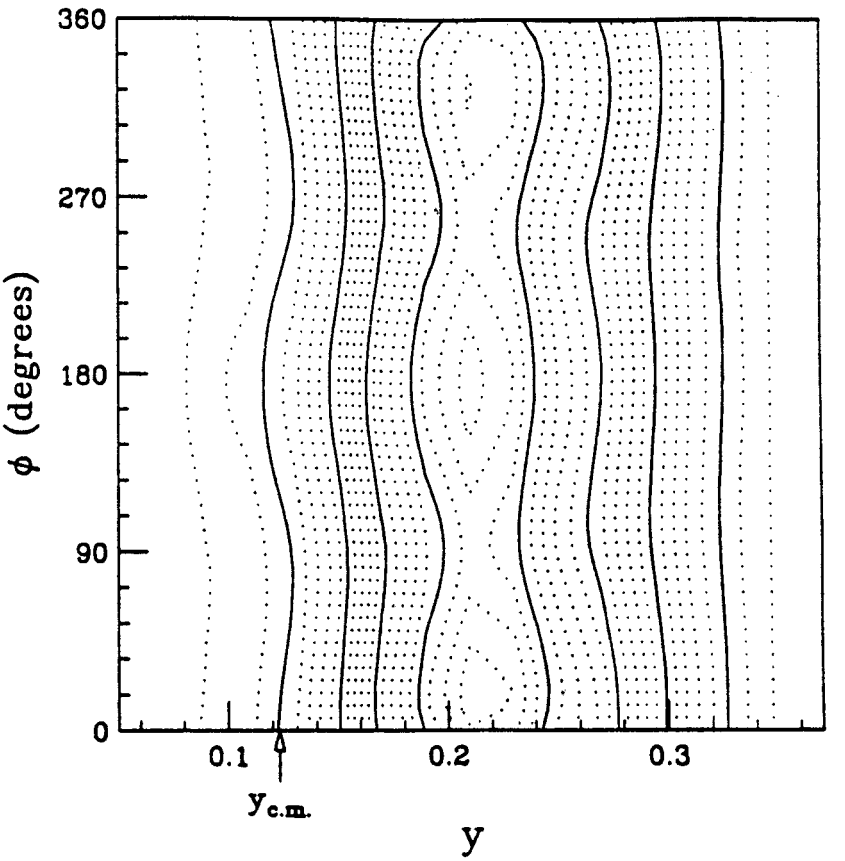


Figure 3.3: The cross section for charged particles from 35 MeV/nucleon Ar+V collisions. The azimuthal angle with respect to the forward flow side of the reaction plane is labeled $\phi$, and $y$ is the lab rapidity.

between the line and the particles in the $p^x$–$p^y$ plane as shown in figure 3.4. The slope corresponds to the tangent of the azimuthal angle of the reaction plane (measured from the $p^x$ axis), $\phi_{rp}$ in the figure. The deviation $D$ as a function of the slope of the reaction plane's projection onto the $p^x$–$p^y$ plane is:

$$D^2 = \sum_{\nu=1}^{N}[d_\nu^2] = \sum_{\nu=1}^{N}[(p_\nu^x)^2 + (p_\nu^y)^2 - \frac{(p_\nu^x + p_\nu^y a)^2}{1+a^2}]. \tag{3.3}$$

The condition that the derivative of $D^2$ with respect to $a$ vanish produces a quadratic equation whose roots,

$$a = \frac{\sum_{\nu=1}^{N}[(p_\nu^y)^2 - (p_\nu^x)^2] \pm \sqrt{(\sum_{\nu=1}^{N}[(p_\nu^x)^2 - (p_\nu^y)^2])^2 + 4(\sum_{\nu=1}^{N}[p_\nu^x p_\nu^y])^2}}{2\sum_{\nu=1}^{N}[p_\nu^x p_\nu^y]} \tag{3.4}$$

determine $a$. Plugging the roots back in to the original equation allows one to pick the root that minimizes $D$ and hence maximizes the in-plane enhancement. Since the technique exploits the correlation between the azimuthal angle of the reaction plane and the azimuthal angles of the particles produced in the collision, it will be referred to as the **azimuthal correlation** method.

Both the transverse momentum and sphericity tensor techniques provide not only the azimuthal angle of the reaction plane but also determine the forward flow side as defined in Figure 3.2. The forward half of the momentum flow ellipsoid lies in the forward flow side of the reaction plane, and the $\vec{Q}$ points toward the forward flow side. The angular correlation method, however, does not distinguish between the two sides of the reaction plane; therefore, this method must be supplemented by one of the two previous techniques in order to be sensitive to transverse momentum flow. We employ the transverse momentum $\vec{Q}$ vector to determine which side of the rection plane, already found using azimuthal correlations, contains the forward flow component. We used the mass weighting scheme presented earlier, and restricted the sum to well identified particles that punched through the $\Delta E$ plastic. The sums in

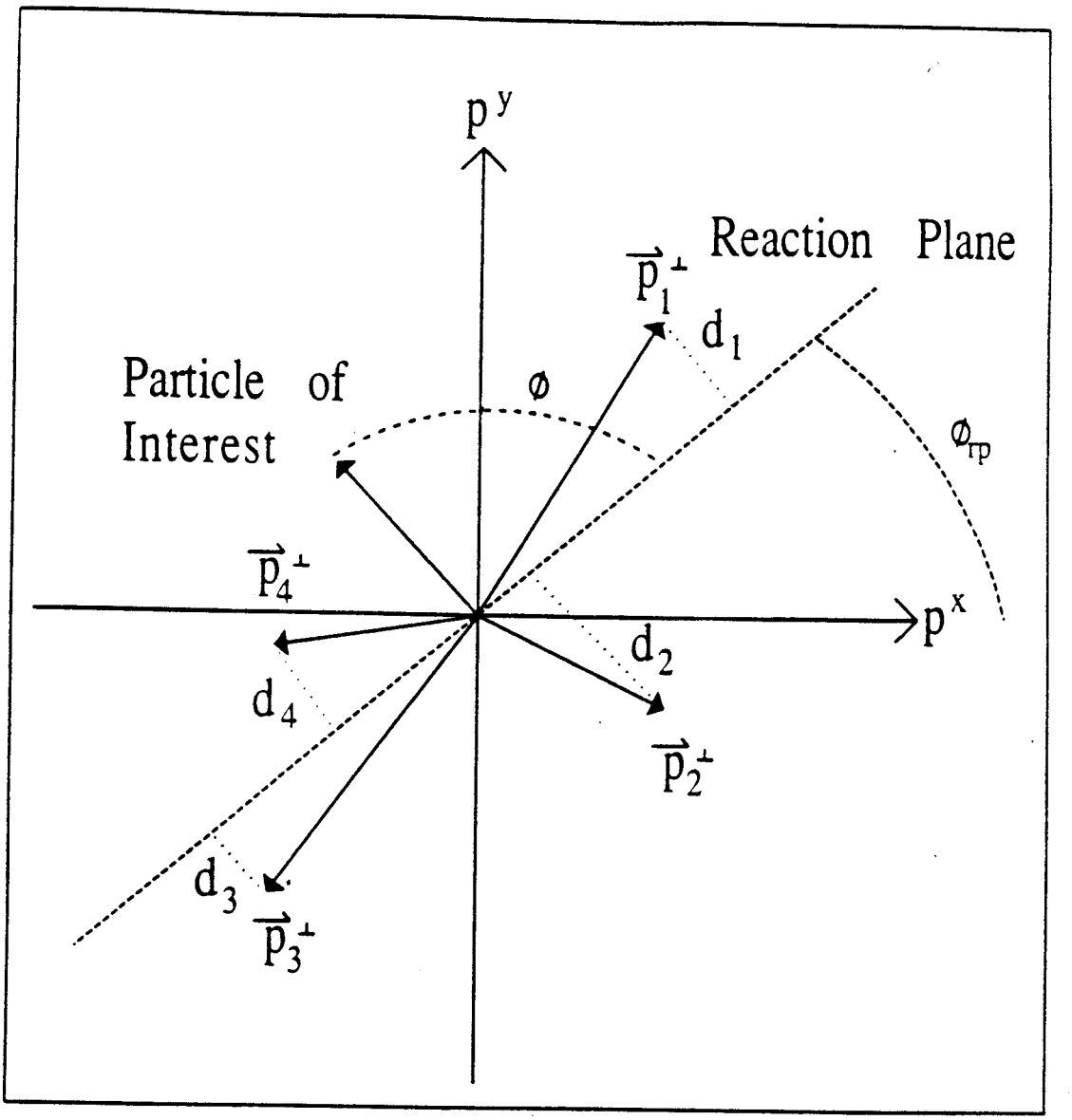


Figure 3.4: The quantities used in finding the reaction plane for an event projected on the $p^x$–$p^y$ plane. The angle of a particle of interest with respect to the forward flow side of the reaction plane is labeled $\phi$.

the azimuthal correlation equations, however, were taken over all the particles in the event. Thus, the procedure for determining the reaction plane consists of two distinct operations, first finding the plane by azimuthal correlations and then choosing the forward flow side from $\vec{Q}$. Each operation is expected to have its own efficiency.

In Figure 3.4, the azimuthal angle a particle of interest makes with the forward flow side of the reaction plane is labeled $\phi$. If this angle is to be studied, then the particle of interest (POI) must be left out of the sums in the previous equations for all three techniques. Otherwise, a spurious **autocorrelation** between the POI and the reaction plane will result. As an example, Figure 3.5 shows the distribution of azimuthal angles between POIs and reaction planes for isotropic emission. The data in this figure were generated using a 10 MeV thermal distribution with a nucleon multiplicity of 10, similar to the temperatures and multiplicities observed in this beam energy regime by the $4\pi$ Array. The dotted histogram shows the in-plane enhancement which results from including the POI in the reaction plane sums; when it is excluded the isotropic distribution is recovered as shown in the solid histogram. The correct procedure for creating histogram of the azimuthal angles of emission with respect to the reaction plane thus involves a separate reaction plane calculation for each POI in an event.

Leaving out the POI reduces the number of particles used in finding the reaction plane and hence slightly reduces the accuracy of the reaction plane determination. The strength of this effect can be gauged by measuring the difference between the azimuthal angle of the reaction plane calculated using the whole event and the plane calculated while leaving out the POI. The distribution of these differences is shown in Figure 3.6 for the 35 MeV/nucleon Ar+V events. There is a sharp peak at 0° difference, indicating that the reduction in the accuracy due to leaving out the POI is small. A peak also appears at 180°, corresponding to a slight probability for $\vec{Q}$ to

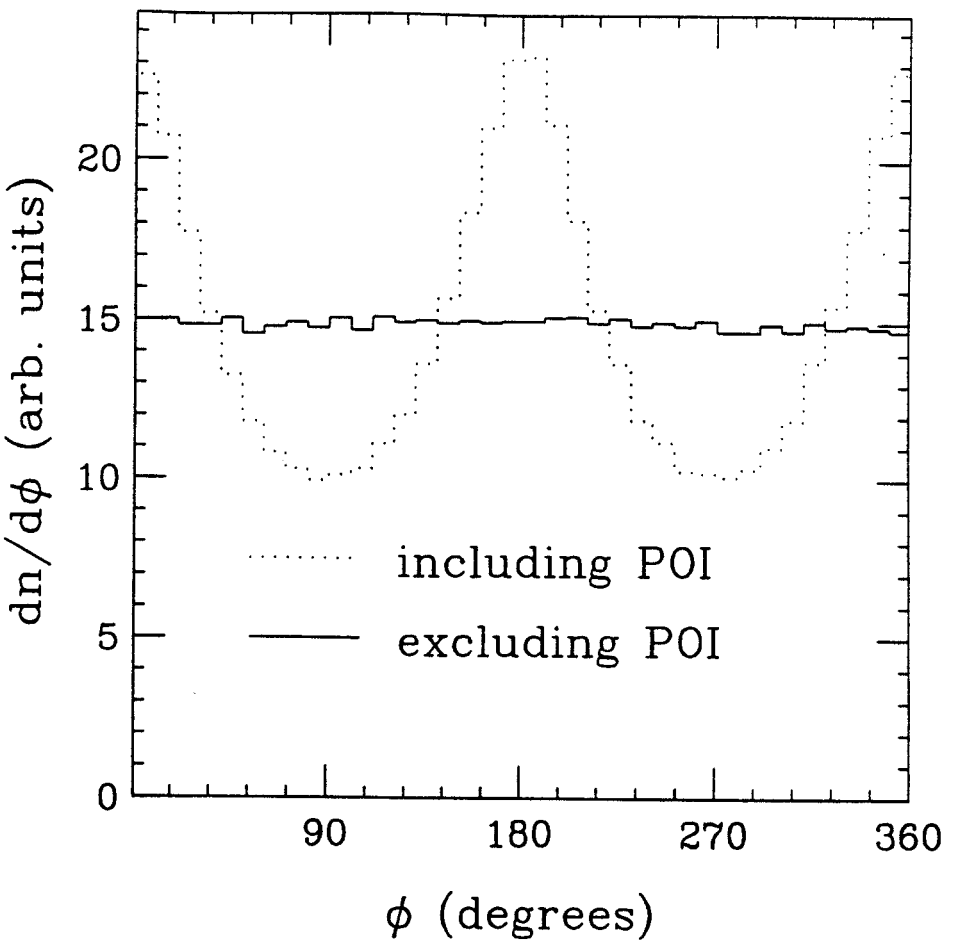


Figure 3.5: The spurious in-plane enhancement in $dn/d\phi$ due to including the particle of interest in the reaction plane determination is shown as a dashed histogram for simulated events. Removing the POI restores azimuthal symmetry. The azimuthal angle that the POI makes with respect to the reaction plane is labeled $\phi$.

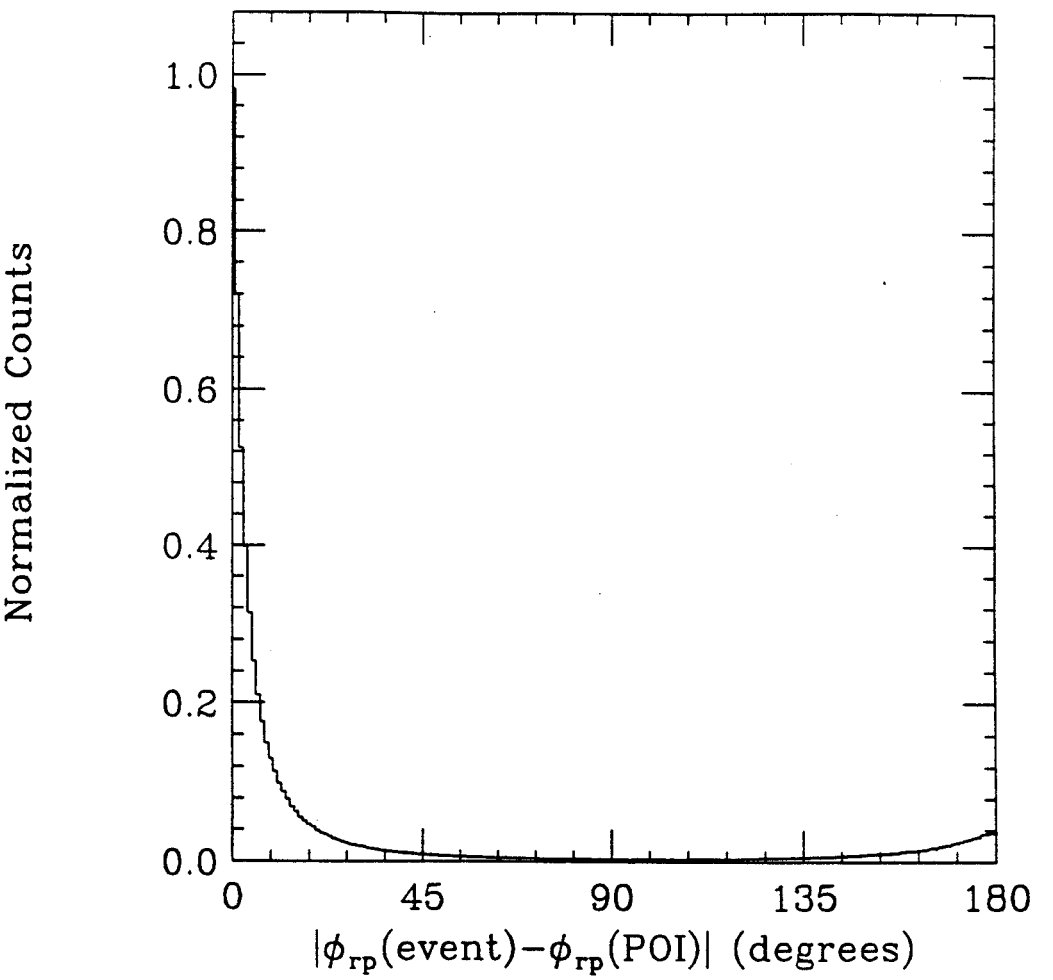


Figure 3.6: The azimuthal distribution of differences between reaction planes found for the entire events ($\phi_{rp}(event)$) and reaction planes found leaving out a particle of interest ($\phi_{rp}(POI)$).

switch sides of the reaction plane when the POI is removed.

We have evaluated different weighting schemes in the azimuthal correlation method by substituting $\sigma_\nu k_\nu^i$ for $p_\nu^i$ in equation 3.4, where $\sigma_\nu$ is a weighting factor assigned to particle $\nu$ and $k_\nu^i$ is the $i$th component of a unit vector $\hat{k}_\nu$ pointing in the $\vec{p}_\nu^{\perp}$ direction. Transverse momentum weighting ($\sigma_\nu = p_\nu^\perp$) recovers equation 3.4. Other possibilities explored were no weighting ($\sigma_\nu = 1$), mass weighting ($\sigma_\nu = m_\nu$), and center of mass polar angle weighting ($\sigma_\nu = \sin\theta_{cm}$). The latter choice was motivated by the observation that the in-plane enhancement is strongest near $y = y_{cm}$. The results of the four weighting choices are shown in Figure 3.7 which displays the distribution of azimuthal emission angles of POIs relative to the reaction plane for 35 MeV/nucleon Ar+V data taken with the MSU $4\pi$ Array. The data were smoothed over $\phi$ to remove structure due to the azimuthal granularity of the detector array. Transverse momentum weighting exhibits the strongest peaking in the reaction plane at $\phi = 180°$ and the strongest valleys perpendicular to the reaction plane at $\phi = 90°$ and $270°$, and must therefore provide the most accurate reaction plane determination.

An additional source of bias in reaction plane determination is momentum conservation in the emission of the particle of interest. This causes the remaining particles in the event to recoil away from the POI, creating an axis in the $p_x - p_y$ plane which can be mistaken for the reaction plane. Because of the detector energy thresholds, most of the detected particles are going forward in the c.m. frame of reference, and thus the momentum conservation effect causes the forward flow side of the reaction plane to be preferentially found $\approx 180°$ away from the POI. Momentum conservation can therefore be thought of as an effective anti-autocorrelation. Even if each particle is emitted from its source in a random direction, an enhancement in the reaction plane will be observed in the azimuthal distributions due to momentum conservation.

This effect is illustrated in Figure 3.8 for a simulation of nucleons emitted from

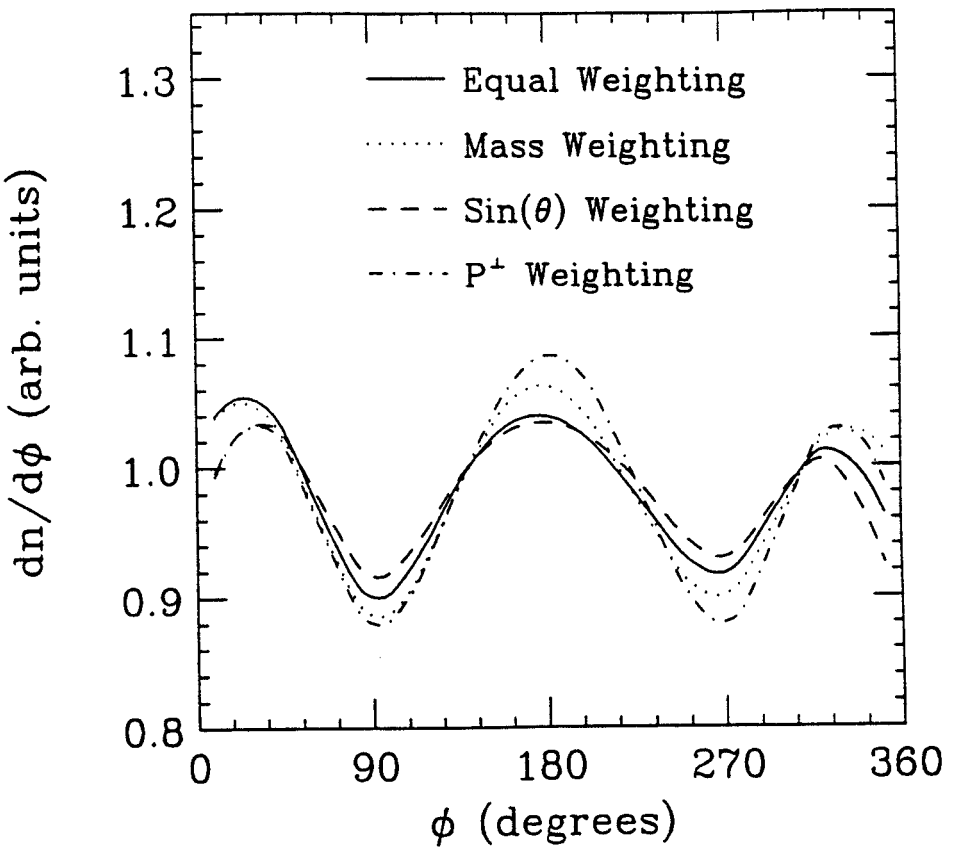


Figure 3.7: Comparison of azimuthal distributions of particles of interest with respect to the reaction plane using different weightings in determining the plane. Transverse momentum weighting supplies the most accurate reaction plane determination.

mass number 10 sources with temperatures of 10 MeV. In the first panel, the sources emitted nucleons isotropically with no momentum conservation constraints, resulting in a flat azimuthal distribution. In the second panel, the emission again was isotropic, but with the constraint that the total momentum of the event (including the POI) be identical with the initial source momentum. As a result, the azimuthal distribution shows enhanced emission in the reaction plane. This spurious enhancement is due to the correlation between the momentum of the POI and the momenta of the remaining particles, biasing the reaction plane determination toward the plane containing the POI.

To cancel the effect of momentum conservation, as each particle of interest was chosen, the observed transverse momenta of the remaining particles were boosted toward the POI before using them to find the reaction plane. We assumed that the whole system, $m_{proj.} + m_{targ.}$, shared the recoil momentum. This should be a good approximation, since our multiplicity requirements for reaction plane determination restricts us to near-central collisions in which the participant region should encompass nearly the whole of the projectile and target. This assumption gives a boost velocity

$$\vec{V}^{\perp}_{boost} = \frac{\vec{p}^{\perp}_{POI}}{m_{total} - m_{POI}}, \tag{3.5}$$

where $\vec{p}^{\perp}_{POI}$ is the transverse component of the momentum of the POI, $m_{total}$ is the total mass of the the system, and $m_{POI}$ is the mass of the particle of interest. This was the most conservative approach since it resulted in the minimum correction. The velocities parallel to the beam axis were not modified since they play no role in the reaction plane determination. When this boost was applied to the data created for the middle panel of Figure 3.8, it restored the isotropic symmetry to the azimuthal distribution, as shown in the bottom panel.

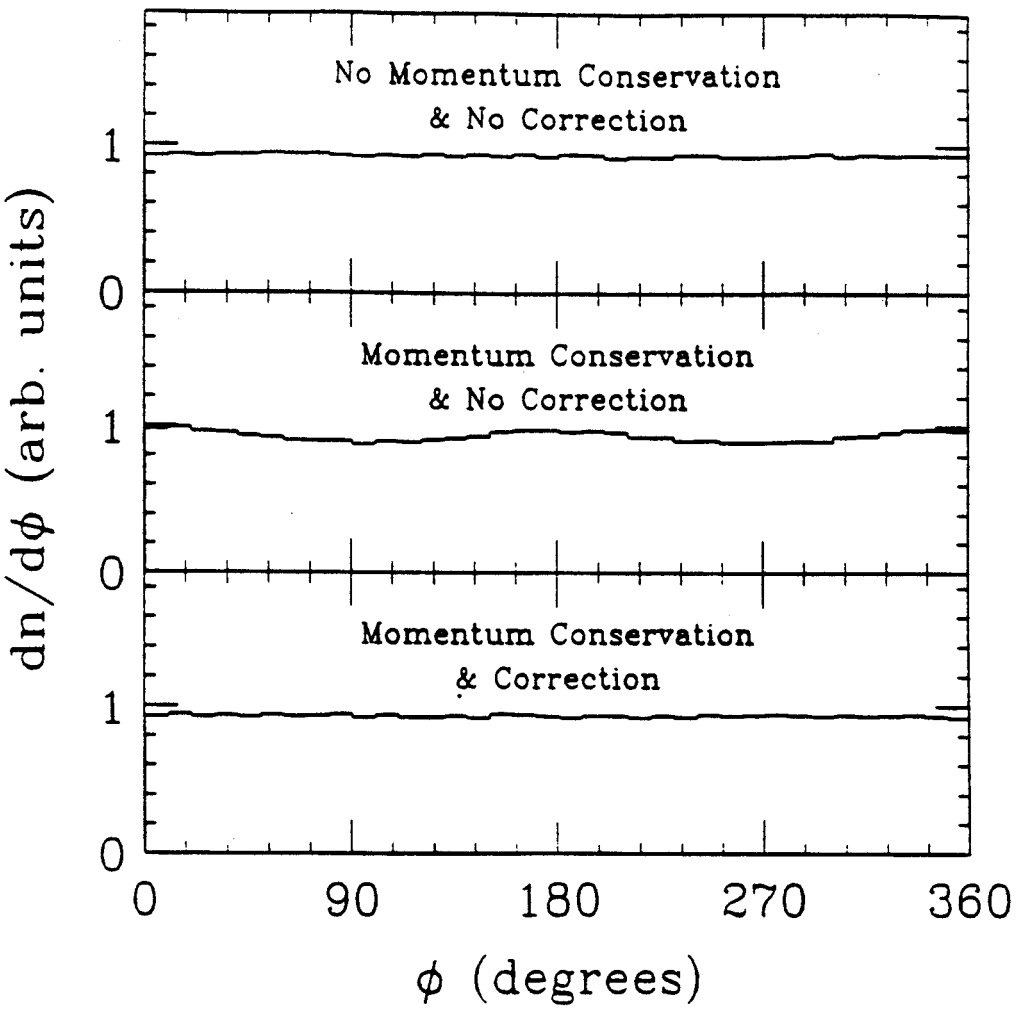


Figure 3.8: The effects of momentum conservation are investigated using simulated events. In the top panel, momentum conservation is turned off and an isotropic distribution results. Turning on momentum conservation, middle panel, produces an in-plane enhancement, but the correction restores isotropy as shown in the bottom panel.

## 3.5 Checks of the New Technique

It is important to verify that the trends of the observed azimuthal distributions are not created by biases in the reaction plane determination or detector acceptance. This can be checked by analyzing simulated distributions that have been passed through a filter containing the properties of the detection system and comparing the results with unfiltered distributions. (See Appendix B for details on the filter code.) The efficiency of this approach, however, depends on the accuracy of the physics in the simulation of the data and the degree to which an exact replica of the detector acceptance can be created. An alternate approach is to generate events using observed particles taken from separate events. Since the created events contain no physics correlations, analysis of these events should produce flat azimuthal distributions if there are no biases due to detector acceptance or in the reaction plane determination. These events will be referred to as **randomized events** because they are created by randomly choosing particles from different observed events. This approach is more convincing than filtering simulated distributions since the created events precisely reflect the actual acceptance of the detector array.

Our procedure for generating randomized events was as follows. An observed event with multiplicity m was used as the starting point and one particle was chosen at random from each of the subsequent m events. These random particles were taken as a new event and analyzed in the same fashion as a real event. The process was repeated for each observed event, generating a multiplicity distribution for the randomized events identical to that of the observed distribution. Only events that could have met the analysis criteria; i.e. multiplicity cuts, energy cuts, etc., were used in the generation of randomized events. This guaranteed that the randomized events contained all the biases that were present in the real events.

Results of the analysis of randomized events are presented in Figure 3.9 for 35 MeV/nucleon Ar+V collisions. The azimuthal distribution of events created following the procedure outlined above are displayed in the top panel. The isotropy of the distribution indicates that there are no biases in the technique. There is, however, a bias in the detection system that can be seen if we examine our procedure for generating random events more closely. Using the procedure outlined earlier, when particles are chosen from different events, it is possible for the same detector to be multiply hit within a single created event. Since each detector can really see only one particle per event, this possibility should be avoided by constraining the choice of particles. The azimuthal distribution of particles from randomized events without multiple hits is shown in the lower panel. The dip at 0° is due to this new constraint and reflects the finite azimuthal granularity of the detector array. This occurs because it is difficult to place a POI close to the found reaction plane since some of the detectors at azimuthal angles near the reaction plane must already have been hit. This "repulsion" from the reaction plane should be born in mind when interpreting observed azimuthal distributions; for example, it gives rise to the dips at 0° in figs 3.3 and 3.7.

A further test of the azimuthal correlation procedure for determining the reaction plane can be performed by examining the distribution of found reaction planes in the coordinate system of the detector array. If the array is azimuthally symmetric, then the distribution of found reaction planes should also be symmetric. The observed distribution, shown in Figure 3.10, exhibits a flat background with peaks at the azimuthal positions of the detector elements, located at the arrows. Two detectors were non-operational during this run and thus two arrows (dashed) are not accompanied by peaks.

The peaks can be understood as a manifestation of the finite multiplicity of par-

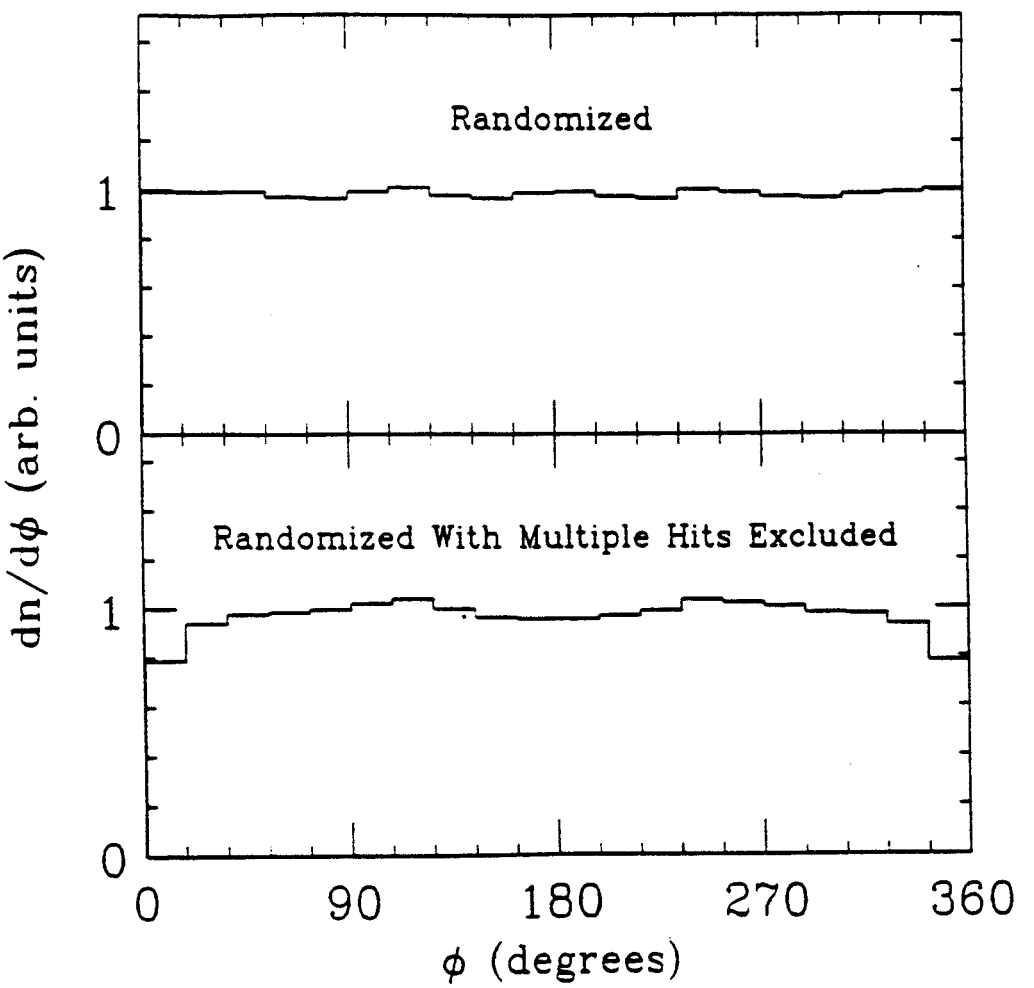


Figure 3.9: A search for azimuthal anisotropies due to detector bias in the analysis of randomized events.

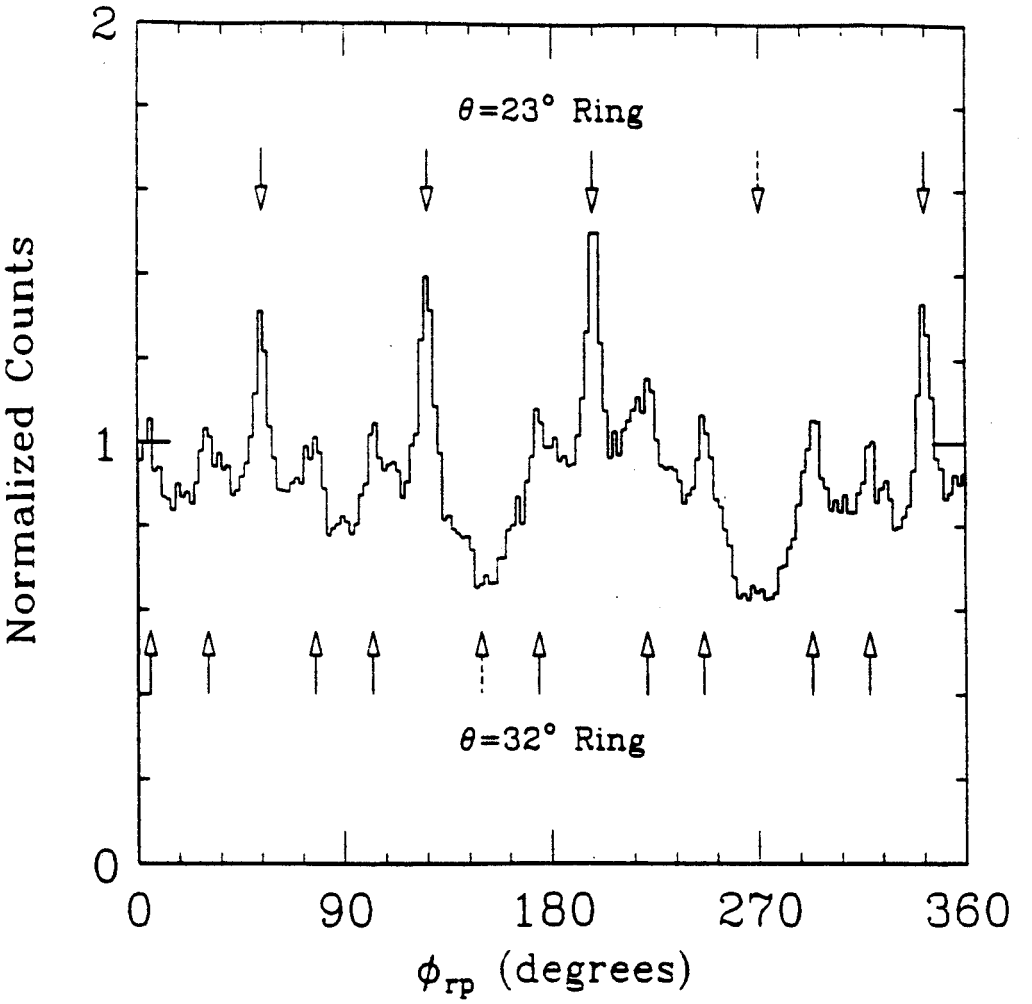


Figure 3.10: The distribution of reaction plane azimuthal angles in the detector coordinate system for 35 MeV/nucleon Ar+V. Detector positions are indicated by arrows. The dashed arrows indicate detectors that were off during this run. The polar angle $\theta$ is with respect to the beam axis.

ticles in the events. For example, in the extreme case of multiplicity 1 events, the azimuthal angles of the reaction planes would exactly correlate with the detector positions. As the multiplicity increases, the correlation would become weaker. The events displayed in fig 3.10 have three or more particles. These peaks, which simply follow the azimuthal symmetry of the array, do not bias the azimuthal distributions of particles; this was demonstrated by the analysis of randomized events described in the previous paragraph. Since there is no deviation from the symmetry of the array, we can conclude that the reaction plane determination was implemented properly.

## 3.6 Comparison with Transverse Momentum Analysis

We have compared the efficiency of the new azimuthal correlation technique for finding the reaction plane with the standard transverse momentum analysis of Danielewicz and Odyniec. The distribution of differences between the azimuthal angles of reaction planes found using the two techniques, shown in Figure 3.11, indicate strong agreement between the two methods. Since transverse momentum analysis uses the presence of flow to find the reaction plane, this implies that the flow and the general in-plane enhancement are coplanar. This correspondence may break down at beam energies > 100 Mev/nucleon where compressional effects can lead to enhanced emission *out* of the reaction plane[Gutb89b].

Although the two techniques provide similar reaction planes, our tests show that the azimuthal correlation method is slightly more accurate for Ar+V at 35 MeV/nucleon. In the azimuthal distribution shown in Figure 3.12, the azimuthal corelation technique provides a stronger enhancement in the reaction plane than the transverse momentum method, implying a more accurate reaction plane determination.

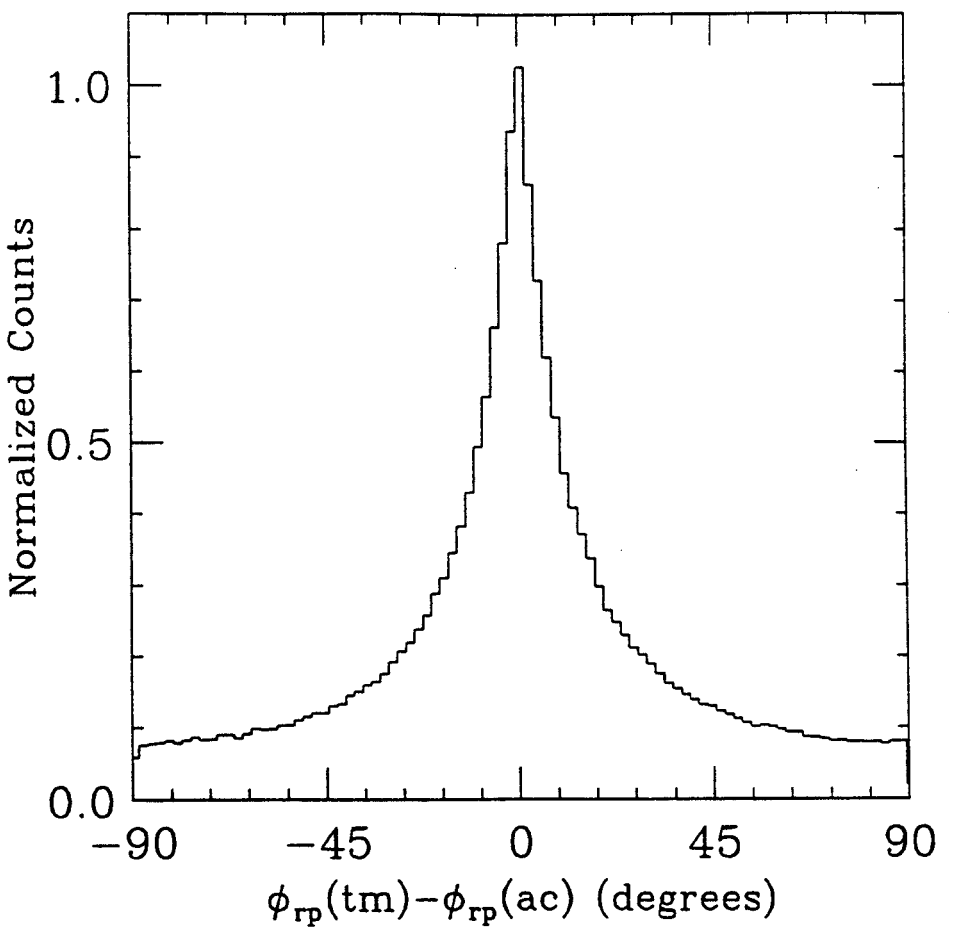


Figure 3.11: The distribution of azimuthal angle differences between reaction planes found using the transverse momentum analysis ($\phi_{rp}(tm)$) and the azimuthal correlation technique ($\phi_{rp}(ac)$) for 35 MeV/nucleon Ar+V events.

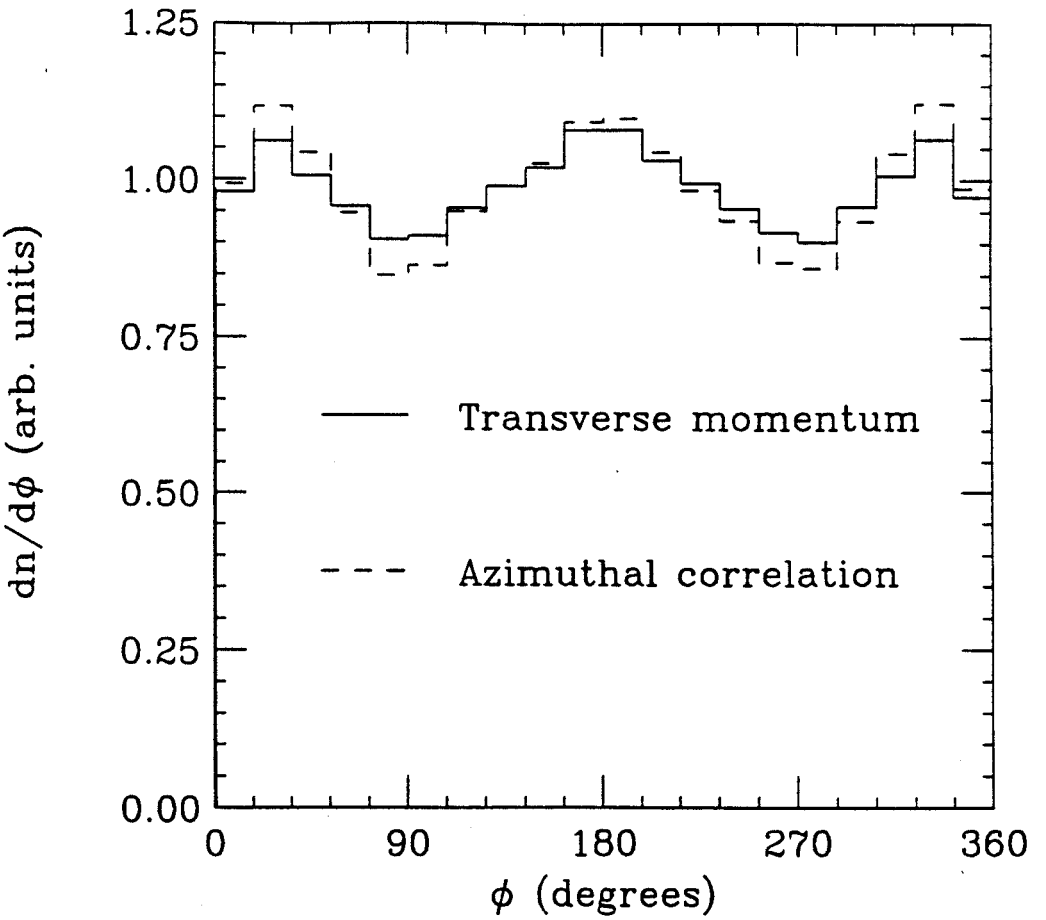


Figure 3.12: A comparison of the azimuthal angle of particles of interest with respect to the reaction planes found using two different techniques.

## 3.7 Accuracy

In order to interpret azimuthal distributions, it is necessary to quantify the accuracy of the determination of the reaction plane. As a first step, the reaction planes found using the azimuthal correlation technique were compared to the known reaction planes in simulated events. The events were generated using a 10 MeV temperature source of nucleons with an azimuthal distribution similar to that observed in the data,

$$\frac{dN}{d\phi} \propto 1 + \cos^2 \phi. \tag{3.6}$$

The various effects of the detector acceptance, such as energy thresholds and finite angular granularity, were applied one at a time to gauge their relative impact on the accuracy of the reaction planes. We found particle multiplicity to be the most important variable. In fig 3.13 we show the distribution of differences, $D_{ft}$, between found and true reaction planes for different multiplicities. The accuracy in the reaction plane determination improves as the multiplicity increases from 4 to 50. For comparison, the average observed multiplicity in the events which meet all our analysis requirements is $\approx 6$ for 35 MeV/nucleon Ar+V.

It is not possible to obtain a quantitative measure of the accuracy using simulated events, since these only roughly approximate the attributes of the actual data. The accuracy of the reaction plane determination can be estimated for real data by studying the difference between reaction planes found for single events using different sets of particles. If the difference between two planes found for the same event is small, then the planes must have been well determined. This procedure has been previously employed to measure the accuracy of the transverse momentum technique in the following manner[Dani85]. First, each event was divided into two sub-events by randomly picking particles from the original event. Then the difference between the reaction planes for the two sub-events was calculated for each original event, creating

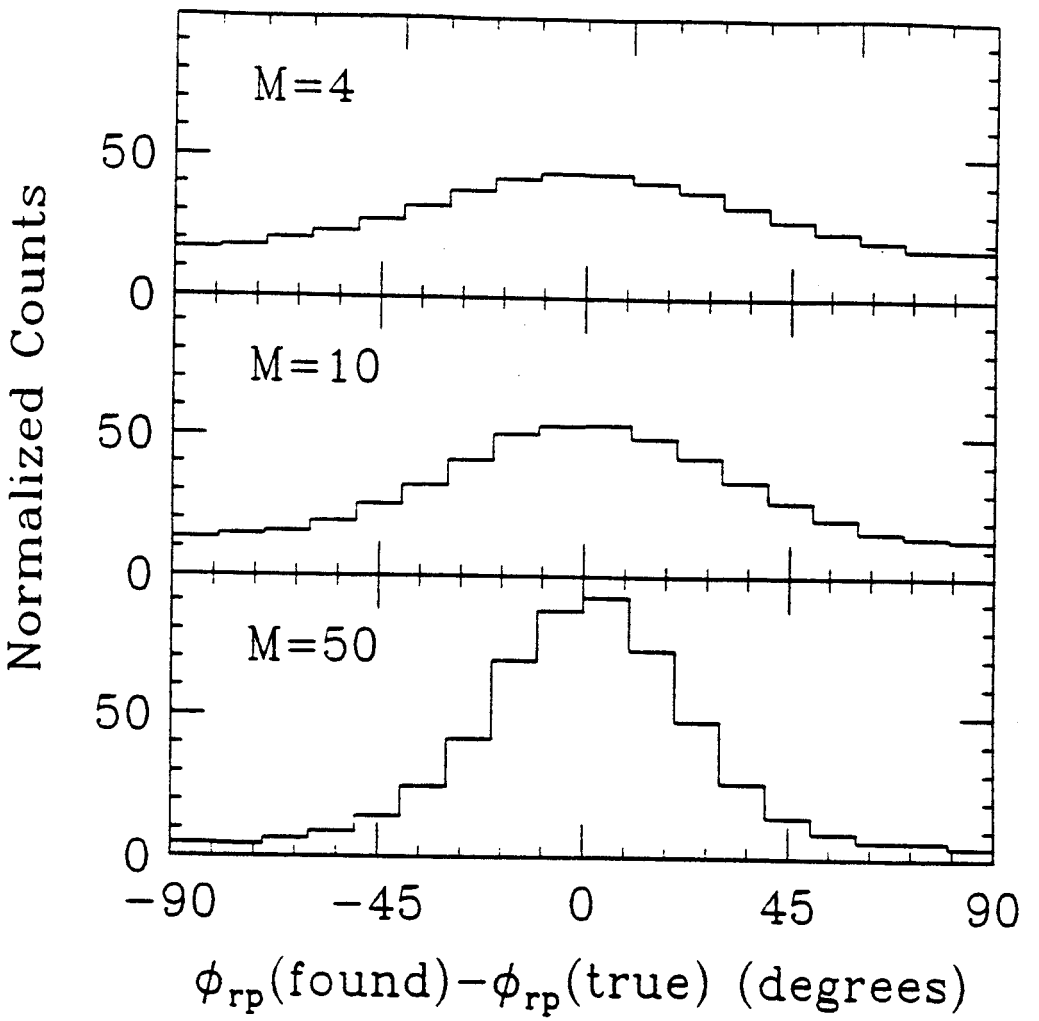


Figure 3.13: The distribution of differences between found and true reaction planes for multiplicity 4 to 50 simulated events.

a distribution of differences which peaked at 0° with a width $\sigma$. This width was found to be related to the width of the distribution of found reaction planes around the true reaction planes, $\sigma_o$, by

$$\sigma_o = \frac{1}{2}\sigma. \tag{3.7}$$

The factor of $\frac{1}{2}$ arises from a factor of $\frac{1}{\sqrt{2}}$ due to doubling the multiplicity of particles used to find the reaction plane in going from sub-events to whole events, and a factor of $\frac{1}{\sqrt{2}}$ in going from differences between two found planes to the deviation of one found plane. In this way, the accuracy of the reaction plane determination, $\sigma_o$ was deduced from the observable $\sigma$. We have investigated the accuracy of our new technique in a similar manner, comparing reaction planes for sub-events.

As a simplifying approximation, we chose to represent the differences between reaction planes by a Gaussian distribution with width $\sigma$. Since our data show an enhancement in the reaction plane on both sides of the beam axis (Figure 3.3), we expect the distribution of differences to peak at both 0° and 180°. These two directions in the reaction plane are nearly indistinguishable if transverse momentum flow is weak. Thus we represent the distribution of differences between sub-events by two equal width Gaussians of different heights centered at 0° and 180°. If $\phi_{rp}(1)$ and $\phi_{rp}(2)$ are the azimuthal angles of the reaction planes found for sub-events, then the distribution of differences $D_{12}$ is given by

$$D_{12}(\phi = |\phi_{rp}(1) - \phi_{rp}(2)|) \approx (R\, e^{-\frac{\phi^2}{2\sigma^2}} + e^{-\frac{(\phi - 180°)^2}{2\sigma^2}}), \tag{3.8}$$

where $R$ is the ratio of the heights of the peaks.

The widths $\sigma$ are constrained to be equal because they both reflect the accuracy of the first step in the azimuthal correlation technique, finding the reaction plane. The second step, finding the forward flow side of the reaction plane using the $\vec{Q}$ (eq. 3.2), distinguishes between the 0° and 180° sides of the reaction plane. Thus, the

relative heights of the two Gaussians reflect how well the orientation of the reaction plane was established, and how much flow was present. If flow is strong, then $R \gg 1$ and $D_{12}$ peaks primarily at 0°, as is the case at higher beam energies. For our system, however, $R \approx 1$ since flow is weak.

The observable $\sigma$ must be related to the difference between found and true reaction planes. We also took this distribution to be approximated by a Gaussian, so that the distribution of differences $D_{ft}$ between the found and true planes is simply ($R = 1$)

$$D_{ft}(\phi = |\phi_{rp}(found) - \phi_{rp}(true)|) \approx N(e^{-\frac{\phi^2}{2\sigma_o^2}} + e^{-\frac{(\phi-180°)^2}{2\sigma_o^2}}), \tag{3.9}$$

where the width $\sigma_o$ is the accuracy of the reaction plane determination. The accuracy $\sigma_o$ can be related to the width $\sigma$ observed from the differences between sub-events. Since the distribution of differences between planes of sub-events involves the accuracy $\sigma_o$ twice, the width $\sigma$ of the resulting Gaussian (3.8) is given by the rules for folding together two Gaussians:

$$\sigma(2m) = \sqrt{[\sigma_o(m)]^2 + [\sigma_o(m)]^2} = \sqrt{2}\sigma_o(m), \tag{3.10}$$

where $\sigma(m)$ represents the width for multiplicity $m$. In order to measure the accuracy of reaction plane determination for events of multiplicity $m$, we must divide events of multiplicity $2m$ into sub-events, and measure the width of the distribution of differences between sub-events. This procedure will help the multiplicity dependence of $\sigma_o$ to be taken into account.

It is important to note that eq. 3.9 is only an approximation of Gaussians centered at 0° and 180° since it is not periodic. The approximation is good for $\sigma_o$ less than $\approx$ 70°. If the width of the distribution is larger then the approximation can be improved by adding more Gaussians at −180°, 360°, etc.

For figs. 3.14, 3.15, and 3.16 we have fit the distribution of differences between the

azimuthal angles of reaction planes for sub-events from unfiltered and filtered simulations generated according to eq. 3.6, and real 35 MeV/nucleon Ar+V Collisions. The results of the fits are contained in Table 3.1, for the simulated and real events. Note

Table 3.1: Fit parameters for double Gaussian fits to the distribution of differences between reaction planes for several different multiplicity sub-events

| | Unfiltered | | Filtered | | Ar+V Data | |
|---|---|---|---|---|---|---|
| M | $\sigma$ | $R$ | $\sigma$ | $R$ | $\sigma$ | $R$ |
| 1 | $76.2 \pm 0.5$ | $1.020 \pm 0.009$ | $82.8 \pm 1.0$ | $0.98 \pm 0.02$ | – | – |
| 2 | $74.4 \pm 0.5$ | $0.989 \pm 0.008$ | $84.5 \pm 0.8$ | $0.95 \pm 0.01$ | $78.1 \pm 0.1$ | $0.980 \pm 0.002$ |
| 3 | $72.6 \pm 0.5$ | $1.000 \pm 0.008$ | $81.6 \pm 0.7$ | $0.938 \pm 0.010$ | $72.4 \pm 0.1$ | $0.998 \pm 0.002$ |
| 4 | $68.4 \pm 0.4$ | $1.010 \pm 0.008$ | $77.6 \pm 0.6$ | $0.965 \pm 0.009$ | $70.0 \pm 0.1$ | $1.023 \pm 0.002$ |
| 5 | $67.6 \pm 0.4$ | $0.998 \pm 0.008$ | $77.6 \pm 0.6$ | $0.965 \pm 0.009$ | $71.0 \pm 0.2$ | $1.020 \pm 0.004$ |
| 6 | $64.4 \pm 0.4$ | $1.012 \pm 0.008$ | $71.8 \pm 0.5$ | $0.967 \pm 0.009$ | $71.8 \pm 0.7$ | $1.02 \pm 0.01$ |

that $R$ is slightly greater than 1 for real data at the higher multiplicities, indicating the presence of weak flow. This parameter is expected to be unity for the simulations since eq. 3.6 does not distinguish between angles of 0° and 180°. The peaks narrow with increasing multiplicity, as is summarized in Figure 3.17 which shows the extracted widths $\sigma_0$ of the difference between found and true reaction planes.

We found that the uncertainty in our reaction plane determination is $\approx 50°$ for a multiplicity 6 35 MeV/nucleon Ar+V collision. This should be considered an upper limit on the width, however, since multiple hit exclusion effects artificially broaden the distribution of differences between the reaction planes of sub-events. Just as in our previous discussion of the effect of excluding multiple hits on the azimuthal distribution of POIs, it is difficult to place the reaction plane of the second sub-event near that of the first since some of the detectors in the first azimuthal plane must have already been hit.

The validity of the assumptions used in extracting the efficiency of the reaction

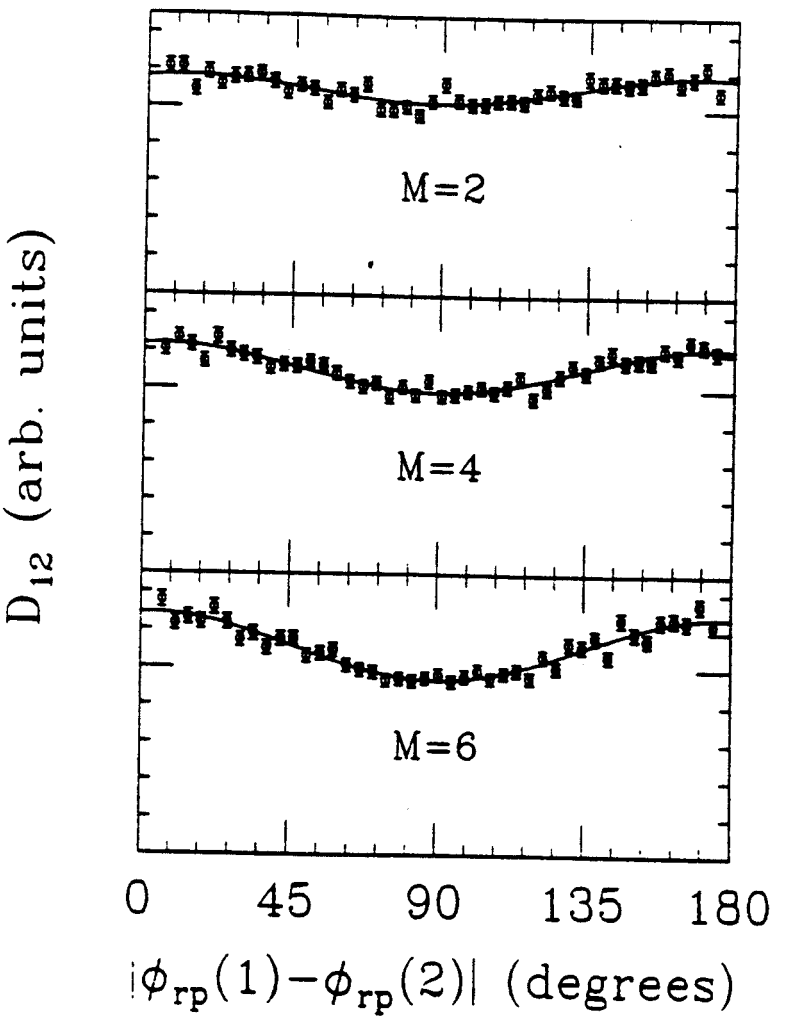


Figure 3.14: The distribution of differences, $D_{12}$, between azimuthal angles of reaction planes found for sub-events of multiplicity 2, 4, and 6 is shown for simulated data. The lines are due to the Gaussian fits described in the text.

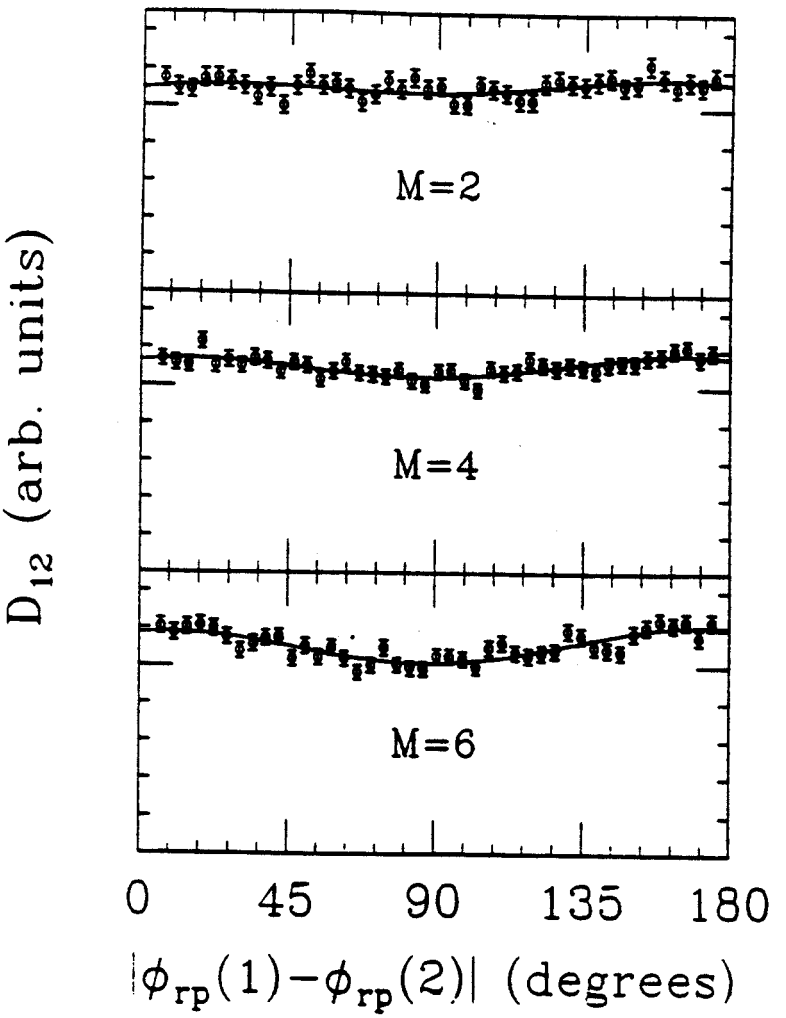


Figure 3.15: The same simulation as the previous figure, after filtering through a software representation of the detector acceptance.

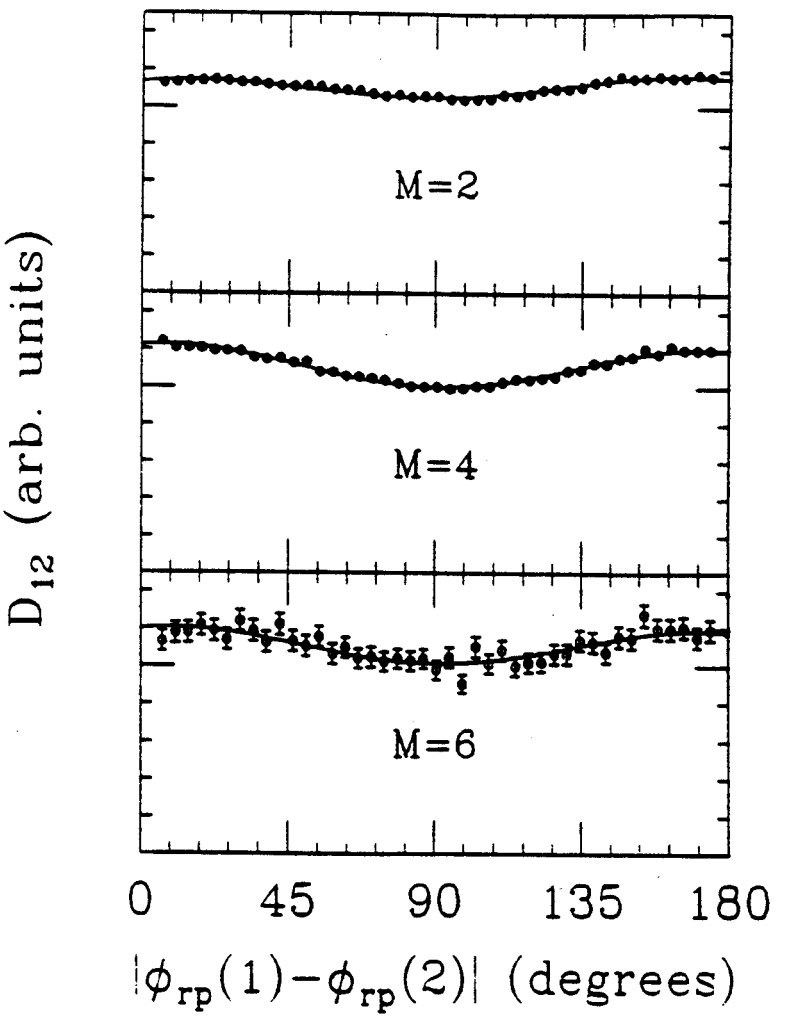


Figure 3.16: Results from the analysis of 35 MeV/nucleon Ar+V collisions are shown in the same manner as previous two figures.

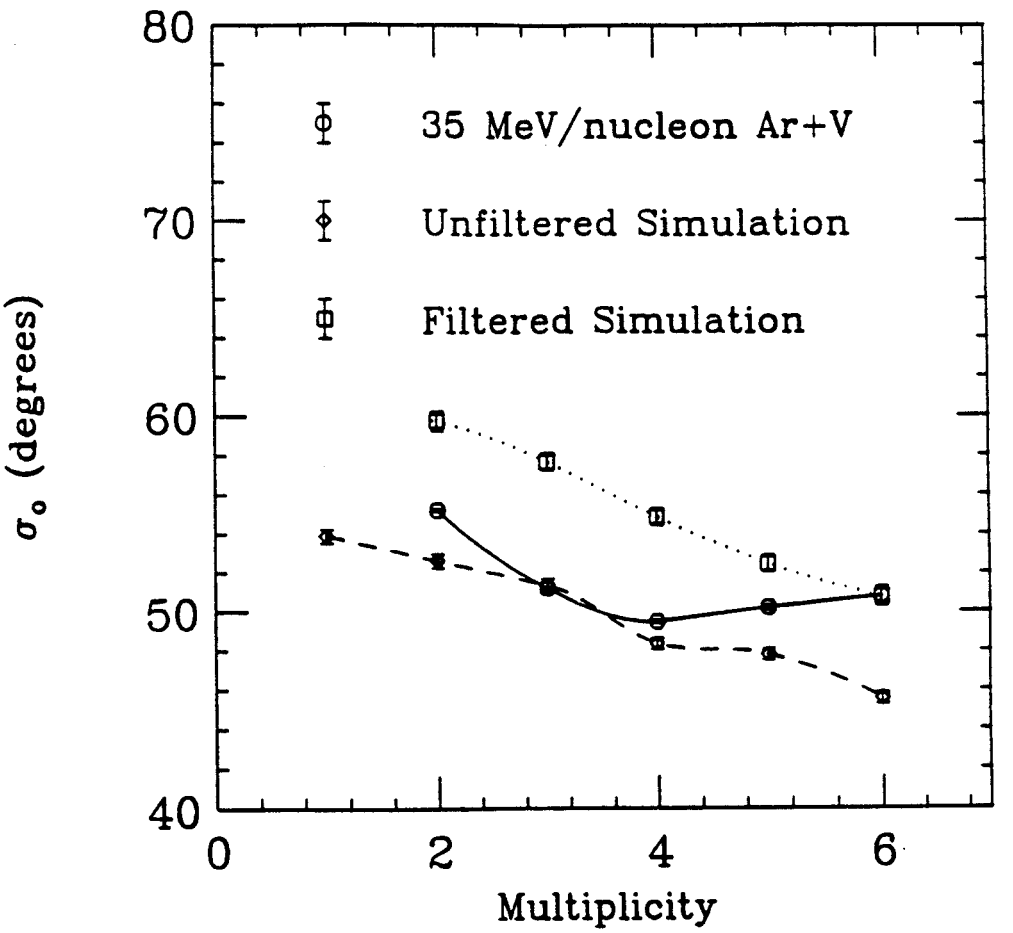


Figure 3.17: The extracted widths ($\sigma_o$) from the Gaussian fits the data in previous three figures are shown as a function of multiplicity.

plane determination can be tested for simulated data, since in that case the true reaction plane is known and the accuracy can be measured directly. In fig. 3.18, the upper panel displays the Gaussian fit to the difference between reaction planes of multiplicity 5 sub-events. The solid line in the lower panel is a prediction for the dispersion of found reaction planes around the true reaction plane using equations 3.9 and 3.10. The data points show the actual dispersion for simulated multiplicity 5 events, in good agreement with the prediction.

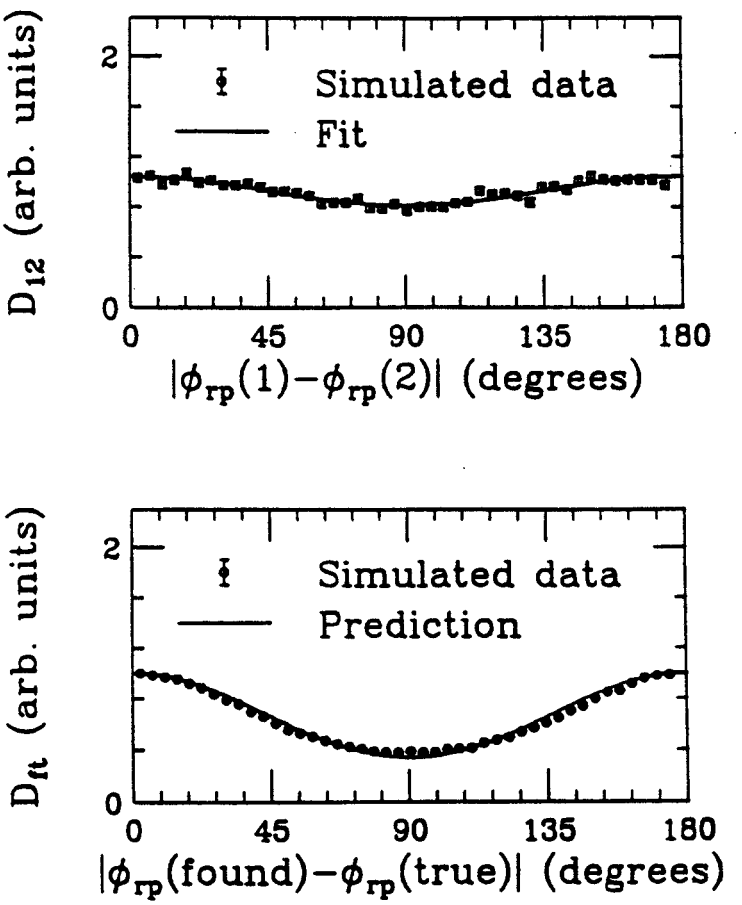


Figure 3.18: An exploration of the accuracy of the reaction plane determination for simulated events. The panels are described in the text.

# Chapter 4

# Azimuthal Anisotropies and Collective Motion

## 4.1 Introduction

We saw in the previous chapter that particle emission was enhanced in the reaction plane. In this chapter, we will investigate this enhancement to obtain a picture of the collective motion which drives the system away from isotropy.

We will begin by examining the influence of two forms of collective motion, rotation and attractive flow, on the azimuthal distributions of emitted particles. A new parameterization of the azimuthal anisotropy will be introduced which will allow us to distinguish between the contributions of different modes of collective motion. Using these parameters in the analysis of 35 MeV/nucleon Ar+V collisions, we will find that signatures of both rotation and flow are present. The influence of detector acceptance on the anisotropy parameters will be carefully checked. Finally, we will explore the beam energy dependence of collective motion as $E_{beam}$ is increased to 100 MeV/nucleon.

## 4.2 Effects of Collective Motion on Azimuthal Distributions

In order to characterize the collective motion that produces the enhancement in the reaction plane observed in the previous chapter, it is desirable to parameterize the azimuthal anisotropy in a manner which decouples the possible forms of collective motion. Two distinct modes of collective motion have been proposed to explain various attributes of collisions observed in this beam energy range: **rotation** and **flow**. Rotational collective motion of the compound system about an axis perpendicular to the reaction plane was suggested by Tsang et al.[Tsan84a] in the interpretation of two particle azimuthal correlation data. Flow due to attractive deflection by the mean-field was invoked by Ogilvie et al.[Ogil89b] to explain the dependence of average transverse momentum in the reaction plane on rapidity. (Ogilvie et al. used the term "directed transverse momentum" for this collective motion.) Figure 4.1, illustrates both forms of collective motion.

Preferential emission in the reaction plane is observed for both rotation and flow, but the rapidity dependence is different for the two mechanisms. As can be seen from Figure 4.1, rotation should enhance particle emission equally on both sides of the reaction plane at all rapidities. Flow, on the other hand, leads to an enhancement on one side of the reaction plane for particles going forward and on the other side for particles going backwards in the center of momentum frame of reference.

The difference between the effects of rotation and flow on azimuthal distributions is demonstrated in figs. 4.2 and 4.3 using simulated events. The top histograms of the two figures are rapidity distributions, divided into six regions of roughly equal statistics as indicated by the numbers used as plotting symbols. The six azimuthal distribution histograms underneath show the azimuthal distribution of particles of

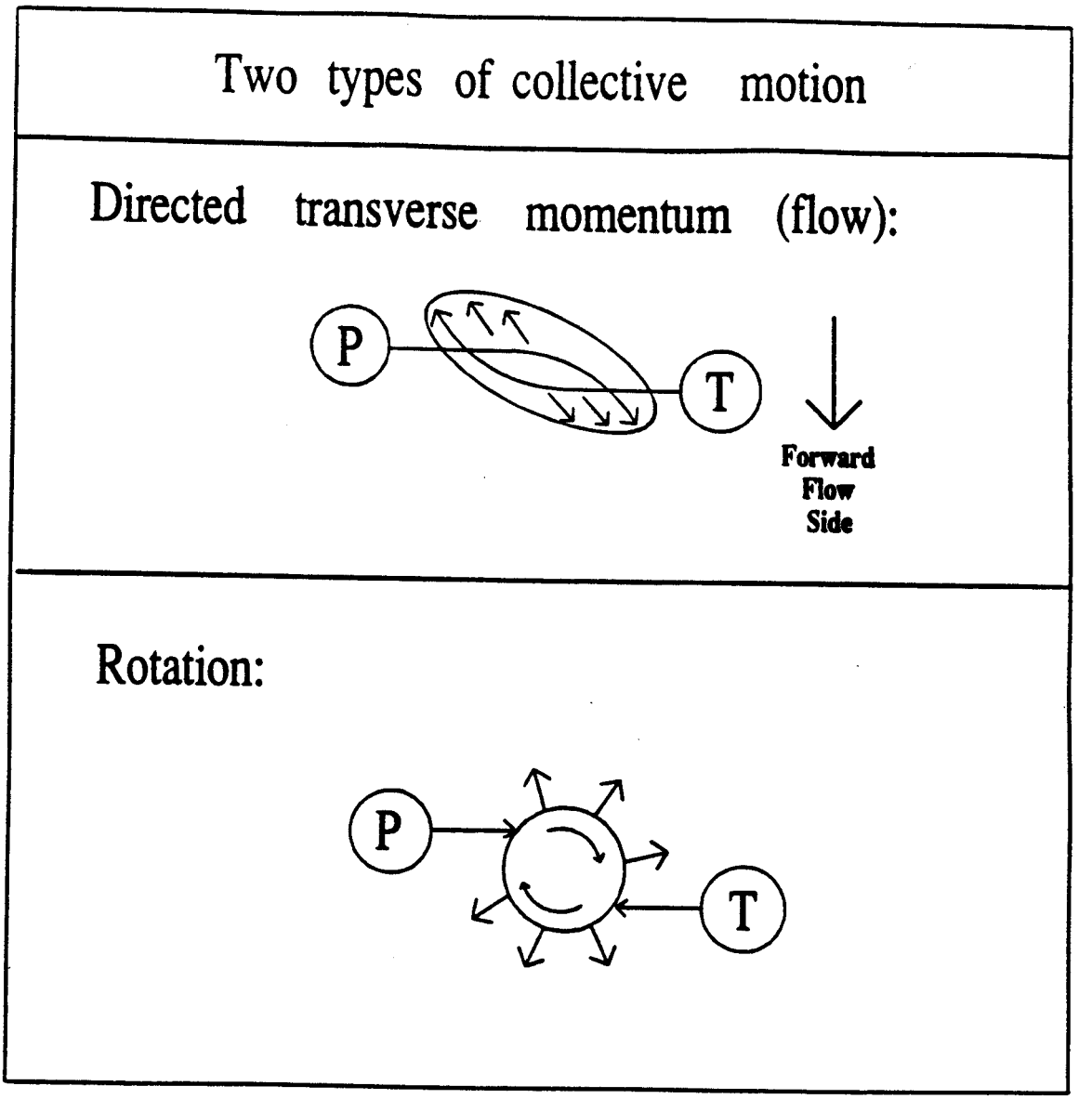


Figure 4.1: Schematic representation of the two forms of collective motion under investigation. Both drawings are in the center of momentum frame of reference, looking down on the reaction plane.

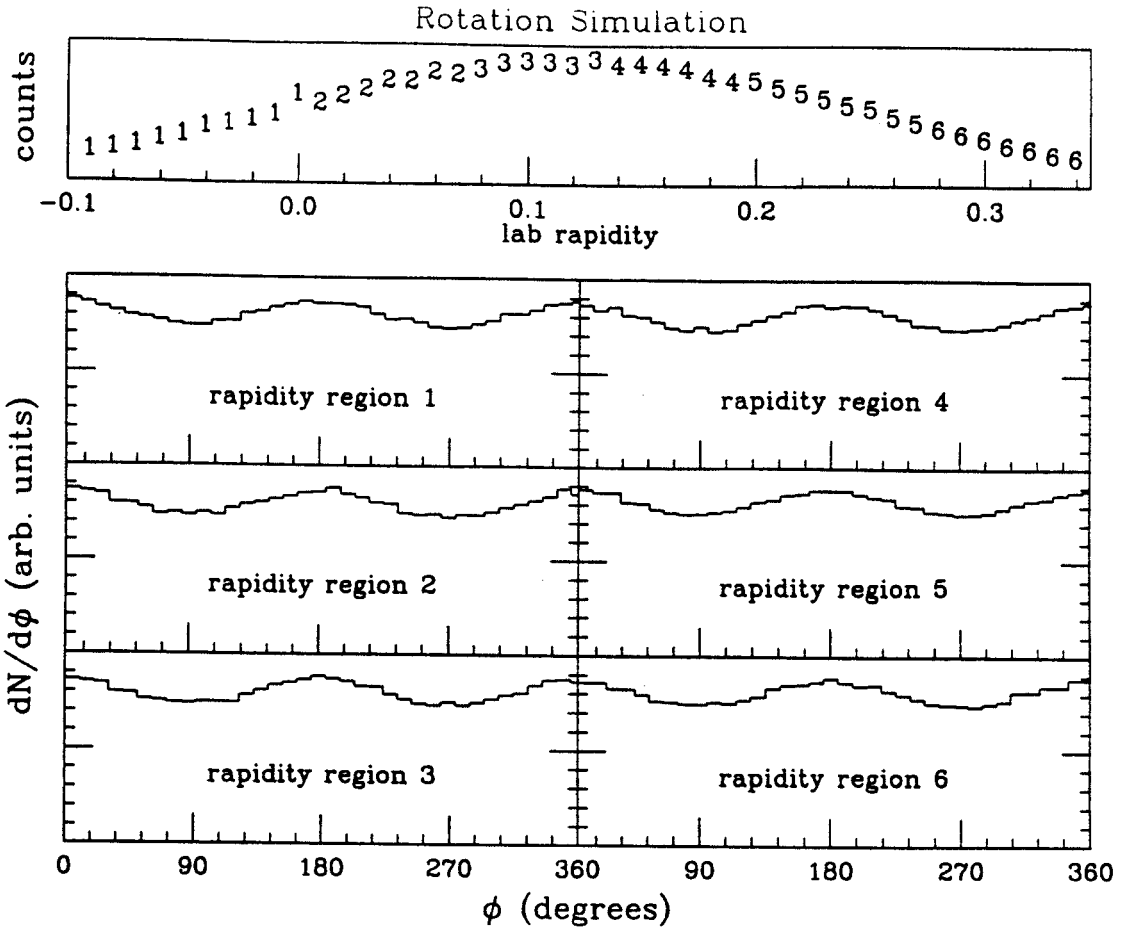


Figure 4.2: Azimuthal distributions with respect to the reaction plane for an oblate momentum distribution. The top histogram shows the positions of the 6 rapidity regions. The vertical axes are scaled linearly from 0 in all the histograms.

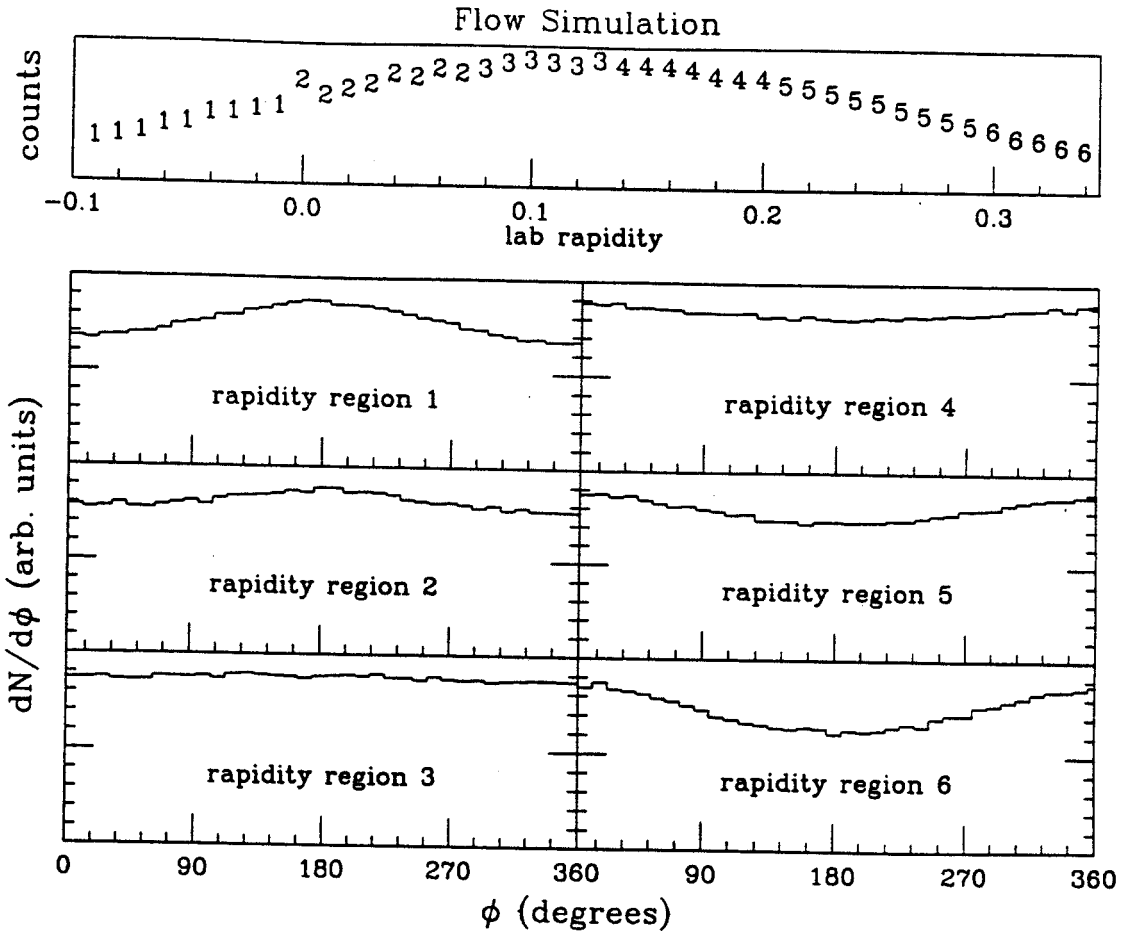


Figure 4.3: Azimuthal distributions with respect to the reaction plane for a simulated source with transverse momentum flow.

interest with respect to the reaction plane for POIs within the different rapidity cuts.

The effects of rotation were simulated for Figure 4.2 by flattening a Gaussian momentum distribution into an oblate shape,

$$\sigma_x = \sigma_z > \sigma_y, \tag{4.1}$$

where the z-axis is the beam axis, $\hat{x}$ is in the reaction plane, and $\hat{y}$ is normal to the surface of the plane. Consequently, the azimuthal distributions in Figure 4.2 peak equally at 0° and 180° at all rapidities. In order to simulate flow for Figure 4.3, the Gaussian distribution was first stretched along the beam axis to a prolate shape, and then rotated slightly around the y axis (perpendicular to the reaction plane). Because the azimuthal angle of the POI is measured from the forward flow side of the reaction plane, peaks appear in the azimuthal distributions of Figure 4.3 at 0° at high rapidities, i.e. for POIs going forward in the c.m. frame of reference. At mid-rapidity, near rapidity region 3, the distribution is isotropic, while at the low rapidities (regions 5 and 6) the peaks reappear, but 180° away from the forward flow side. We exploited the difference between the effects of rotation and flow in our creation of the **anisotropy parameters.**

## 4.3 Parameterization of Azimuthal Distributions

We found that the data could be conveniently characterized by two parameters, each chosen to be sensitive to only one form of motion. The rapidity dependence of the parameters clearly show which forms of collective motion are present and their relative strengths. The rotation sensitive parameter is $F_{ip}$, the fraction of particles of interest found in the reaction plane. The flow sensitive parameter is $F_{fs}$, the fraction on the forward flow side of the reaction plane. The fractions are calculated by integrating

over the azimuthal distributions,

$$F_{ip} = \frac{\int_{-45°}^{45°} \frac{dn}{d\phi} d\phi + \int_{135°}^{225°} \frac{dn}{d\phi} d\phi}{\int_{0°}^{360°} \frac{dn}{d\phi} d\phi} \tag{4.2}$$

and

$$F_{fs} = \frac{\int_{-90°}^{90°} \frac{dn}{d\phi} d\phi}{\int_{0°}^{360°} \frac{dn}{d\phi} d\phi}, \tag{4.3}$$

Thus, $F_{ip}$ is simply the fraction of particle with azimuthal angles within 45° of the reaction plane, and $F_{fs}$ is the fraction of particles within 90° of the forward flow side. The fractions are shown geometrically in Figure 4.4, and the azimuthal positions of the in-plane and forward flow side gates are shown with hypothetical distribution in Figure 4.5. Both fractions $= \frac{1}{2}$ if the azimuthal distribution is isotropic, indicating the absence of collective motion.

These parameters have several advantages. They are less sensitive than peak to valley ratios to the dip in the azimuthal distributions at 0° caused by multiple hit exclusion. A second advantage over peak to valley ratios is that the size of the deviation from isotropy $(F - \frac{1}{2})$ is equal in magnitude for equal asymmetries of opposite directions. The new parameters represent an intuitive quantity, i.e. the probability for finding a particle of interest within a given range of azimuthal angles with respect to the reaction plane. Quantitative relationships between the new parameters and other commonly employed characterizations of azimuthal asymmetry are presented in Appendix D.

The effects of rotation and flow on these parameters are displayed in figs. 4.6 and 4.7 respectively. The upper panels of the figures show $F_{ip}$ vs. rapidity. This fraction deviates from isotropy only for the rotating source. Since flow only transfers particles from one side of the reaction plane to the other, it leaves the net number in the plane unchanged.

In the lower panels, $F_{fs}$ is displayed vs. rapidity. The rotating source exhibits an

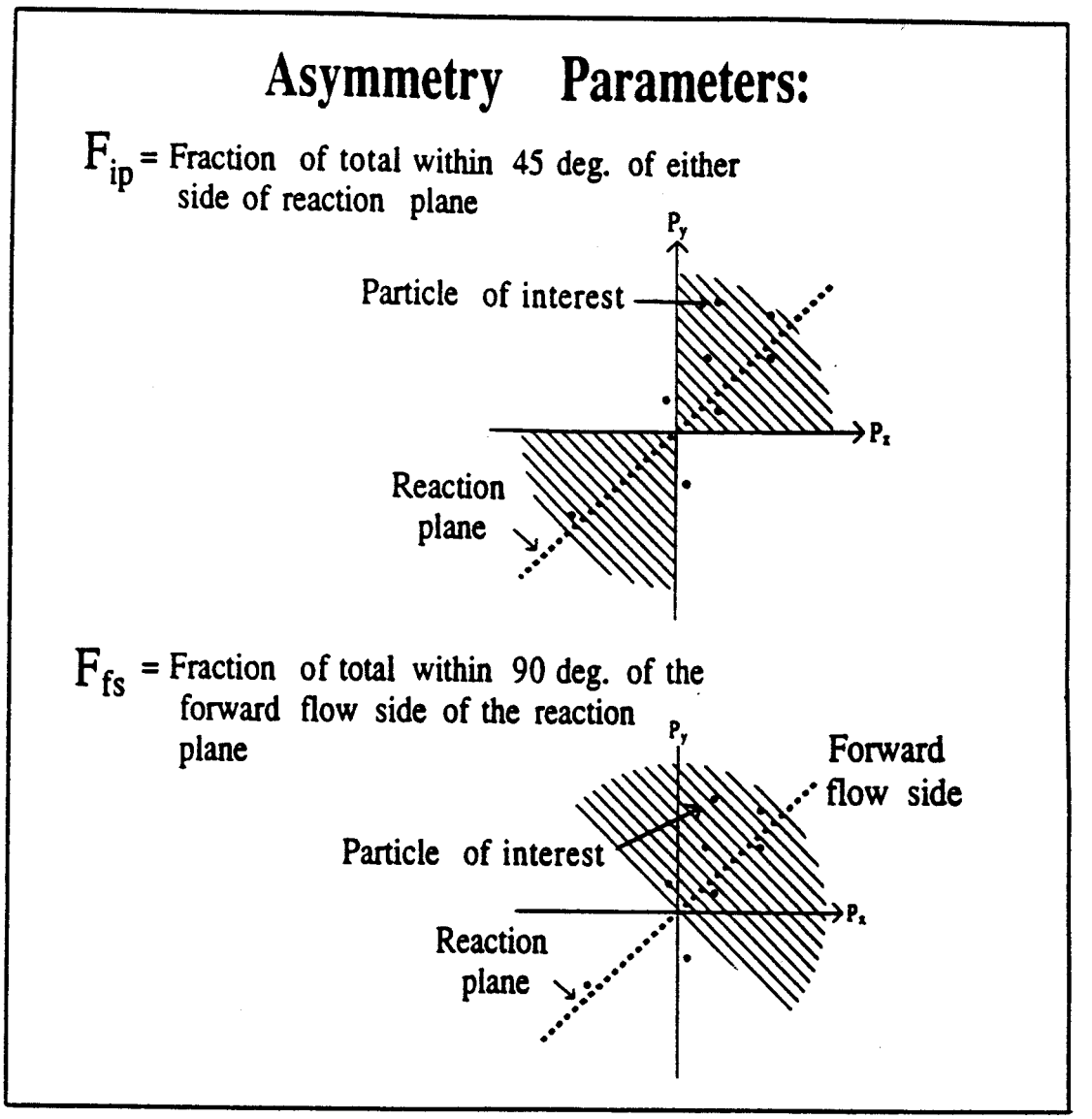


Figure 4.4: Geometrical definition of the anisotropy parameters $F_{ip}$ and $F_{fs}$ projected onto the $p_x - p_y$ plane.

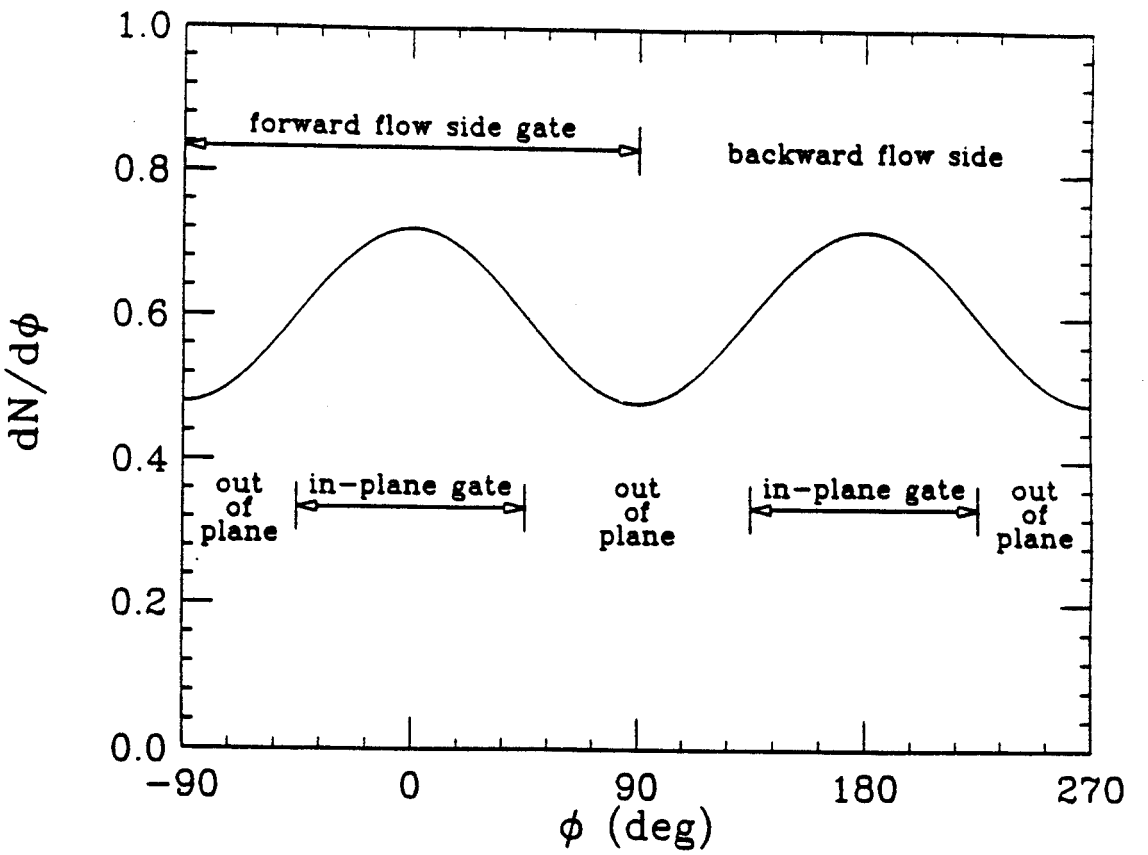


Figure 4.5: Azimuthal angles of the in-plane and forward flow side gates are shown for a hypothetical azimuthal distribution

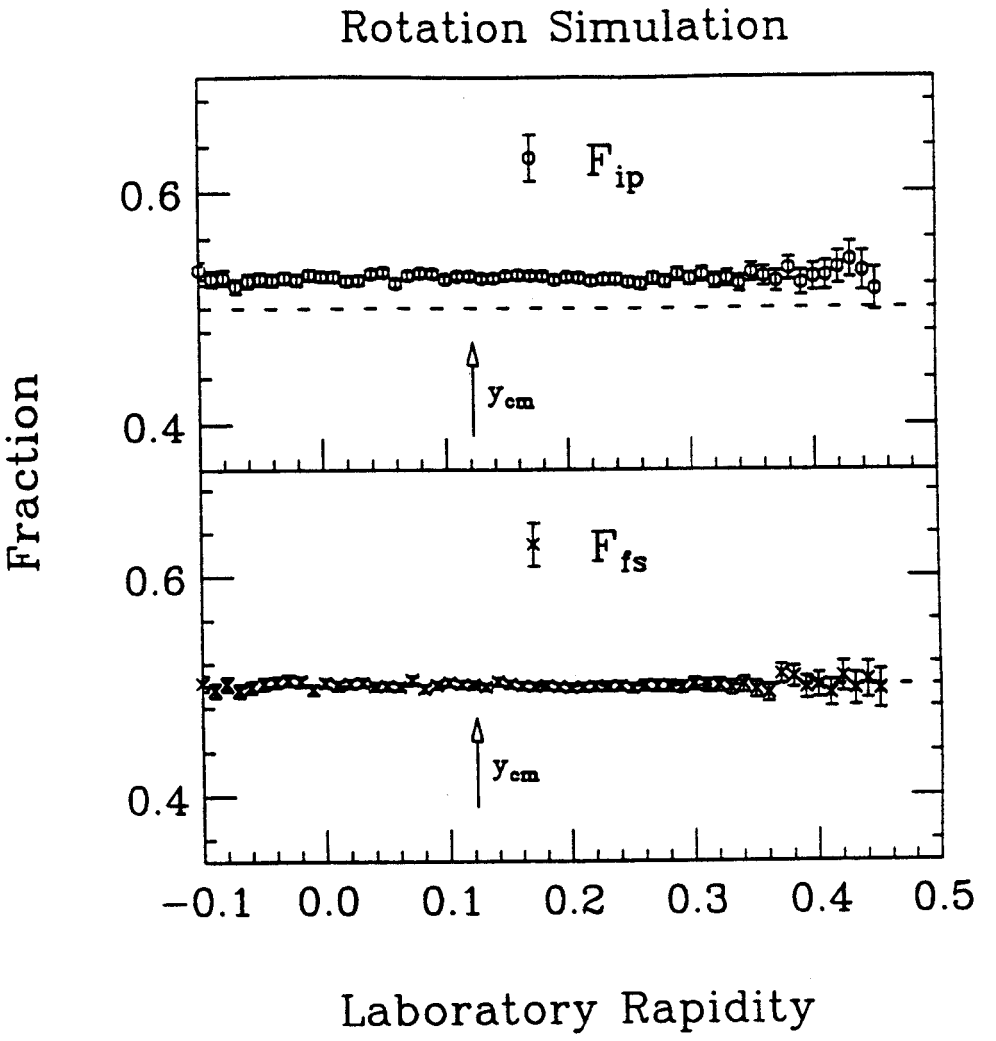


Figure 4.6: Anisotropy fractions $F_{ip}$ (upper panel) and $F_{fs}$ (lower panel) as a function of rapidity for a simulated oblate momentum distribution. The dashed line represents the fractional value expected in the case of azimuthal isotropy.

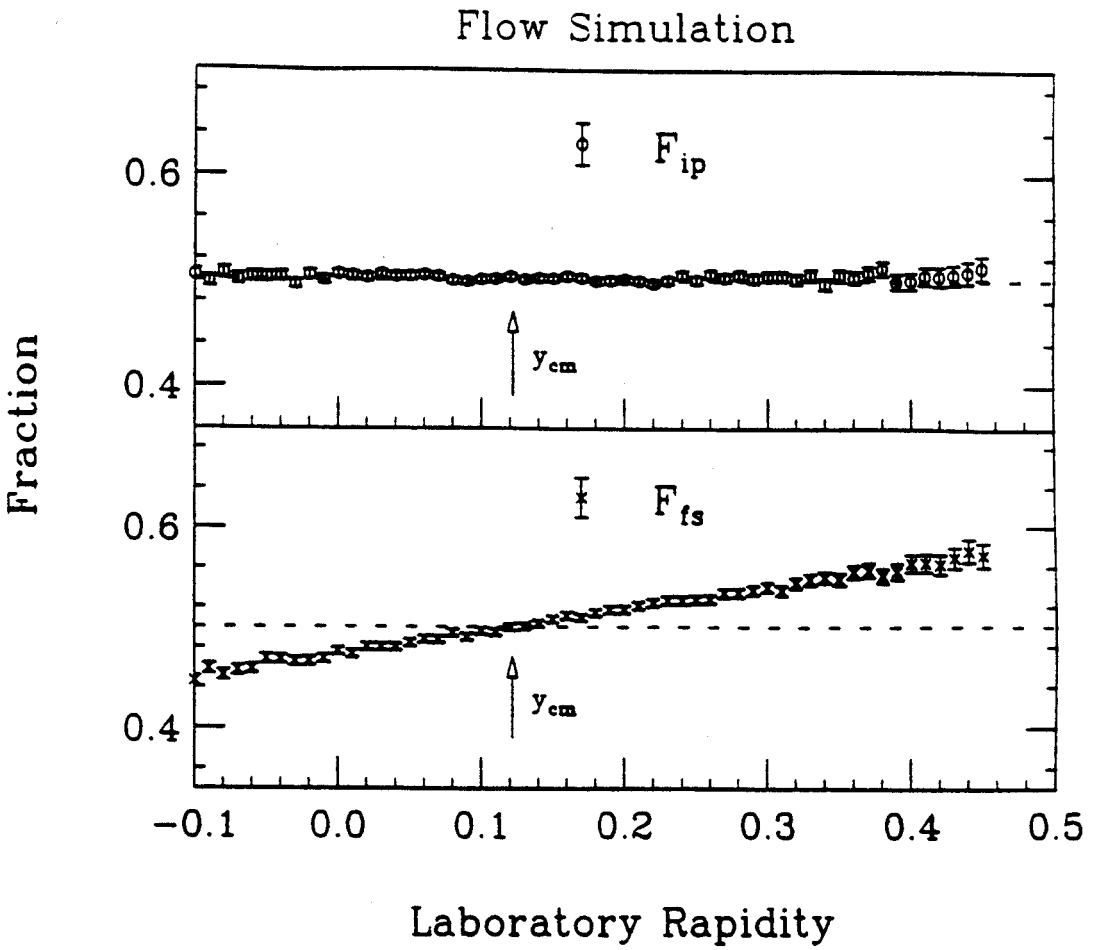


Figure 4.7: Anisotropy fractions $F_{ip}$ (upper panel) and $F_{fs}$ (lower panel) as a function of rapidity for a simulated prolate momentum distribution with transverse momentum flow.

$F_{fs} = 0.5$ at all rapidities because the in-plane enhancement occurs simultaneously on both sides of the reaction plane. Flow, on the other hand, produces a non-zero slope in $F_{fs}$ since particles are deflected towards the forward flow side of the reaction plane at high rapidities and towards the opposite side at low rapidities. To summarize, an $F_{ip} > \frac{1}{2}$ is a signature of an momentum distribution similar to that expected due to the decay of a rotating source, while a slope in $F_{fs}$ as a function of rapidity indicates the presence of collective flow in the reaction plane. These parameters are specific in the sense that $F_{ip}$ is only sensitive to rotation and $F_{ps}$ is only sensitive to flow.

## 4.4 The Influence of Detector Acceptance

In order to isolate physical effects using experimentally observed anisotropy fractions, we need to be aware of the influence of detector acceptance on the parameters. The simulated data thus far presented were not filtered through the detector acceptance. Turning on the filter produces the results shown in figs. 4.8 and 4.9. See Appendix B for a description of the filter code. (Points with very low statistics and hence error bars larger than $\pm 0.04$ are suppressed in these and all the forthcoming plots involving the anisotropy fractions in order to produce cleaner plots. Such very large error bars only occur at the extreme limits of the rapidity distribution.) Three significant effects emerge when the filtered data is compared to the unfiltered data.

The first effect is a discontinuity around $y_{lab} = 0$ in $F_{ip}$ for the simulation of rotation and in $F_{fs}$ for the source simulating flow. The discontinuity is due to the finite polar angle granularity of the Main Ball. In the preceeding analysis in this chapter, particles were assumed to be detected at the center of each telescope. There are no telescopes centered at 90° ($y_{lab} = 0$), and data from telescopes on either side (87° and 93°) fall into several neighboring rapidity bins. The two bins closest to 90°

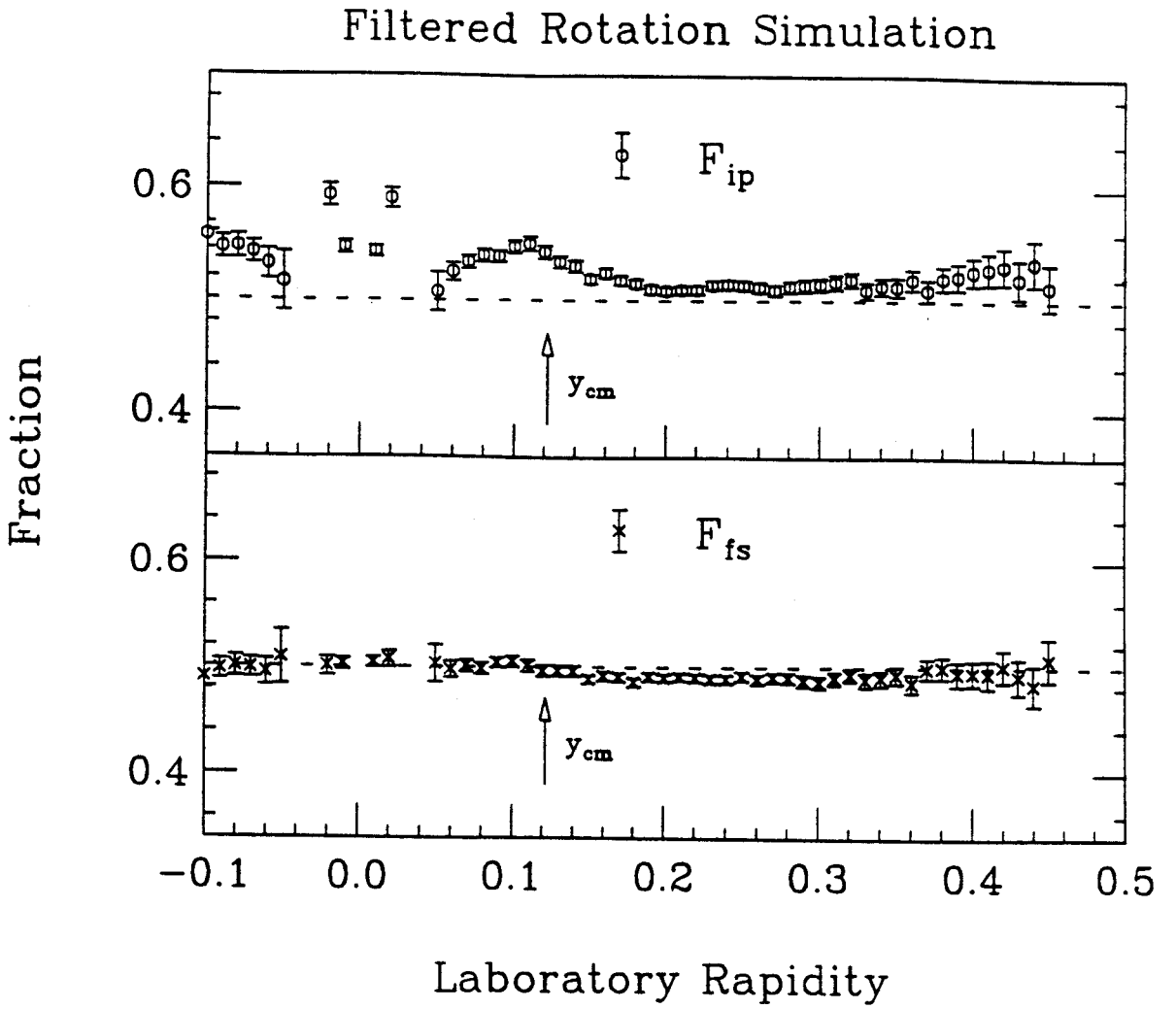


Figure 4.8: Anisotropy fractions $F_{ip}$ (upper panel) and $F_{fs}$ (lower panel) as a function of rapidity for a simulated oblate momentum distribution after filtering through a software model of the detector acceptance.

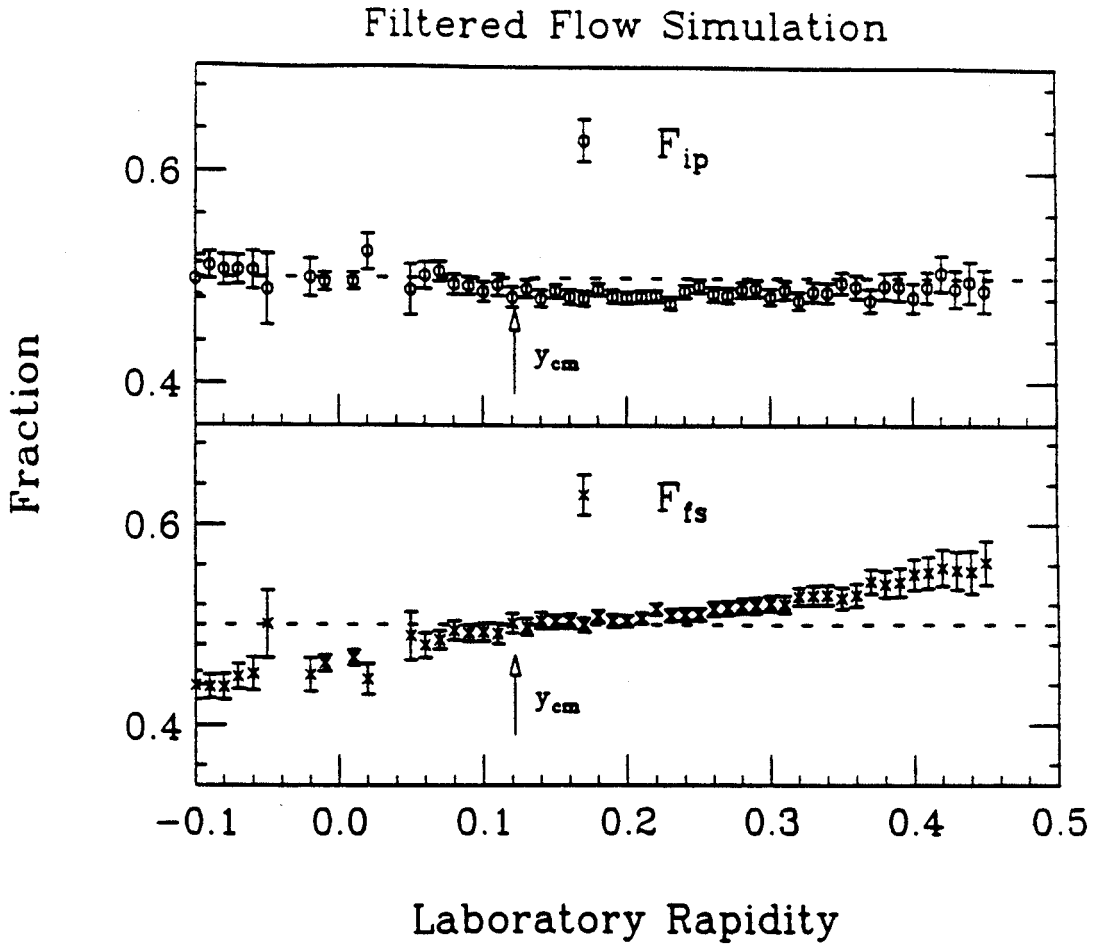


Figure 4.9: Anisotropy fractions $F_{ip}$ (upper panel) and $F_{fs}$ (lower panel) as a function of rapidity for a simulated prolate momentum distribution with transverse momentum flow after filtering through the detector acceptance.

contain only the lower energy particles from these telescopes, while the next nearest set contains the higher energy particles from the same telescopes. Higher energy particles always show the collective motion more strongly in these simulations. One way to see this is to note that higher energy particles can only result when the thermal velocity adds constructively with the collective velocity, creating a stronger apparent collective motion. Therefore, it is the energy difference between particles found in the four bins around $y_{lab} = 0$ that causes the discontinuity.

This type of discontinuity is suppressed in the other rapidity regions since the polar angles (with respect to the beam axis) of the detectors overlap so as to contribute a wider range of particle energies to each the rapidity bin. Smearing the assigned angles of detected particles over the faces of the telescopes rather than concentrating them at the centers will eliminate the discontinuity described above due to the relationship between the rapidity bins and the polar angles.

The second effect of detector acceptance is a drop in $F_{ip}$ as the rapidity increases from 0.1 to 0.2 in the laboratory frame. Note that particles see a lower transverse momentum threshold as the rapidity increases over this region, as shown in Figure 2.7 in the second chapter. Therefore, the drop occurs because lower thresholds show the collective motion more weakly, again due to the addition of collective and thermal velocities as discussed in the last paragraph. This drop can be eliminated by equalizing the transverse momentum cuts as a function of rapidity by excluding a cylindrically shaped region around the $p_z$ axis (beam direction) in momentum space. The radius of the cylinder should be chosen to equal the maximum $p^{\perp}$ cut imposed by the detector acceptance. (Refer to Figure 2.7)

The final influence of detector acceptance on the anisotropy parameters is due to multiple hit exclusion. As was discussed in the previous chapter, multiple hit exclusion acts to "repulse" the particle of interest from the reaction plane, creating

a dip in the azimuthal distributions near 0° and 180°. This causes $F_{ip}$ to decrease slightly for the filtered data, mainly at the higher rapidities (smaller polar angles) since forward focusing of the reaction products makes the finite azimuthal granularity more important in that region. For Figure 4.9, in which we would expect $F_{ip}$ to be $\frac{1}{2}$, we find that this effect causes $F_{ip}$ to drop below the dashed isotropy line for the high rapidity bins.

Another aspect of multiple hit rejection is its effect on the $F_{fs}$ parameter. Since the dip is deeper at 0° than at 180°, $F_{fs}$ is lowered from its unfiltered value, as can be clearly seen in Figure 4.8. The dip is deeper at 0° because in the forward rapidity direction in the center of momentum frame, most particles are emitted in the reaction plane on the forward flow side (0°), increasing the multiple hit probability.

In addition, a similar effect not related to detector acceptance should also be kept in mind. In the last chapter we stated that our correction for momentum conservation bias in finding the reaction plane was the minimum correction since it assumed that the recoil was divided among all the particles available in the system. Any residual momentum conservation bias remaining after the correction will act to push the particles, and hence the reaction plane, away from the particle of interest. This will also result in a decrease in the observed $F_{fs}$ values. Incomplete correction for momentum conservation combined with the effect of multiple hit exclusion will cause $F_{fs}$ to pass through isotropy at a rapidity slightly higher than the center of momentum rapidity and result in generally lower $F_{fs}$ values.

## 4.5 35 MeV/nucleon Ar+V Data

Anisotropy fractions for 35 MeV/nucleon Ar+V collisions are shown in Figure 4.10 for both H and He data taken using the MSU $4\pi$ Array. All of the features of the

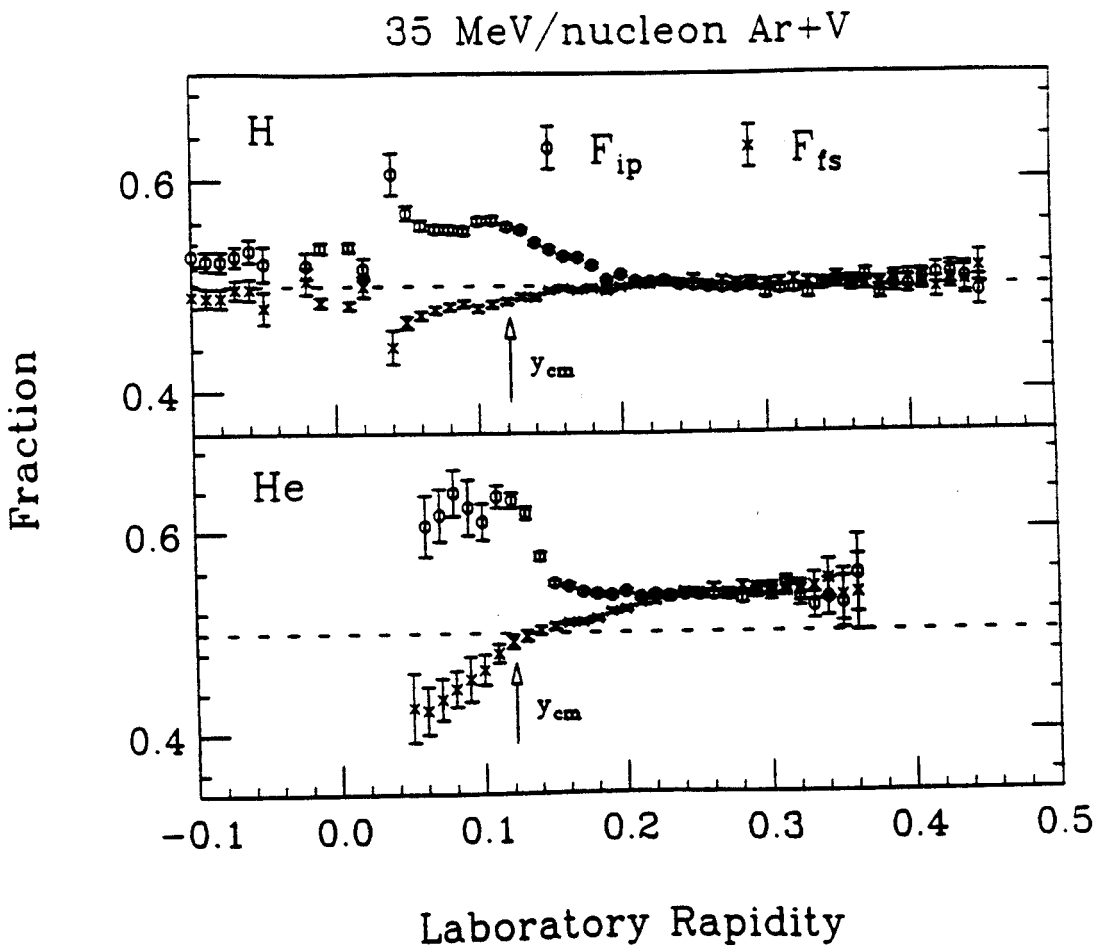


Figure 4.10: Anisotropy fractions as function of rapidity for 35 MeV/nucleon Ar+V data.

filtered rotation and flow simulations are reflected in the data, suggesting the presence of both modes of collective motion.[Wils90, Ogil90]

The presence of flow is revealed by Figure 4.10 in the non-zero slope in $F_{fs}$ at mid-rapidity. The flow is stronger for He than for H, a trend that would be expected for collective velocity superimposed on random thermal motion. This is because thermal velocities decrease with increasing mass of the particles, leading to less random smearing of the collective velocity for helium than for hydrogen. Multiple hit exclusion and possibly incomplete correction for momentum conservation shifts $F_{fs}$ to lower values, causing it to cross the dashed isotropy line at a rapidity slightly ahead of the center of momentum rapidity.

The signature of preferential emmission in the reaction plane particles, $F_{ip} > 0.5$, is particularly clear, suggesting that rotational collective motion may be present. Again, the effect is stronger for the heavier particles, as expected. Just as in the filtered simulations, $F_{ip}$ varies with rapidity due to the variation in the detector thresholds.

To provide a qualitative feeling for the magnitude of the observed anisotropies, the azimuthal distributions of H and He are shown in figs. 4.11 and 4.12 respectively.

As stated earlier, the influence of changing $p^{\perp}$ thresholds can be eliminated by applying a common $p^{\perp}$ cut at all rapidities, and the effects due to polar angle granularity can be reduced by smearing the assigned angles over the solid angles subtended by the telescopes. When both of these techniques are applied, as in Figure 4.13, the resulting fractions are smoothly varying and more symmetric around the mid-rapidity region. There is a decrease in $F_{ip}$ at low rapidities compared to Figure 4.10 caused by two separate mechanisms which we will discuss next.

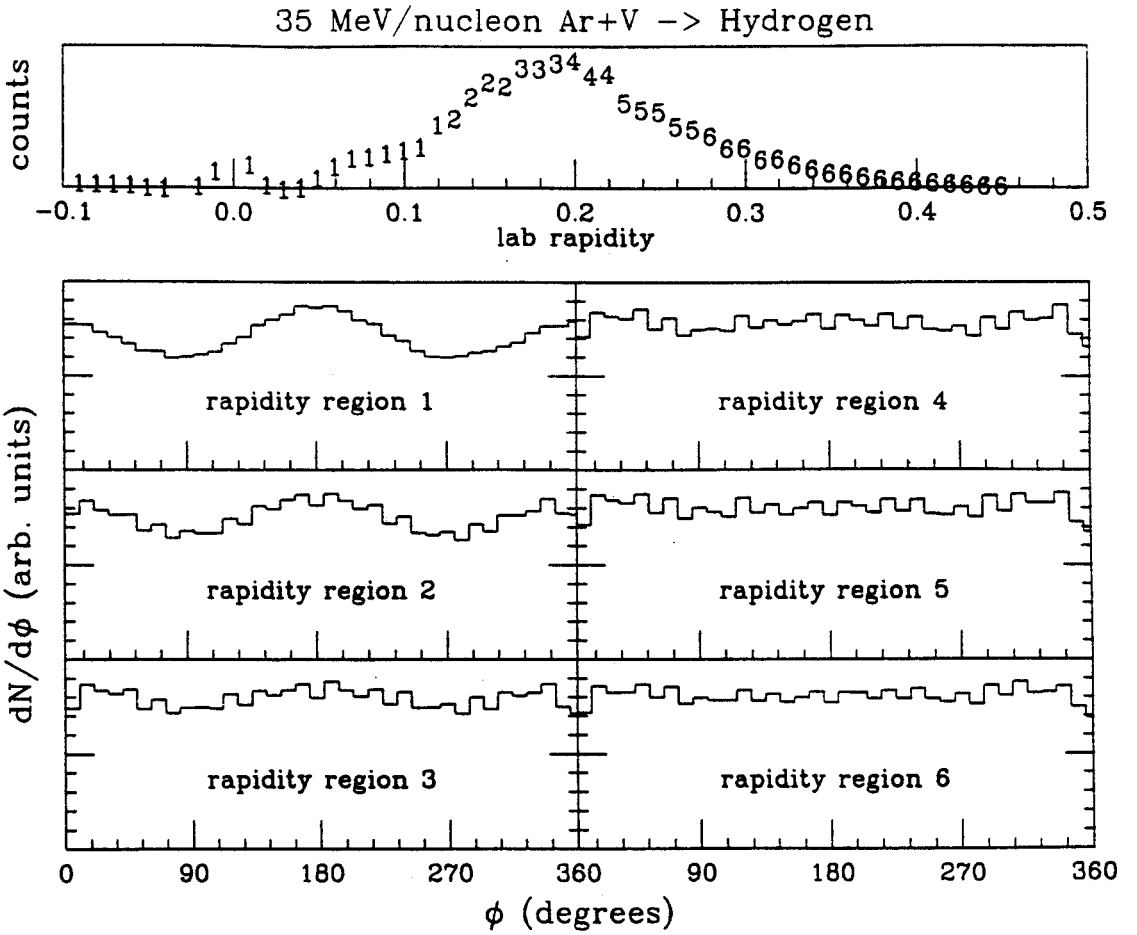


Figure 4.11: Azimuthal distributions of hydrogen produced in 35 MeV/nucleon Ar+V collisions divided into six rapidity bins.

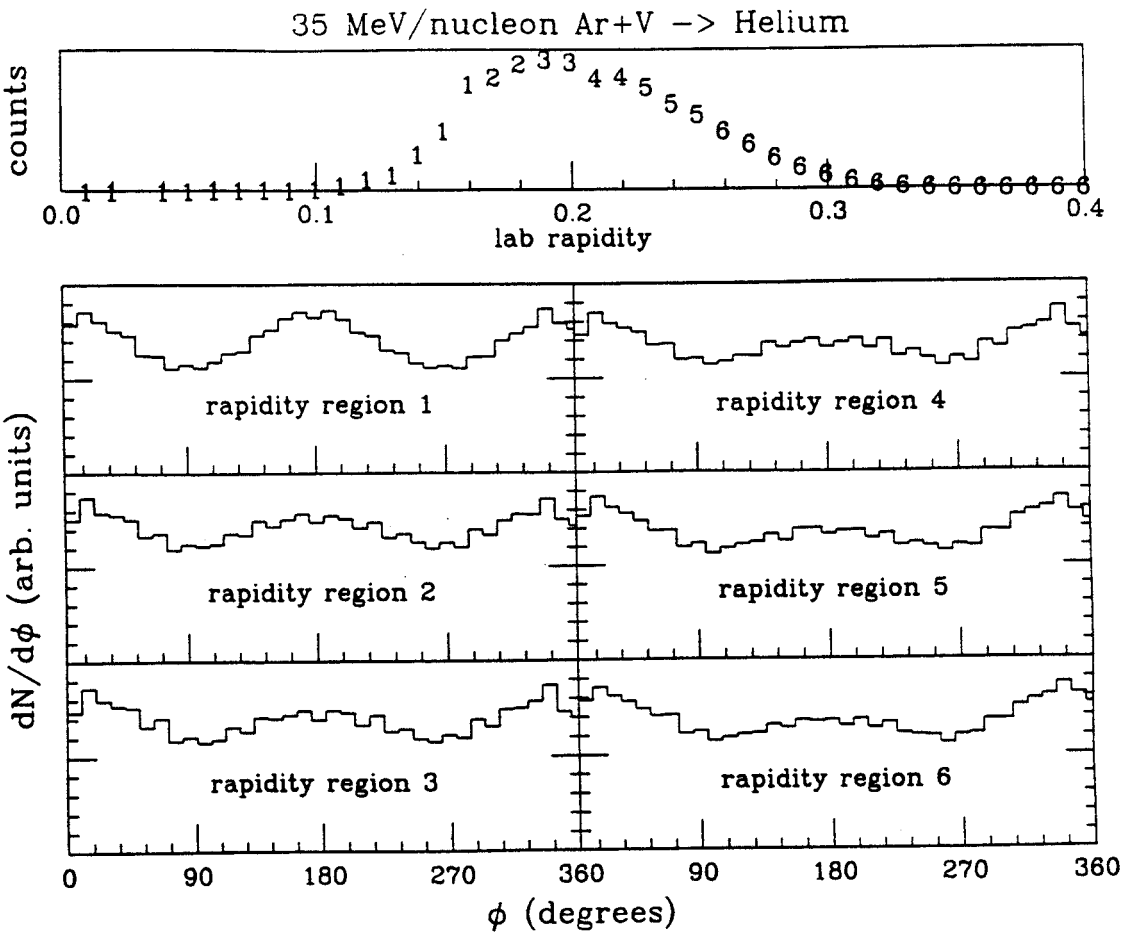


Figure 4.12: Azimuthal distributions of helium produced in 35 MeV/nucleon Ar+V collisions divided into six rapidity bins.

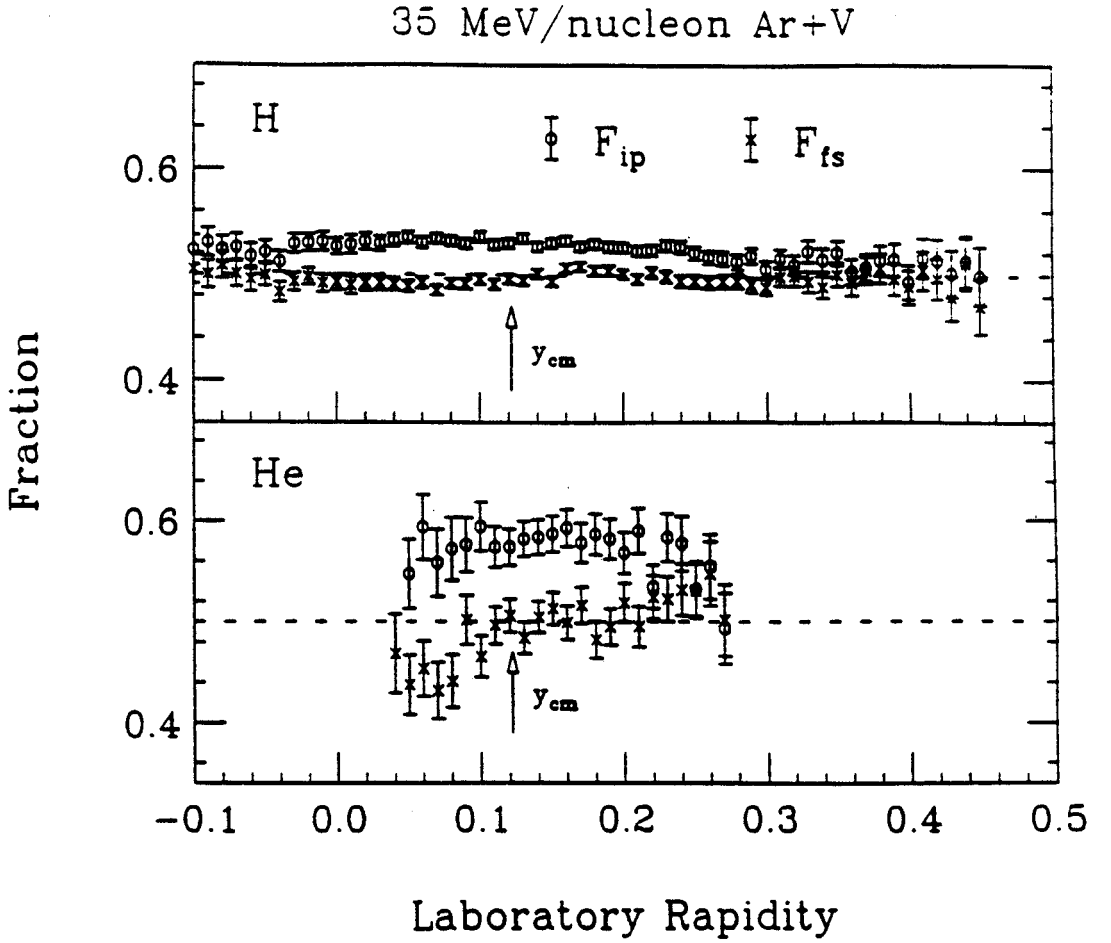


Figure 4.13: Anisotropy fractions for 35 MeV/nucleon Ar+V data with $p^{\perp} \geq 210$ MeV/c per nucleon, and smeared in angular assignments as described in the text.

A slight loss in the accuracy of the reaction plane determination occurs for the angle smeared data compared to the raw data. This is because the smearing used in the azimuthal direction was based on the maximum azimuthal width of the detectors. (The same smearing was used when the accuracy of the reaction plane determination was evaluated in the previous chapter.) An improved technique would be to take the polar width as a function of the azimuthal width into consideration in the smearing, but this would not change the basic trends in the data.

There is an additional effect which causes the drop in $F_{ip}$ in the H data which can be found from an inspection of the momentum dependence of $F_{ip}$ for various particle types. In Figure 4.14 we see that the H ion with counts up to the highest transverse momentum is the proton, which also shows the weakest in-plane enhancement. Therefore, a large $p^{\perp}$ cut tends to enrich the number of protons in the H sample, accounting for the lower values of $F_{ip}$ seen in Figure 4.13 as compared with the raw data. Also note that Figure 4.14 demonstrates that the enhancement increases with as mass increases from 1 to 4 nucleons as expected for collective motion. There is evidence in Figure 4.14 for an increase in the in-plane enhancement up to a plateau value as the transverse momentum increases. We will discuss the possibility of a plateau in the next chapter.

## 4.6 Beam Energy Dependence

As the beam energy is increased to 100 MeV/nucleon, the collisions produce much more azimuthally symmetric distributions of light particles. This can be seen from the anisotropy parameters shown in figs. 4.15 and 4.16 for 65 and 100 MeV/nucleon Ar+V data respectively. Note that in the higher rapidity regions of Figure 4.16, $F_{ip}$ indicates a slight out-of-plane enhancement. This should not be interpreted as

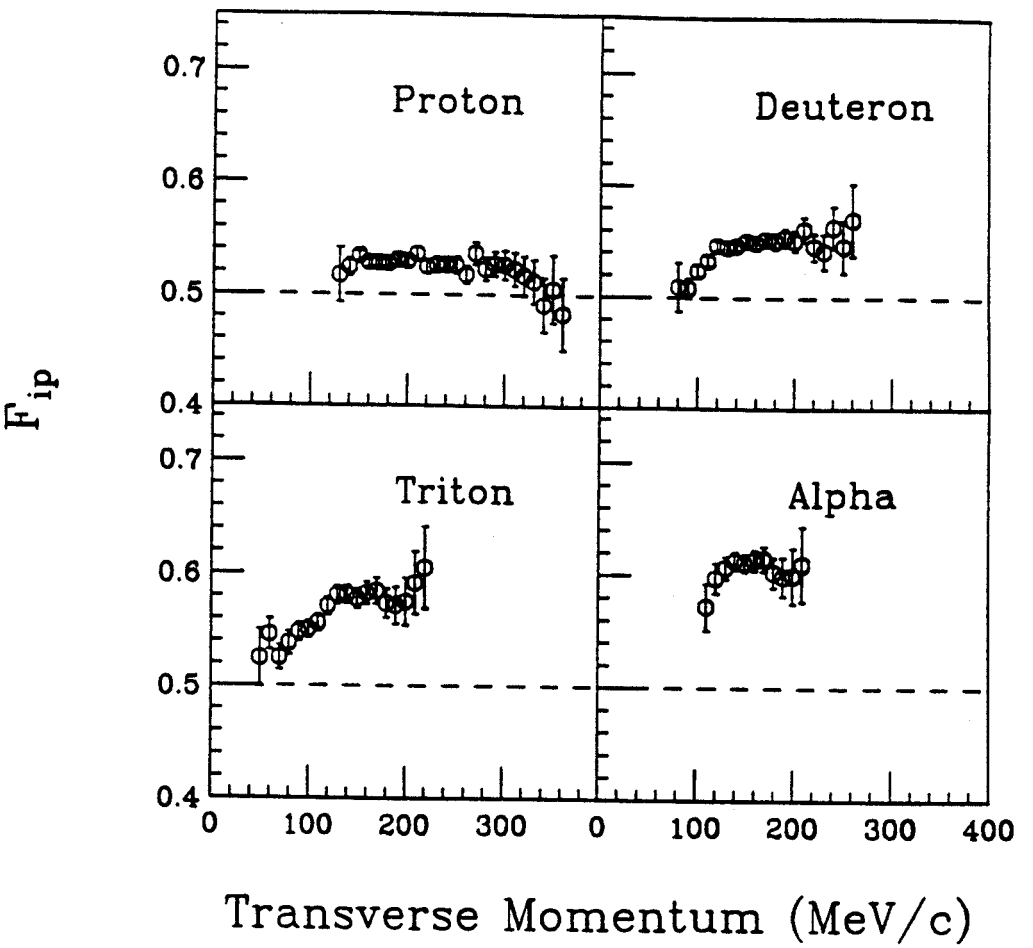


Figure 4.14: Anisotropy fractions for 35 MeV/nucleon Ar+V data as function of $p^{\perp}$/nucleon. The rapidity of the particles was restricted to $y_{cm} \pm .02$ for this figure.

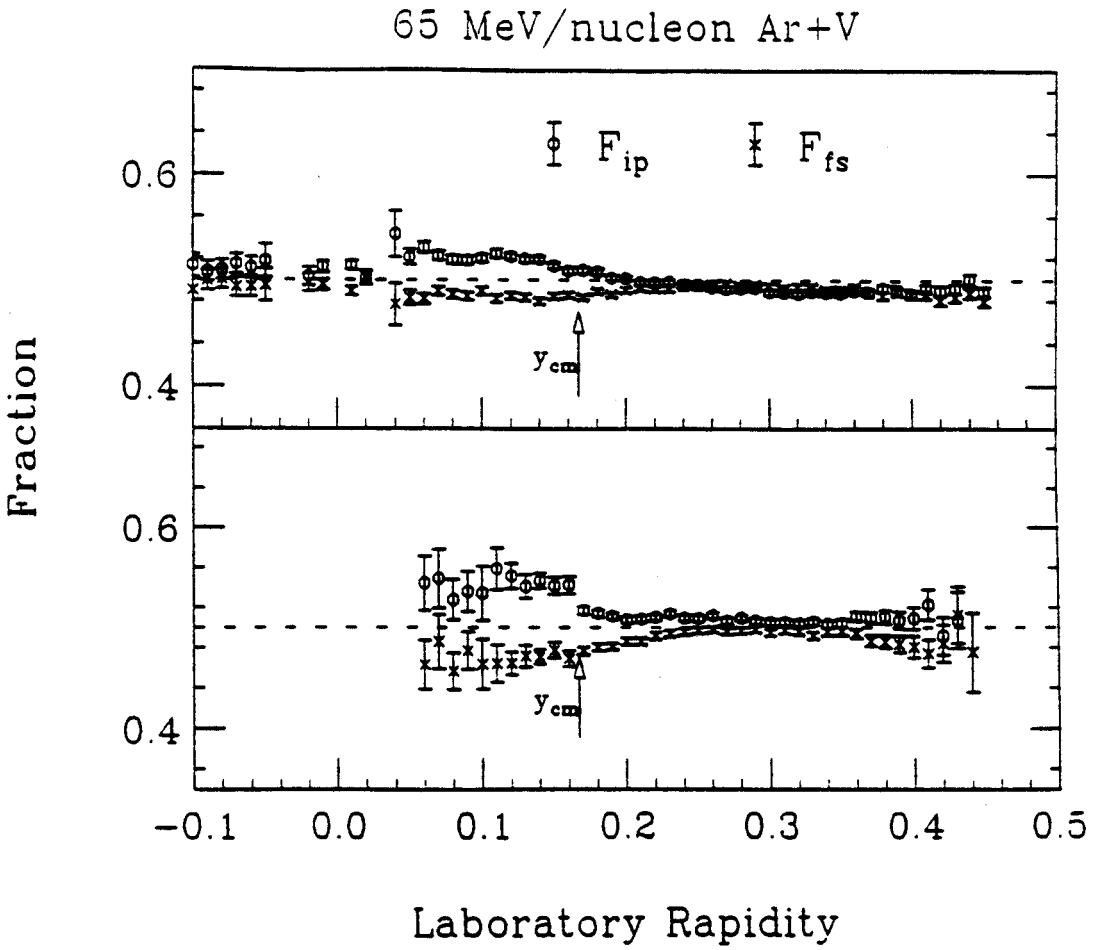


Figure 4.15: Anisotropy fractions as function of rapidity for 65 MeV/nucleon Ar+V data.

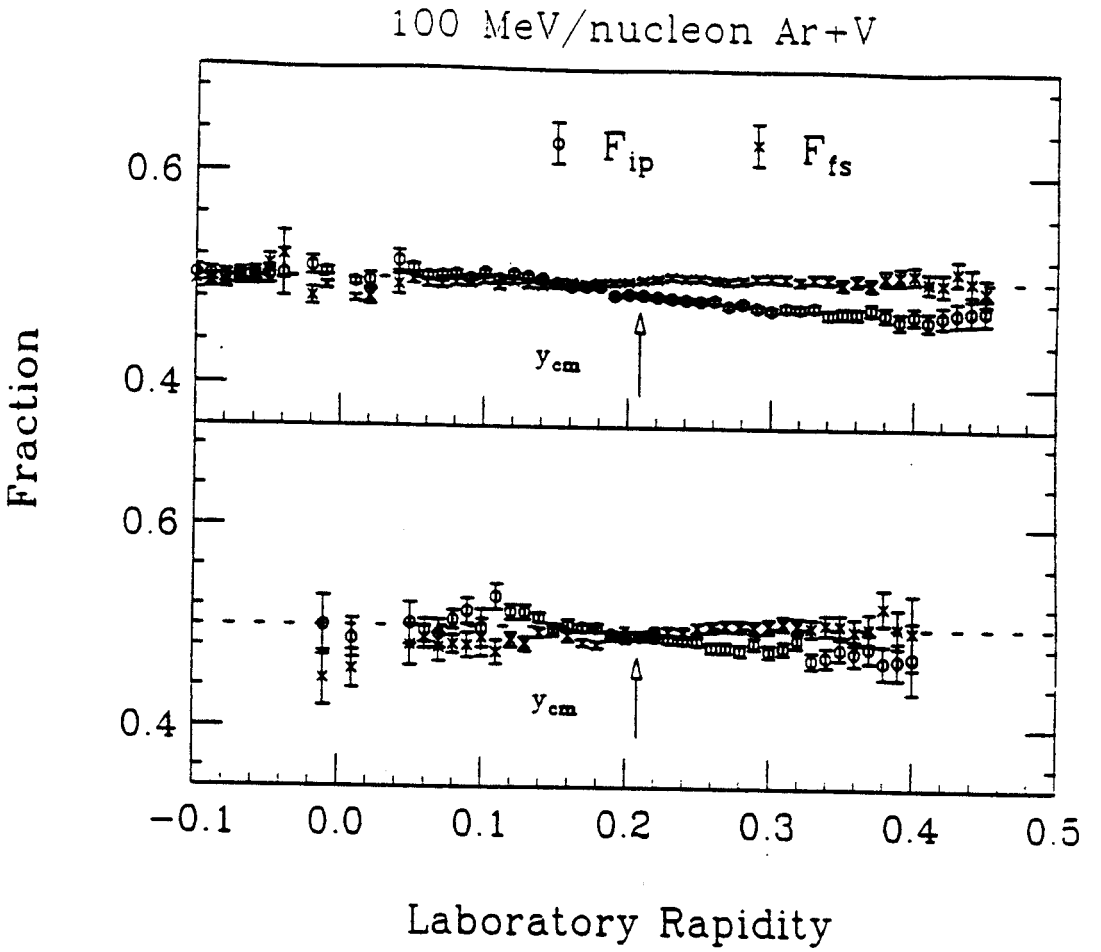


Figure 4.16: Anisotropy fractions as function of rapidity for 100 MeV/nucleon Ar+V data.

evidence for the squeeze-out effect described in the introduction, however. It is the increased forward focusing at the higher beam energies enhancing the influence of multiple hit exclusions that causes the out-of-plane enhancement. We saw the same effect in our examination of the filtered simulations earlier, and it also occurs in randomized 100 MeV/nucleon data.

The increasing isotropy of the events at higher beam energies is not due to the decrease of the energy thresholds relative to the temperature of the composite system. Examination of Figure 4.17 shows that there is no enhancement in the reaction plane at any $p^{\perp}$ value for the 100 MeV/nucleon data at mid-rapidity.

We can conclude that there must be a change in the mechanisms of collective motion as the beam energy is increased. For flow, this change can be mapped out by plotting the slope of $F_{fs}$ at mid-rapidity as a function of beam energy. The slopes shown in Figure 4.18 were obtained by fitting the three rapidity bins on either side of $y_{cm}$. The slope shows a minimum at $E_{beam} \approx 80$ to 90 MeV/nucleon. This observation is equivalent to that made during an earlier analysis of the same data using the average transverse momentum in the reaction plane as a function of rapidity to characterize the flow.[Ogil90, Krof91]

As for rotational collective motion, the in-plane enhancement decreases monotonically with increasing beam energy. In Figure 4.19, the maximum $F_{ip}$ from the raw data is presented as a function of beam energy. Unlike flow, the collective motion creating the in-plane enhancement shows no minimum at beam energies around 80 and 90 MeV/nucleon, and no maximum around 45 MeV/nucleon.

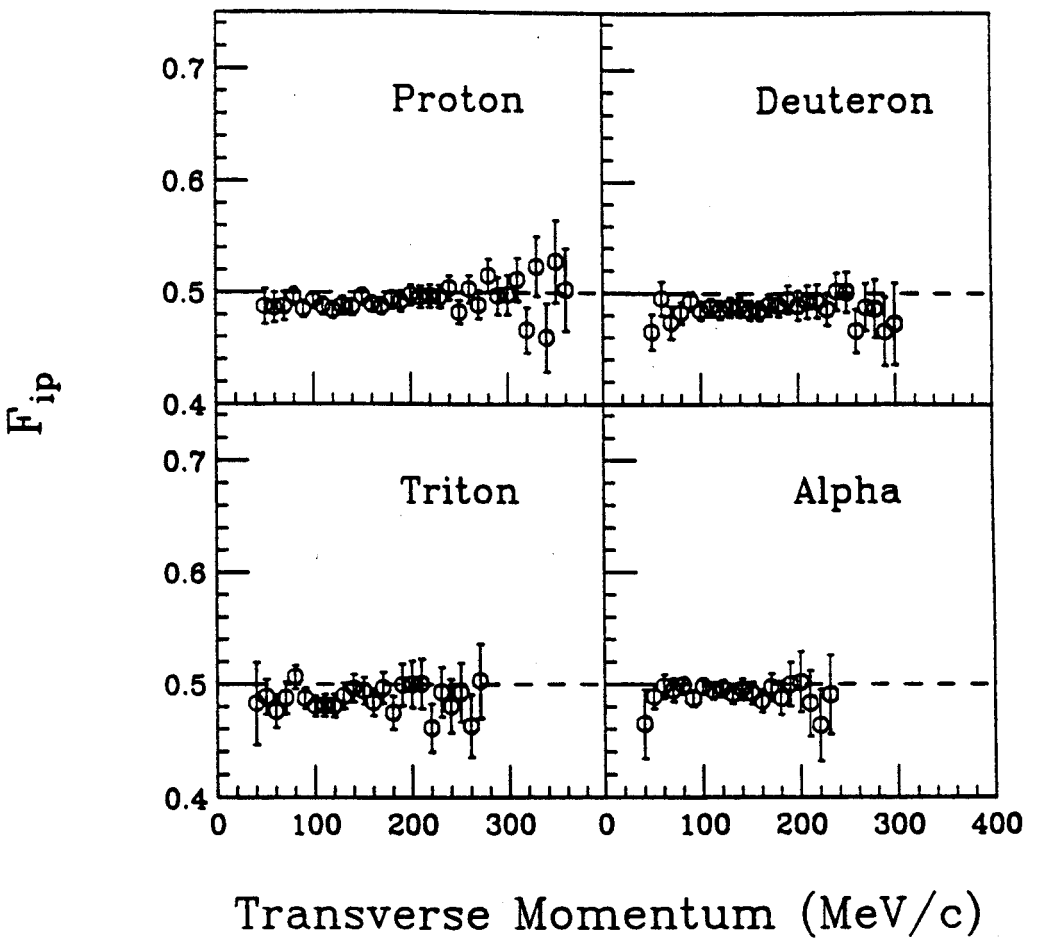


Figure 4.17: Anisotropy fractions for 100 MeV/nucleon Ar+V data as function of $p^{\perp}$/nucleon. The rapidity of the particles was restricted to $y_{cm} \pm .02$ for this figure.

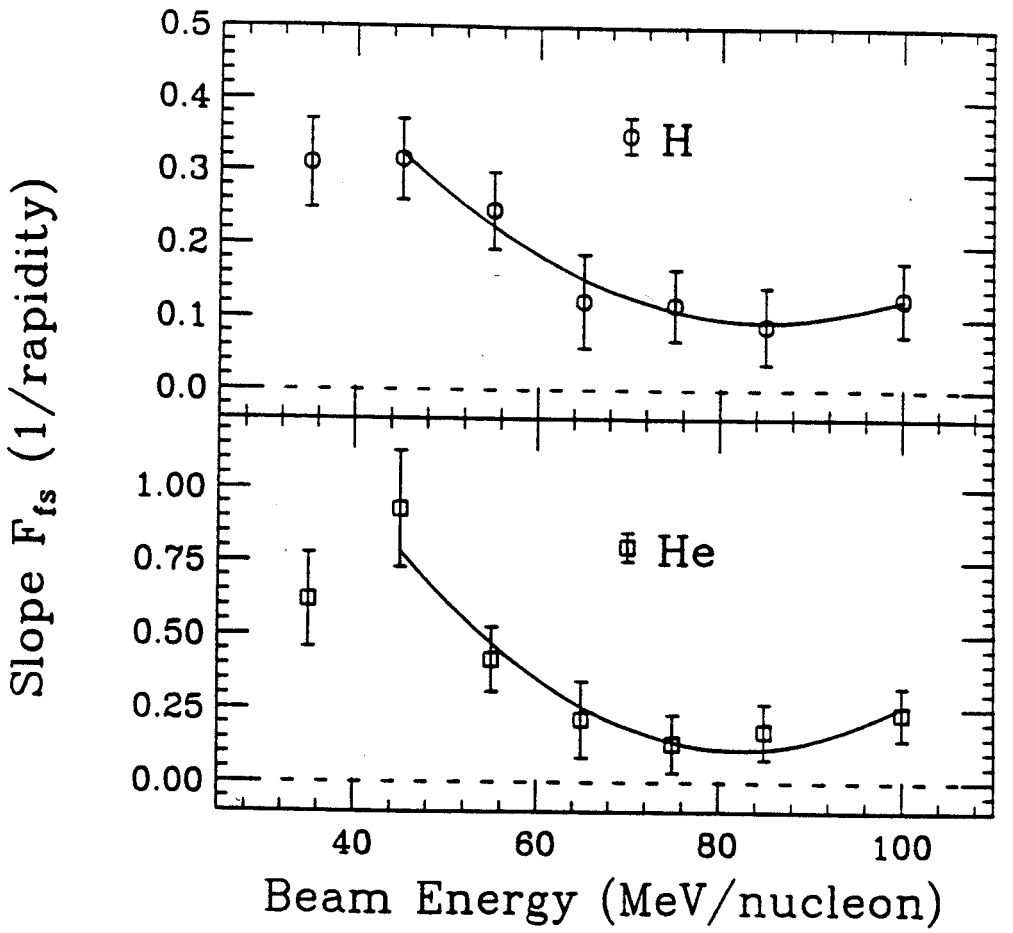


Figure 4.18: The slope of $F_{fs}$ at mid-rapidity is used to measure the transverse momentum flow Ar+V collisions as a function of beam energy. The lines are drawn to guide the eye.

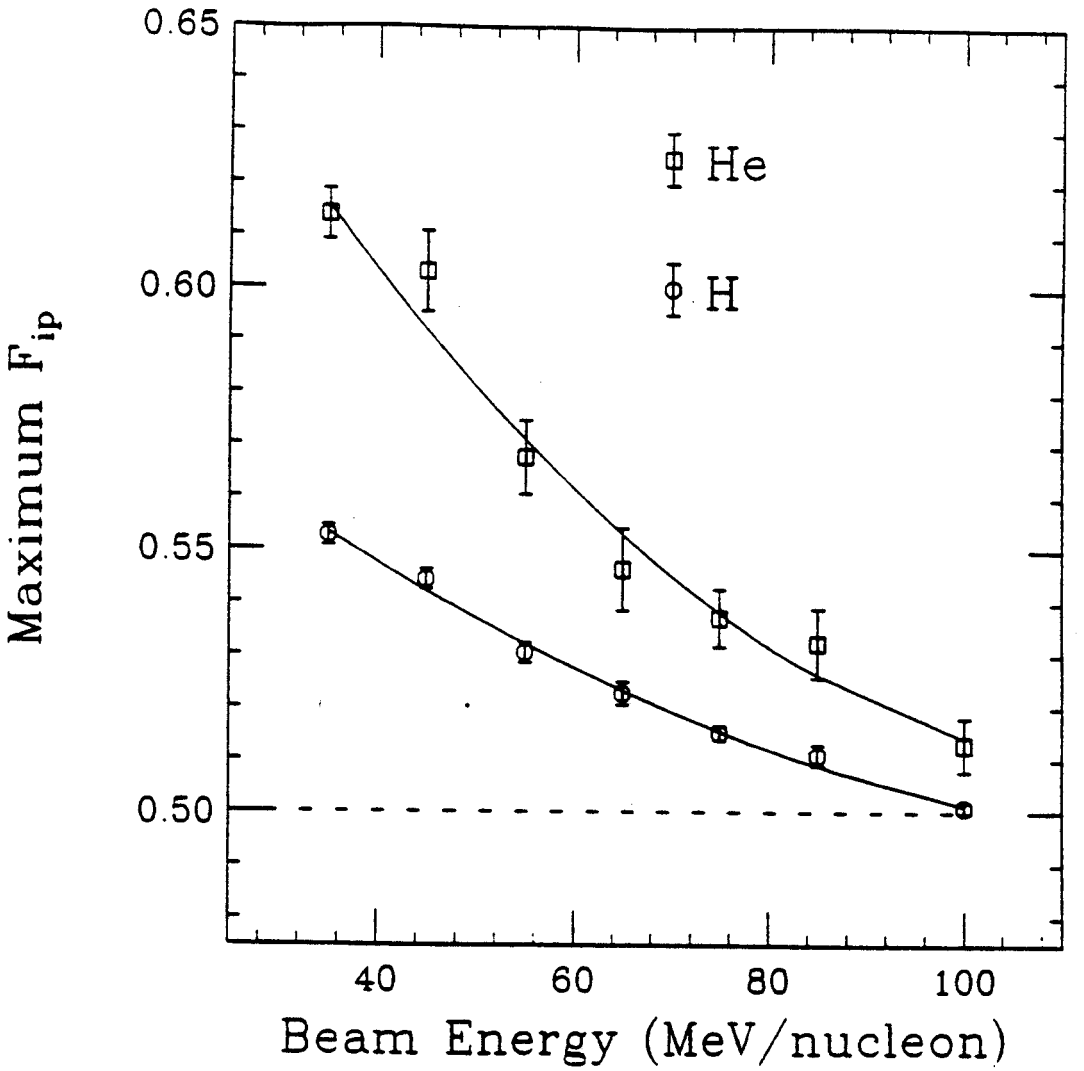


Figure 4.19: The maximum of $F_{ip}$ is used to measure the in-plane enhancement of particle emission in Ar+V collisions as a function of beam energy. The lines are drawn to guide the eye.

## 4.7 Summary

We have shown that there are two types of azimuthal anisotropies exhibited by light charged particles produced in 35 MeV/nucleon Ar+V collisions. The momentum distributions produced in the events show preferential emmission in the reaction plane which resembles rotational collective motion. There is also evidence for collective flow, i.e. particles being deflected towards one side of the reaction plane at forward rapidities and toward the other side at backward rapidities in the center of momentum frame of reference. Both anisotropies increase with the mass and the $p^{\perp}$ of the particle of interest, as would be expected if a collective velocity was superimposed on random thermal motion. Both forms of collective motion change in character as the beam energy is increased, with flow showing a minimum between 80 and 90 MeV/nucleon, and rotation decreasing in importance as the beam energy goes to 100 MeV/nucleon.

# Chapter 5

# Comparison With Theory

## 5.1 Introduction

In the previous chapters we saw that collective motion in heavy-ion collisions generates azimuthal anisotropy. Enhancement of the light particle emission in the reaction plane suggests rotation of the emitting system around an axis $\perp$ to the plane. There is also a shifting of the enhancement from one side of the reaction plane to the other as a function of parallel rapidity, which has been interpreted as collective flow. In this chapter, we compare the observed in-plane enhancement to that expected due to emission from a rotating spherical source. We find that this picture cannot account for the particle energy dependence of the in-plane enhancement, showing the need for comparison with models which include the dynamics of the reaction. Techniques are currently being developed to numerically solve the dynamical equations describing heavy-ion reactions. In the second part of this chapter, we compare the results of one such calculation with our observed azimuthal distributions. We shall see if the anisotropies can be reproduced by the BUU model, and if they can be connected with simple modes of collective motion.

## 5.2 Background on the Rotating Sphere Model

Particle emission from a rotating sphere[Chit86], has been employed by Tsang and coworkers in the interpretation of azimuthal correlations. Their work falls into two categories, light particle - light particle coincidence studies[Tsan84a, Chit86] and light particle - fission fragment studies.[Tsan84b, Tsan90]

In the two experiments which detected fission fragments, beams of N and Ar from 20 to 50 MeV/nucleon were incident on Au and U targets. The massive targets were employed in order to insure that fission was a likely channel of deexcitation. The angular momentum of the compound system around an axis $\perp$ to the reaction plane causes fission fragments to be aligned with the reaction plane.[Vaz83]. Tsang et al.[Tsan84b] found that light particles (Z=1,2) detected in coincidence with fission fragments were preferentially emitted in the reaction plane. They noted that this enhancement increased with both the mass and energy of the light particles. These trends were reproduced by a model assuming emission from the surface of a sphere rotating with $r\omega \approx 0.04c$ to $0.08c$ where r is the radius of the sphere and $\omega$ is its angular frequency.

Enhanced emission in the reaction plane should cause the distribution of differences between azimuthal angles of two light particles emitted during the same event to peak at 0° and 180°. This effect was observed in 25 MeV/nucleon O+Au collisions, and was also reproduced by particle emission from the surface of a rotating source with similar $r\omega$ values[Tsan84b].

Chitwood et al.[Chit86] explored the effects of rotational collective motion on azimuthal angle integrated kinetic energy spectra. Rotation with these $r\omega$ values was shown to substantially elevate the apparent temperature of the source, lowering the actual temperature needed to fit the kinetic energy spectra. This result underscored

the need to characterize the dynamics of the reaction before conclusions about the thermal properties of nuclear matter can be drawn.

One criticism of the application of the rotating sphere model to heavy-ion collisions was that the extracted angular velocities implied a system with extremely high angular momentum. Using

$$L = I\omega = \left(\frac{2}{5}Mr^2\right)\omega \tag{5.1}$$

for a rotating sphere of mass M and radius

$$r = 1.2A^{\frac{1}{3}} \text{ fm}, \tag{5.2}$$

one obtains an angular momentum

$$L = 2.3A^{\frac{4}{3}}\frac{r\omega}{c}\hbar\,. \tag{5.3}$$

For $^{35}$Ar+$^{238}$U, an $r\omega$ of 0.06 c implies an angular momentum in excess of 240$\hbar$. In Figure 5.1 we show the highest angular momentum a system can sustain as a function of mass.[Cohe74] For an $A$=273 system, the fission barrier would disappear near 70$\hbar$. The choice of radius is somewhat arbitrary, but the radius of the compound system would have to be unreasonably small to bring the angular momentum down to a stable value. Certainly, the effects of deformation on the barrier to particle emission cannot be ignored for systems with such a high angular momentum.

## 5.3 Particle Emission From a Rotating Sphere

The cross section for the emission of a particle of mass $m$ and kinetic energy $E$ from the surface of a sphere with a radius r, rotating with an angular frequency $\omega$ is

$$\frac{d^2\sigma}{dE\,d\Omega} \propto \frac{J_1(iK)}{iK}Ee^{-\frac{E}{T}} \tag{5.4}$$

with

$$K = \frac{r\omega}{T}\cos(\phi)\sqrt{2mE} \tag{5.5}$$

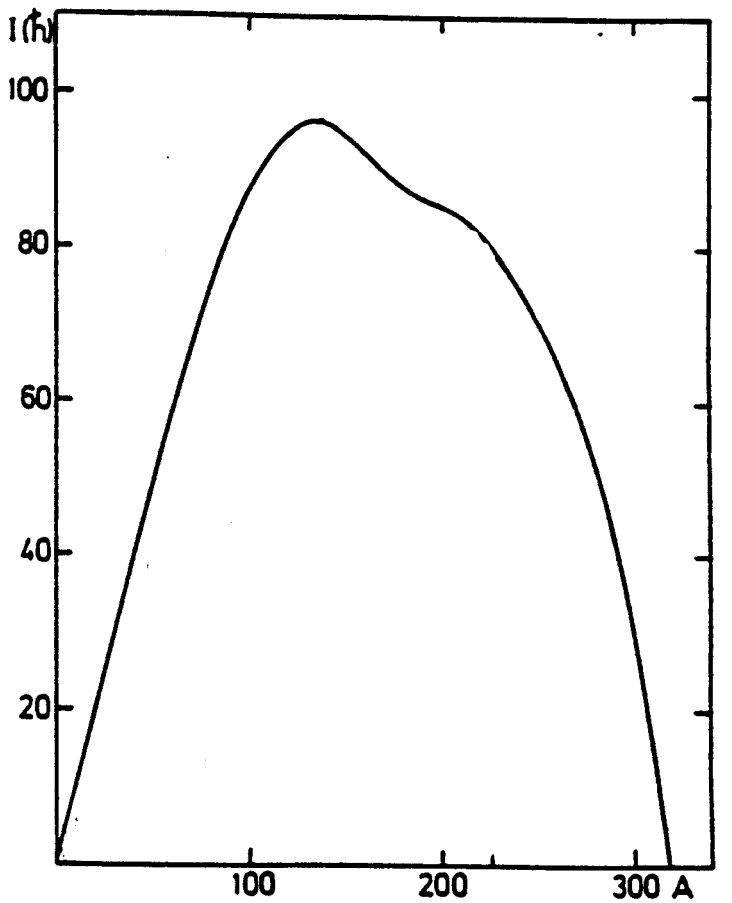


Figure 5.1: Maximum angular momentum that a nucleus with mass number $A$ can support. For each $A$, the nucleus in the valley of $\beta$ stability was used in the calculation.[Cohe74]

in the source frame of reference.[Chit86] In the equation, $T$ is the temperature of the source, $\phi$ is the angle with respect to the reaction plane, and $J_1$ is the first order Bessel function. The kinetic energy must be increased by the energy due to Coulomb repulsion between the source and the emitted particle when eq. 5.4 is compared to the data. If $r\omega$ goes to 0, the equation reduces to that for emission from the surface of a thermal source,

$$\frac{d^2\sigma}{dE\,d\Omega} \propto Ee^{-\frac{E}{T}}. \tag{5.6}$$

This equation differs from the more commonly used equation for volume emission, eq. 2.4, by a factor of $\sqrt{E}$, and consequently gives slightly lower temperatures, but both equations fit energy spectra equally well.

Integrating over energy[Lace87] provides the more intuitive result

$$\frac{dN}{d\phi} \propto e^{\left(\frac{E_R}{T}\right)\cos^2\phi} \tag{5.7}$$

where $E_R$ is simply the rotational energy of the particle on the surface,

$$E_R = \frac{1}{2}mr^2\omega^2 \tag{5.8}$$

Thus, the degree of in-plane enhancement depends on the ratio of the rotational energy of the emitted particle to the temperature of the source. Increasing the temperature tends to smear out the collective effects.

## 5.4 Comparison of Rotating Sphere With Data

We have used the rotating sphere model to estimate the amount of angular momentum needed by the compound system to produce the observed in-plane enhancement. The distribution of He produced in 35 MeV/nucleon Ar+V collisions was chosen for the comparison since it shows the strongest anisotropy. The extracted angular momentum should be considered only a lower limit, however, since we did not correct for the

dispersion of found reaction planes around the true planes. This correction was not feasible because the upper limit on the dispersion found in chap. 3 (50°) is only a few degrees narrower than the He azimuthal distribution, so the correction would produce an unrealistically strong focusing of He in the reaction plane. We would need both an upper and lower limit on the dispersion in order to make a reliable correction to the observed azimuthal distribution.

The upper left hand panel in Figure 5.2 shows the kinetic energy spectra of He at 90° in the center of mass system. Fitting with equation 5.6 produces $T = 11.5 \pm 0.5$ MeV for the case of negligible rotation. Since any increase in $r\omega$ would decrease the temperature necessary to fit the spectrum, this apparent temperature should be considered as an upper limit.

The upper right hand panel shows the azimuthal distribution for He with respect to the reaction plane in the center of mass system. A fit using eq. 5.4 with $T = 11.5$ MeV and E numerically integrated from 55 to 300 MeV gives $\frac{r\omega}{c} = 0.047 \pm 0.001$ , shown as curve in the figure. The energy $E$ in eq. 5.4 was increased by 20 MeV to account for the /coulomb boost described earlier. This number was arrived at by calculating the Coulomb repulsion between the compound system and the emitted He approximated as touching spheres.

As we have noted, the actual temperature may decrease by up to a factor of 2 when the effects of rotation are taken into account.[Chit86] We therefore display the $r\omega$ values obtained for a range of temperatures in the bottom panel of Figure 5.2. The angular velocity lies between 0.027 and 0.048 c, and the quality of the fits did not vary with temperature. The angular momentum of the sphere would then be between 25 and 45 $\hbar$, well below the limit of stability for an A=91 system.

The rotating sphere model cannot account for the energy dependence of the in-

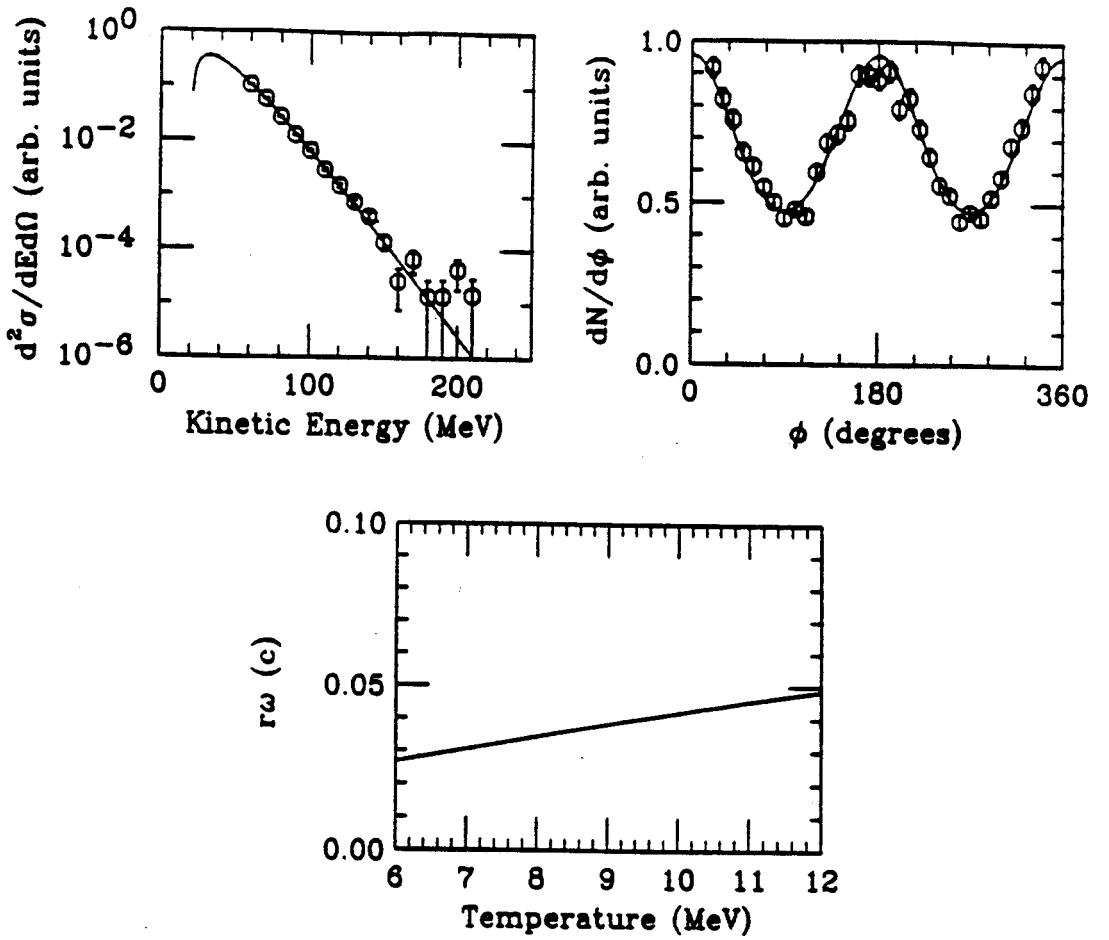


Figure 5.2: A fit to He emitted from 35 MeV/nucleon Ar+V collisions using the rotating sphere parameterization. The upper left hand panel show the extraction of $T$ from the center of mass kinetic energy spectra, while the upper right hand panel shows the extraction of $r\omega$ from the azimuthal distribution. The range of temperature and rotational velocity parameters allowed by the data is shown in the bottom panel.

plane enhancement. In Figure 5.3 we show that the fraction of He ions emitted within 45° of the reaction plane, $F_{ip}$ is essentially constant with respect to energy at a polar angle of 90° in the center of mass frame of reference. The rotating sphere equation predicts a steep increase in $F_{ip}$ as a function of energy, shown in Figure 5.3 as curves for two extremes of temperature. The $r\omega$ values were taken from the calculations for the previous figure.

We must be careful in our interpretation of the plateau in $F_{ip}$ as observed in figs. 4.14 and 5.3. If the 50° upper limit on the uncertainty in the reaction plane determination is the true uncertainty, then the uncorrected He azimuthal distribution in Figure 5.2 is at the upper limit of observable in-plane enhancements. Even if the He distribution is a delta function at $\phi = 0°$ and 180°, the measured azimuthal distribution must be as broad as the dispersion in the found reaction planes about the true reaction planes. An uncertainty of 50° in the reaction plane determination is not enough to explain the plateau in $F_{ip}$ exhibited by the lighter particles in Figure 4.14. We can conclude that there is a suggestion of a saturation of the in-plane enhancement with increasing energy and transverse momentum, but a more definitive statement will depend on an improved estimation of the accuracy of the reaction plane determination.

## 5.5 Deformation

It is not surprising that the simple rotating sphere model is unable to account for the details of the observed azimuthal asymmetries since it does not contain any of the dynamics of the formation and decay of the compound system One important dynamical effect that can strongly influence the azimuthal distribution of particles evaporated from a rotating nuclear system is **deformation**.[Rive82, Dilm82, Maij87,

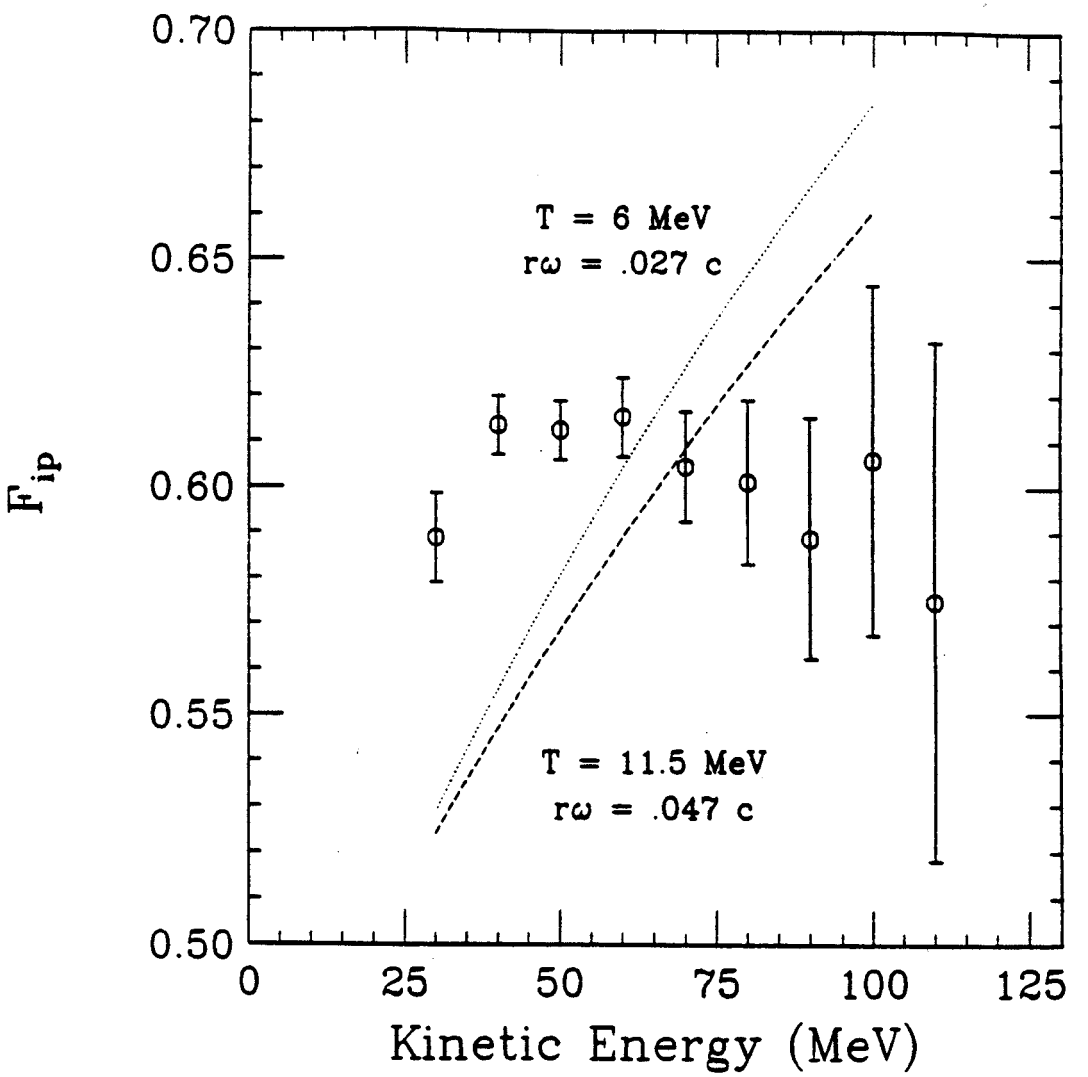


Figure 5.3: Energy dependence of the in-plane enhancement for He emitted emitted from 35 MeV/nucleon Ar+V collisions at a polar angle of 90° in the center of mass frame of reference. The curves are the predictions of the rotating sphere model for two extremes in temperature.

Bruc88] In Figure 5.4 we show the evolution of the deformation of a $^{158}$Yb as a function of the angular momentum (I). The deformation is parameterized in terms of the **Hill-Wheeler coordinates**[Hill53] $\gamma$ and $\beta$ given by

$$\begin{aligned} a &= R_0 e^{-\delta \cos(\gamma+60°)} \\ b &= R_0 e^{-\delta \cos(\gamma-60°)} \\ c &= R_0 e^{-\delta \cos(\gamma)} \\ R_0 &= \sqrt[3]{abc} \\ \beta &= \sqrt{\frac{4\pi}{5}}\delta \end{aligned} \tag{5.9}$$

where $a$, $b$, and $c$ are the three semi-axis lengths of the ellipsoidal nucleus. If $\gamma$ is 0° then the system is prolate, if −60° then it is oblate, while intermediate values indicate a triaxial shape. The parameter $\beta$ increases with the severity of the deformation.

Small amounts of angular momentum lead to oblate deformations with the minor axis perpendicular to the reaction plane. If the angular momentum exceeds a critical value, the system passes through the **Jacobi-bifurcation point**, and a triaxial shape develops with the major axis perpendicular to the angular momentum vector. Larger angular momentum values increase the prolateness of the system until it becomes unstable with respect to fission.

All of these shapes have their major axis perpendicular to the rotation axis, lowering the barrier for particle evaporation in the reaction plane. Using a deformed nucleus allows the observed in-plane enhancement to be accounted for by a lower angular momentum than would be necessary if the nucleus was spherical.[Bruc88] Thus, it was probably the assumption of spherical symmetry in early work on two particle azimuthal correlations that led to the unphysically high angular velocity values cited earlier.[Tsan84b, Chit86]

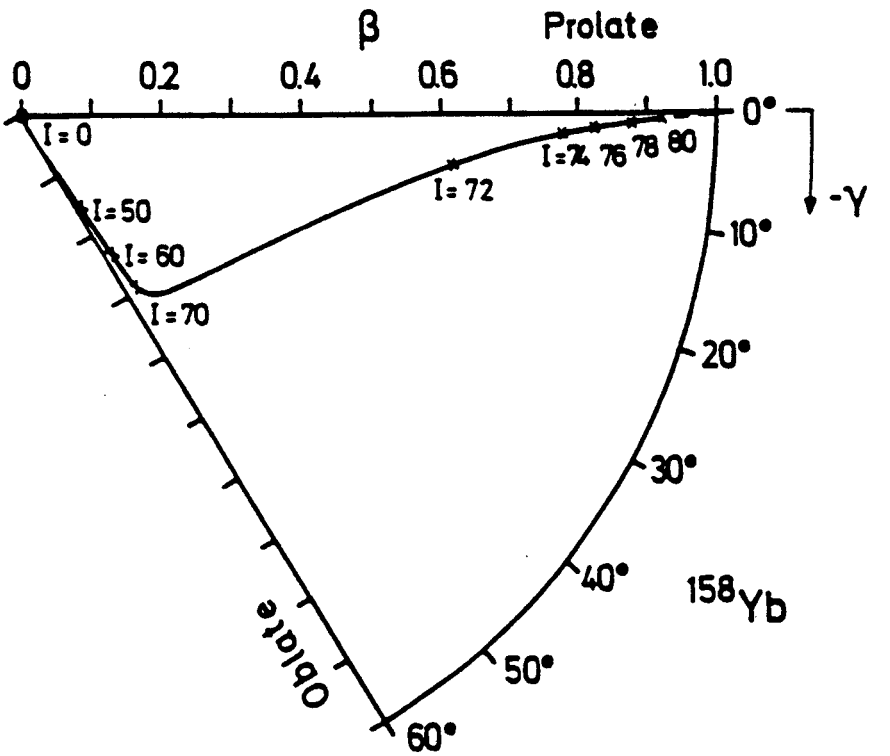


Figure 5.4: Hill-Wheeler coordinates for a $^{158}$Yb nucleus are shown as a function of the angular momentum (I) using the liquid drop model.[Ande76]

## 5.6 Decay Channels of Rotating Systems

Another dynamical effect that we have ignored so far in our discussion of the rotating source is the competition between different decay modes. This effect has recently been studied using the BUU approach to track the deexcitation of a hot, rotating $^{40}$Ca nucleus.[Garc91] In addition to the two conventional modes of disassembly, particle evaporation and fission, Garcias et al. found that under certain conditions the system could undergo **multi-fragmentation** into 3 or more substantial pieces. Their map of trajectories in Hill-Wheeler coordinates for three different starting conditions is shown in Figure 5.5.

All of the calculations took a spherical nucleus rotating rigidly as their starting point, and then tracked the development of deformations as a function of time. Particle evaporation begins immediately, reducing the angular momentum of the system. The system starting with $L = 47\hbar$ is able to loose enough angular momentum through particle emission to escape fission, unlike the $L = 65\hbar$ system. The highest angular momentum system, $L = 75\hbar$, is torn apart into fragments before it can become prolate and undergo fission. The main conclusion drawn from these calculations it that systems with a large amount of angular momentum can avoid fission or fragmentation if the internal excitation is enough to cause it to dissipate its angular momentum quickly through particle emission.

Although the calculations of Garcias et al. shed light on the competition between the processes that dissipate angular momentum in rotating systems, they do not address the dynamics involved in the formation of these systems. The actual system formed in a heavy-ion collision is likely to begin with large deformations as well as non-randomized longitudinal momentum. In order to explore the full dynamics of the creation and decay of a compound system, we have performed BUU calculations of

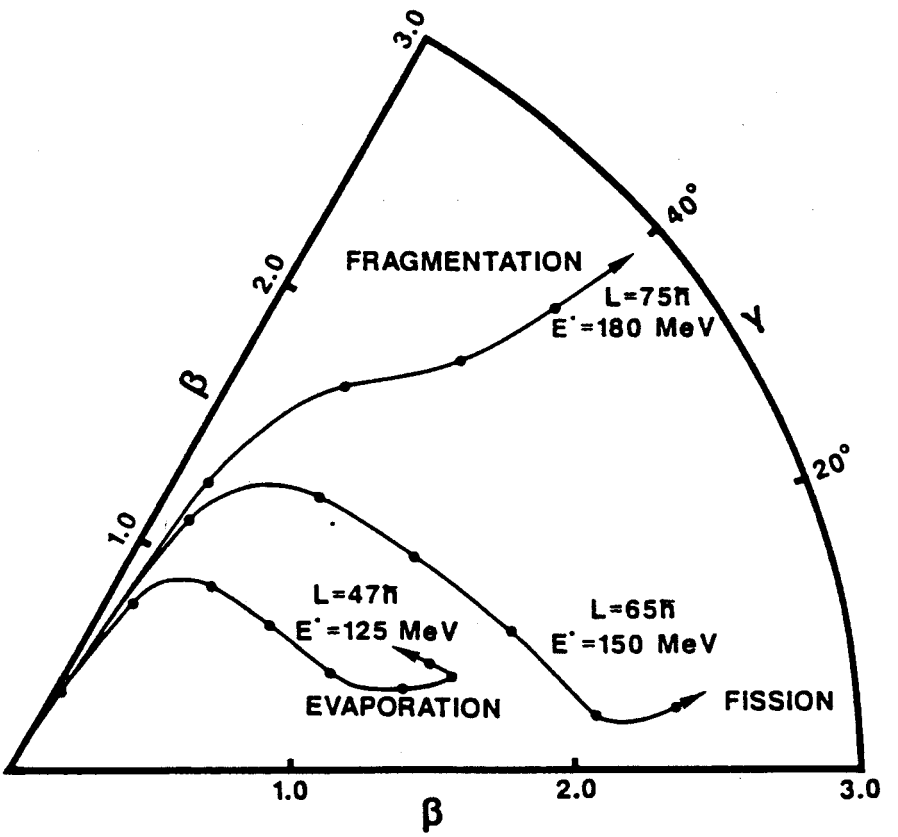


Figure 5.5: BUU predictions for the evolution of an excited Ca nucleus with high angular momentum for different initial conditions (displayed next to the arrow at the end of each trajectory). Each point on the curves is separated by a time step equal to 30 fm/c. [Garc91]

nuclear reactions focusing on collisions in which the projectile and target fuse.

## 5.7 Description of the BUU Approach to Solving Nuclear Dynamics

A short historical overview of the development of microscopic models of heavy-ion reactions and their relationship with progress in relativistic collisions was presented in Chap. 1. In this section we will give a brief summary of the BUU model; a more detailed but highly accessible summary has been written by Bertsch and Das Gupta.[Bert88]

We begin by taking a **mean-field** approach to the interactions between the nucleons. Since it is impossible to write down and solve the time dependent many-body Hamiltonian describing a heavy-ion collision, we replace the nucleon-nucleon force with a one-body interaction between each individual nucleon and the mean-field created by all the remaining nucleons. The equation for the classical dynamics of a phase space distribution ($f(\vec{r},\vec{p})$) in a potential $U$ is

$$\frac{\partial f}{\partial t} + \frac{\vec{p}}{m} \cdot \vec{\nabla}_r f + -\vec{\nabla}_r U \cdot \vec{\nabla}_p F = 0 \tag{5.10}$$

in the absence of nucleon-nucleon collisions. This expression, called the **Vlasov equation**, can be derived from quantum mechanics, with $f$ interpreted as the **Wigner transform**, the Fourier transform of the quantum phase space density matrix.

This equation can be numerically integrated for short times as

$$f(\vec{r},\vec{p},t+\delta t) = f(\vec{r} - \frac{\vec{p}}{m} \cdot \delta t, \vec{p} + \vec{\nabla} U \cdot \delta t, t). \tag{5.11}$$

The reaction is simulated by replacing the individual nucleons with a large number of **test particles** representing their phase space distribution, and propagating the particles according to equation 5.11.

Because the Liouville theorem says that the density in phase space remains constant in a frame moving with the particles, if our initial phase space distribution obeys the Pauli exclusion principle, then the principle will be obeyed at all future times. To initialize a nucleus, we therefore assign test particles random positions in coordinate space up to the radius of the nucleus and random values in momentum space up to the Fermi momentum, taking care not to place test particles in regions of phase space that are already occupied. Two nuclei so constructed are then allowed to collide, and the evolution of the phase space distribution obeys the Pauli principle automatically.

This simple one-body approach can be improved by adding a two-body interaction in the form of nucleon-nucleon collision. As each test particle travels through space, we check to see if it comes close to another test particle. If two particles pass through their point of closest approach in a given time step, then we check to see if they would have scattered. The cross section for scattering is taken from the cross section for free neutron-proton scattering.[Part88] We must further check that the final positions in phase are not already occupied in order to insure that the Pauli principle is not violated. If the final state is already occupied then the collision is suppressed, or **Pauli blocked**. As shown in figure 5.6, this effect becomes pronounced as the beam energy is decreased because the available phase space then decreases.

Since the nucleons have been replaced by test particles, the nucleon-nucleon cross section should be lowered by a factor equal to the number of test particles per nucleon. In the calculations presented in this thesis, each nucleon was replaced by 375 test particles. It is very time consuming to check each possible pair of test particles for collisions in every time step, but a computational trick can simplify the task. The test particles are divided into 375 **parallel ensembles**, the number of test particles in each ensemble equalling the number of nucleons in the reaction to be simulated.

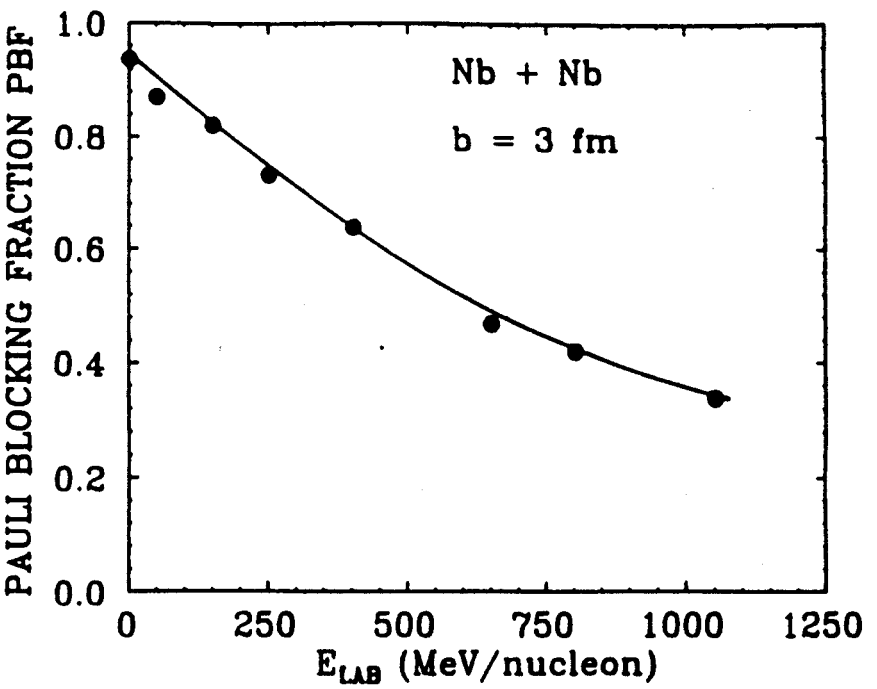


Figure 5.6: The fraction of collisions that are Pauli blocked is shown for BUU calculations of Nb+Nb collisions with an impact parameter of 2 fm over a range of beam energies.[Stöc86]

Collisions are then allowed only within each individual ensemble, not between test particles in different ensembles, and the full nucleon-nucleon cross section is used. This drastically reduces the number of pairs that have to be considered, making the calculation tractable. The mean-field is still calculated using all the test particles.

A modification of the scattering due to quantum mechanics must also be considered. Since such a large amount of the available phase space is occupied when the beam energy is near the fermi energy, it is possible that a significant fraction of the intermediate states in the quantum mechanical picture of scattering are blocked, lowering the cross section in the nuclear medium below that of free nucleons. This effect is usually approximated by simply reducing the nucleon-nucleon cross section used in the code below that of the free n-n cross section. The precise reduction factor is not known, so it is hoped that comparisons between BUU-like theories and observations of heavy-ion collisions will provide constraints on the in-medium n-n cross section as well as the equation of state. In fact, the transverse momentum flow produced by the BUU model at beam energies below 100 MeV/nucleon is more sensitive to $\sigma_{nn}$ than the compressibility of nuclear matter.[Bert87, Ogil90]

## 5.8 The Direction of the Flow

The inversion of the collective flow as the beam energy is lowered from the regime in which compressional forces cause a hydrodynamic side-splash to the regime in which attractive mean field deflection dominates was discussed in chap. 1. (see also Figure 3.2) However, we noted in our discussion of reaction plane determination in chap. 3 that the experimenter cannot distinguish between these two phenomena. One can say which side of the reaction plane contained the forward going component of the momentum flow, but not which side originally contained the projectile. Thus, it is

not possible to know whether the nucleons in the projectile were repulsively scattered away from the overlap region (to positive angles) or attractively deflected toward it (to negative angles). The x-axis in the reaction plane, from which the azimuthal angles are measured, is thus always chosen to coincide with the forward flow side of the reaction plane. This convention causes the flow parameter (i.e. the slope of the average transverse momentum as a function of rapidity) to always be positive.

This convention is not necessary in the analysis of BUU events since in this case we know the initial orientation of the system. Traditionally, the x-axis is chosen to lie within the side of the reaction plane which initially contained the projectile. If the projectile nucleons are splashed away from the interaction region, they will be found with positive values of $P^x$, while if they are attracted towards the interaction region they will be found on the negative x side of the reaction plane. In the latter case, the flow parameter will be negative.

## 5.9 Goals of our BUU Calculation

Previous calculations using the BUU model at beam energies below 100 MeV/nucleon have focused upon transverse momentum in the reaction plane and azimuthal distributions around the reaction plane at a late stage in the time evolution of the event.[Moli85b, Bert87, Tsan89, Ogil90, Xu90] They found that attractive flow and enhanced emission in the reaction plane. As an example, we show in Figure 5.7 the results of BUU calculations performed by Bertsch et al.[Bert87] for a mass 40 projectile incident on a symmetric target. The plot displays the mean transverse momentum in the reaction plane for particles going forward in the c.m. frame of reference for a variety of impact parameters and beam energies. A stiff equation of state ($K = 375$ MeV) was used in the calculations denoted by open symbols, while a soft equation of

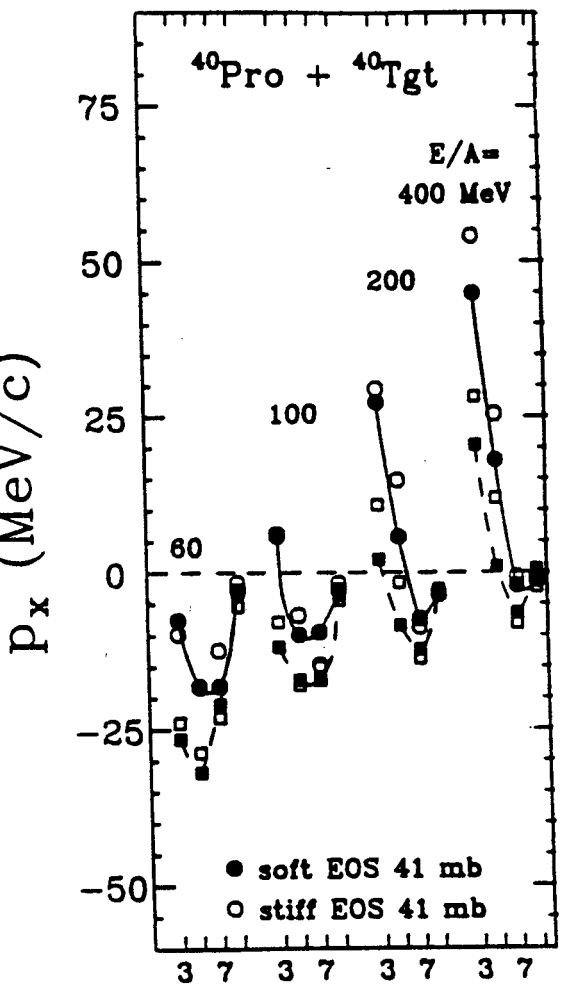


Figure 5.7: BUU calculations of the transverse momentum flow for different equations of state and in-medium n-n cross sections. The mean transverse momentum in the forward c.m. hemisphere is plotted along the horizontal axis.[Bert87]

state ($K$ = 200 MeV) was used for the solid symbols. The calculations denoted by circles used the full free cross section for $\sigma_{nn}$, while the squares were calculated using a cross section half as large. The side-splash phenomena at $E_{beam}$ = 400 MeV/nucleon causes the values of $P^x$ to be positive, but at 60 MeV/nucleon the attractive mean field dominates and particles in the forward c.m. hemisphere are deflected to the other (-x) side of the reaction plane.

Three conclusions can be drawn about collective motion in collisions below 100 MeV/nucleon based on previous BUU calculations. First, based on the work presented in [Moli85b] and [Bert87], the attractive component of the nuclear mean-field can create collective flow that is observationally similar to the flow found in relativistic collisions. Second, studies of asymmetric systems (such as O+Au[Tsan89] and Ar+Al[Xu90]) showed a enhanced particle emission in the reaction plane. Third, both of the previously mentioned effects are strongest at middle to peripheral impact parameters. These calculations did not study the collective motion as a function of time in detail or investigate the relationship between the in-plane enhancement and the collective flow.

Our goal in performing the BUU calculations presented in this thesis was to better understand the nature of these two modes of collective motion. We wanted to know whether both could be present in the same collision. We also wanted to know if the in-plane enhancement was actually due to the rotation of the emitting source. As a preliminary step toward answering these questions, we decided to study the time evolution of a single system in detail. Because of the current limitations inherent in the BUU model employed to describe intermediate energy collisions, we did not investigate the dependence of observables on impact parameter, $\sigma_{nn}$, or the equation of state. Rather, we hoped that in the process of a detailed analysis of a collision with a fixed set of parameters, we could develop techniques which could be of help in

the future when the theoretical underpinnings of the BUU calculations are at a more advanced state.

## 5.10 Initial Conditions Used in the BUU Calculation

In order to investigate the possibility of rotational collective motion establishing an in-plane enhancement in the BUU model, we chose to investigate a 30 MeV/nucleon mass 40 on mass 40 collision on with an impact parameter of 2 fm.[Baur91] As we shall see, this beam energy and impact parameter leads to the formation of a residue with a large angular momentum, a natural starting place to look for the influence of rotational motion on the distribution of emitted particles. The compressibility used was $K = 380$ MeV, and the in-medium n-n cross section was taken as half the free value. This parameterization is within the range of parameters explored by other researchers.[Moli85b, Bert87, Tsan89, Ogil90, Suli90, Xu90] The dependence of our results on $K$ should not be strong since the beam energy is insufficient to take the system very far away for normal nuclear matter density. A time step of 0.5 fm/c was used in the integration, and the results were recorded in 15 fm/c intervals up to 600 fm/c.

## 5.11 Results of the BUU Calculation 1: The Residue

In this section we will examine the time development of the residue formed during the collision. In figs. 5.8 and 5.9 we show snapshots of the coordinate space density projected onto the x-z and x-y planes. After 30 fm/c, a deformed compound system is apparent which rotates about the y axis.

In order to study this system, it is necessary to distinguish between particles which

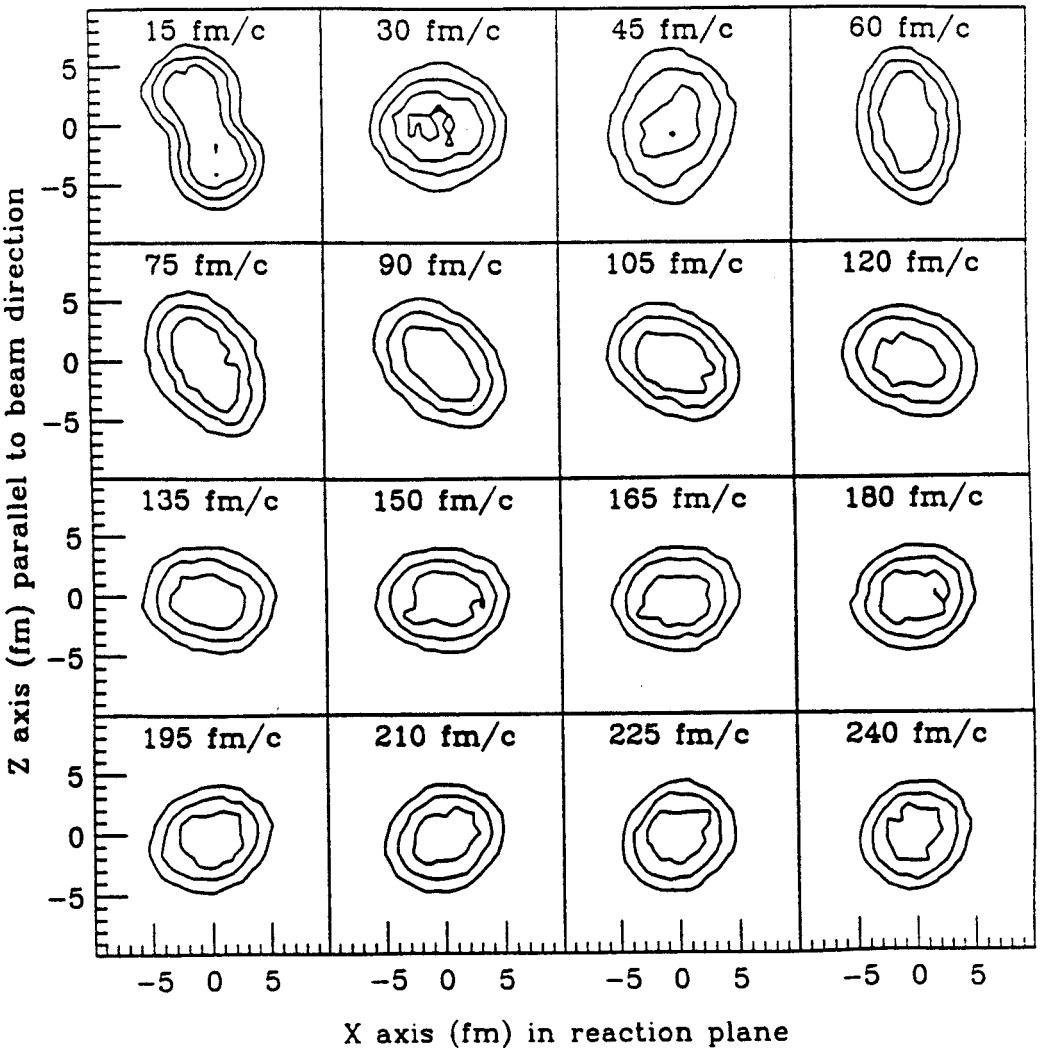


Figure 5.8: Coordinate space density distribution projected on to the x-z plane. The projectile begins on the lower right hand region in the 15 fm/c snapshot, offset in the positive x direction by convention.

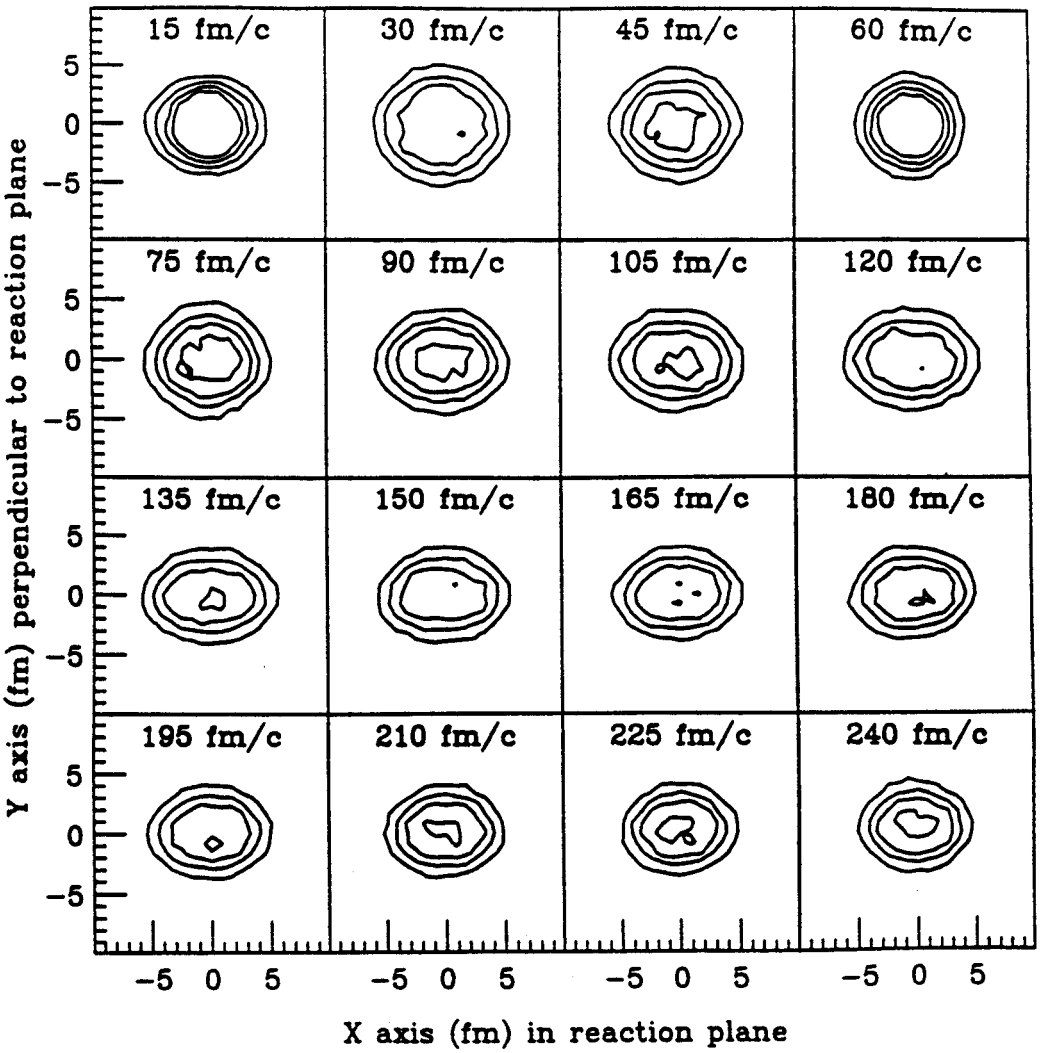


Figure 5.9: Coordinate space density distribution projected on to the x-y plane.

have evaporated and those still bound in the residue. We show in Figure 5.10 the number density as a function of the distance from the c.m. at 150 fm/c. We assumed that all particles with space coordinates lying inside a region of local density greater than $\frac{1}{10}\rho_o$ were members of the residue. Since the residue is created by the nuclear mean-field generated from the contributions of all of the separate ensembles in the calculation, the local density used to test for inclusion in the residue was the ensemble averaged density.

For each quantity that follows, error bars were obtained by performing the calculation (for all the parallel ensembles) 4 times, finding the mean value of the quantity and then the uncertainty in the mean from the variences.

Following Garcias et el.,[Garc91] we use Hill-Wheeler coordinates to study the changes in shape of the residue. The lengths of the semi-major axes were parameterized using the square roots of the eigenvalues of the $3 \times 3$ matrix $\sum_{n=1}^{n=N} x_i^n x_j^n$ where N is the number of test particles in the residue. The result is shown in Figure 5.11 with time intervals of 15 fm/c separating the small circles. There are strong oscillations from prolate-like to more oblate shapes, with the largest prolate deformation in the t=60 fm/c snapshot. If the beam energy had been higher or the impact parameter larger, the system could have proceeded to fission at this stage. Instead, the attractive mean-field pulls the nucleons back toward the c.m. leading to a series of oscillations with smaller and smaller amplitudes. These shape oscillations can be most clearly seen in the upper panel of Figure 5.12 which displays gamma as a function of time. Garcias et al. did not encounter these oscillations in their BUU calculations because they started with an equilibrated spherical system.

Next we turn to a consideration of the angular momentum. In the n-n collisions, angular momentum is only conserved on average in the nucleon-nucleon system. This is not a problem, however, since the collective rotation of the residue is around the

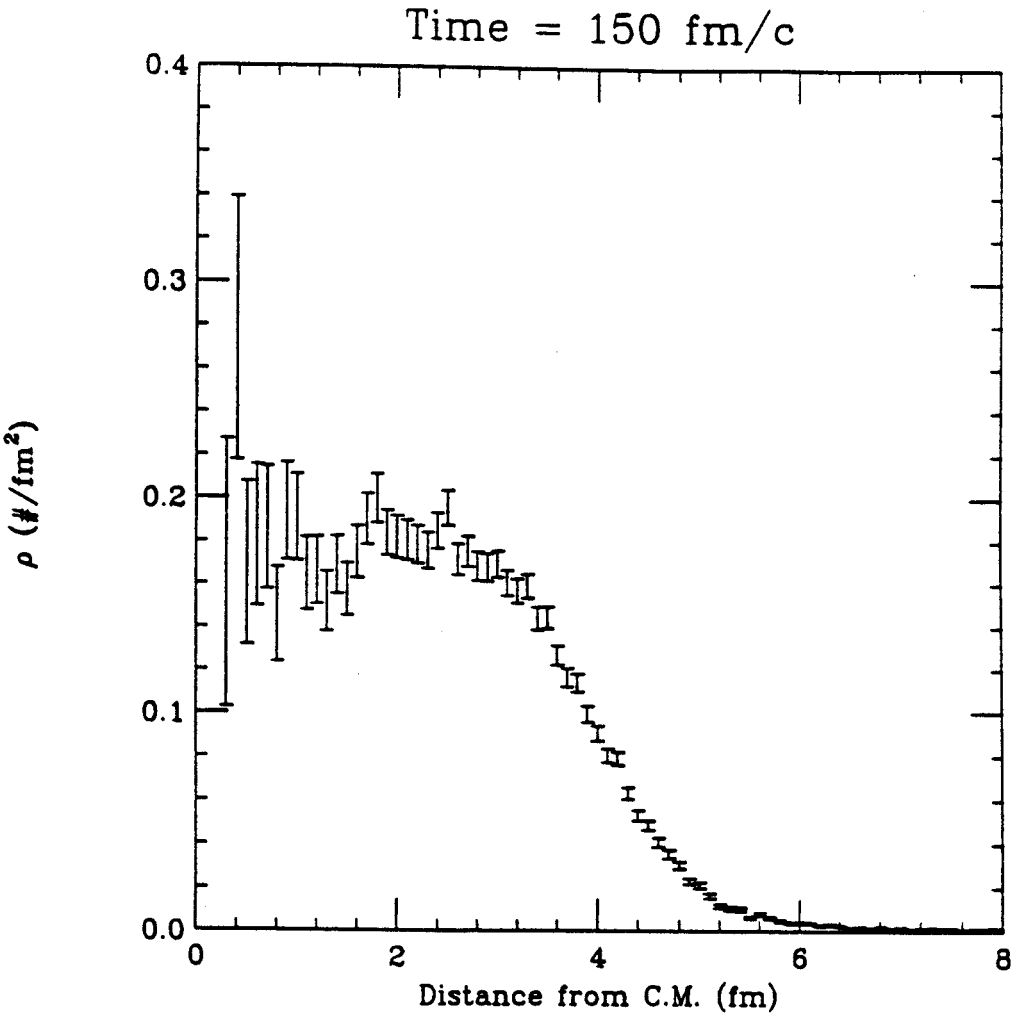


Figure 5.10: Number density as a function of distance from the center of mass in coordinate space at t=150 fm/c for one BUU calculation. The error bars in this figure are taken from the square root of the number of counts.

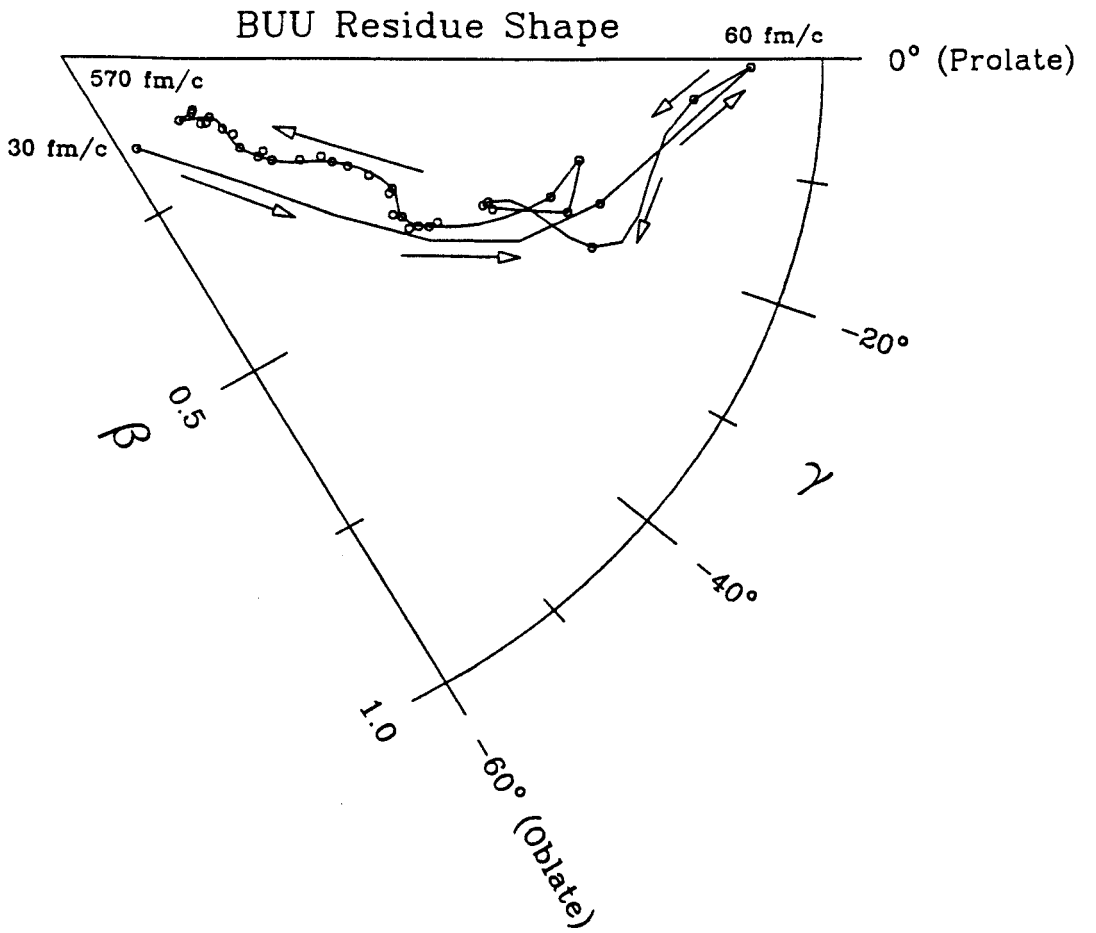


Figure 5.11: Evolution of BUU residue in Hill-Wheeler coordinate space. The snapshots, denoted by small circles, are plotted from t=30 fm/c to t=570 fm/c in 15 fm/c intervals. The line is drawn to guide the eye.

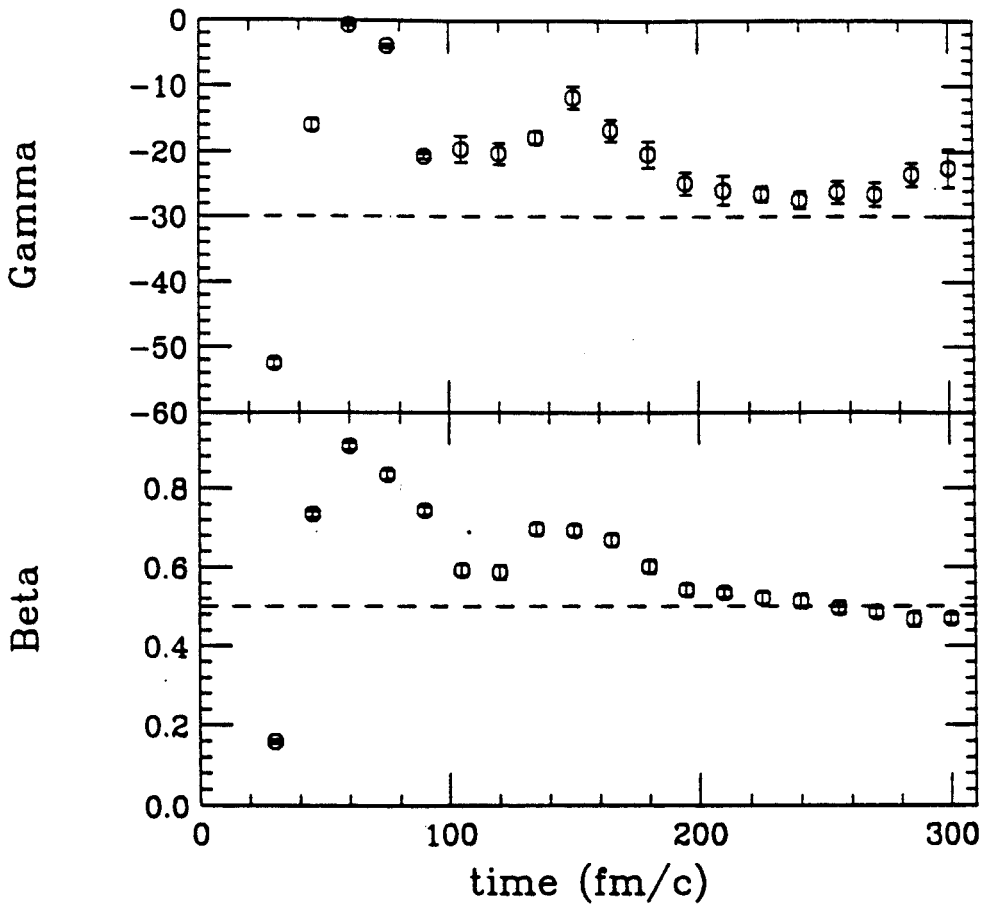


Figure 5.12: Hill-Wheeler coordinates as a function of time.

center of mass created by the mean-field. The angular momentum of the residue is denoted by circles in Figure 5.13. Beginning with $\approx 40\hbar$ the residue loses angular momentum at a decreasing rate with time. If we take the emitted particles to be all those found at a distance greater than 10 fm from the c.m., we see that all the angular momentum lost by the residue is accounted for in the emitted particles (denoted by squares). The angular momentum of the residue is always less than the maximum allowable liquid drop angular momentum shown in Figure 5.1.

## 5.12 Results of the BUU Calculation 2: Emitted Nucleons

In Figure 5.14 we show the change in the populations of residue nucleons and emitted nucleons with time. The total number of nucleons is slightly less than $A_{proj} + A_{targ}$ because some nucleons can be less than 10 fm away from the center of mass yet not be bound in the residue. The population of emitted nucleons with c.m. energies greater than 25 MeV saturates early in the collision. This behavior can be seen more clearly in Figure 5.15, which shows the emission rate for various groups of particles. Nucleons with c.m. kinetic energies in excess of 25 MeV come primarily from the earlier stages of the reaction. For reference, the energy of the projectile and target in the center of mass is $\approx 7.5$ MeV/nucleon. It is the addition of the intrinsic Fermi energy on top of the beam energy that allows the production of these high energy nucleons.

If we carefully examine the final distribution of nucleons emitted from the simulated collisions, we find both of the patterns of collective motion we located in the data during the the last chapter. In Figure 5.16 we present the anisotropy parameters extracted from the BUU calculation after 570 fm/c using all emitted nucleons. Since the initial orientation of the reaction plane is known for the simulation, there is no

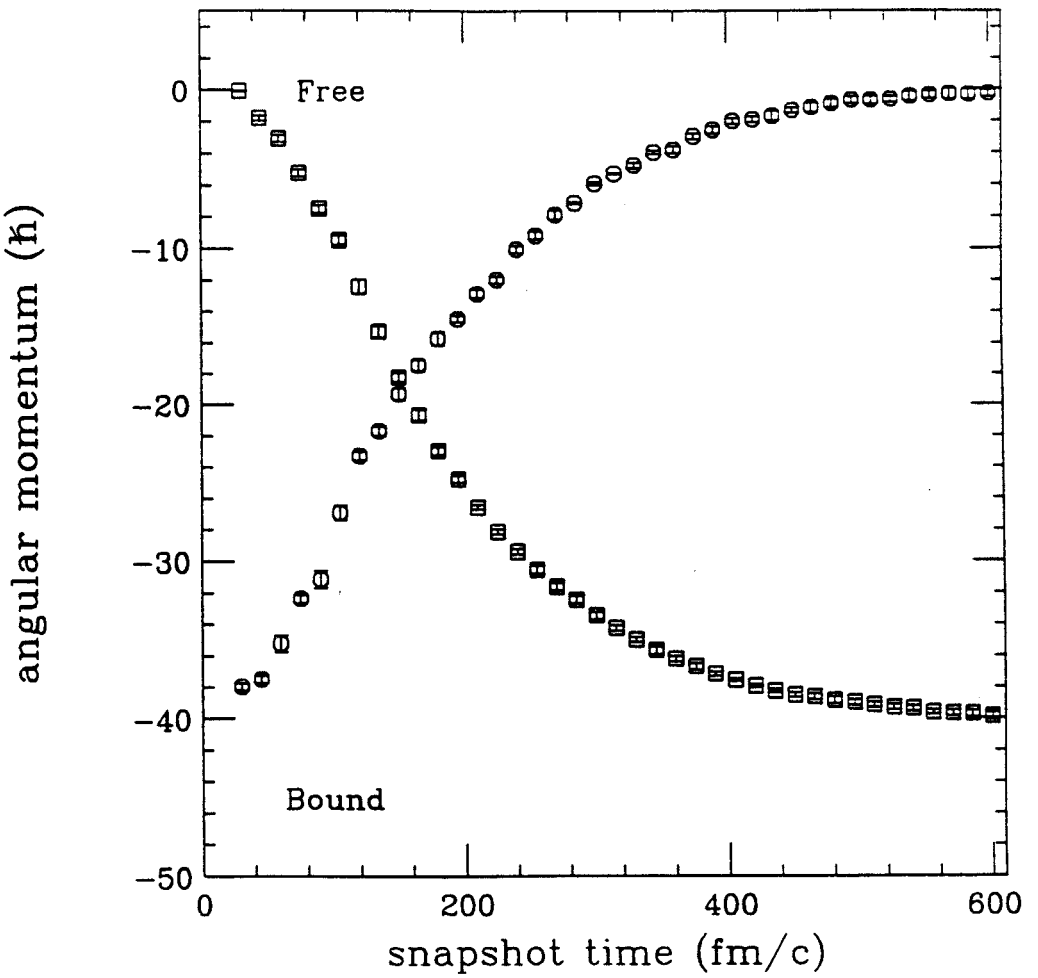


Figure 5.13: Angular momentum in the BUU calculation as a function of time

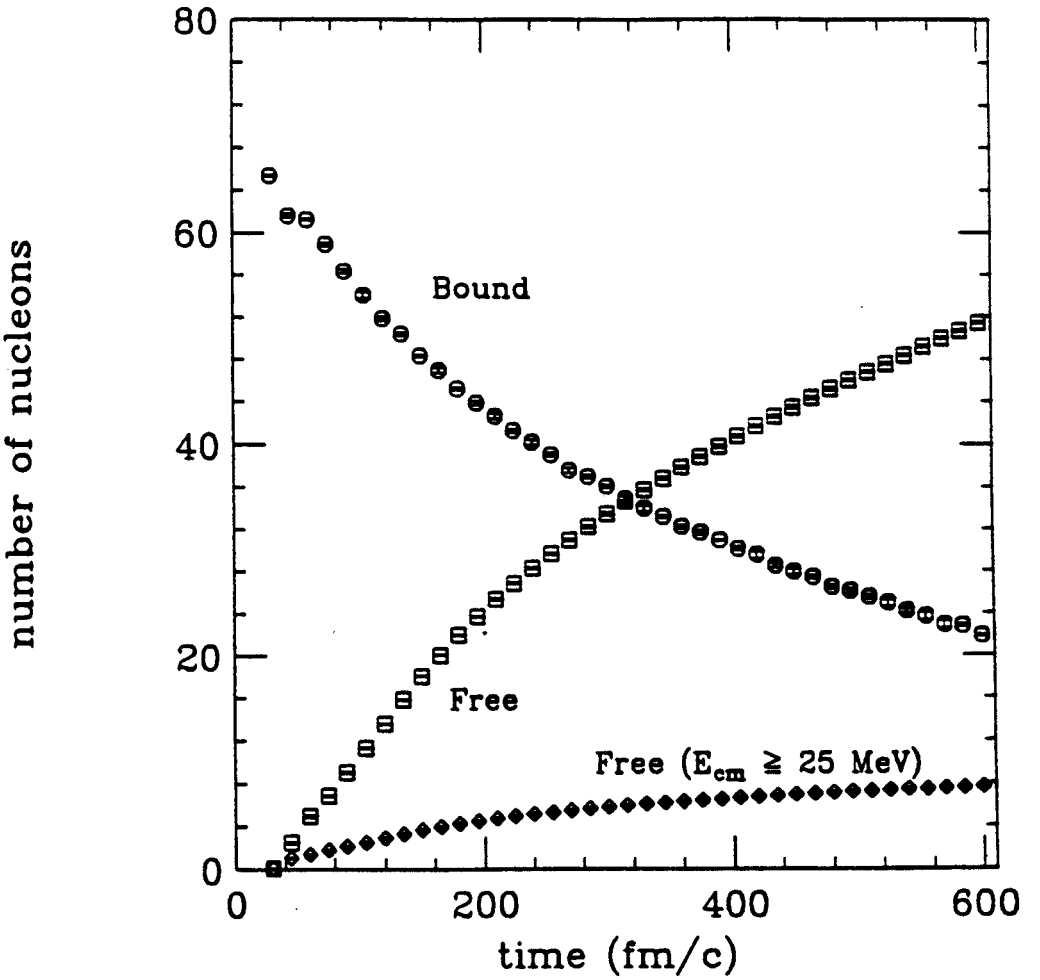


Figure 5.14: The number of nucleons in the residue (circles) and the number of nucleons emitted (squares) is shown as a function of time. Those emitted with a center of mass energy greater than 25 MeV are denoted by diamonds.

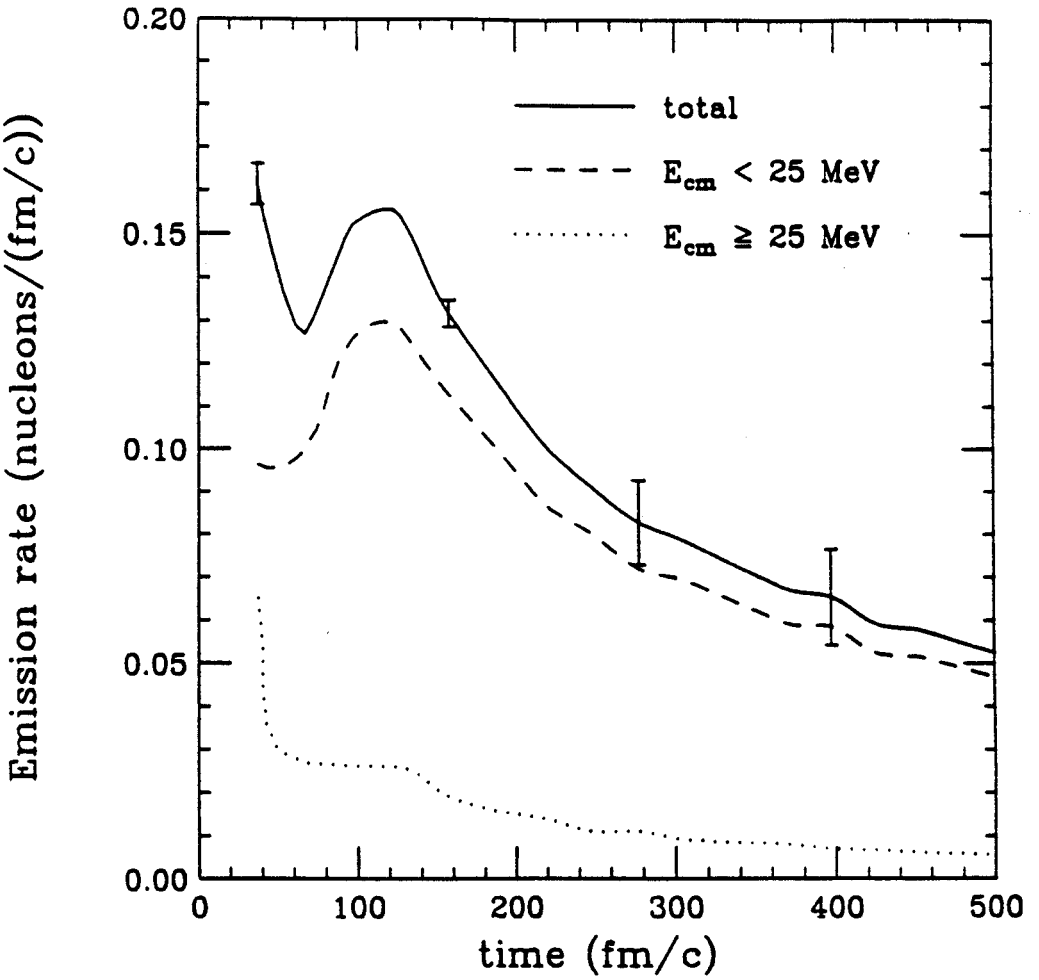


Figure 5.15: Emission rate of nucleons with various energies in the center of mass frame of reference. The size of the uncertainties are shown by the error bars on the total emission rate.

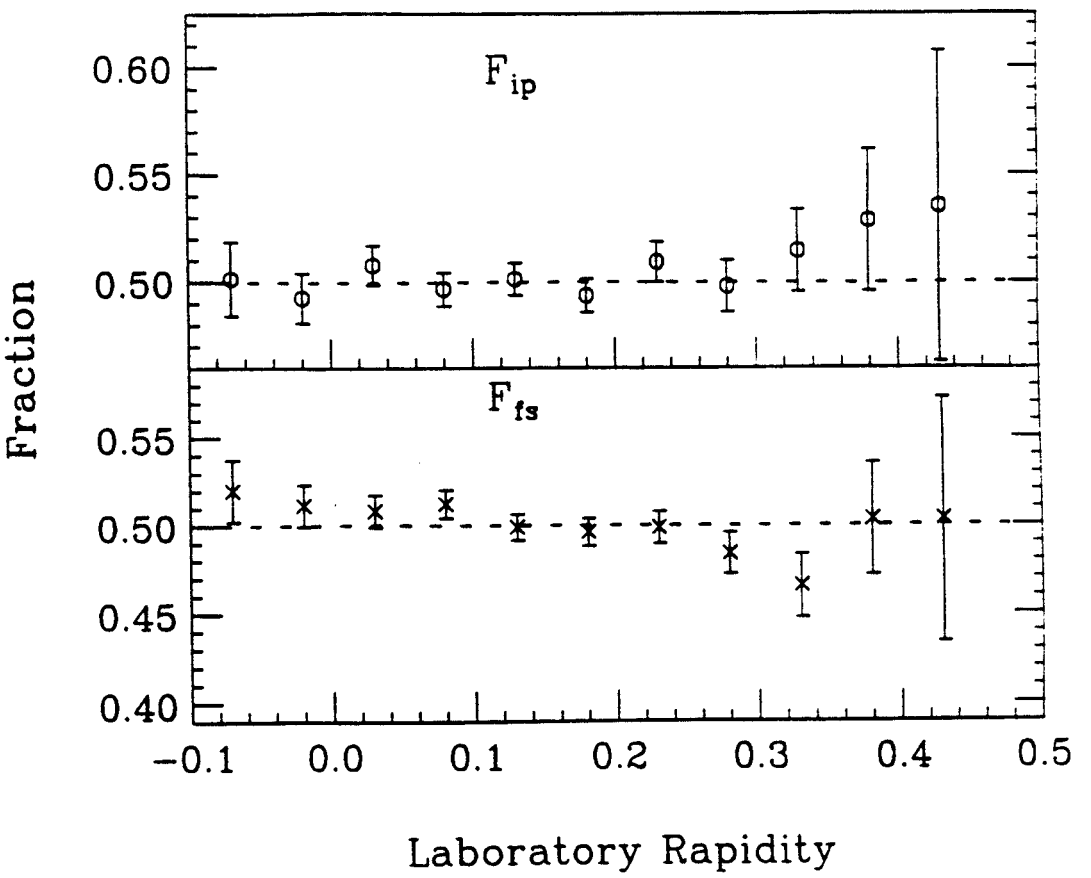


Figure 5.16: Anisotropy fractions 570 fm/c after the beginning of the collision

need to invoke the techniques of chap. 3 to find the reaction plane. As a convention, we place the positive x axis on the side of the reaction plane originally containing the projectile. This will give $F_{fs}$ a negative slope at mid-rapidity ($y = .13$) if the scattering is attractive, as is clearly the case for this system. The fraction of particle in the reaction plane, $F_{ip}$, formulated to be sensitive to rotational collective motion, shows no significant deviation from isotropy. However, if we demand that the nucleons considered have $E_{c.m.} \geq 25$ MeV, then we can find an in-plane enhancement as shown in the upper panel in Figure 5.17. The in-plane enhancement shows some sign of peaking near mid-rapidity, but conclusions about the rapidity dependence are suspect due to the limited statistics available. Note that the flow shown previously in the bottom panel of Figure 5.16 disappears due to the energy threshold imposed in Figure 5.17. This is a indication that the two types of anisotropies have different causes.

Both anisotropies can be seen more convincingly if we combine the data for the different rapidity bins. For the in-plane enhancement, we can sum over all rapidities before calculating $F_{ip}$ to increase the statistics. For the flow we introduce a new parameter, $\Delta F_{fs}$, the difference between $F_{fs}$ in the forward and backward directions in the c.m. frame of reference. The new parameter is negative if the flow is attractive and positive if the flow is repulsive.

In figs. 5.18 and 5.19 we display snapshots of the evolving anisotropy parameters as a function of time. The largest anisotropies occur early in the collision, but a clear signature of flow is present in the end for the ungated data, while a significant in-plane enhancement is present for nucleons with $E_{c.m.} \geq 25$ MeV.

The c.m. energy dependence of the azimuthal anisotropies can be more closely examined by filtering the emitted particles through an energy window before calculating the parameters. A set of 5 MeV wide windows was used to create the results

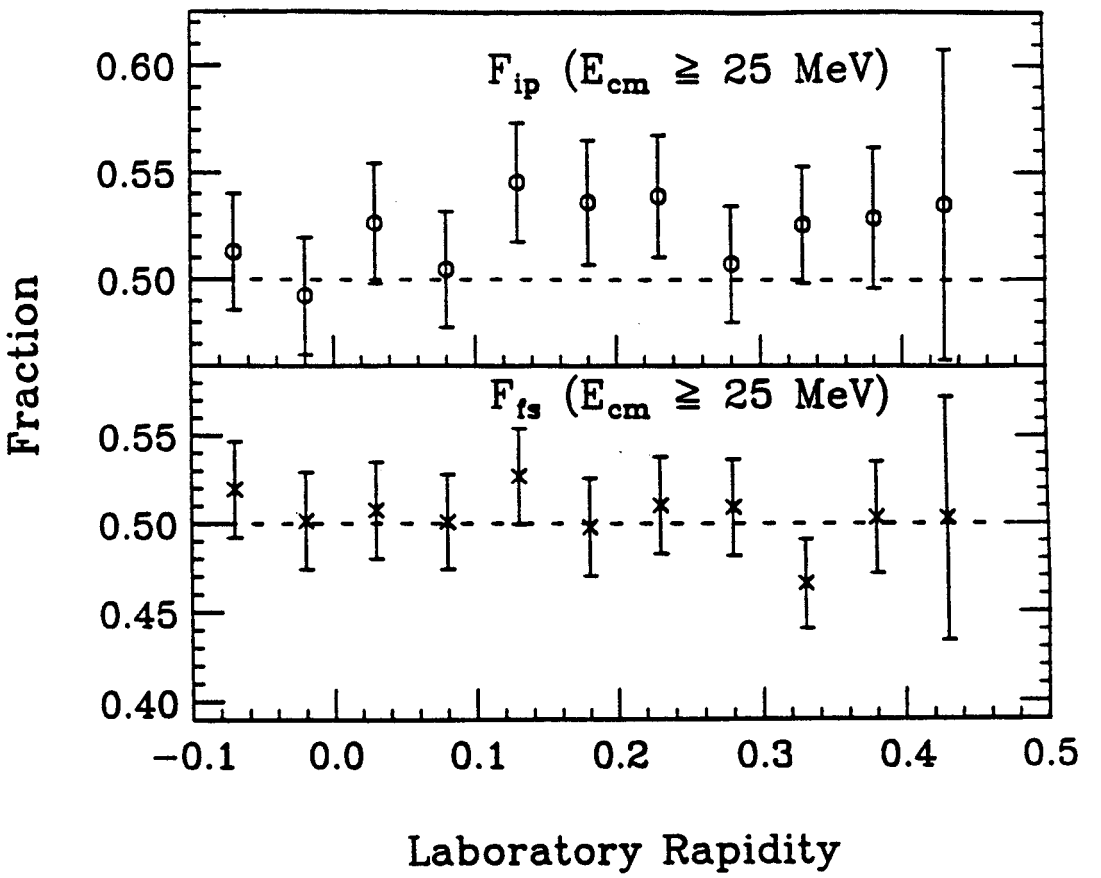


Figure 5.17: Anisotropy fractions 570 fm/c after the beginning of the collision using a 25 MeV low energy threshold

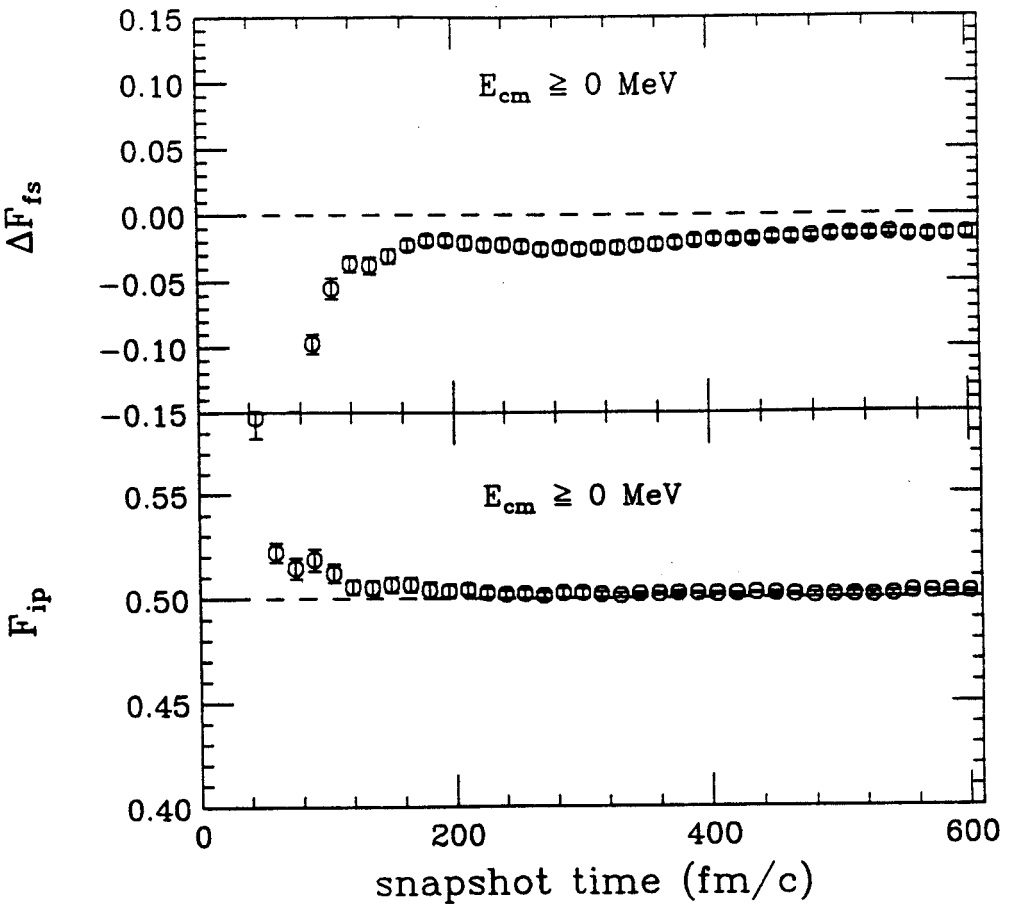


Figure 5.18: Snapshots of the anisotropy fractions as a function of time. The new parameter in the top panel is designed to be sensitive to flow and is described further in the text. The negative value of $\Delta F_{fs}$ late in the time development of the system is a signature of flow.

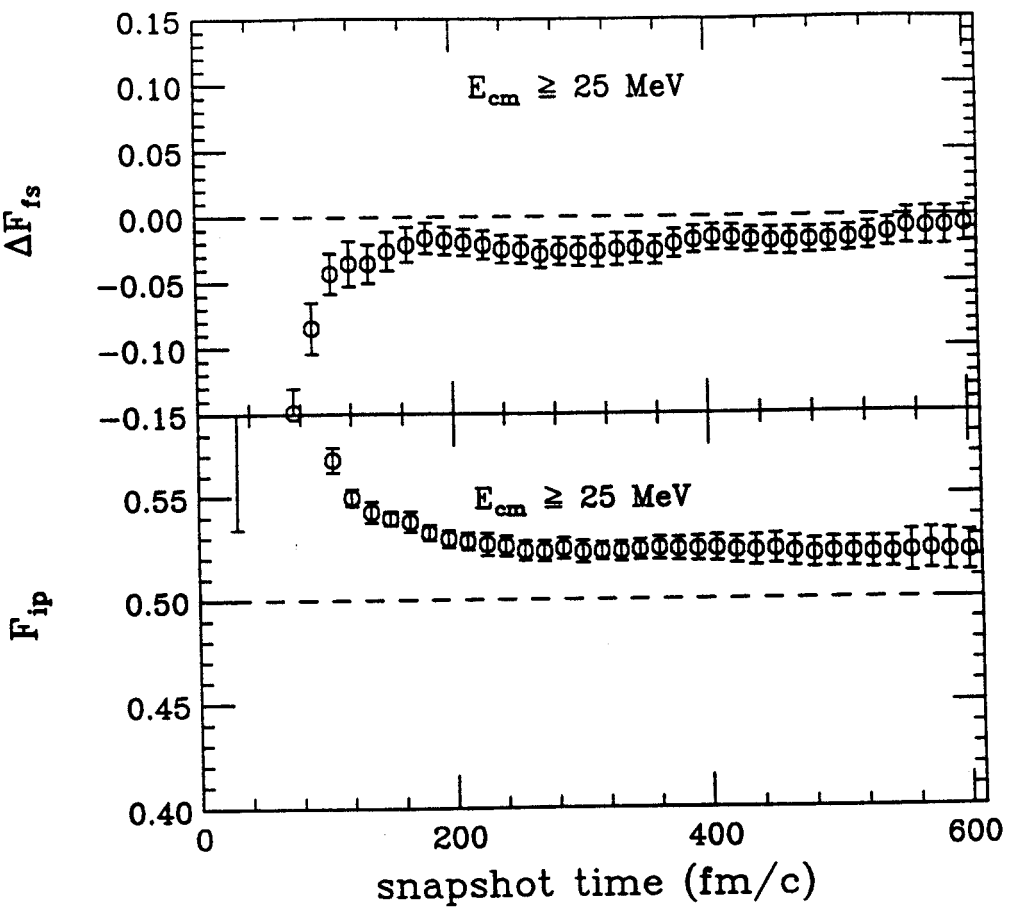


Figure 5.19: Snapshots of the anisotropy fractions as a function of time for nucleons with at least 25 MeV/nucleon.

shown in Figure 5.20. The in-plane enhancement increased with the energy in the center of the window, but there is some indication that the flow is strongest for energies around 15 to 20 MeV. This is another indication that the two anisotropies are created by different physical processes.

Further study shows that the smooth evolution of the anisotropy with time indicated by figs. 5.18 and 5.19 is deceptive. If we look at the anisotropy parameters for nucleons emitted within 15 fm/c time windows rather than all of the nucleons emitted up to a specific time, we find that the anisotropies vary strongly with time. We show the asymmetry parameters for particles emitted in time windows as a function of the center of the window in figs. 5.21 and 5.22. The flow can actually change directions as the system evolves, but the strongest negative flow is seen in few tens of fm/c. The oscillations in $\Delta F_{fs}$ and $F_{ip}$ in figs. 5.21 and 5.22 seem to be correlated with the shape oscillations displayed in Figure 5.12. It is important to note that, even though $F_{ip}$ oscillates in Figure 5.22, it indicates an in-plane enhancement for almost all time windows. This suggests that although the flow seen at the end of the calculation is created in the early stages of the collision, the in-plane enhancement is created by contributions from over the entire time of the residue disassembly.

This hypothesis is confirmed in Figure 5.23 which shows the final anisotropy fractions (t=540 fm/c) with and without including **promptly emitted particles** (PEP), taken to be particles emitted in the first 60 fm/c. After 60 fm/c, approximately the first 5 nucleons have been emitted. The data denoted by circles include all emitted nucleons, and demonstrate the c.m. energy dependence already noted, i.e. the in-plane enhancement increases with energy, but the flow appears to be stronger for particles near 15 MeV in energy. The data denoted by crosses do not include particles emitted in the first 60 fm/c, and show no negative flow at all. The flow in this BUU calculation is thus due to the very first particles emitted in the collisions. On

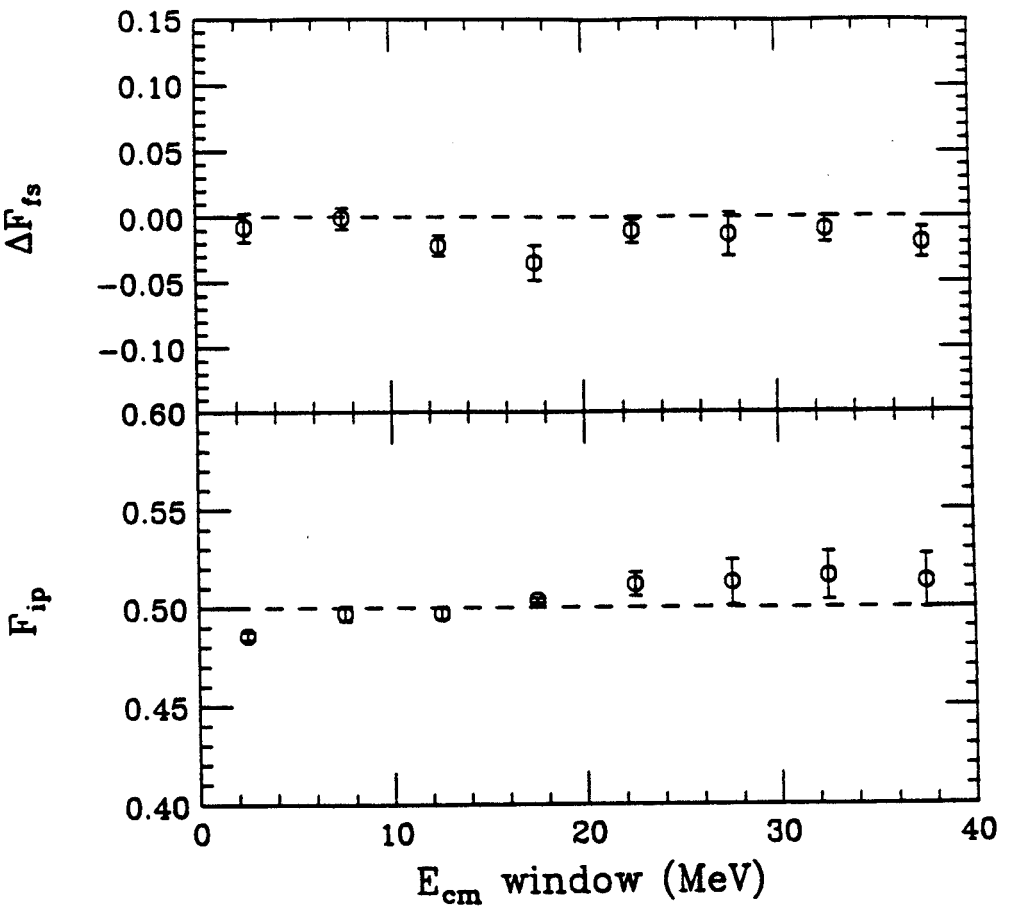


Figure 5.20: Anisotropy fractions in 5 MeV wide windows as a function of the energy in the center of the window.

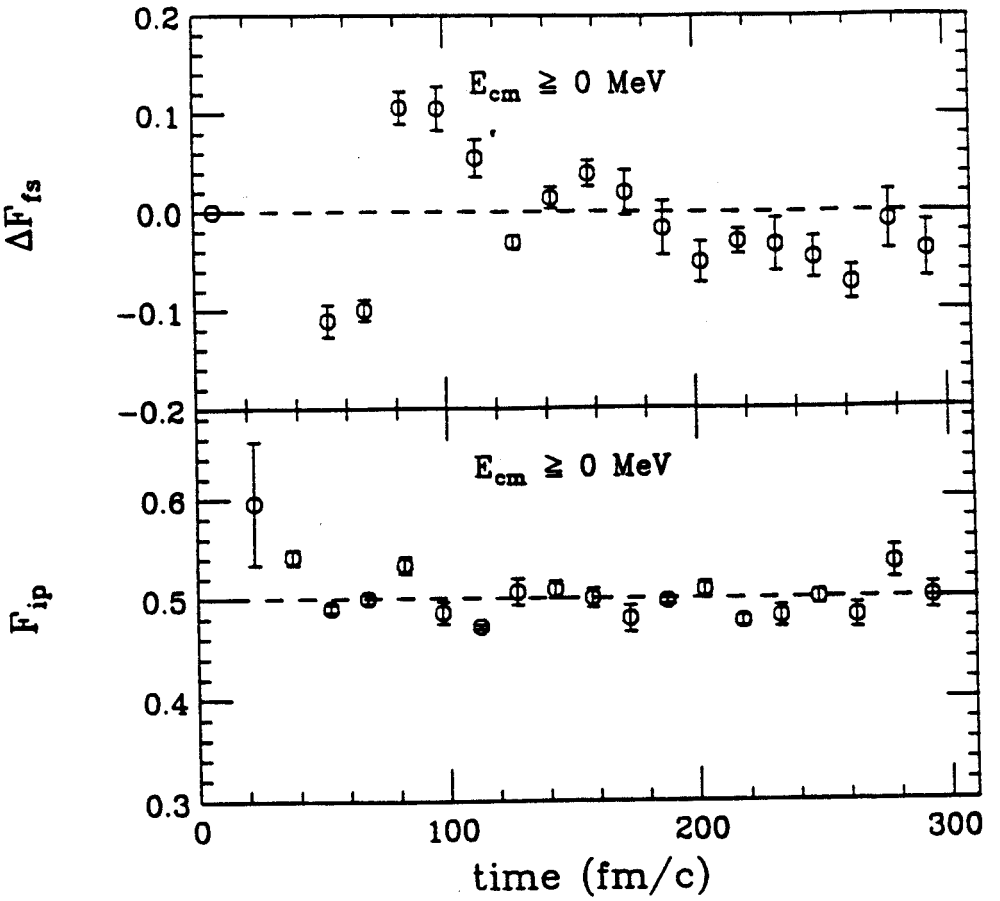


Figure 5.21: Anisotropy fractions for nucleons emitted in specific time windows.

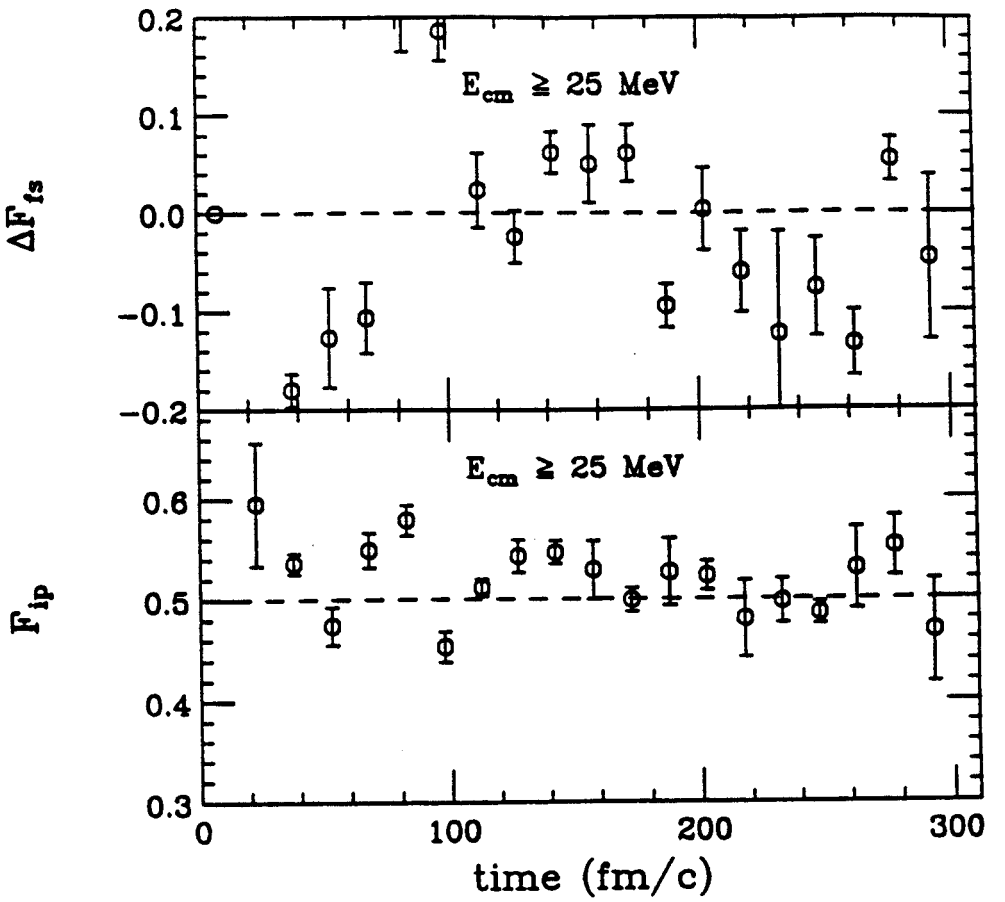


Figure 5.22: Anisotropy fractions for nucleons emitted in specific time windows with c.m. energies $\geq 25$ MeV.

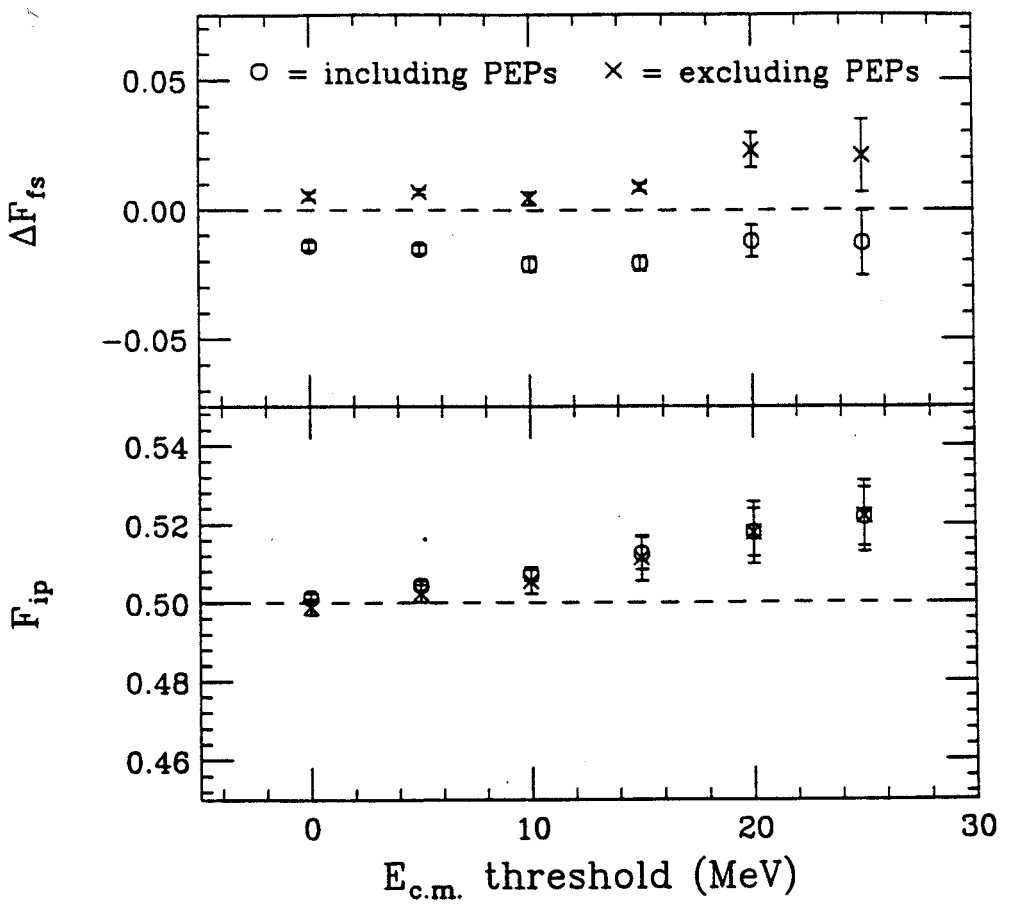


Figure 5.23: Final anisotropy fractions calculated with and without including nucleons emitted in the first 60 fm/c (PEPs).

the other hand, removing the PEPs from the sample has practically no effect on the in-plane enhancement.

Because of Pauli blocking of collisions, some nucleons of the projectile can pass directly through the target unscattered. The addition of the intrinsic Fermi motion on top of the projectile motion allows particles to directly escape the mean-field of the target. These unscattered particles should show the effect of mean-field deflection more clearly than particles whose motions have been randomized by successive n-n collisions. Early models of promptly emitted particles based on simple geometrical concepts predicted that such **Fermi Jets** will be aligned with the axis joining the center of the projectile and target when they first contact.[Robe79, Bond79, Bond80] The jets are most favored along this line because the addition of the projectile velocity and Fermi velocity vectors have the largest radial component (in the c.m. frame) in this configuration, creating the most favorable conditions for the jetted nucleons to escape the mean-field. Since the system is symmetric, there should also be a jet of target nucleons through the projectile in this picture.

The simple geometry and assumptions used in the Fermi jets picture have been replaced by more detailed dynamical calculations which include absorption and scattering of potential jets.[Rand87] A full microscopic model like BUU that contains Fermi momentum, the mean-field, n-n scattering, and Pauli blocking automatically contains all of these prompt emission processes. In Figure 5.24 we show the momentum distribution projected on the $P_x - P_z$ plane for particles emitted in the first 60 fm/c. Flow is clearly present in the enhanced emission toward the negative $P_x$ side of the reaction plane in the forward direction and toward the positive side in the backward direction. The dashed circle has a radius of 120 MeV/c, approximately the c.m. momentum of the nucleons (neglecting the Fermi momentum). The dashed line is at the angle with respect to the Z axis made by the centers of the two nuclei when

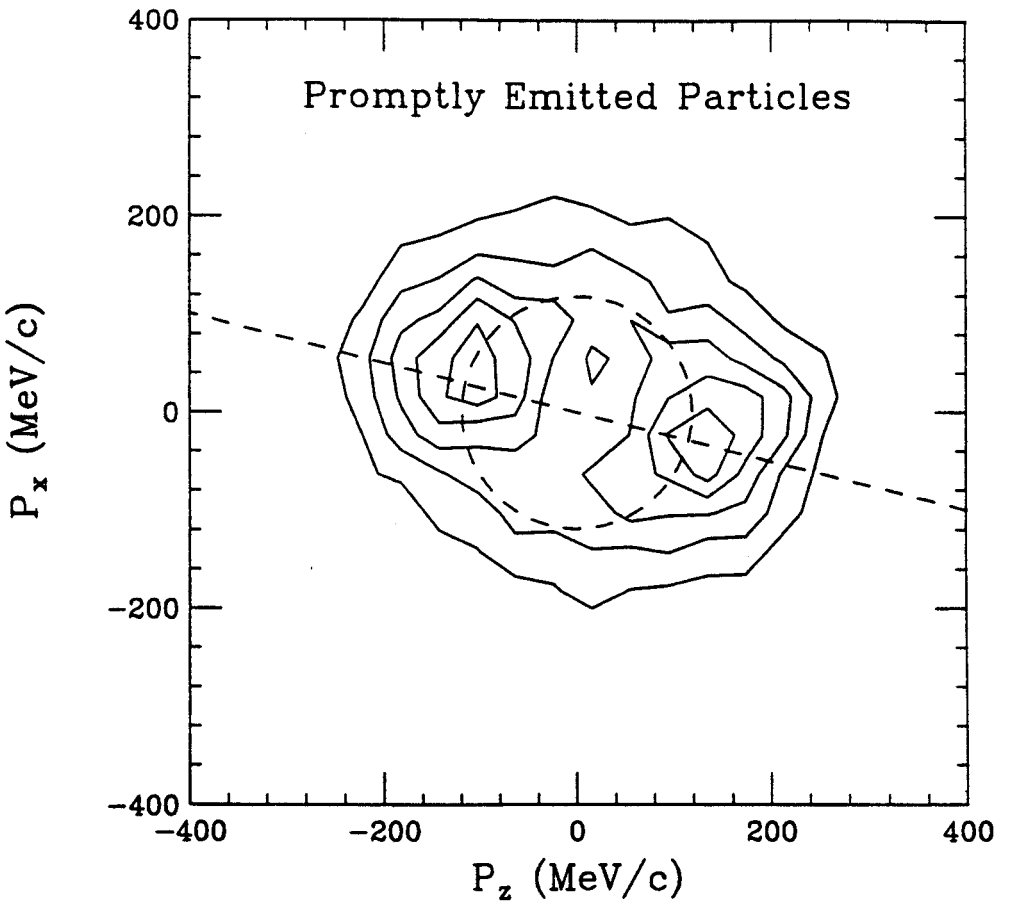


Figure 5.24: Momentum distribution of particles emitted in the first 60 fm/c projected onto the reaction plane in the c.m. frame of reference. The contribution from Fermi jets would be strongest where the dashed circle and line intersect.

they first contact. There is enhanced emission of particles with the c.m. beam velocity deflected by the angle joining the centers of the two nuclei at their first contact, resembling the proposed Fermi jet phenomena.

## 5.13 Conclusions

In this chapter we have seen that a rotating spherical source cannot reproduce the observed energy trends of the in-plane enhancement in our Ar+V data. Powerful deformations and shape oscillations, coupled with the fact that the angular momentum of the residue is decreasing with time cast doubt on the possibility of assigning any physical meaning to $r\omega$ parameters extracted using the rotating sphere model. Our initial explorations using BUU simulations show that the in-plane enhancement contains contributions from early and later stages of the disassembly of the compound system, but that the negative flow is established in the early stages of the collision by particles that appear to have been emitted without scattering. Both forms of collective motion can be present in the same system, but they reflect its development at different times.

## 5.14 Improvements to the Model

The BUU model we used was limited in several ways. For example, the Coulomb force was neglected. Versions of the BUU code have been created which include the Coulomb force, and the predicted collective flow is altered when compared with calculations ignoring the Coulomb force.[Tsan89] As noted in the introduction, the inclusion of momentum dependent interactions modifies the effects of the compressibility in the nuclear equation of state.[Gale87] Momentum dependent interactions were not included in our code. Techniques for improving energy conservation in the

numerical integration have also been developed.[Lenk89] In the future, more detailed studies of the impact parameter, beam energy, and equation of state dependence of the collective motion will be carried out using BUU codes incorporating the improvements outlined above.

A serious impediment to comparisons between BUU and experimental results involves the treatment of clusters of nucleons. One of the most challenging features of intermediate energy heavy-ion collisions is the wide range of fragment masses produced. It is therefore difficult to evaluate the effects of detector acceptance on the output of BUU calculations since the acceptance is wholly dependent on the size of a given fragment. The BUU code described above does not produce fragments because fragments result from density fluctuations, and replacing nucleons by a smooth distribution of test particles tends to smooth out fluctuations. Procedures for handling fluctuations in BUU are currently under development.[Baur87, Bert88]

Another approach to microscopic calculations of a nuclear reaction is to specify a n-n interaction potential explicitly and solve the classical equations of motion for each individual nucleon. This **molecular dynamics** model has recently been extended to include quantum effects by Peilert et al.[Peil89] Since molecular dynamics calculations alow nucleons to cluster into bound fragments, they can potentially supply much more realistic predictions of observables in heavy-ion collisions than simple mean-field theories.

# Chapter 6

# Flow Analysis of Peripheral Collisions

## 6.1 Introduction

Several published BUU calculations predict an impact parameter dependence for the attractive flow created in intermediate energy heavy-ion collisions.[Bert87, Tsan89] For example, in Figure 5.7 from the previous chapter, we saw the strongest collective motion occurring for collisions with medium to large impact parameters.[Bert87] Using the $4\pi$ Array, we can characterize the impact parameter of the events by their mid-rapidity charge.[Ogil89a] (See Appendix C.) Using this approach in our original studies[Ogil89b, Ogil89c] of collective motion in 35 MeV/nucleon Ar+V and 50 MeV/nucleon C+C reactions, we found no conclusive evidence for impact parameter dependence within the range of impact parameters examined. A further inspection of the dependence of $F_{ip}$ on the total mid-rapidity charge per event has also revealed no systematic trends. This may in part be because our requirement of at least three identified particles per event biases the event sample towards more central events, removing the correlation between impact parameter and mid-rapidity charge. Another important effect is the changing accuracy of the reaction plane determination. Even if peripheral events have stronger flow than more central events, the observed flow

will be weakened since the lower multiplicity of peripheral events lowers the accuracy of the reaction plane determination.

Another group,[Suli90] however, has reported strong impact parameter dependence of the transverse collective motion for the reverse kinematical system Ar+Al from 25 to 85 MeV/nucleon. It is important to understand the impact parameter dependence of the collective motion in this beam energy regime because it will affect the manner in which the observed collective motion should be compared with microscopic calculations. In this chapter we will present a further analysis of our previously published 50 MeV/nucleon C+C data (the system which showed the strongest collective motion) with a view towards analyzing the most peripheral events. We will summarize some of the difficulties in interpreting collective motion for peripheral events in this beam energy regime, such as contributions from simple sequential decay of deflected projectile fragments. By comparing with data taken with a Au target, we will also be able to assess the influence of momentum conservation, since recoils should be weaker in the heavier system.

In order to determine the reaction plane for low multiplicity peripheral events, we have used projectile-like fragments, which are expected to lie in the reaction plane. Analysis of two previous sets of polarization data suggested that there may be a complex interplay between attractive and repulsive scattering.[Tsan86, Asah87] Observation of the polarization of gamma rays produced by the heavy residue in 20 and 30 MeV/nucleon N induced reactions on a Sm target has shown that the so called **pre-equilibrium** (promptly emitted) light particles are attractively deflected by the nuclear mean field.[Tsan86] However, the polarization of deflected projectile fragments produced in 40 MeV/nucleon N+Au reactions has been interpreted as repulsive projectile scattering.[Asah87] Our observations reported here indicate that, once sequential decay products from the projectile fragment are eliminated from the

analysis, protons in the mid-rapidity region show a directed transverse momentum opposite to that of the projectile fragment, providing a link between the conclusions of the polarization experiments cited above.

## 6.2 Analysis Technique

Velocity spectra for projectile fragments ($Z \geq 3$) in the Forward Array detected in coincidence with protons detected in the Main Ball are shown in Figure 6.1 using A=2Z to approximate the fragment masses. The spectra have been divided into three polar angle bins and normalized by the solid angles of the detectors. Both the C+C and the C+Au reactions produce fragment spectra with pronounced peaks close to the beam velocity.

Using the projectile fragment to determine the reaction plane, a coordinate system for each event was chosen such that the z axis lay along the beam axis and the positive x axis had the same azimuthal angle as the fragment. The momentum distribution of mid-rapidity protons ($y \approx \frac{1}{2}y_{beam}$) detected in the Main Ball is shown in Figure 6.2 projected onto the $P^x$ axis. In order to avoid discontinuities in the momentum distribution due to the granularity of the detector array, the polar and azimuthal angles assigned to the protons were smeared over the angular acceptance of the detectors. The usual procedure for measuring the transverse collective motion in the reaction plane calls for plotting the average of this distribution, $\langle P^x \rangle$, as a function of rapidity.[Dani85] (See also Figure 1.6 in the first chapter.) The average, however, is affected by the detector low energy threshold which carves out a sphere in momentum space centered on the origin and creates the dip observed in the center of the $P^x$ distribution shown in Figure 6.2. (See also Figure 2.7 for a description of the acceptance of the $4\pi$ Array in momentum space.) As a result, the average of the

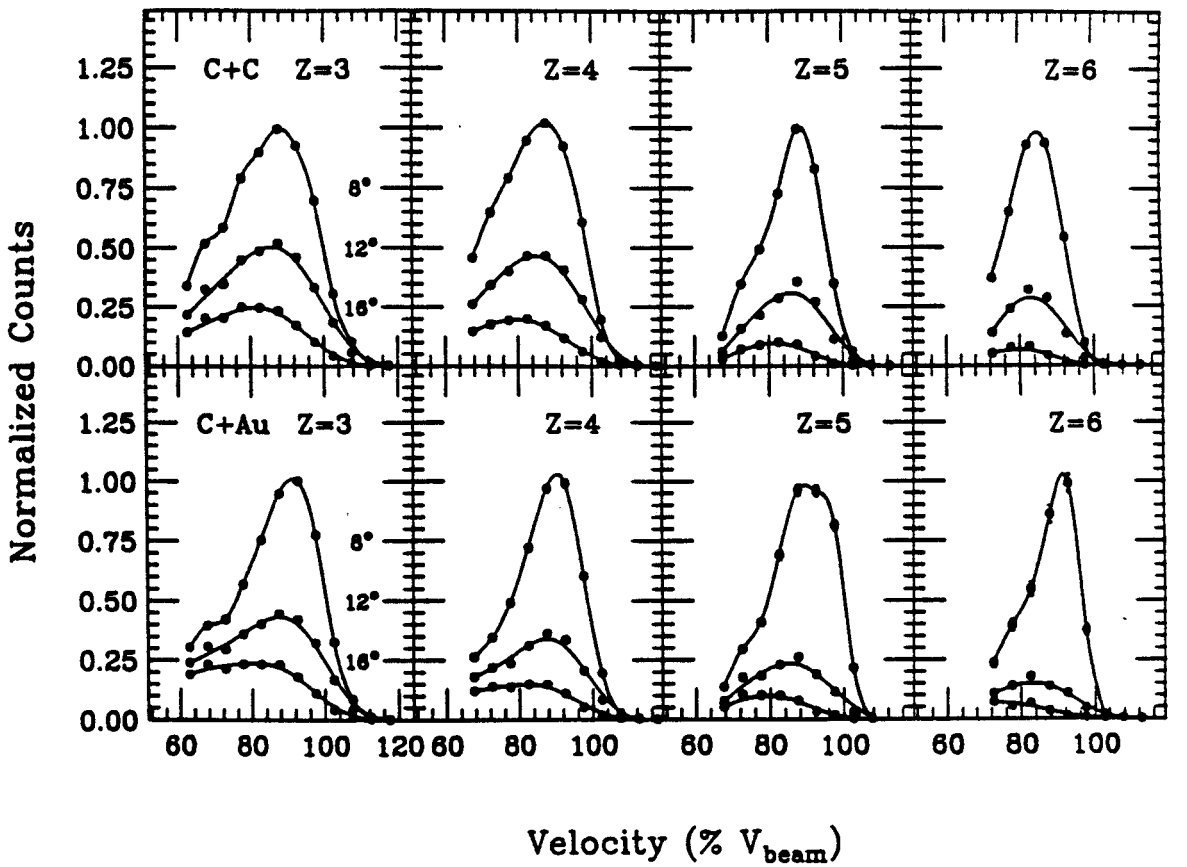


Figure 6.1: Velocity spectra for projectile fragments detected in the Forward Array in coincidence with protons in the Main Ball for 50 MeV/nucleon C+C (upper panels) and C+Au (lower panels).[Wils91]

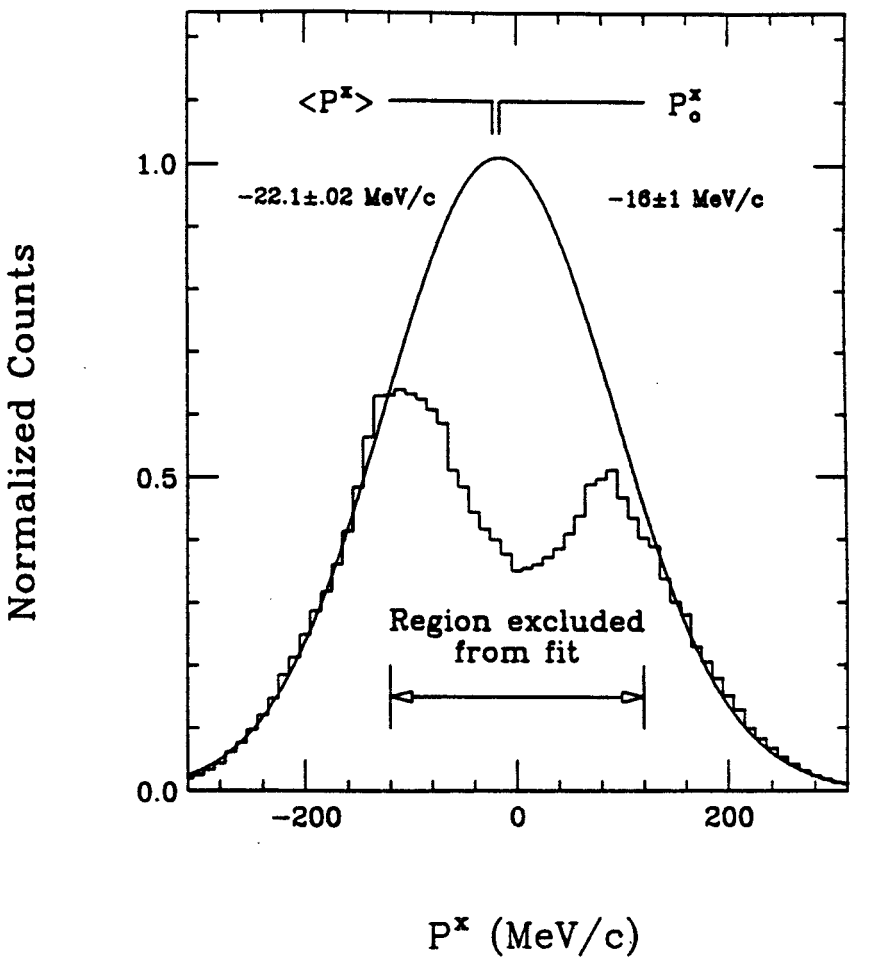


Figure 6.2: Histogram of the transverse momentum distribution projected on to the reaction plane for mid-rapidity protons detected by the Main Ball in C+C reactions. The valley around $P^x \approx 0$ MeV/c is due to detector low energy thresholds and was excluded from the Gaussian fit which is shown as a solid curve.[Wils91]

distribution will overestimate the magnitude of the offset from the origin, depending on the relationship between the distribution's width and the energy threshold of the detectors. In our previous analysis of collective motion observed using the $4\pi$ Array,[Ogil90] this effect was minimized by calculating $\langle \frac{P^x}{P_T} \rangle$ which is significantly less sensitive to energy thresholds than $\langle P^x \rangle$. The overestimation of the offset can be eliminated entirely if the center of the $P^x$ distribution ($P^x_o$) is extracted by fitting a Gaussian to the regions in momentum space unaffected by the energy thresholds. This is the approach we have used in the present work.

## 6.3 Results

The average transverse momenta in the reaction plane resulting from Gaussian fits to the $P^x$ distributions are shown in Figure 6.3 for protons produced in C+C and C+Au reactions. The general trends of the data share two important characteristics with results obtained for peripheral events in 45 MeV/nucleon Ar+Al reactions by Sullivan et al.[Suli90] and 200 MeV/nucleon Au+Fe reactions by Harris et al.[Harr89] As shown in figs. 6.3 and 6.4, the data from all four systems show an offset in the negative $P^x$ direction (away from the projectile fragment), and a positive slope at mid-rapidity. We will investigate the cause of the offset first.

Harris et al. suggested that the offset was a signature of attractive deflection of light particles by the nuclear mean field, but Sullivan et al. associated the effect with momentum conservation, arguing that the negative $\langle P^x \rangle$ of the light particles was balanced by the positive $\langle P^x \rangle$ of the projectile fragments. The latter explanation is in agreement with the results of light particle - projectile fragment coincidence experiments ([Wada90] and references therein) in which the authors found that particles produced in the hot mid-rapidity region were best characterized by a source

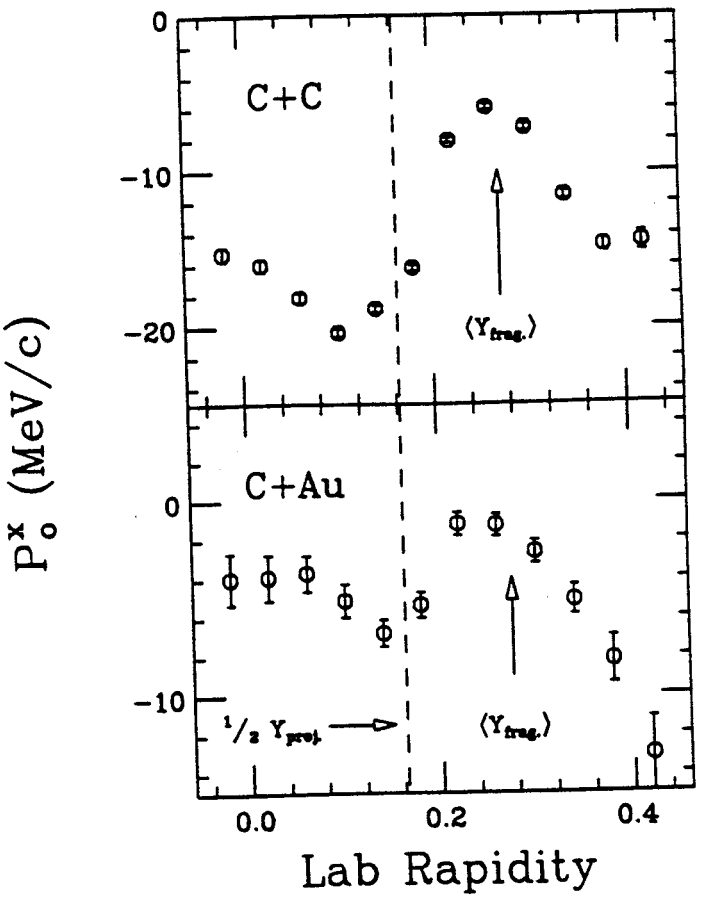


Figure 6.3: The center of the transverse momentum distribution of protons in the reaction plane as a function of rapidity for C+C (upper panel) and C+Au (lower panel). The centers were extracted using single Gaussian fits as described in the previous figure and the error bars reflect the uncertainties of the fits.[Wils91]

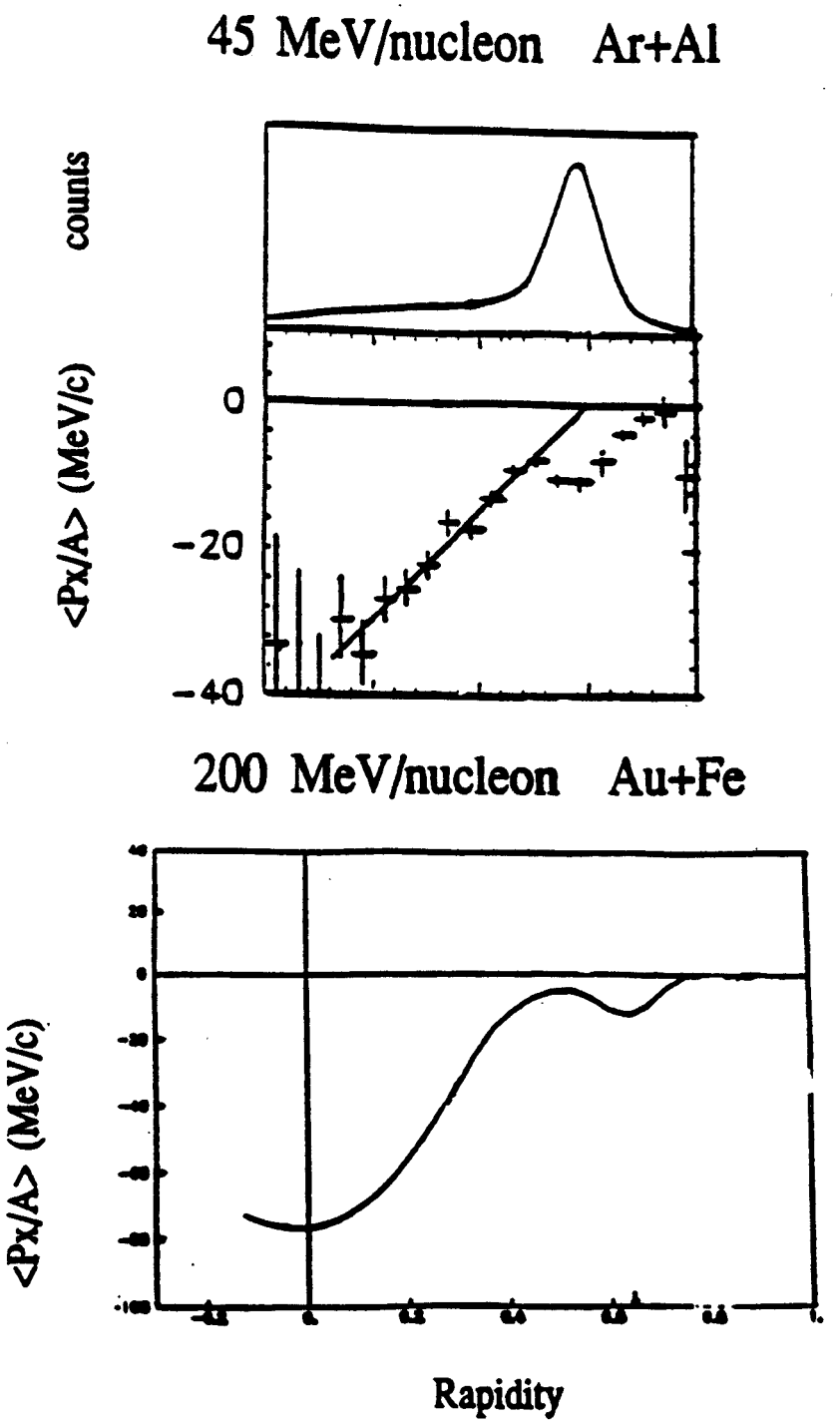


Figure 6.4: The mean transverse momentum distribution of light particles in the reaction plane as a function of rapidity for collisions using 45 and 200 MeV/nucleon projectiles. In the top panel, the reaction plane determination was "dominated" by a projectile fragment.[Suli90] In the bottom panel, the reaction plane was determined using a projectile fragment only.[Harr89]

whose velocity had a recoil component directed away from the projectile fragment. The recoil scenario is most strongly supported by the data of Rabe et al.[Rabe87] for 84 MeV/nucleon O induced reactions on Ni and Au targets. They found enhanced light particle emission on the opposite side of the beam from the projectile fragment, and the enhancement increased linearly with projectile fragment transverse momentum. In our C+C data shown in Figure 6.5, the linear relationship between the mid-rapidity proton $P_o^x$ offset and the transverse momentum of the projectile fragment demonstrates that, in this system, the offset is a recoil due to momentum conservation and not a signature of attractive deflection.

In contrast to the results of Rabe et al.[Rabe87] who found a nearly identical recoil for reactions with the heavy Au target and the lighter Ni target, we show in Figure 6.5 that the correlation between proton and projectile fragment transverse momenta is strongly suppressed for the Au target. This implies that a large percentage of the gold nucleus participated in the recoil, making the $P_o^x$ per proton insensitive to the $P^x$ of the projectile fragment. Our observations are consistent with conclusions drawn from the analysis of peripheral 35 MeV/nucleon O+Ni collisions[Gont88] which supported strong target participation in the emission of intermediate velocity alphas. It is tempting to speculate that the mid-rapidity protons produced in 50 MeV C+Au collisions may be emitted from a localized zone on the target, while the 84 MeV/nucleon O+Au reaction may produce a independently recoiling, detached fireball. The small offset ($\approx -7.0$ MeV/c) in the C+Au proton transverse momentum distribution at mid-rapidity will be discussed at a later point.

The second feature common to the transverse momenta versus rapidity data presented in [Harr89], [Suli90], and the present work is their positive slope at mid-rapidity. In our C+C and C+Au data, the slope at mid-rapidity is caused by the presence of a peak in $P_o^x$ near the projectile fragment rapidity. We expect a contri-

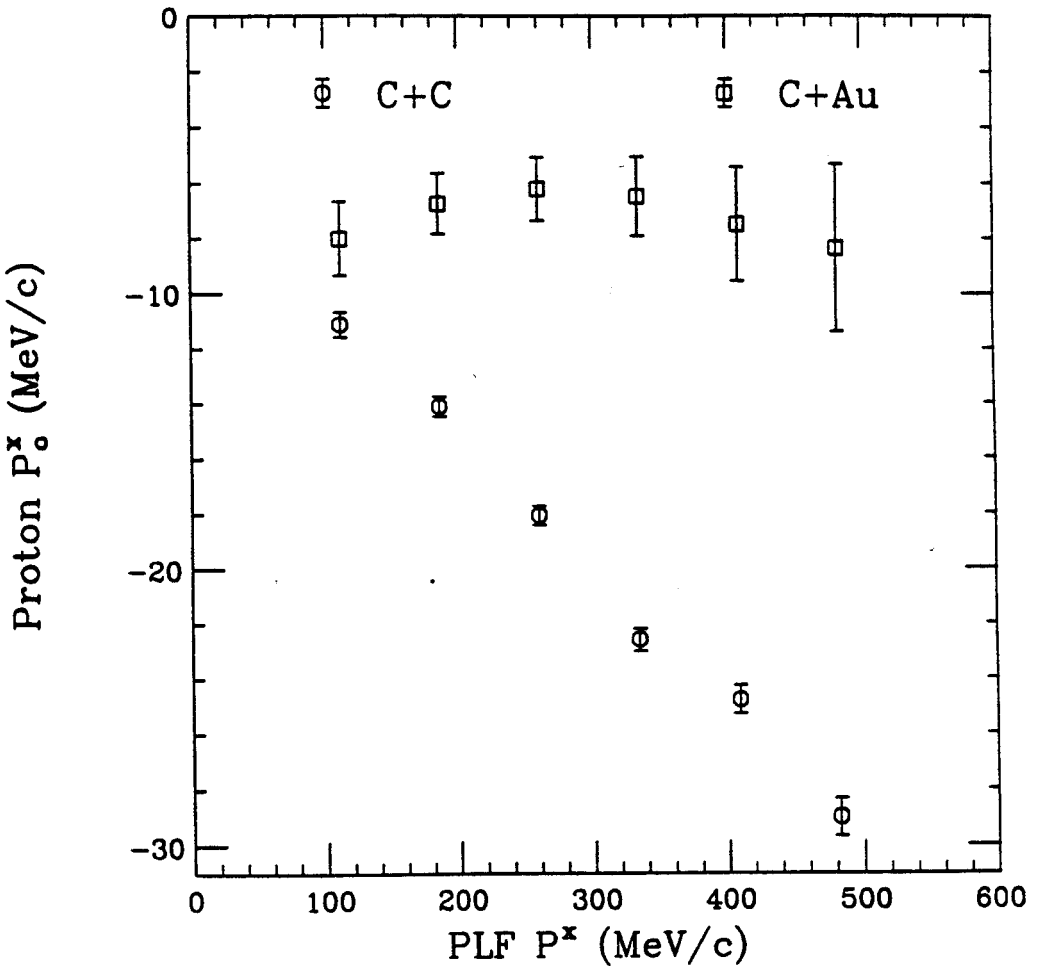


Figure 6.5: The negative offset for the center of the mid-rapidity proton transverse momentum distribution is shown as a function of the transverse momentum of the projectile fragment for C+C (circles) and C+Au (squares) collisions.[Wils91]

bution in this rapidity region from protons emitted sequentially from the projectile fragment after the collision. Therefore, it is necessary to distinguish between the various potential sources of the observed protons.

The energy spectra of protons produced in C+C and C+Au reactions at 40 to 50 MeV/nucleon can be described in terms of three components,[Fox88] although the separation between the components is somewhat indistinct. Two components are associated with the decay of remnants of the original projectile and target. In peripheral collisions, we can apply the term "projectile-like" to the source of protons moving with very nearly the beam velocity. A fit to this source with a Maxwell-Boltzmann energy distribution gives a temperature of 5 to 6 MeV, but this should not be taken as evidence of thermal equilibrium since the dynamic evolution of the source is not known. The temperature parameter is simply a characterization of the final kinetic energy distribution of the emitted particles.

The third component of the energy spectra is well described by a temperature parameter 2 to 3 times larger (hotter) than that used for the projectile-like source and a velocity of about half of the projectile velocity.[Fox88] The nature of this source is the subject of considerable debate. Models invoking an thermal source,[West82] pre-equilibrium emission,[Péte90] a rotating hot spot,[Ho87] and fermi jets[Bond80] have been proposed. For simplicity, we will occasionally refer to these particles as originating from a mid-rapidity source, a reference to the velocity parameter in the Maxwell-Boltzmann fit. The term "source" should be viewed with caution, however, and does not imply a clean separation between these particles and those produced by the projectile fragment since these distributions overlap.

Using these distinctions between the components of the proton energy distributions, we can show that the peak in the proton $P_o^x$ at the fragment rapidity is due to contributions from a projectile-like source. When we examine the proton $P^x$ distribu-

tion at the fragment rapidity we find two distinct components. This is demonstrated in Figure 6.6 in which we display the $P^x$ distribution of protons detected with a parallel velocity equal to that of the average projectile fragment.

The low momentum region which is affected by our energy thresholds is not plotted. In the upper panel of the figure, we have restricted a Gaussian fit to the high $|P^x|$ tails of the momentum distribution, $|P^x| \geq 250 MeV/c$. The lack of agreement between the data and the fit at low $|P^x|$ values indicates the presence of an additional set of protons offset toward the projectile fragment side of the reaction plane at low $|P^x|$.

In the lower panel of Figure 6.6 we have attempted to study both groups of protons using a double Gaussian fit. Although the two distributions, indicated by dashed lines, are not well separated, the general features are of a broad (hot) distribution with a negative $P_o^x$ and a narrower (cooler) distribution with a positive $P_o^x$. Using the relationship $\sigma = \sqrt{m\tau}$, where $\sigma$ is the width of the Gaussian and m is the mass of a proton, temperature parameters of $\tau$ of $\approx$ 10 MeV and $\approx$ 5 MeV are obtained for the two sources. Thus, the peak in $P_o^x$ at the average projectile fragment rapidity is thus produced by a cool momentum distribution on the same side of the beam as the fragments. We can conclude that, even though protons in the Forward Array were excluded from the analysis, we are still getting an important contribution from a projectile-like source.

This interpretation can be tested by examining the shape of the relative momentum distributions. The circles in the upper portion of Figure 6.7 represent the $\Delta P$ distribution between protons detected in the Main Ball and coincident projectile fragments in the Forward Array. We have divided the observed $\Delta P$ of each pair by the $\Delta P_{coul}$ that would be expected due to Coulomb repulsion. The distributions in the upper panels were then divided by random distributions created by pairing protons with

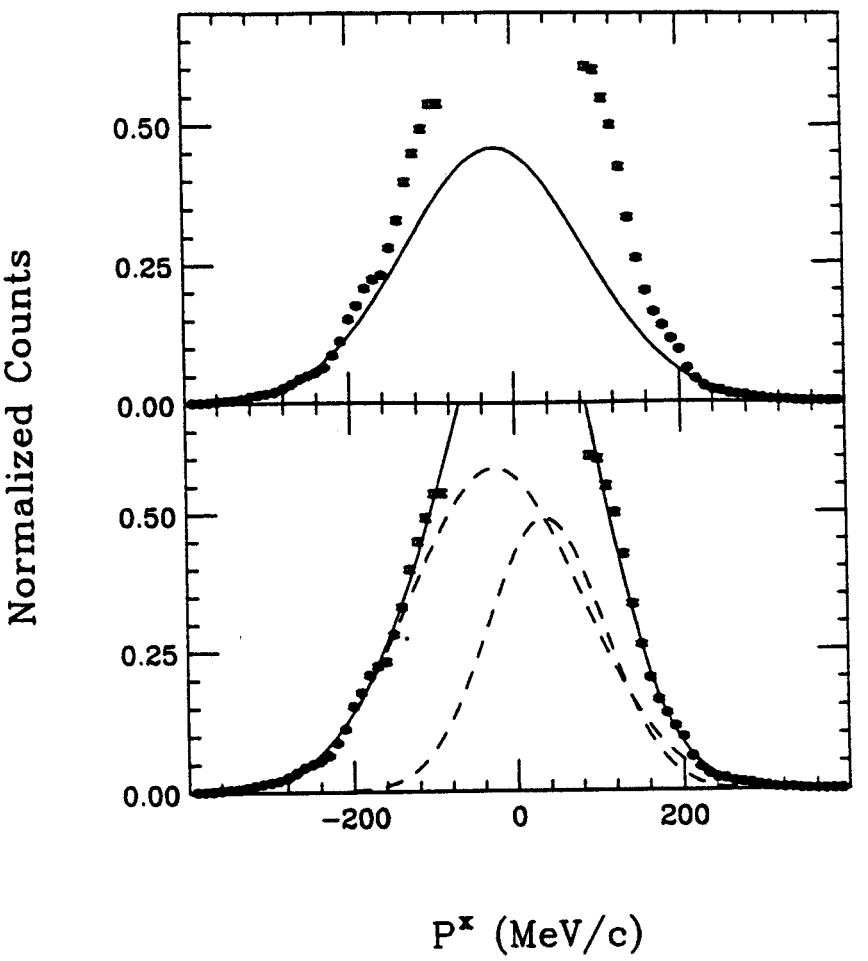


Figure 6.6: The proton transverse momentum distribution projected on the reaction plane for C+C reactions, gated on proton rapidities near the average rapidity of the projectile fragment. In the top panel, the high $|P^x|$ tails of the distribution have been fit using a single Gaussian (solid curve), which is unable to account for the low $|P^x|$ region. In the lower panel two Gaussians (dashed curves) are able to fit simultaneously the entire $P^x$ distribution.[Wils91]

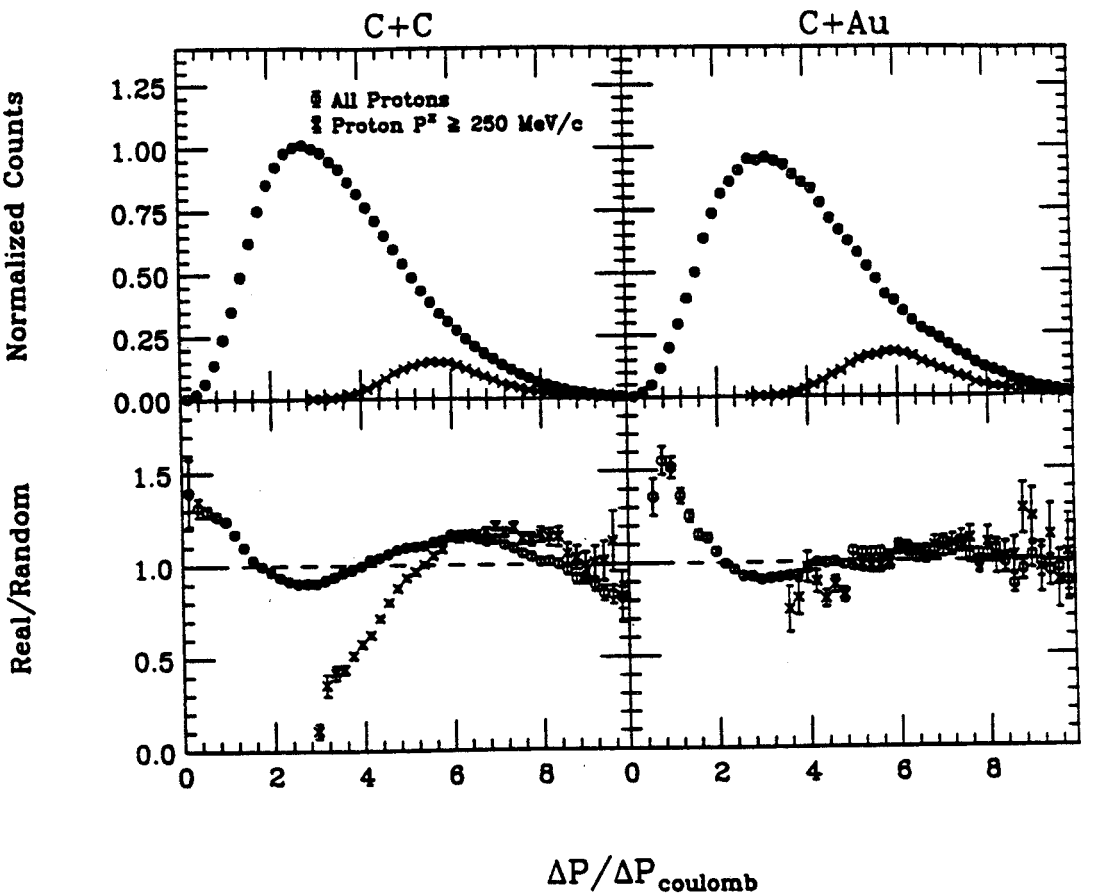


Figure 6.7: Yields (upper panels) and correlation functions (lower panels) for C+C (left hand panels) and C+Au (right hand panels) reactions. The momentum difference, $\Delta P$, has been divided by the expected momentum kick due to Coulomb repulsion. The data denoted by circles include all protons in coincidence with projectile fragments; the contribution from fragment sequential decay is minimized for the data denoted by crosses.[Wils91]

projectile fragments from different events to create the correlation functions shown in the lower panels. A strong correlation is observed for $\Delta P \approx \Delta P_{Coul}$, indicating the presence of projectile fragment sequential decay products in our proton sample. Thus, the positive slope of the data at mid-rapidity in Figure 6.3 is primarily due to the combination of a mid-rapidity source with a negative offset due to momentum conservation and projectile-like source at $y = y_{frag}$ with a positive offset, rather than mean field deflection.

In order to study the mid-rapidity source of protons, we next excluded protons with a $|P^x| \leq 250 MeV/c$ from the Gaussian fits. This minimizes the effect of protons produced by the relatively cool projectile-like source and is the largest practical cut that still allows us to characterize the $P^x$ distributions. The resulting data are denoted by crosses in fig 6.7. They demonstrate that the kinematical region dominated by projectile fragment sequential decay has been eliminated. For C+C, a correlation remains at high $\Delta P$ values, corresponding to the recoil effect discussed previously.

Using this high $|P^x|$ gate, we display $P_o^x$ vs. rapidity for the protons from the mid-rapidity source in Figure 6.8. Isolating this subset of the protons has removed the peak at the projectile fragment velocity, revealing a *negative* slope at mid-rapidity. Three points on either side of $y = \frac{1}{2} y_{beam}$ were fit with a straight line. For C+C we find the slope $(\frac{dp_o^x}{dy})$ to be $-26 \pm 3$ MeV/c, while for C+Au we obtain $-33 \pm 6$ MeV/c. This mid-rapidity slope, when multiplied by the beam rapidity in the center of mass system, is the "flow" parameter extracted from heavy-ion collisions at higher beam energies.[Gutb89a] The point at which the line crosses the rapidity axis corresponds to a velocity of -0.47 $\pm$ 0.02 c for the C+C system due to the negative offset discussed earlier. The C+Au system shows a crossing point of 0.06 $\pm$ 0.05 c, consistent with the velocity of the center of mass. Thus, the small $P_o^x$ offset in the C+Au system noted in the discussion of Figure 6.5 is caused by calculating the offset at mid-rapidity

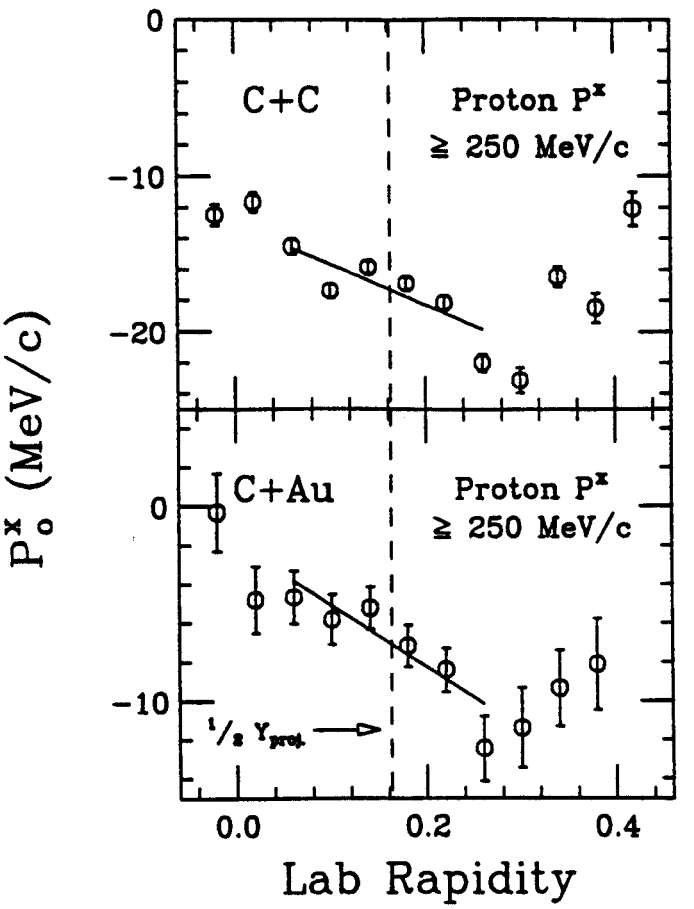


Figure 6.8: The center of the transverse momentum distribution in the reaction plane as a function of rapidity for C+C (upper panel) and C+Au (lower panel). The centers were extracted using single Gaussian fits to the high energy mid-rapidity protons ($|P^x| \geq 250 MeV/c$) and show a negative slope at mid-rapidity (solid line).[Wils91]

rather than the center of mass rapidity. There is a increase in $P_o^x$ at high rapidities in Figure 6.8 that may be due to contamination from the tail of the projectile-like source distribution. At high rapidities, the cross section from the mid-rapidity source decreases relative to that from the projectile-like source, so we would expect that the simple $|P^x|$ gate would no longer be sufficient to isolate protons from the mid-rapidity source.

In order to verify that the correlations observed in the data are not merely artifacts of our detector acceptance, we generated uncorrelated events using projectile fragments and protons taken from separate events. Analysis of these uncorrelated events proceeded in parallel with the real data, and it was found at each stage that the observed trends were not due to detector biases. As an example, we show in Figure 6.9 the centers of the transverse momentum distributions extracted using Gaussian fits to the uncorrelated events.

## 6.4 Discussion

Since the angular acceptances for projectile fragments extend down to the grazing angle for the C+Au system, approximately 6°, and since the fragments are only lightly damped, we can assume that the fragments in the peak of the velocity spectra were positively deflected by the repulsive Coulomb interaction. Although the grazing angle for the C+C reaction is less than 1°, a similar lightly damped peak is present. If we take the projectile fragments as being positively scattered, then the negative slope in the $P_o^x$ distribution implies that high energy mid-rapidity protons were simultaneously attractively deflected. The geometry of this concept is displayed in Figure 6.10.

As a check, we repeated the analysis dividing the events into projectile fragment velocity bins of weaker damping ($v_{frag.} \geq 85\%\ v_{beam}$) and stronger damping

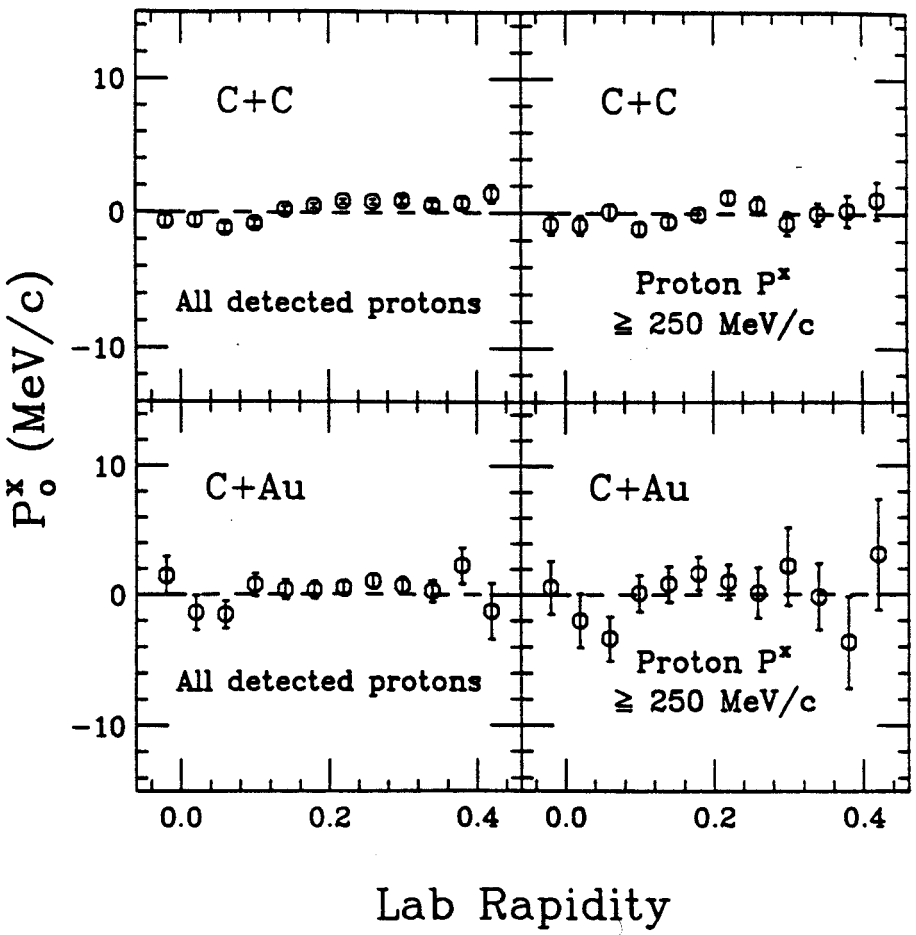


Figure 6.9: Analysis of uncorrelated events. The left hand panels correspond to the analysis shown in Figure 6.3; the right hand panels correspond to Figure 6.8.[Wils91]

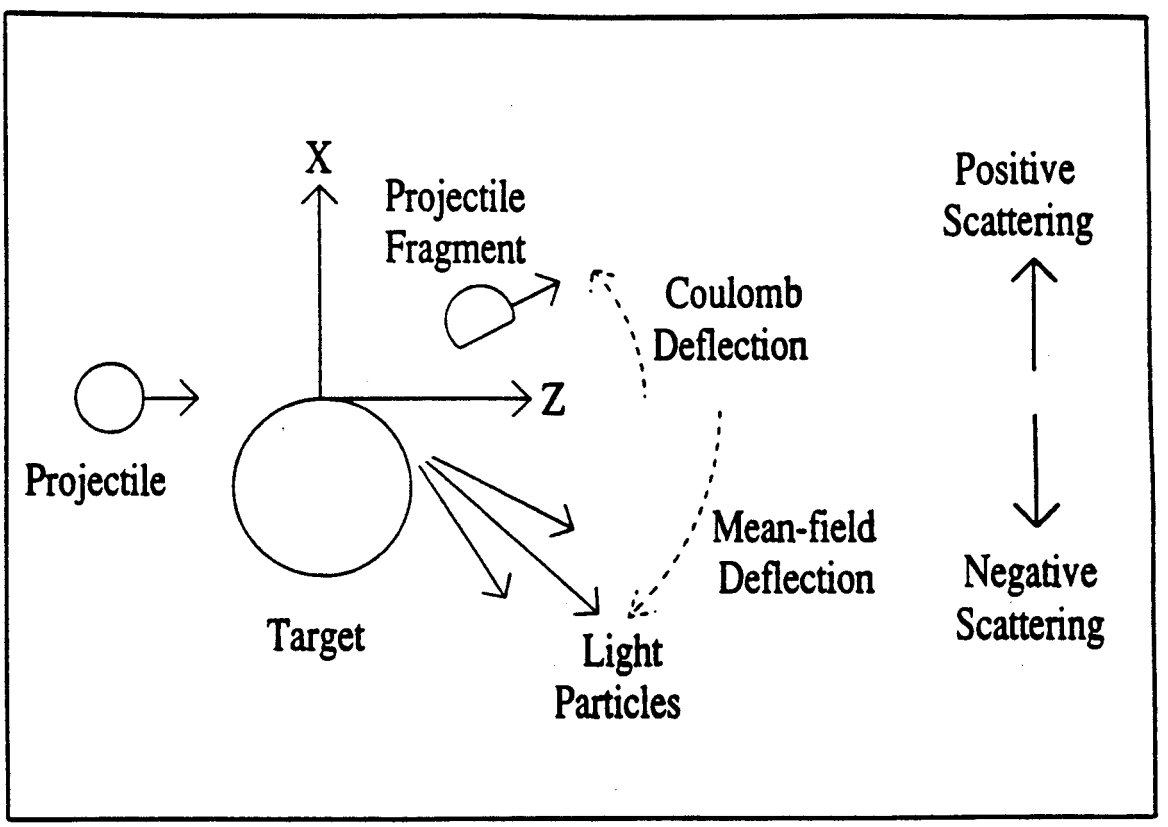


Figure 6.10: Schematic drawing of the proposed deflections in peripheral events.

($\approx 70\%\ v_{beam} \leq v_{frag.} \leq 80\%\ v_{beam}$). The overall trends of both data sets were identical to the velocity summed data, indicating that the fragments and the mid-rapidity source protons are deflected in opposite directions down to fragment velocities of $\approx \frac{3}{4} v_{beam}$.

Projectile fragmentation models which pre-divide the projectile prior to its collision with the target show similar behavior[Wada90, Mohr88, Roye87]; i.e. lightly damped projectile fragments are Coulomb trajectory dominated, but the part of the projectile closest to the target undergoes friction, is slowed, and is deflected attractively. In Figure 6.11 we show the results of a three body dynamical calculation performed by Wada et al.[Wada90] for 30 MeV/nucleon $^{32}$S + Ag reactions. The upper left hand panel of the figure shows the geometry used to pre-divide the $^{32}$S projectile into a $^{28}$Si projectile-like fragment and an alpha particle. The alpha particle will feel friction in its interaction with the target, separating the alpha from the projectile-like fragment. The range of impact parameters and angular orientations of the projectile, $b$ and $\tau$, which lead to a three body final state are shown in the right hand panel. The bottom panels display the velocity parallel and perpendicular to the beam direction for $^{4}$He and $^{28}$Si ions. Given this geometry, the simulations show that the projectile-like fragment is scattered away from the target, while the alpha particle is attractively deflected. In this model the target plays a passive role. Thus, simple projectile fragmentation alone cannot completely account for our observations because the C+Au data does not exhibit a recoil relationship between the projectile fragment and mid-rapidity protons, indicating strong target participation.

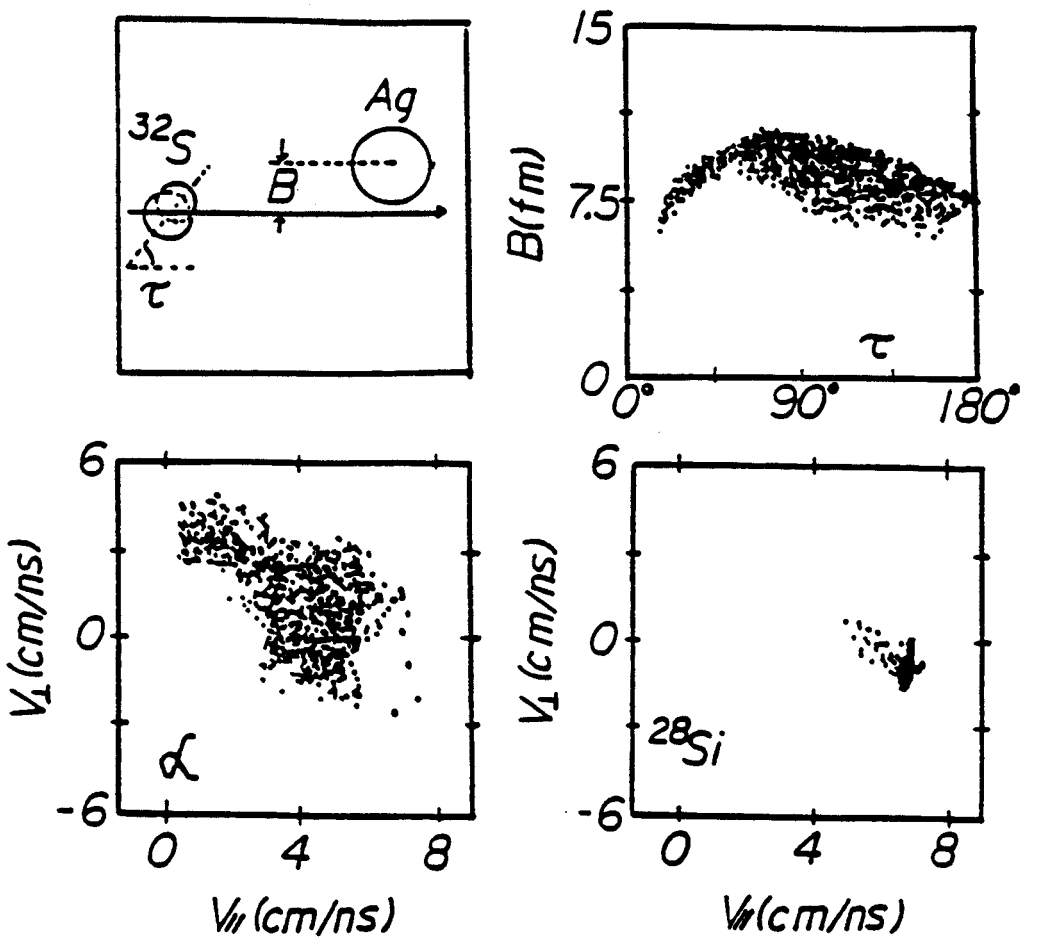


Figure 6.11: Results of a three body dynamical simulation of projectile fragmentation using the model of Royer et al.[Roye87] The simulation is described in the text.

## 6.5 Conclusion

The interplay between attractive and repulsive forces in peripheral events makes the application of the commonly used global transverse momentum analysis[Dani85] to find the reaction plane problematic because this technique assumes that all particles are deflected primarily in the same direction. If both projectile fragments and mid-rapidity light particles are detected, then restricting consideration to only the projectile fragments and their sequential decay products should allow for unambiguous characterization of the reaction plane. Light particles in the mid-rapidity region should only be included in the global transverse momentum analysis with weights that reflect their different flow direction.

This new approach to the analysis of peripheral heavy-ion collisions is promising since it provides both the magnitude and the *direction* of the transverse collective motion. Use of lightly damped projectile fragments to find the reaction plane should allow experimenters to observe directly the change in the sign of the flow as the beam energy is increased from the regime in which the attractive interaction dominates to that where repulsive nucleon-nucleon scattering takes over.

# Chapter 7

# Conclusion

## 7.1 Summary

From our observations of the azimuthal distributions of light particles produced in intermediate energy heavy-ion collisions, we can conclude that there is sufficient collective motion to cause substantial azimuthal anisotropies with respect to the reaction plane. We have verified the work of others who noted enhanced emission in the reaction plane, and extended their work to more symmetric systems and higher beam energies. In addition, we have noted a separate azimuthal anisotropy due to collective flow, and developed a parameterization which distinguishes between the two modes of collective motion.

Both forms of anisotropy are consistent with the influence of an attractive mean-field. From our BUU simulations, we conclude that the collective flow pattern may be established very early in the collision, and our studies of peripheral collisions show directly that the collective flow is an attractive deflection. Our BUU simulations also indicate that the in-plane enhancement is built up as the system rotates while emitting particles. Although the attractive mean-field is strong enough to bind the projectile and target into a rotating compound system, we have seen that the system is not well approximated as a sphere or any other stable shape. The residue oscillates,

usually but not always preferentially emitting particles in the plane. Thus, one of the important lessons learned from the simulations is the need to examine the development of theoretically predicted observables with time, an approach that is rarely taken.

Increasing the beam energy leads to a diminution of the azimuthal anisotropy. This can be understood in terms of the decreasing role of the attractive mean-field. The minimum in the collective flow around 85 MeV/nucleon for Ar+V is in line with BUU predictions that the hard core repulsive part of the mean-field should cause the onset of hydrodynamical side-splash near this beam energy. As for the general in-plane enhancement, increasing the beam energy may simply overcome the ability of the mean-field to form a compound rotating system. Thus the increasing isotropy adds to the experimental evidence that fusion to form a compound system becomes more and more incomplete as the beam energy increases. (See ref. [Hage89] and refs. therein.)

## 7.2 Directions for Future Research

The data in this thesis provide only a qualitative outline of the features of azimuthal distributions produced in these collisions. In order to make detailed comparisons with theory, the methods for estimating the accuracy of the reaction plane determination must be improved. The approach used in chap. 3 is not sufficient because it provides only a upper limit on the dispersion. It may be possible to extract this information from the variation of $D^2$ (defined in eq. 3.3) with the azimuthal angle of the reaction plane, drawing an analogy with the $\chi^2$ function.

Lack of accurate methods for evaluating the uncertainty in the reaction plane determination and then correcting the observed azimuthal distributions blocks several

avenues of investigation. For example, the dependence of $F_{ip}$ on impact parameter cannot be made clear without removing the effect of the changing reaction plane dispersion. We noted in sect. 5.4 that the saturation of $F_{ip}$ with increasing particle energy may be related to the uncertainty of the reaction plane determination. In view of the gains which an improved uncertainty estimate would allow, it is the pivotal issue to be resolved in future research.

Once this hurdle is overcome, comparisons should be made with more realistic BUU codes than the simple one employed in this thesis. The Coulomb force must be included in order to understand peripheral collisions such as those studied in chap. 6. As was also learned in the study of relativistic collisions, using beam energy evolution of the collective motion to constrain the equation of state of nuclear matter requires the most up-to-date theory of nucleon-nucleon interactions, including momentum dependent effects. In the end, fragment production must also be included in the microscopic models used to study intermediate energy nuclear collisions so that theory predictions can be accurately filtered through the detector acceptance.

For future experiments, the beam energy dependence of the Ar+V in-plane enhancement could be studied in greater detail. Lower energy thresholds would allow lower beam energies to be explored. One might expect that the in-plane enhancement has a *maximum* at lower beam energies, somewhere between the fusion barrier and the 35-55 MeV/nucleon beam energy regime where the enhancement is clearly weakening. This maximum should be related to the maximum angular momentum that a hot nuclear system can maintain, and could therefore shed light on the dynamics of highly excited nuclei. It would also be interesting to increase the beam energy above 100 MeV/nucleon to see when the out-of-plane squeeze-out begins. Just as the collective flow $E_{bal}$ beam energy has been proposed as an observable capable of constraining the equation of state, the cross over energy at which the mid-rapidity

in-plane enhancement is canceled by squeeze-out could also prove useful.

# Appendix A

# Trigger Stream

In this appendix we will examine the trigger system of the $4\pi$ Array. The diagram shown in Figure A.1 begins where the logic stream breaks off after the splitter shown in Figure 2.3.

The analog signals produced by the photomultiplier tubes travel along ribbon cables in groups of fifteen. (12 groups for the Main Ball, 3 for the Forward Array) The groups pass into Phillips 7106 leading edge discriminators whose thresholds are set to fire on particles that just punch into the $\Delta$E plastics. Since the discriminators contain 16 channels each, the last (16th) channel in each discriminator is unoccupied. The Phillips provide a "sum" output which consists of a square negative pulse whose amplitude is proportional to the number of channels above threshold in the discriminator. The 12 sum signals of the Main Ball and Forward Array are separately combined in an in-house analog summer. The complete sum of the Main Ball and Forward Array discriminators are further combined to provide a sum signal proportional to the total multiplicity of the entire detector system.

As noted in chap. 2, the array can take data in any one of three different trigger modes: Main Ball multiplicity, Forward Array multiplicity, and total system (Ball+Forward Array) multiplicity. These three trigger possibilities are realized by

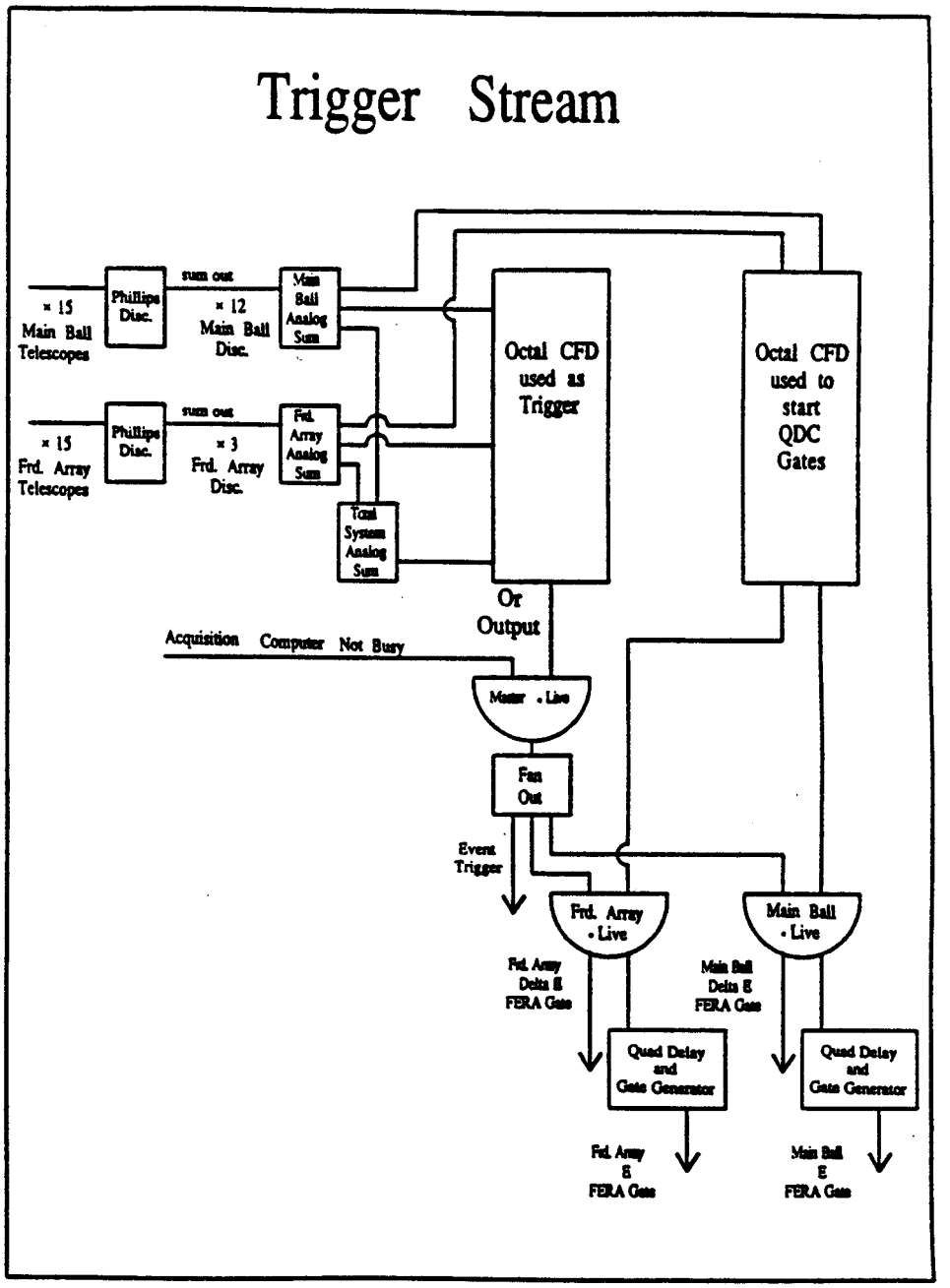


Figure A.1: Electronics diagram for the $4\pi$ trigger system.

passing the three corresponding sum signals into a constant fraction discriminator (CFD). The or output of the EG&G CCF8000 octal CFD shown on the left in Figure A.1 provides a logic signal which is used as the master trigger. The thresholds of the CFD are remotely programmable, enabling selection of multiplicity greater than or equal to a given value for any of the three inputs. A bit mask is loaded into the CFD to select the source of the trigger (Ball, Forward Array, or total system).

Once the presence of an event which meets the multiplicity requirements is established, we must check whether the data acquisition computer is free to record the event. This occurs in the AND gate labeled "Master·Live". If the computer is not busy, then an event trigger logic signal is created which tells the data acquisition system to read all QDCs (charge to digital converters) which contain signals above their set thresholds. The master and master·live signal are also sent to scaler modules which count the number of events seen and the number accepted. The ratio $\frac{\text{master·live}}{\text{master}}$ is called the "live-time" and 1.0−live-time tells what fraction of events were rejected because the computer was still processing the previous event. A typical value for the live time is 0.8 during an actual run. This information is valuable in choosing the optimum beam current to provide the maximum number of counts which can be recorded by the computer.

The timing for the signals arriving from the Forward Array is $\approx$ 10 ns behind those from the Main Ball. Since the $\Delta$E gates are only around 30 ns wide, the Main Ball and Forward Array cannot be used to trigger QDC gates for each other. Separate gate generation for the two sets of telescopes is achieved by using separate channels in the Octal CFD on the right. The thresholds of the two channels used in this discriminator are set so that the channels will fire if one or more of their detectors fired. Separate outputs for each of the two CFD channels (Ball and Forward Array) are used to start the gates.

Before the gating begins, an opportunity is provided to abort the gates if there is no event trigger. This prevents the gates from starting QDC conversion for unacceptable events which could then block good events later. This coincidence between the gates and the event trigger is required in the and gates labeled "Forward Array·Live" and "Main Ball·Live". Note that in order to have the Main Ball and Forward Array telescopes set their own timing, the gate triggers must arrive in the coincidence boxes *after* the event triggers.

The $\Delta$E gate must reach the QDCs quickly, so they are taken directly from the coincidence boxes. The E gates are delayed and stretched before being passed to the QDCs. All of the phoswich signals are digitized using Lecroy 4300B FERA (fast encoding and read out ADC) charge sensitive converters. Because they integrate the current over a given gate period, they are referred to as QDCs. The gates are shown along with the analog signals in Figure 2.3.

# Appendix B

# The $4\pi$ Filter Code

## B.1 Introduction

The filter code is a software representation of the acceptance of the $4\pi$ Array. In general, it is very difficult to correct experimental observations for the efficiency of a multi-element detector system. The filter code provides the simpler option of modifying the theoretical predictions for direct comparison to experimental results. Since the filtering must proceed on an event by event basis, however, this approach demands a high degree of sophistication from theoretical models. For instance, simulations that do not include clustering, such as BUU, are difficult to filter accurately. In such cases, although it is not possible to control for every aspect of the detector acceptance, the influence of several major factors may be evaluated.

The current version of the filter code contains the 215 phoswich telescopes of the $4\pi$ array in its Mark 1 configuration. The following characteristics of the detectors are included in the code:

- Angular and energy acceptances
- Response to different species of particles
- Shadowing due to the target support mechanism
- Tentative identification of particles that stop in the $\Delta$ E plastic

- Mis-identification due to multiple hits in one detector element

## B.2 The Original Filter

The sequence of steps used to filter a simulated event are displayed in Figure B.1. The operations listed in each box are completed for all of the particles in an event before proceeding to the next box.

First, the neutral particles (neutrons and $\gamma$-rays) are deleted. This could be improved in principle by simulating the detector response to these particles. For example, neutrons have about a 50% chance of colliding with a nucleus in the E plastic, which will cause scintillation as it recoils. This and similar effects may be included future versions of the filter.

Next, detector numbers are assigned to the particles. In general, this can be done by simply finding which detector center a particle falls closest to. If the two closest detectors are a hexagonal (hex) sub-element and a pentagonal (pent) sub-element from the Main Ball, then the task is a little more complex. Because the pent sub-elements are smaller than their hex counterparts, a particle can hit closer to a pent sub-element but still fall within the hex. An additional complication is the G-10 plastic rimming the front of the Main Ball modules. In the future, this plastic will be used to mount ion chambers in front of the phoswichs, but for now it is simply dead space. Particles which strike this plastic, or pass through any other empty zone are vetoed. With all of the dead zones taken into account, the array covers about 85% of $4\pi$ sr.

A phoswich telescope can only accurately identify and measure the energy of one particle per event. In the filter code as it now stands, when more than one particle

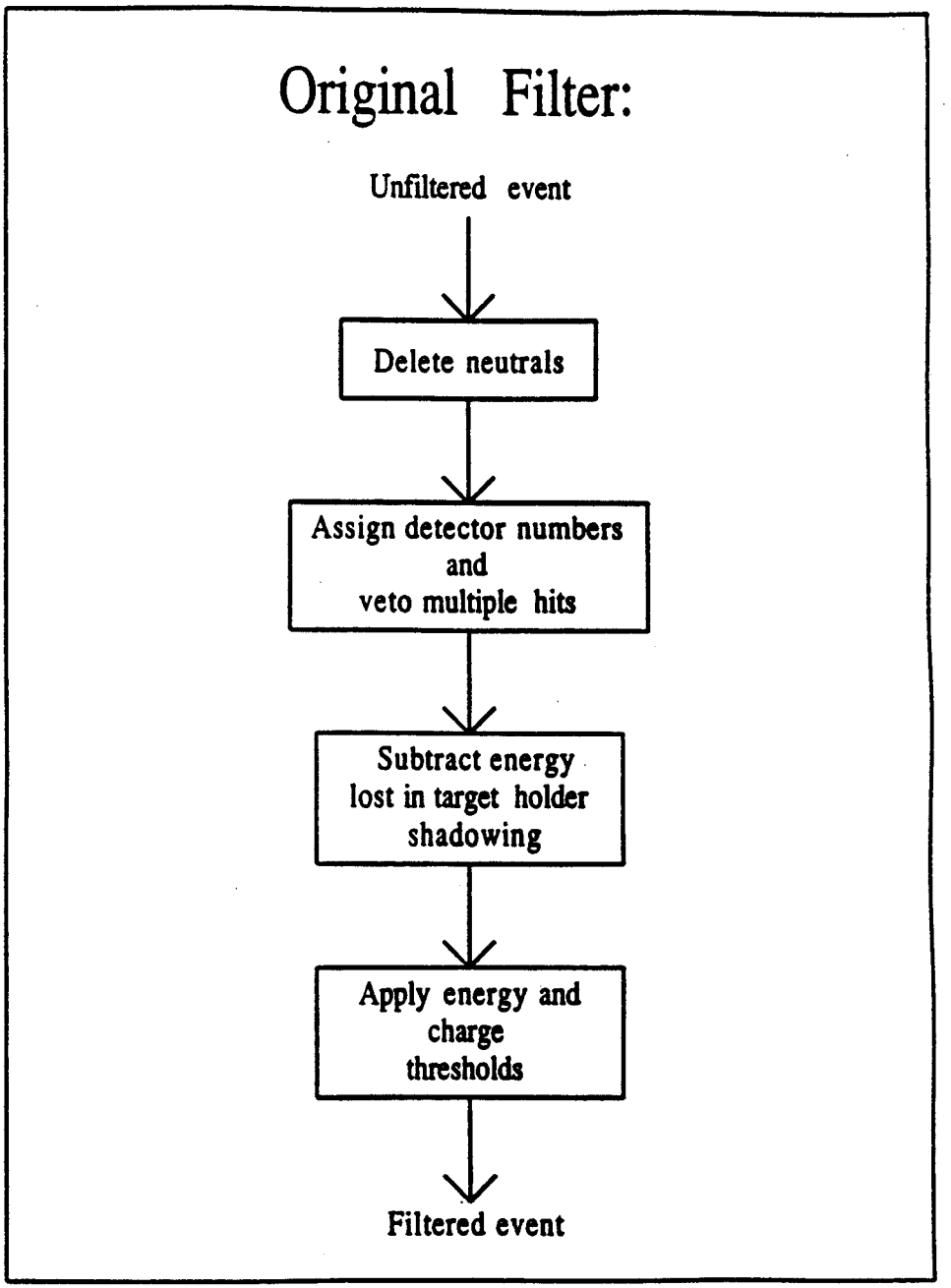


Figure B.1: Steps followed in the original simulated event filter.

strikes a single detector, it and all other particles striking that element are vetoed. Since neutrals have already been rejected, they cannot cause a multiple hit veto. Particles with very low energy or very high mass, like fission fragments, can cause a veto via multiple hits since particles outside the $4\pi$ energy and species acceptance have not yet been vetoed.

A more realistic method for handling multiple hits would be to simulate the phoswich response to the sum of the particles. The light response of each particle hitting a phoswich would be summed, perhaps using Monte Carlo techniques to include the energy resolution, and then the particle would be re-identified according to its $\Delta$E-E value just as for the real data. Although potentially CPU cycle intensive, this may be implemented in future versions of the filter code.

The next step involves the interaction between particles emitted from the collisions and the aluminium structure supporting the target foil. The distance traveled through the aluminium (if any) is calculated, and then the energy loss is computed. Note that heavy particles can be completely absorbed by the target holder. Tests using simple isotropic simulations such as those described in chaps. 3 and 4 suggest that the shadowing due to the target mechanism can create a pattern in the detected particles resembling flow, but at a much much weaker level than is observed in the data.

Finally, the energy and charge thresholds of the phoswichs are applied to the event. Particles that stop in the $\Delta$E are mid-identified in the same fashion as in the real data. The light response of the fast scintillator is calculated and the "best guess" identity and energy are assigned as described in chap. 2.

This version of the filter code was sufficiently advanced to produce the effects observed in the real azimuthal distributions by energy thresholds, angular granularity, and multiple hit exclusion as demonstrated in chap. 4. It was found to be prohibitively

slow when very high statistics simulations were required, so a new faster version was developed.

## B.3 The Fast Filter

The primary consumer of CPU cycles in the original filter code was the detector number assignment. A look-up table in polar and azimuthal angles ($180 \times 360$) was developed for a faster version. The fast filter was originally intended to be a stripped-down filter for quick preliminary analysis, but it will probably succeed the original in the end because it is so much quicker.

The procedure used to loop through an event with the fast filter is shown in Figure B.2. Besides the difference in the detector assignment technique, the fast filter vetoes low energy and high Z particles before checking for double hits. This modification is not expect to significantly alter the results, but it models the response of the scintillator more correctly.

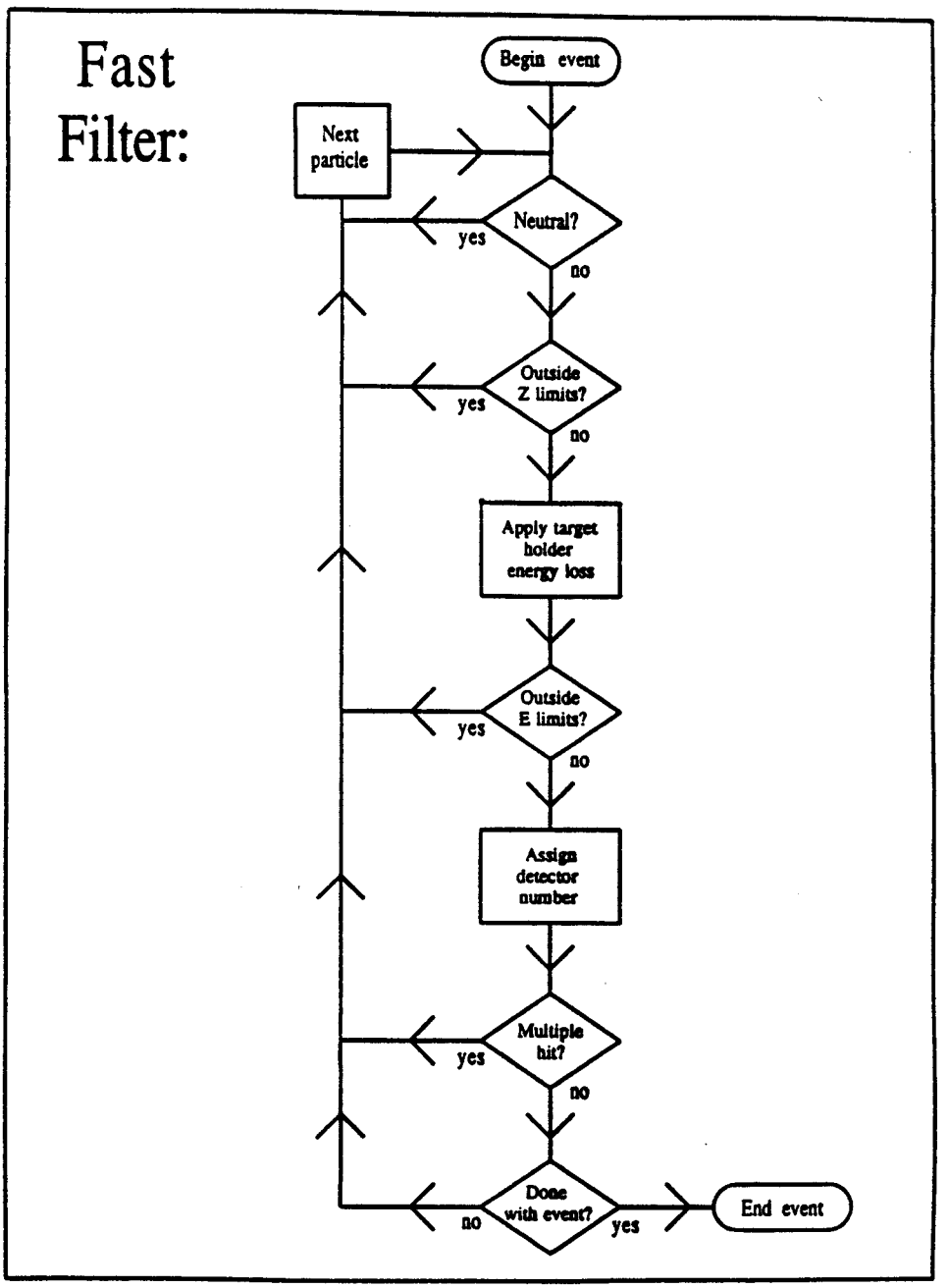


Figure B.2: Fast filter event loop.

# Appendix C

# Impact Parameter Determination

In this appendix we will review the method used to determine the impact parameter for $4\pi$ Array data. The discussion is based on the work of Ogilvie et al.[Ogil89a]

As the impact parameter decreases, the overlap volume of the projectile and target increases. The particles in the participant region form a mid-rapidity source which dominates the high energy portion of the energy spectra at polar angles near 90° in the c.m. frame. The projectile and target residues contribute little to the mid-rapidity region since, in the participant-spectator model, the spectator sources continue with nearly the same velocities that the projectile and target had prior to the collision. Thus the multiplicity of particles in the mid-rapidity region can be used as a measure of the participant source size and the impact parameter can be deduced. This reasoning was successfully applied to relativistic collisions by the Plastic Ball Group to examine collective flow as a function of impact parameter.[Gutb89a]

In intermediate energy collisions, the contributions from the projectile and target spectators overlap the mid-rapidity region. In order to see whether the multiplicity of mid-rapidity protons could still be used to determine the impact parameter, we performed simulations using the event generator FREESCO.[Fai86] This code employs the participant- spectator geometry to create sources which then decay into fragments

via classical statistics.

The results of the simulations are shown in Figure C.1 for unfiltered and filtered simulations of Ca+Ca collisions at beam energies of 40, 70, and 100 MeV/nucleon. The mid-rapidity gate is defined as

$$\frac{3}{4}y_{targ} \leq y \leq \frac{3}{4}y_{proj} \tag{C.1}$$

in the c.m. frame of reference, and the mid-rapidity charge is the multiplicity of protons summed over fragments appearing within this region during an event. For unfiltered peripheral collisions, there is very little mid-rapidity charge. For impact parameters less than $\approx 0.7b_{max}$, the spectators are slowed enough to fall inside the mid-rapidity gate. The energy thresholds of the $4\pi$ Array tend to exclude contributions from the projectile and target remnants and their sequential decay products, so in the filtered simulations mid-rapidity charge is still a good measure of the participant size. Therefore, the overlapping of the spectator and participant angular distributions is not a problem due to the energy and charge thresholds of the $4\pi$ Array.

Our method for sorting the events by centrality is to place four gates on the mid-rapidity charge to select out particular ranges of impact parameters. The values of the gates are chosen by inspection of filtered FREESCO runs for the system under consideration to correspond to mean impact parameters near 0.3, 0.5, 0.7, and 0.9 times $b_{max}$.

In order to verify that the impact parameter dependence of the mid-rapidity charge is not merely an artifact of the participant-spectator model incorporated into FREESCO, we examined He spectra at forward angles for the contributions from spectators. A peripheral event should produce many alphas near the beam velocity at forward angles due to sequential decay of the large projectile spectator. On the

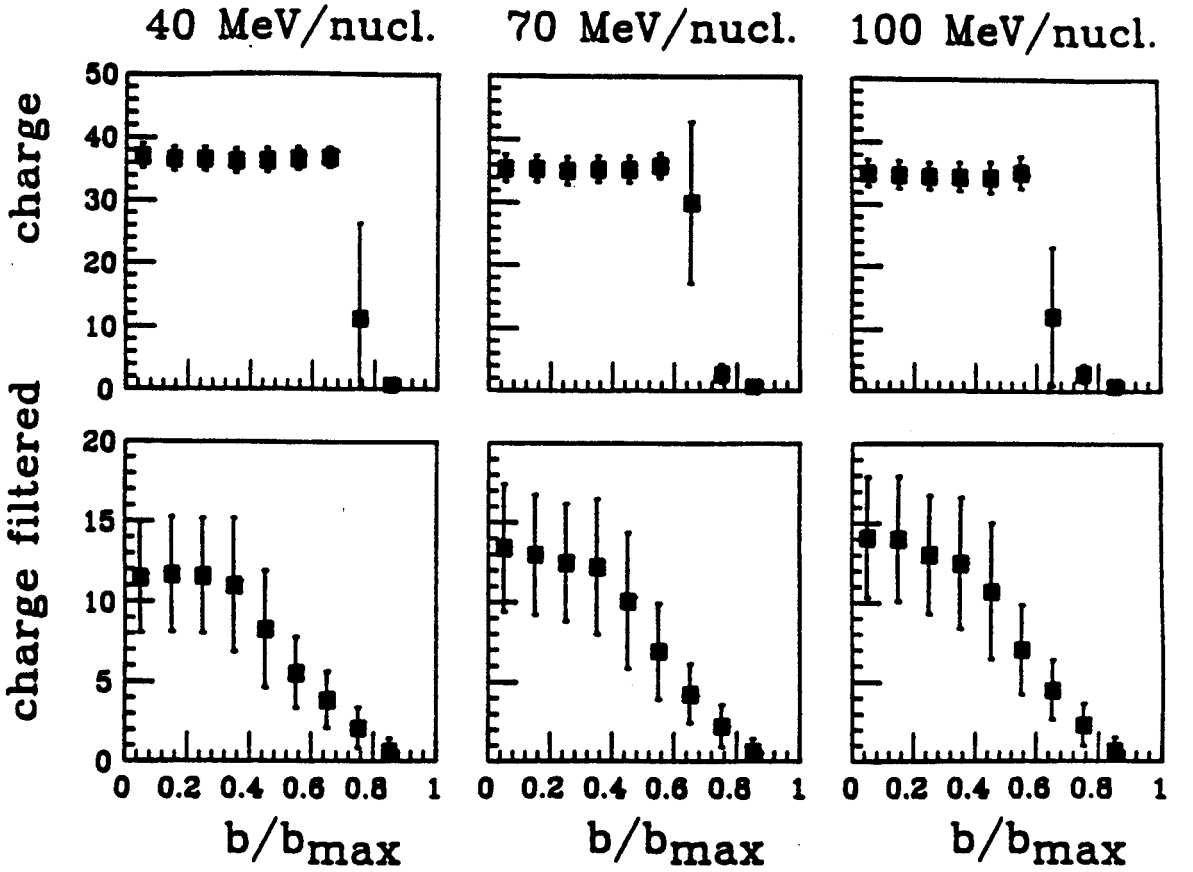


Figure C.1: Impact parameter dependence of mid-rapidity change in Ca+Ca FREESCO simulations. The data points represent the mean values and the error bars represent on standard deviation width at each impact parameter.[Ogil89a]

other hand, the projectile should be absorbed into the compound system during a central event. This pattern is confirmed in Figure C.2 by He particles produced in 50 MeV/nucleon C+C collisions. An alpha particle produced by projectile fragment sequential decay would have a kinetic energy of near 200 MeV. The peak in the He spectra near 200 MeV clearly vanishes for the highest mid-rapidity charge gate (1), demonstrating the correlation between high mid-rapidity charge and central events.

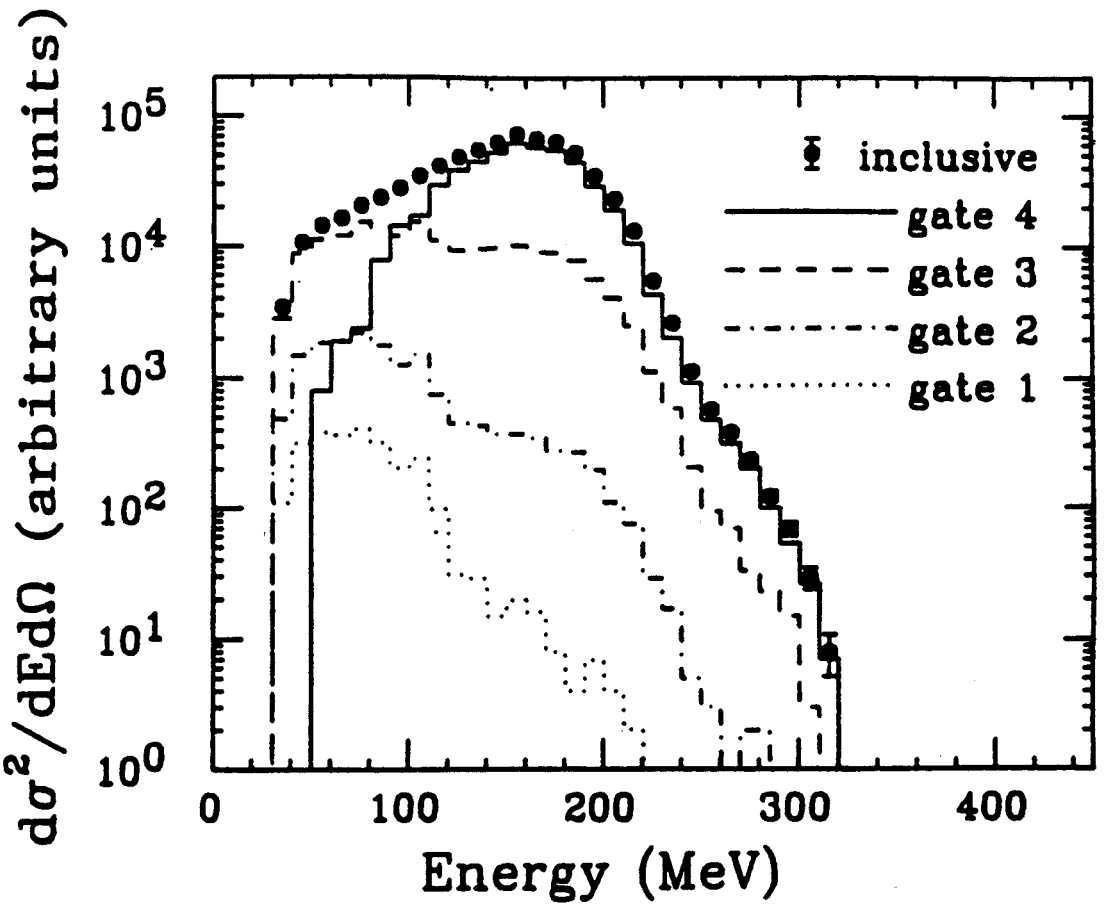


Figure C.2: Impact parameter dependence of He kinetic energy spectra at 7° from the beam axis in the lab frame produced by 50 MeV/nucleon C+C collisions. Mid-rapidity charge gates range from peripheral (4) to central (1).[Ogil89a]

# Appendix D

# Parameterization of Azimuthal Anisotropy

In addition to the anisotropy fractions presented in chap. 4, two other parameterizations have been used to characterize the azimuthal distributions produced in heavy-ion collisions. In this appendix we will derive the relationships between the parameterization used in this thesis and those favored by other authors.

## D.1 Peak/Valley Ratios

Peak/valley ratios, or in/out of plane ratios, are used by Tsang et al. to characterize the in-plane enhancement observed in heavy-ion collisions. The ratio $R$ is defined by

$$R = \frac{\left.\frac{dN}{d\phi}\right|_{\phi=0°}}{\left.\frac{dN}{d\phi}\right|_{\phi=90°}} \tag{D.1}$$

where $\phi$ is the azimuthal angle around the beam axis and $N$ is the number of particles detected. The connection with the $F_{ip}$ parameter used in this thesis is

$$R = \frac{1 + \pi(F_{ip} - \frac{1}{2})}{1 - \pi(F_{ip} - \frac{1}{2})} \tag{D.2}$$

and

$$F_{ip} = \frac{1}{2} + \frac{R - 1}{\pi(R + 1)} \tag{D.3}$$

if the azimuthal distribution is of the form

$$\frac{dN(\phi)}{d\phi} \propto 1 + a\cos 2\phi. \tag{D.4}$$

We chose not to use this parameterization because it is inappropriate for describing flow. Even if the ratio is taken between $\phi = 0°$ and $\phi = 180°$, there are still problems with the symmetry of the deviation from isotropy as a function of rapidity. This can be illustrated by a simple example. Consider a case in which twice as many particles appear on the forward flow side as compared to the opposite side of the reaction plane at high rapidities. Then, for a symmetric system, at low rapidities the forward flow side would contain half as many particles as its opposite. Our $F_{fs}$ parameter would go from $\frac{1}{3}$ to $\frac{2}{3}$, passing through $\frac{1}{2}$ at mid-rapidity. The deviation from isotropy would go from -0.17 to +0.17, making a symmetric curve like that shown in Figure 4.7. Now consider the behavior of $R$ taken between opposite sides of the reaction plane. At high rapidities $R = 2$, while at low rapidities $R = \frac{1}{2}$. Isotropy is represented by a ratio of 1, so the deviation from isotropy goes from $-\frac{1}{2}$ to 1, and does not cross isotropy at mid-rapidity. The effect is to exaggerate the flow in the forward c.m. direction at the expense of the flow in the backward direction.

## D.2 Expansion in Cosines

For a particular value of the parallel rapidity, flow causes particles to be deflected preferentially to one side of the reaction plane. This behavior can be included into eq. D.4 by the addition of another term:

$$\frac{dN(\phi, y)}{d\phi} \propto 1 + a(y)\cos 2\phi + b(y)\cos(\phi). \tag{D.5}$$

In eq. D.5 the parameter $a(y)$ is sensitive to the enhancement that occurs simultaneously on both sides of the reaction plane (rotation), while $b(y)$ is sensitive to

flow. This parameterization has been employed by the Plastic Ball Group[Gutb90] and others.[Welk88] Integrating eq. D.5 over the appropriate $\phi$ regions, we find that our anisotropy parameters are given by

$$F_{ip} = \frac{1}{2} + \frac{a}{\pi} \tag{D.6}$$

and

$$F_{fs} = \frac{1}{2} + \frac{b}{\pi}. \tag{D.7}$$

This demonstrates that $F_{ip}$ is only sensitive to rotation and $F_{fs}$ is only sensitive to flow within this cosine parameterization.

# Bibliography


[Ande76] C.G. Andersson, S.E. Larsson, G. Leander, P. Möller, S.G. Nilsson, I. Ragnarsson, S. Aberg, R. Bengtsson, J. Dudek, B. Nerlo-Pomorska, K. Pomorski, and Z. Szymański, Nucl. Phys. **A268**, 205 (1976)

[Artu73] A.G. Artukh, G.F. Gridnev, V.L. Mikheec, V.V. Volkov, and J. Wilczyński, Nucl. Phys. **215**, 91 (1973)

[Asah87] K Asahi, M. Ishihara, H. Takanashi, M. Koguchi, M. Adachi, M. Fukuda, N. Inabe, D. Mikolas, D. Morrissey, D. Beaumel, T. Ichihara, T. Kubo, T. Shimoda, H. Miyatake, and N. Takahashi, RIKEN preprint, RIKEN-AF-NP-87 (1987)

[Baur87] W. Bauer, G.F. Bertsch, and S. Das Gupta, Phys. Rev. Lett. **58**, 863 (1987)

[Baur91] The BUU calculations presented in chap. 5 were performed by professer Wolfgang Bauer.

[Bert84] G.R. Bertsch, H. Kruse, and S. Das Gupta, Phys. Rev. C **29**, 673 (1984)

[Bert87] G.F. Bertsch, W.G. Lynch, and M.B. Tsang, Phys. Lett. **189B**, 384 (1987)

[Bert88] G.F. Bertsch and S. Das Gupta, Phys. Rep. bf 160, 190 (1988)

[Bicr85] BICRON Corporation data sheets

[Bona87] A. Bonasera and L.P. Csernai, Phys. Rev. Lett. **59**, 630 (1987)

[Bond79] J.P. Bondorf, J.N. De, A.O.T. Karvinen, G. Fái, and B. Jakobsson, Phys. Lett. **84B**, 162 (1979)

[Bond80] J.P. Bondorf, J.N. De, A.O.T. Karvinen, G. Fái, B. Jakobsson, and J. Randrup, Nucl. Phys. **A333**, 285 (1980)

[Bruc88] A. Brucker, B. Lindl, M. Bantel, H.Ho, R. Muffler, L. Schad, M.G. Trauth, and J.P. Wurm, Phys. Lett. **206b**, 13 (1988)

[Buch84] G. Buchwald, G. Graebner, J. Theis, J. Maruhn, W. Greiner, and H. Stöcker, Phys. Rev. Lett. **52**, 1594 (1984)

[Bibb85] K. Van Bibber and A. Sandoval, **Treatise on Heavy-Ion Science 7**, 333 (1985)

[Cebr90] D. Cebra, PhD. Thesis, Michigan State University, 161

[Chit86] C.B. Chitwood, D.J. Fields, C.K. Gelbke, D.R. Klesch, W.G. Lynch, M.B. Tsang, T.C. Awes, R.L. Ferguson, F.E. Obenshain, F. Plasil, R.L. Robinson, and G.R. Young, Phys. Rev. C **34**, 858 (1986)

[Cohe74] S. Cohen, F. Plasil, and W.J. Swiatecki, Ann. Phys. **82**, 557 (1974)

[Cugn83] J. Cugnon and D. L'Hôte, Nucl. Phys. **A397**, 519 (1983)

[Dani85] P. Danielewicz and G. Odyniec, Phys. Lett. **157B**, 146 (1985)

[Dani88] P. Danielewicz, H. Ströbele, G. Odyniec, D. Bangert, R. Bock, R. Brockmann, J. W. Harris, H.G. Pugh, W. Rauch, R.E. Renfordt, A. Sandoval, D. Schall, L.S. Schroeder, and R. Stock, Phys. Rev. C **38**, 120 (1988)

[Dilm82] F.A. Dilmanian, D.G. Sarantities, M. Jääskeläien, H. Puchta, R. Wookward, J.R. Beene, D.C. Hensley, M.L. Halbert, R. Novotny, L. Adler, R.K. Choudhury, M.N. Namboodiri, R.P. Schmitt, and J.B. Natowitz, Phys. Rev. Lett. **49**, 1909 (1982)

[Fai86] G. Fai and J. Randrup, Phys. Commun. **42**, 385 (1986)

[Fox88] D. Fox, D.A. Cebra, J. Karn, C. Parks, A.Pradhan, A. Vander Molen, J. van der Plicht, G.D. Westfall, W.K. Wilson, and R.S. Tickle, Phys. Rev. C **38**, 146 (1988)

[Gale87] C. Gale, G. Bertsch, and S. Das Gupta, Phys. Rev. C **35**, 1666 (1987)

[Garc91] F. Garcias, V. De La Mota, B. Remaud, G. Royer, and F. Sébille, Phys. Lett. **265B**, 311 (1991)

[Glen88] N.K. Glendenning, Phys. Rev. C **37**, 2733 (1988)

[Gont88] P.L. Gonthier, J.D. Lenters, M.T. Vonk, D.A. Cebra, W.K. Wilson, A. Vander Molen, J. Karn, S. Howden, A. Nadasen, J.S. Winfield, and G.D. Westfall, submitted to Phys. Rev. C

[Greg87] C. Gregoire, B. Renaud, F. Sébille, L. Vinet, and Y. Raffray, Nucl. Phys. **A465** 317 (1987)

[Grei85] W. Greiner and H. Stöcker, Sci. Amer. **252**, 76 (Jan. 1985)

[Gutb89a] H.H. Gutbrod, A.M. Poskanzer, and H.G. Ritter, Rep. Prog. Phys. **52**, 1267 (1989)

[Gutb89b] H.H. Gutbrod, k.H. Kampert, B.W. Kolb, A.M. Poskanzer, H.G. Ritter, and H.R. Schmidt, Phys. Lett. **216B**, 267 (1989)

[Gutb90] H.H. Gutbrod, K.H. Kampert, B. Kolb, A.M. Poskanzer, H.G. Ritter, R. Schicker, and H.R. Schmidt, Phys. Rev. C **42**, 640 (1990)

[Gyul82] M. Gyulassy, K.A. Frankel, and H. Stöcker, Phys. Lett. **110B**, 185 (1982)

[Hage89] K. Hagel, A. Péghaire, G.M. Jin, D. Cussol, H. Doubre, J. Péter, F. Saint-Laurent, G. Bizard, R. Brou, M. Louvel, J.P. Patry, R. Regimbart, J.C. Steckmeyer, B. Tamain, Y. Cassagnou, R. Legrain, C. Lebrun, E. Rosato, R. Macgrath, S.C. Jeong, S.M. Lee, Y. Nagashima, T. Nakagawa, M. Ogihara, J. Kasagi, and T. Motobayashi, Phys. Lett. **229B**, 20 (1989)

[Harr89] J.W. Harris, B.V. Jacak, K.-H. Kampert, G. Claesson, K.G.R. Doss,R. Ferguson, A.I. Gavron, H.-A. Gustafsson, H. Gutbrod, B. Kolb, F. Lefebvres, A.M. Poskanzer, H.-G. Ritter, H.R. Schmidt, L. Teitelbaum, M. Tincknell, S. Weiss, H. Wieman, and J. Wilhelmy, Nucl. Phys. **A471**, 241c (1987)

[Hill53] D.L. Hill and J.A. Wheeler, Phys. Rev. **89**, 1102 (1953)

[Ho87] H. Ho, R. Albrecht, W. Duennweber, G. Graw, S.G. Steadman, J.P. Wurm, D. Disdier, V. Rauch, and F. Scheibling, Z. Phys. **A283**, 235 (1987)

[Krof91] D. Krofcheck, D.A. Cebra, M. Cronqvist, R. Lacey, T. Li, C.A. Ogilvie, A. Vander Molen, K. Tyson, G.D. Westfall, W.K. Wilson, J.S. Winfield, A. Nadasen, and E. Norbeck, Phys. Rev. C **43**, 350 (1991)

[Krus85] H. Kruse, B.V. Jacak, and H. Stöcker, Phys. Rev. Lett. **54**, 289 (1985)

[Lace87] R.A. Lacey, PhD. Thesis, State University of New York at Stoney Brook, 15

[Lenk89] R.J. Lenk, and V.R. Pandharipande, Phys. Rev. C **39**, 2242 (1989)

[Li91] Tong Li, private communication

[Maij87] Z. Maijka, D.G. Sarantites, L.G. Sobotka, K. Honkanen, E.L. Dines, L.A. Dines, L.A. Adler, L. Ze, M.L. Halbert, J.R. Beene, D.C. Hensley, R.P. Schmitt, and G. Nebbia, Phys. Rev. Lett. **58**, 322 (1987)

[Mohr88] K. Möhring, T. Srokowski, D.H.E. Gross, and H. Homeyer, Phys. Lett. **203B**, 210 (1988)

[Moli85a] J.J. Molitoris and H. Stöcker, Phys. Rev. C **32**, 346 (1985)

[Moli85b] J.J. Molitoris, D. Hahn and H. Stöcker, Nuc. Phys. **A447**, 13c (1985)

[Morr84] D.J. Morrissey, W. Benenson, E. Kashy, B. Sherrill, A.D. Pantogiotou, R.A. Blue, R.M. Ronningen, J. van der Plicht, and H. Utsunomiya, Phys. Lett. bf 148B, 432 (1984)

[Naya89] T.K. Nayak, T. Murakami, W.G. Lynch, K. Swartz, D.J. Fields, C.K. Gelbke, Y.D. Kim, J. Pochodzalla, M.B. Tsang, H.M. Xu, F. Zhu, and K. Kwiatkowski, Phys. Rev. Lett. **62**, 1021 (1989)

[Nord28] L.W. Nordheim, Proc. Roy. Soc. (London) **A119**, 689 (1928)

[Ogil89a] C.A. Ogilvie, D.A. Cebra, J. Clayton, S. Howden, J. Karn, A. Vander Molen, G.D. Westfall, W.K. Wilson, and J.S. Winfield, Phys. Rev. C **40**, 654 (1989)

[Ogil89b] C.A. Ogilvie, D.A. Cebra, J. Clayton, P. Danielewicz, S. Howden, J. Karn, A. Nadasen, A. Vander Molen, G.D. Westfall, W.K. Wilson, and J.S. Winfield, Phys. Rev. C **40**, 2592 (1989)

[Ogil89c] C.A. Ogilvie, D.A. Cebra, J. Clayton, P. Danielewicz, S. Howden, J. Karn, A. Nadasen, A. Vander Molen, G.D. Westfall, W.K. Wilson, and J.S. Winfield, Phys. Lett. **231B**, 35 (1989)

[Ogil90] C.A. Ogilvie, W. Bauer, D.A. Cebra, J. Clayton, S. Howden, J. Karn, A. Nadasen, A. Vander Molen, G.D. Westfall, W.K. Wilson, and J.S. Winfield, Phys. Rev. C **42**, R10 (1990)

[Part88] Particle Data Group, Phys. Lett **204b**, 126 (1988)

[Peil89] G. Peilert, H. Stöcker, W. Greiner, A. Rosenhauer, A. Bohnet, and J. Aichelin, Phis. Rev. C **39**, 1402 (1989)

[Péte90] J. Péter, J.P. Sullivan, D. Cussol, G. Bizard, R. Brou, M. Louvel, J.P. Patry, R. Regimbart, J.C. Steckmeyer, B. Tamain, E. Crema, H. Doubre, K. Hagel, G.M. Jin, A. Péghaire, F. Saint-Laurent, Y. Cassagnou, R.Legrain, C. Lebrun, E. Rosato, R. Macgrath, S.C. Jeong, S.M. Lee, Y. Nagashima, T. Nakagawa, M. Ogihara, J. Kasagi, and T. Motobayashi, Phys. Lett. **237b**, 187 (1990)

[Poch85] J. Pochodzalla, W.A. Friedman, C.K. Gelbke, W.G. Lynch, M. Maier, D. Ardouin, H. Delagrange, H. Doubre, C. Grégoire, A. Kyanowski, W. Mittig, A. Péhaire, J. Péter, F. Saint-Laurent, Y.P. Viyogi, B. Zwieglinski, G. Bizard, F. Lefèbveres, B. Tamain, and J. Québert, Phys. Rev. Lett. **55**, 177 (1985)

[Rand87] J. Randrup and R. Vandenbosch, Nucl. Phys. **A474**, 219 (1987)

[Rabe87] H.J. Rabe, K.D. Hildenbrand, U. Lynen, W.F.J. Müller, H. Sann, H. Stelzer, W. Trautmann, R. Trockel, R. Wada, J. Pochodzalla, E. Eckert, P. Kreutz, A. Kühmichel, N. Brummund, R. Glasow, K.H. Kampert, R. Santo, and D. Pelte, Phys. Lett. **196B**, 439 (1987)

[Rive82] M.F. Rivet, D. Logan, J.M. Alexander, D. Guerreau, E. Duek, M.S. Zisman, and M. Kaplan, Phys. Rev. C **25**, 2430 (1982)

[Robe79] M.C. Robel, Lawerence Berkeley Laboratory report, LBL-8181 (1979)

[Roye87] G. Royer, Y. Raffray, A. Oubahadou, and B. Remaud, Nucl. Phys. **A466**, 139 (1987)

[Schm90] R.P. Schmidt and B.K. Srivastava, Z. Phys. A. **335**, 49 (1990)

[Schm91] H.R. Schmidt, GSI Report, GSI-91-03, ISSN 0171-4546 (1991)

[Shar89] M.M. Sharma, W. Stocker, P Gleissl, and M. Brack, Nucl. Phys. **A504**, 337 (1989)

[Step65] F.S. Stephens, N.L. Lark, and R.M. Diamond, Nucl. Phys. **63**, 82 (1965)

[Stöc80] H. Stöcker, J.A. Maruhn, and W. Greiner, Phys. Rev. Lett. **44**, 725 (1980)

[Stöc82] H. Stöcker, L.P. Csernai, G. Grabner, G. Buchwald, H. Kruse, R.Y. Cusson, J.A. Maruhn, and W. Greiner, Phys. Rev. C **25**, 1873 (1982)

[Stöc86] H. Stöcker and W. Greiner, Phys. Rep. **137**, 279 (1986)

[Suli90] J.P. Sullivan, J Péter, D. Cussol, G. Bizard, R. Brou, M. Louvel, J.P. Patry, R. Regimbart, J.C. Steckmeyer, B. Tamain, E. Crema, H. Doubre, K. Hagel, G.M. Jin, A. Péghaire, F. Saint-Laurent, Y. Cassagnou, R. Lebrun, E. Rosato, R. Macgrath, S.C. Jeong, S.M. Lee, Y. Nagashima, T. Nakagawa, M. Ogihara, J. Kasagi, and T. Motobayashi, Phys. Lett. **249B**, 8 (1990)

[Trau84] W. Trautmann, Ole Hansen, H. Tricoire, W. Hering, R. Ritzka, and W. Trombik, Phys. Rev. Lett. **53**, 1630 (1984)

[Tsan84a] M.B. Tsang, W.G. Lynch, C.B. Chitwood, D.J. Fields, D.R. Klesch, C.K. Gelbke, G.R. Young, T.C. Awes, R.L. Ferguson, F.E. Obenshain, F. Plasil, and R.L. Robinson, Phys. Lett. **148B**, 265 (1984)

[Tsan84b] M.B. Tsang, C.B. Chitwood, D.J. Fields, C.K. Gelbke, D.R. Klesch, W.G. Lynch, K. Kwiatkowski, and V.E. Viola, Jr., Phys. Rev. Lett. **52B**, 1967 (1984)

[Tsan86] M.B. Tsang, R.M. Ronningen, G. Bertsch, Z. Chen, C.B. Chitwood, D.J. Fields, C.K. Gelbke, W.G. Lynch, T. Nayak, J. Pochodzalla, T. Shea, W. Trautmann, Phys. Rev. Lett. **57**, 559 (1986)

[Tsan89] M.B. Tsang, G.F. Bertsch, W.G. Lynch, M. Tohyama, Phys. Rev. C **40**, 1685 (1989)

[Tsan90] M.B. Tsang, Y.D. Kim, N. Carlin, Z. Chen, C.K. Gelbke, W.G. Gong, W.G. Lynch, T. Murakami, T. Nayak, R.M. Ronningen, H.M. Xu, F. Zhu, L.G. Sobotka, D.W. Stracener, D.G. Sarantities, Z. Majka, and V. Avenante, Phys. Rev. C **42**, R15 (1990)

[Uehl33] E.A. Uehling and G.E. Uhlenbeck, Phys. Rev. **43**, 552 (1933)

[Vaz83] L.C. Vaz and J.M. Alexander, Phys. Rep. **97**, 1 (1983)

[Wada90] R. Wada, D. Fabris, M. Gonin, M. Gui, K. Hagel, Y. Lou, D. Utley, J.B. Natowitz, G. Nebbia, R. Billerey, B. Cheynis, A. Demeyer, D. Drain, D. Guinet, C. Pastor, L. Vagneron, K. Zaid, J. Alarja, A. Giorni, D. Heuer, C. Morand, B. Viano, C. Mazur, C. Ngô, S. Leray, R. Lucas, M. Ribrag, and E. Tomasi, Texas A&M Cyclotron Institute preprint, #90-10, submitted to Phys. Rev. C

[Welk88] G.M. Welke, M. Prakash, T.T.S. Kuo, S. Das Gupta, and C. Gale, Phys. Rev. C **38**, 2101 (1988)

[West76] G.D. Westfall, J. Gosset, P.J. Johansen, A.M. Poskanzer, W.G. Meyer, H.H. Gutbrod, A. Sandoval, and R. Stock, Phys. Rev. Lett. **37**, 1202 (1976)

[West82] G.D. Westfall, B.V. Jacak, N. Anataraman, M.W. Curtin, G.M. Crawley, C.K. Gelbke, B. Hasselquist, W.G. Lynch, D.K. Scott, B.M. Tsang, M.J. Murphy, T.J.M. Symons, R. Legrain, T.J. Majors, Phys. Lett. **116B**, 118 (1982)

[West85] G.D. Westfall, J.E. Yurkon, J. Van der Plicht, Z.M. Koenig, B.V. Jacak, R. Fox, G.M. Crawley, M.R. Maier, and B.E. Hasselquist, Nucl. Instr. and Meth. **A238**, 347 (1985)

[Wilc73] J. Wilczyński, Phys. Lett. **47B**, 484 (1973)

[Wilk52] D.H. Wilkinson, Rev. Sci. Instr. **23** 414 (1952)

[Wils90] W.K. Wilson, W. Benenson, D.A. Cebra, J. Clayton, S. Howden, J. Karn, T. Li, C.A. Ogilvie, A. Vander Molen, G.D. Westfall, J.S. Winfield, B. Young, and A. Nadasen, Phys. Rev. C **41**, R1881 (1990)

[Wils91] W.K. Wilson, D. Cebra, S. Howden, J. Karn, D. Kroftcheck, R. Lacey, T. Li, A. Nadasen, T. Reposeur, A. Vander Molen, C.A. Ogilvie, G.D. Westfall, and J.S. Winfield, submitted to Phys. Rev. C

[Wong90] S.S.M Wong, **Introductory Nuclear Physics** (Prentice-Hall Enflewood Cliffs, New Jersey) p. 180 (1990)

[Xu90] H.M. Xu, W.G. Lynch, P. Danielewicz, and G.F. Bertsch, Phys. Rev. Lett. **65**, 843 (1990)

[Yari79] Y. Yariv and Z. Fraenkel, Phys. Rev. C **20**, 2227 (1979)